

# Studies of Chamber Organic Aerosol Using an Aerodyne High-Resolution Time-of-Flight Aerosol Mass Spectrometer

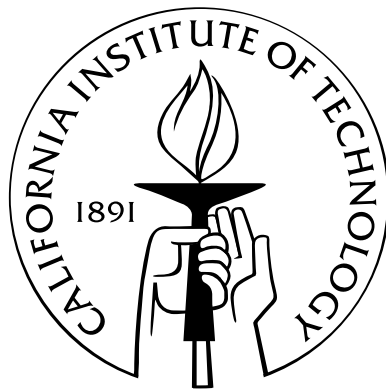
Thesis by

Puneet Singh Chhabra

In Partial Fulfillment of the Requirements

for the Degree of

Doctor of Philosophy



California Institute of Technology

Pasadena, California

2011

(Defended May 5, 2011)

© 2011

Puneet Singh Chhabra

All Rights Reserved

ਨਿਰਭਉ ਭਏ ਸਗਲ ਭਉ ਮਿਟਿਆ ਰਾਖੇ ਰਾਖਨਹਾਰੇ ॥  
ਐਸੀ ਦਾਤਿ ਤੇਰੀ ਪ੍ਰਭ ਮੇਰੇ ਕਾਰਜ ਸਗਲ ਸਵਾਰੇ ॥੩॥  
ਆਸਾ ਮਹਲਾ ੫, ੫. ੩੮੩

To Mom and Dad

# Acknowledgements

I am truly blessed to have had the support of so many loving and motivating individuals during my tenure at Caltech. They have made these last six years in California an incredible experience I will forever cherish. This work would not have been possible without them.

When I first mentioned that I wanted to pursue graduate research in environmental quality and air pollution, my undergraduate research advisor at the University of Illinois at Urbana-Champaign, Professor Richard Braatz, emphatically advised me to “Work for John Seinfeld and Rick Flagan at Caltech.” Considerably ignorant of the field of atmospheric chemistry, I naively visited Caltech and met with both John and Rick and learned about their research. I was immediately impressed by their zeal for scientific inquiry, the quality of their work, and their standing in the scientific community; however being a young adult from Chicago, I was most impressed by Southern California weather and geography.

Once I began research at Caltech, I started to understand what a privilege it was to have John and Rick as advisors. Initially, John was aware of my research inexperience and gave me a small aerosol thermodynamics problem to get me started. By meeting with him regularly and showing him my progress, I steadily gained confidence in my abilities as a scientist. Over time as I developed research skills and intuition, John gave me more independence, and soon I was in charge of my own instrument in the Roof Lab. His role as an advisor eventually evolved into that of a colleague; he has treated me professionally and as an equal, trusting my analysis and experimental decisions. I am very grateful for his management, which has consistently challenged me and rewarded me to a point where I can effectively pass my knowledge to younger students and independently tackle scientific questions. He was a clear and organized teacher, and being a TA for him was a pleasure,

never a chore. I am most thankful for his patience and ability to motivate me when I needed it. I will always look up to him as my role model for a manager, mentor, and scientist.

I am extremely lucky to have Rick Flagan as a second advisor during my time at Caltech. His breadth of scientific and engineering knowledge never ceases to amaze me. Whenever I had a technical problem that no one seemed able to understand or solve, Rick would have a solution (or several), and he would not hesitate to help me in lab. Aside from science, I felt I could talk to him regarding any subject like teaching, administration, lab safety, or our general well-being. He could always entertain us about stories of students past and was so gracious enough to host several social events at his house. I am very grateful for his advice and friendship.

Much of the day-to-day laboratory and analysis skills I have learned have been passed down to me by several mentors. In AMS discipleship at Caltech, Jose-Luis Jimenez discipled Roya Bahreini who discipled Shane Murphy who in turn passed his knowledge to me. Shane was a wonderful mentor who taught me to question every bit of analysis I did for consistency and never let me “hand-wave” anything. His hardware and technical expertise were available to me at all hours of the day. Jesse Kroll and I overlapped for only a short while, yet he taught me different ways of understanding the organic aerosol system. He was very supportive and appreciative of my contributions when I was struggling on Roof Lab’s steep learning curve. Sally Ng, probably the most popular member of the Roof Lab, extended to me a friendship that I enjoy to this day. Her warm, cheerful personality is complimented by a scientific rigor recognized by many in the aerosol community. I am grateful that I am able to collaborate with her even after she left Caltech.

I cannot imagine life at Caltech without my friend and colleague Arthur Chan. I often called him “my brother” because I have worked with him under John, studied with him, lived with him, and traveled with him. I have learned so much about running a lab while working with him and from having many scientific discussions with him. When we were not discussing science, we were undoubtedly cracking jokes. I look forward to progressing through academia with him in the future.

The rest of the Seinfeld/Flagan group have been unforgettable. I joined the group with Andrew Metcalf and Havala Pye, both of whom are great scientists and whose expertise I have come to rely

on. I want to thank Jason Surratt and Joey Ensberg for putting up with me as a roommate and colleague at the same time; so many late nights were spent discussing the profound and the silly. The postdocs in our group have been like older siblings to me; Beth Kautzman, Andreas Kürten, and Andi Zuend have been great mentors. The Roof Lab is now run by an amazing pair of scientists, Lindsay Yee and Christine Loza. I wish them the best of luck in the new lab. A very, very special thanks to Jill Craven. I was a great pleasure to be her AMS mentor and her friend and older brother of sorts. Her enthusiasm for all things is well recognized in the lab and in the AMS community. I know I will see her achieve many things in the years to come. A big thanks to everyone else: Armin Sorooshian, Harmony Gates, Man Nin Chan, Kate Schilling, Xerxes Lopez-Yglesias, Andy Downard, Mandy Grantz, Scott Hersey, Jason Gamba, Tristan Day, Ruoyu Zhang, Wei-Ting (Anne) Chen, Chinghang (Candy) Tong, Daven Henze, Amir Hakami, Phillip Stier, Zach Lebo, Yi-Chun (Jean) Chen, Alan Kwan, Nathan Eddingsaas, Fabien Paulot, John Crounse, Jason St. Clair, and Melinda Beaver. Thank you Yvette Grant, you are my Dearheart too. Thank you to my Sikh sangat and Jakara for their spiritual support.

Graduate life was so much easier with the AMS community to support me. John Jayne, Joel Kimmel, Doug Worsnop, Manjula Canagaratna, Donna Sueper, Jose-Luis Jimenez, Bill Brooks, James Allan, John Shilling, Tim Onasch, and Achim Trimborn have all helped me at some point.

I could not have made it through the first year of graduate school without my war buddies: Mary, Yvonne, Andy, Andrew May, Leo, Kate, Eric, Erik, Diana, Kathleen, and Morgan. Thank you, thank you, thank you.

I thank God everyday for giving me a beautiful family who has taken care of me at every step of the way and shown me the love only family can. Thank you Rami Maasi, Narinder Uncle, Aman, and Harpreet for giving me a home away from home and especially for taking me in during the hard times. This thesis is dedicated to my Mom and Dad. Their sacrifices for me are unparalleled. I love you so much.

# Abstract

Secondary organic aerosol (SOA) contributes a substantial fraction to total ambient particulate mass. SOA is a complex mixture of different organic species formed via many gas- and particle-phase reaction pathways. The Aerodyne aerosol mass spectrometer (AMS) has become a standard tool in measuring the bulk chemical composition of SOA in realtime. In addition to acquiring mass spectra of SOA, the high-resolution time-of-flight AMS, or HR-ToF-AMS, can distinguish and quantify ions with the same nominal mass but different elemental compositions. This thesis presents results from several studies in which the HR-ToF-AMS is used to chemically characterize SOA generated in chamber experiments.

Glyoxal is a common oxidation product of both biogenic and anthropogenic volatile organic compounds (VOCs) and is known to partition into wet inorganic aerosol. Chamber studies of glyoxal uptake onto ammonium sulfate aerosol are conducted to better understand the mechanisms controlling glyoxal uptake onto ambient aerosol. Organic growth due to glyoxal uptake was found to be reversible under dark conditions. HR-ToF-AMS spectra provide evidence for glyoxal dimers and trimers existing in the particle phase. HR-ToF-AMS spectra indicate the irreversible formation of carbon-nitrogen compounds in the aerosol. Organosulfates are not detected under dark conditions; however, active photochemistry was found to occur within aerosol during irradiated experiments. Carboxylic acids and organic esters are identified within the aerosol. An organosulfate, which had been previously assigned as glyoxal sulfate in ambient samples and chamber studies of isoprene oxidation, is observed only in the irradiated experiments. Comparison with a laboratory-synthesized standard and chemical considerations strongly suggest that this organosulfate is glycolic acid sulfate, an isomer of the previously proposed glyoxal sulfate.

Developments in HR-ToF-AMS data analysis have allowed for the measurement of the elemental composition of SOA. Additional graphical representations of AMS spectra and elemental composition have been developed to explain the oxidative and aging processes of SOA. It has been shown previously that oxygenated organic aerosol (OOA) components from ambient and laboratory data fall within a triangular region in the  $f_{44}$  vs.  $f_{43}$  space, where  $f_{44}$  and  $f_{43}$  are the ratios of the organic signal at  $m/z$  44 and 43 to the total organic signal, respectively; we refer to this model as the “triangle plot.” Alternatively, the Van Krevelen diagram has been used to plot the elemental composition of SOA and describe the evolution of functional groups in SOA. The variability of SOA formed in chamber experiments from twelve different precursors in both “triangle plot” and Van Krevelen domains are investigated. Spectral and elemental data from the high-resolution Aerodyne aerosol mass spectrometer are compared to offline species identification analysis and FTIR filter analysis to better understand the changes in functional and elemental composition inherent in SOA formation and aging. SOA formed under high- and low- $\text{NO}_x$  conditions occupy similar areas in the “triangle plot” and Van Krevelen diagram, and SOA generated from already-oxidized precursors starts higher on the “triangle plot.” The most oxidized SOA come from the photooxidation of methoxyphenol precursors which yielded SOA O/C ratios near unity.  $\alpha$ -pinene ozonolysis and naphthalene photooxidation SOA systems have had the highest degree of mass closure in previous chemical characterization studies and also show the best agreement between AMS elemental composition measurements and elemental composition of identified species. In general the elemental composition of chamber SOA follows a slope shallower than  $-1$  on the Van Krevelen diagram. From the spectra of SOA studied, the triangular region originally constructed with ambient OOA components with chamber aerosol can be reproduced. Ambient data in the middle of the triangle represent the ensemble average of many different SOA precursors, ages, and oxidative processes.



# Contents

<b>Acknowledgements</b>	<b>iv</b>
<b>Abstract</b>	<b>vii</b>
<b>1 Introduction</b>	<b>1</b>
<b>2 Glyoxal Uptake on Ammonium Sulfate Seed Aerosol: Reaction Products and Reversibility of Uptake under Dark and Irradiated Conditions</b>	<b>5</b>
2.1 Abstract . . . . .	5
2.2 Introduction . . . . .	6
2.3 Experimental Procedures . . . . .	10
2.3.1 Teflon Filter Collection and Offline Chemical Analysis . . . . .	12
2.3.2 Aerodyne Aerosol Mass Spectrometer . . . . .	13
2.3.3 Madison Laser-Induced Phosphorescence Instrument . . . . .	13
2.4 Results . . . . .	14
2.4.1 Glyoxal Uptake in the Absence of Light . . . . .	14
2.4.2 Glyoxal Uptake in the Presence of Light . . . . .	15
2.5 Discussion . . . . .	16
2.5.1 Organosulfate Formation . . . . .	16
2.5.2 Carbon-Nitrogen Containing Compound Formation . . . . .	18
2.5.3 Overall Organic Growth and Glyoxal Oligomer Formation . . . . .	21
2.5.4 Glyoxal Uptake under Irradiated Conditions . . . . .	23

2.5.5	Implications to Ambient Aerosol . . . . .	25
2.6	Conclusions . . . . .	26
2.7	Acknowledgements . . . . .	27
<b>3</b>	<b>Elemental Analysis of Chamber Organic Aerosol Using an Aerodyne High-Resolution Aerosol Mass Spectrometer</b>	<b>49</b>
3.1	Abstract . . . . .	49
3.2	Introduction . . . . .	50
3.3	Experimental Section . . . . .	53
3.3.1	Chamber Operation . . . . .	53
3.3.2	High-Resolution Time-of-Flight Aerosol Mass Spectrometer . . . . .	54
3.4	Results . . . . .	57
3.4.1	SOA from Reactive Uptake of Glyoxal . . . . .	57
3.4.2	$\alpha$ -pinene Ozonolysis SOA . . . . .	59
3.4.3	Isoprene SOA . . . . .	61
3.4.4	Single-Ring Aromatic SOA . . . . .	64
3.4.5	Naphthalene SOA . . . . .	66
3.5	Discussion . . . . .	67
3.5.1	Overall Trends in O/C Ratios from Laboratory Chamber-Generated SOA . . . . .	67
3.5.2	Comparisons with Offline Analytical Techniques . . . . .	69
3.5.3	Uncertainty in the AMS Elemental Analysis . . . . .	71
3.5.4	AMS Marker Ions and SOA Oxygenation . . . . .	74
3.6	Comparison of Chamber and Ambient Elemental Ratios and Spectra . . . . .	75
3.7	Acknowledgements . . . . .	78
<b>4</b>	<b>Elemental Composition and Oxidation of Chamber Organic Aerosol</b>	<b>110</b>
4.1	Abstract . . . . .	110
4.2	Introduction . . . . .	111

4.3	Experimental Section . . . . .	114
4.3.1	Chamber Operation . . . . .	114
4.3.2	High-Resolution Time-of-Flight Aerosol Mass Spectrometer . . . . .	115
4.3.3	Fourier Transform Infrared Spectroscopy (FTIR) . . . . .	115
4.4	Results . . . . .	116
4.4.1	$\alpha$ -pinene SOA . . . . .	117
4.4.2	Isoprene SOA . . . . .	118
4.4.3	Single-Ring Aromatic SOA . . . . .	119
4.4.4	Naphthalene SOA . . . . .	120
4.4.5	Phenol and Methoxyphenol SOA . . . . .	121
4.4.6	Unsaturated Aldehyde SOA . . . . .	121
4.4.7	SOA from Reactive Uptake of Glyoxal . . . . .	122
4.5	Discussion and Conclusions . . . . .	123
4.6	Acknowledgements . . . . .	126
<b>5</b>	<b>Conclusions</b>	<b>148</b>
<b>A</b>	<b>Supplementary Material for “Elemental Analysis of Chamber Organic Aerosol Using an Aerodyne High-Resolution Aerosol Mass Spectrometer”</b>	<b>151</b>
<b>B</b>	<b>Supplementary Material for “Elemental Composition and Oxidation of Chamber Organic Aerosol”</b>	<b>163</b>
<b>C</b>	<b>Changes in Organic Aerosol Composition with Aging Inferred from Aerosol Mass Spectra</b>	<b>176</b>
<b>D</b>	<b>Organic Aerosol Components Observed in Northern Hemispheric Datasets from Aerosol Mass Spectrometry</b>	<b>186</b>
<b>E</b>	<b>Role of Aldehyde Chemistry and NO<sub>x</sub> Concentrations in Secondary Organic Aerosol Formation</b>	<b>204</b>



# List of Tables

2.1	Experimental conditions of dark experiments . . . . .	36
2.2	Experimental conditions of irradiated experiments . . . . .	37
2.3	GL fragments observed via AMS and suggested structures from which the fragments are formed . . . . .	38
2.4	Fragments containing both carbon and nitrogen observed and suggested chemical formulas	39
3.1	Experimental conditions and results . . . . .	91
3.2	Elemental composition of each SOA system . . . . .	92
3.3	O/C ratios of various laboratory SOA systems . . . . .	93
4.1	Experimental conditions and results . . . . .	138

# List of Figures

2.1	Processes contributing to GL uptake on AS seed aerosol. . . . .	40
2.2	Proposed structures for $m/z$ 155; glyoxal sulfate and glycolic acid sulfate. . . . .	41
2.3	Representative unit-mass AMS spectrum. . . . .	42
2.4	High-resolution (“W-mode”) AMS peaks allow unequivocal assignment of a $C_4H_7O_5^+$ formula to the $m/z$ 135, $C_5H_5O_5^+$ formula to the $m/z$ 145, and $C_6H_7O_6^+$ formula to the $m/z$ 175 fragment ions. . . . .	43
2.5	UPLC/ESI-TOFMS extracted ion chromatograms (EICs) of $m/z$ 155 for selected GL experiments. . . . .	44
2.6	The time traces of total organic, $m/z$ 58, 105, and 68 fragment ions normalized by the sulfate ion signal along with gas phase GL concentrations for a dilution experiment. . . . .	45
2.7	The sulfate normalized GL and GL oligomer marker signals $m/z$ 58 and 105. . . . .	46
2.8	High-resolution (W-mode) AMS peaks allow unequivocal assignment of a $C_3H_4N_2^+$ formula to the $m/z$ 68, $C_4H_4N_2O^+$ formula to the $m/z$ 96 fragment ions. . . . .	47
2.9	Proposed formation mechanism of 1H-imidazole-2-carboxaldehyde and observed $m/z$ 68 and 96 fragment ion. . . . .	48
3.1	Experimental profile of AMS organic mass, elemental ratios, and OM/OC for glyoxal uptake experiments. . . . .	94
3.2	High-resolution mass spectra of glyoxal and $\alpha$ -pinene. . . . .	95
3.3	AMS organic mass, O/C, H/C and OM/OC ratios for a typical $\alpha$ -pinene ozonolysis experiment . . . . .	96

3.4	AMS organic mass loading and O/C, H/C and OM/OC ratios of isoprene SOA formed under low-NO <sub>x</sub> conditions. . . . .	97
3.5	High-resolution mass spectra of isoprene SOA. . . . .	98
3.6	AMS organic mass, elemental ratios, and OM/OC for isoprene high-NO <sub>x</sub> experiments. . . . .	99
3.7	Experimental conditions for Experiment 12. . . . .	100
3.8	AMS organic mass, elemental ratios, and OM/OC for single-ring aromatic experiments. . . . .	101
3.9	High-resolution mass spectra of toluene SOA. . . . .	102
3.10	High-resolution mass spectra of <i>m</i> -xylene SOA. . . . .	103
3.11	Organic mass, elemental ratios, and OM/OC for naphthalene high-NO <sub>x</sub> experiments. . . . .	104
3.12	Organic mass, elemental ratios, and OM/OC for naphthalene low-NO <sub>x</sub> experiments. . . . .	105
3.13	Organic mass and O/C ratio as a function of time for typical naphthalene photooxidation experiments. . . . .	106
3.14	High-resolution mass spectra of naphthalene-SOA. . . . .	107
3.15	O/C <sub>HR</sub> vs. f <sub>44</sub> for ambient Mexico City OA and chamber OA. . . . .	108
3.16	O/C ratios for ambient Mexico City organic aerosol, typical AMS components derived from positive matrix factorization (PMF), and chamber SOA as a function of precursor carbon number. . . . .	109
4.1	Structures of the SOA precursors presented in this study. . . . .	139
4.2	Triangle plot and Van Krevelen diagrams for $\alpha$ -pinene SOA formed from ozonolysis and high- and low-NO <sub>x</sub> photooxidation. . . . .	140
4.3	Triangle plot and Van Krevelen diagram for SOA formed from photooxidation of isoprene. . . . .	141
4.4	Triangle plot and Van Krevelen diagram for SOA formed from photooxidation of toluene and <i>m</i> -xylene. . . . .	142
4.5	Triangle plot and Van Krevelen diagram for SOA formed from photooxidation of naphthalene. . . . .	143
4.6	Triangle plot and Van Krevelen diagram for SOA formed from the photooxidation of methoxyphenols. . . . .	144

4.7	Triangle plot and Van Krevelen diagram for SOA formed from unsaturated aldehydes.	145
4.8	Triangle plot and Van Krevelen diagram for SOA formed from the reactive uptake of glyoxal onto wet ammonium sulfate aerosol. . . . .	146
4.9	Triangle plot and Van Krevelen diagram for all systems. . . . .	147



## Chapter 1

# Introduction

Ambient aerosols are liquid or solid particles suspended in air, and they play an important role in many natural processes. Particulate matter can directly influence climate by scattering and absorbing solar and terrestrial radiation (IPCC, 2007). Indirectly, particulate matter can influence the climate by acting as cloud condensation nuclei, thereby affecting cloud formation, albedo, and lifetime. Aerosols also can adversely affect human health and have been correlated with increased mortality rates (Pope and Dockery, 2006). Therefore, understanding the formation and properties of aerosols is crucial to predicting their effects on climate and health.

Recent studies have shown that organic compounds can contribute up to 90% of total aerosol mass (Hallquist et al., 2009). Organic aerosol (OA) is either directly emitted into the atmosphere as primary organic aerosol (POA) or formed in situ via gas-phase oxidation and subsequent partitioning of anthropogenic and biogenic volatile organic compounds (VOCs). This type of aerosol is known as secondary organic aerosol (SOA) and is comprised of a complex mixture of many different organic compounds formed as a result of the variety of reaction pathways leading to semivolatile products.

Many different techniques have been developed to chemically characterize SOA. Offline analysis techniques can typically quantify only a small portion of the wide array of compounds present in SOA. Though generally not able to provide detailed, composition profiles of organic aerosol (OA), bulk, real-time mass spectrometric analysis has become standard in chemically characterizing OA. The widely used Aerodyne aerosol mass spectrometer (AMS) uses thermal vaporization followed by electron impact ionization and a mass spectrometer to quantify the nonrefractory portion of submicron aerosol mass (Jayne et al., 2000; Jimenez et al., 2003; Canagaratna et al., 2007). Recent technological upgrades have led to the development of the high-resolution time-of-flight aerosol mass spectrometer (HR-ToF-AMS) which can distinguish and quantify ions with the same nominal mass but different elemental compositions. The additional information in high-resolution spectra allows for a more detailed analysis of SOA formation mechanisms and the elemental composition of SOA.

Laboratory chambers enable the investigation of a specific SOA system in which the precursor VOC can be chosen and the oxidative environment controlled. Chamber experiments are crucial to constraining SOA models and providing insight into the mechanisms involved in the formation

and evolution of SOA (Kroll and Seinfeld, 2008). This thesis presents several studies in which the HR-ToF-AMS is used to chemically characterize chamber SOA. In chapter 2, the uptake of glyoxal onto wet ammonium sulfate seed aerosol in dark conditions and in the presence of light is examined. In chapters 3 and 4, the elemental composition of chamber SOA from a comprehensive suite of SOA systems is studied. In addition, HR-ToF-AMS data are compared to other laboratory composition and discrepancies and sources of uncertainty are identified. Particularly, in chapter 4, HR-ToF-AMS data of chamber SOA are presented in two different graphical representations to explain the oxidative and aging processes of SOA.

## Bibliography

- Canagaratna, M. R., Jayne, J. T., Jimenez, J. L., Allan, J. D., Alfarra, M. R., Zhang, Q., Onasch, T. B., Drewnick, F., Coe, H., Middlebrook, A., Delia, A., Williams, L. R., Trimborn, A. M., Northway, M. J., DeCarlo, P. F., Kolb, C. E., Davidovits, P., and Worsnop, D. R.: Chemical and microphysical characterization of ambient aerosols with the aerodyne aerosol mass spectrometer, *Mass Spectrom. Rev.*, 26, 185–222, doi:10.1002/Mas.20115, 2007.
- Hallquist, M., Wenger, J. C., Baltensperger, U., Rudich, Y., Simpson, D., Claeys, M., Dommen, J., Donahue, N. M., George, C., Goldstein, A. H., Hamilton, J. F., Herrmann, H., Hoffmann, T., Iinuma, Y., Jang, M., Jenkin, M. E., Jimenez, J. L., Kiendler-Scharr, A., Maenhaut, W., McFiggans, G., Mentel, T. F., Monod, A., Prevot, A. S. H., Seinfeld, J. H., Surratt, J. D., Szmigielski, R., and Wildt, J.: The formation, properties and impact of secondary organic aerosol: current and emerging issues, *Atmos. Chem. Phys.*, 9, 5155–5236, doi:10.5194/acp-9-5155-2009, 2009.
- Intergovernmental Panel on Climate Change (IPCC): *Climate Change 2007: The Physical Science Basis*, Cambridge Univ. Press, Cambridge, United Kingdom, 2007.
- Jayne, J. T., Leard, D. C., Zhang, X. F., Davidovits, P., Smith, K. A., Kolb, C. E., and Worsnop,

- D. R.: Development of an aerosol mass spectrometer for size and composition analysis of submicron particles, *Aerosol Sci. Technol.*, 33, 49–70, doi:10.1080/027868200410840, 2000.
- Jimenez, J. L., Jayne, J. T., Shi, Q., Kolb, C. E., Worsnop, D. R., Yourshaw, I., Seinfeld, J. H., Flagan, R. C., Zhang, X. F., Smith, K. A., Morris, J. W., and Davidovits, P.: Ambient aerosol sampling using the Aerodyne Aerosol Mass Spectrometer, *J. Geophys. Res.-Atmos.*, 108(D7), 8425, doi:10.1029/2001jd001213, 2003.
- Kroll, J. H. and Seinfeld, J. H.: Chemistry of secondary organic aerosol: Formation and evolution of low-volatility organics in the atmosphere, *Atmos. Environ.*, 42, 3593–3624, doi:10.1016/j.atmosenv.2008.01.003, 2008.
- Pope III, C. A. and Dockery, D. W.: Health effects of fine particulate air pollution: Lines that connect, *J. Air Waste Manage.*, 56, 709–742, 2006.

## Chapter 2

# Glyoxal Uptake on Ammonium Sulfate Seed Aerosol: Reaction Products and Reversibility of Uptake under Dark and Irradiated Conditions\*

### 2.1 Abstract

Chamber studies of glyoxal uptake onto ammonium sulfate aerosol were performed under dark and irradiated conditions to gain further insight into processes controlling glyoxal uptake onto ambient aerosol. Organic fragments from glyoxal dimers and trimers were observed within the aerosol under dark and irradiated conditions. Glyoxal monomers and oligomers were the dominant organic compounds formed under the conditions of this study; glyoxal oligomer formation and overall organic growth were found to be reversible under dark conditions. Analysis of high-resolution time-of-flight aerosol mass spectra provides evidence for irreversible formation of carbon-nitrogen (C-N) compounds in the aerosol. We have identified 1H-imidazole-2-carboxaldehyde as one C-N product. To the authors' knowledge, this is the first time C-N compounds resulting from condensed phase reactions with ammonium sulfate seed have been detected in aerosol. Organosulfates were not detected

---

\*Reproduced with permission from "Glyoxal uptake on ammonium sulphate seed aerosol: reaction products and reversibility of uptake under dark and irradiated conditions" by M. M. Galloway, P. S. Chhabra, A. W. H. Chan, J. D. Surratt, R. C. Flagan, J. H. Seinfeld, and F. N. Keutsch, *Atmospheric Chemistry and Physics*, 9, 3331–3345, doi:10.5194/acp-9-3331-2009. Copyright 2009 by the Authors. CC Attribution 3.0 License.

under dark conditions. However, active photochemistry was found to occur within aerosol during irradiated experiments. Carboxylic acids and organic esters were identified within the aerosol. An organosulfate, which had been previously assigned as glyoxal sulfate in ambient samples and chamber studies of isoprene oxidation, was observed only in the irradiated experiments. Comparison with a laboratory-synthesized standard and chemical considerations strongly suggest that this organosulfate is glycolic acid sulfate, an isomer of the previously proposed glyoxal sulfate. Our study shows that reversibility of glyoxal uptake should be taken into account in SOA models and also demonstrates the need for further investigation of C-N compound formation and photochemical processes, in particular organosulfate formation.

## 2.2 Introduction

Organic aerosol has been detected in substantial concentrations in urban and rural atmospheres (Zhang et al., 2007). Secondary organic aerosol (SOA) contributes significantly to particulate matter, though current models considerably underestimate SOA formation (de Gouw et al., 2005; Heald et al., 2005; Volkamer et al., 2006). In order to understand the possible health and climate effects of particulate matter, it is critical that the physical and chemical models of SOA formation be improved. Glyoxal (GL) is produced by a wide variety of biogenic and anthropogenic volatile organic compounds (VOCs), many of which are SOA precursors, and is considered a tracer for SOA formation. One current model estimates global GL production of 45 Tg/yr, with roughly half due to isoprene photooxidation (Fu et al., 2008), and another estimates 56 Tg/yr of global GL production with 70% being produced from biogenic hydrocarbon oxidation (Myriokefalitakis et al., 2008). In addition to acting as a tracer for SOA formation, GL has been suggested as a direct contributor to SOA (Sorooshian et al., 2006; Volkamer et al., 2007; Carlton et al., 2007; Ervens et al., 2008; Fu et al., 2008; Volkamer et al., 2009). A study comparing observed and modelled GL has suggested that GL could contribute at least 15% of the SOA in Mexico City (Volkamer et al., 2007), while a study using the GEOS-Chem model found the modelled GL contribution to SOA to be 2.6 Tg C/year out of a total of 29 Tg C/year (Fu et al., 2008).

Despite existing research aimed at elucidating SOA formation by GL, further quantification of SOA yields as a function of conditions such as relative humidity, irradiation, gas-phase GL mixing ratio, and seed aerosol composition and pH are required in order to allow for the application of laboratory findings to ambient conditions. On a more fundamental level, it is desirable to achieve a detailed understanding of the processes contributing to SOA formation from GL as a function of the above conditions. GL is also promising as an interesting model system for compounds that can yield SOA via purely physical absorption processes and via complex condensed phase processes, such as oligomerization, organosulfate formation, condensation, and photochemical reactions.

The standard models that have been employed to explain organic gas-particle partitioning have generally assumed physical absorption processes (Pankow, 1994a,b; Odum et al., 1996). On this basis, GL, the smallest dicarbonyl, should have virtually no SOA yield because of its high vapour pressure (220 torr at 20°C (Kielhorn et al., 2004)). However, GL partitions strongly to aqueous condensed-phase systems, which is reflected in a surprisingly high effective Henry's law constant,  $K_{H,aq}^* = 3.6 \times 10^5$  M/atm for seawater (Zhou and Mopper, 1990) and  $4.19 \times 10^5$  M/atm in water (Ip et al., 2009). The effective Henry's law constant of GL is higher than that of atmospherically relevant monocarboxylic acids including glyoxylic acid,  $K_{H,aq}^* = 1 \times 10^4$  M/atm (Ip et al., 2009), the acid that results from oxidation of one of the aldehyde groups in GL. Glycolic acid, an isomer of glyoxal monohydrate, also has a lower effective Henry's law constant of  $2.83 \times 10^4$  M/atm (Ip et al., 2009). The high effective Henry's law constant of GL has been explained by the hydration of the aldehyde groups, producing an effectively lower vapor pressure species in aqueous solution. In addition to the physical absorption processes, particle-phase chemical reactions have been identified as a possible driving force for uptake. Carbonyl containing species are known to participate in aldol, acetal, and esterification reactions, which form low-volatility compounds that add to SOA mass. Field and laboratory studies have also yielded evidence for the formation of high molecular weight products within SOA (Gross et al., 2006; Reinhardt et al., 2007; Denkenberger et al., 2007) and it is well known that GL will polymerize in the presence of water (Whipple, 1970; Loeffler et al., 2006).

These properties of GL, together with its production via oxidation of many VOCs, have inspired

chamber investigations into GL partitioning onto a variety of seed particles (Jang et al., 2002; Liggio et al., 2005a,b; Kroll et al., 2005; Corrigan et al., 2008; Volkamer et al., 2009). Liggio et al. (2005b) have demonstrated reactive uptake of GL onto several different types of seed aerosol using an Aerodyne aerosol mass spectrometer (AMS). This study suggested that GL uptake onto ammonium sulfate (AS) aerosol is irreversible and enhanced with acidified seed. However, Kroll et al. (2005) observed negligible acid effect and reversible GL uptake onto AS seed aerosol that is possibly controlled by ionic strength. The authors concluded that GL uptake obeys a modified effective Henry’s Law at equilibrium ( $K_{\text{H,AS}}^* = 2.6 \times 10^7 \text{ M/atm}$ ; using a density of  $1 \text{ g/cm}^3$  to convert volume growth to organic mass and normalizing by the seed volume). Both Liggio et al. (2005b) and Kroll et al. (2005) observed hydration and oligomerization of GL within aerosol and, in addition, Liggio et al. (2005b) proposed irreversible formation of the organosulfate of GL (GL sulfate) to explain certain peaks in the AMS mass spectra. Volkamer et al. (2009) demonstrated that acetylene is an SOA precursor and estimated that almost all particle-phase organic growth was due to its oxidation product, GL. SOA yields were shown to correlate with the liquid water content (LWC) of the AS seed. Therefore, the authors introduced a modified definition of molarity, calculating GL concentrations with respect to LWC fraction of the seed volume, which gave  $K_{\text{H,AS}}^{**} = 1.65 \times 10^8 \text{ M/atm}$ . Evaluating the data from Kroll et al. (2005) in this manner gives  $K_{\text{H,AS}}^{**} = 1.07 \times 10^8 \text{ M/atm}$ . However, in addition to the larger effective Henry’s law constant in the study of Volkamer et al. (2009), this uptake in the presence of OH radicals and UV light was achieved in 90 seconds compared to many hours under dark conditions in the work by Kroll et al. (2005).

The difference between the Henry’s law constant of water and AS aerosol is substantial and the reasons for this are not well understood. Recently, Ip et al. (2009) found that the effective Henry’s Law increases with increasing sulfate concentration. At a sodium sulfate ionic strength of  $0.03 \text{ mol/L (M)}$ ,  $K_{\text{H}}^* = 2.40 \times 10^7 \text{ M/atm}$ . This is 50 times higher than  $K_{\text{H,aq}}^*$  and 12 times higher than with a sodium chloride ionic strength of  $0.05 \text{ M}$ . Ip et al. (2009) concluded that the presence of sulfate has a greater effect on the effective Henry’s Law than ionic strength alone. Increasing the ionic strength of sulfate to  $0.225 \text{ M}$  increases the  $K_{\text{H}}^*$  to the point that it could not be measured,



a value suggested to be  $\geq 10^9$  M/atm. This sulfate concentration is still substantially lower than that in the AS aerosol studies, but the suggested effective Henry's law constant is substantially larger than for the AS aerosol. It is possible that with increasing sulfate concentration and thus decreasing LWC,  $K_{\text{H}}^*$  of GL first increases up to a maximum and then decreases again. A similar effect was found by Ip et al. (2009) for sodium chloride solutions. This indicates that the amount of GL partitioning to the condensed phase is dependent on more than just the LWC over the entire range of sulfate concentrations. The mechanism that is at work is still unknown, and the importance of this observation over the more limited sulfate concentration range of ambient aerosol is unclear.

Bulk studies have also provided valuable insight into the aqueous GL system. Carlton et al. (2007) performed photochemical reactions of GL and hydrogen peroxide and demonstrated that SOA yield from GL depends on photochemical processing. Recent work by Nozière et al. (2009) showed that GL reacts to form high molecular weight compounds and postulated that the ammonium ion is a catalyst for condensed phase GL reactions such as oligomerization. In a different study, Shapiro et al. (2009) showed that light-absorbing complexes were observed in solutions containing AS and GL but not in sodium sulfate or sodium chloride solutions, indicating that nitrogen is central to the formation of light-absorbing complexes.

In light of these investigations, it is clear that particle-phase chemistry plays a crucial role in the gas/particle partitioning of GL, though the processes controlling uptake are still not clear. In this study, we examine the uptake processes onto wet AS seed aerosol using a variety of instrumentation in dark conditions and in the presence of light. Figure 2.1 shows the major processes that could be contributing to GL uptake. The processes that have been identified by previous studies are:

1. GL-hydrate formation is fast and reversible (Schweitzer et al., 1998). Hydration equilibria up to  $\text{GL}\cdot 2\text{H}_2\text{O}$ , the dominant form of GL in dilute aqueous solutions, are included in  $K_{\text{H},\text{aq}}^*$  (Zhou and Mopper, 1990). Some studies have demonstrated correlation of organic growth with water content of aerosol (Volkamer et al., 2009), whereas others have shown growth at extremely low water content and noted that  $\text{GL}\cdot n\text{H}_2\text{O}$  concentrations appear to be independent of gas-phase GL concentrations (Corrigan et al., 2008).

2. Glyoxal oligomers ( $\text{GL}_n$ ) have been detected by time-of-flight and quadrupole AMS studies of aerosol growth from GL uptake in chamber experiments (Kroll et al., 2005; Liggio et al., 2005b); no definitive evidence for  $\text{GL}_n$  in field samples has been found, likely due to analytical challenges.  $\text{GL}_n$  formation is reversible and slow (many minutes to hour timescales) in aqueous GL/ $\text{H}_2\text{O}$  solutions (Whipple, 1970; Fratzke and Reilly, 1986), and there are indications from a previous study that it is reversible in AS aerosol (Kroll et al., 2005).
3. The proposed GL sulfate ( $\text{C}_2\text{H}_3\text{SO}_6^-$ , Fig. 4.1) is of much interest as it has been detected via filter sampling methods in field samples (Surratt et al., 2007, 2008; Gómez-González et al., 2008) and in chamber studies of isoprene oxidation under intermediate- to high- $\text{NO}_x$  conditions (Surratt et al., 2008). The formation conditions for  $\text{C}_2\text{H}_3\text{SO}_6^-$  as well as its contribution to  $K_{\text{H,AS}}^*$  are unclear. Irreversible formation of  $\text{C}_2\text{H}_3\text{SO}_6^-$  would not contribute to  $K_{\text{H,AS}}^*$ , however, reversible formation would have an effect on  $K_{\text{H,AS}}^*$ .

In this study we aim to investigate the processes contributing to overall GL uptake as well as which of these processes are effectively reversible, meaning reversible over aerosol lifetimes. These questions are important for evaluating applicability of laboratory studies to ambient conditions and net SOA yields from GL. If most GL uptake is effectively reversible, the organic aerosol will revolatilize at lower GL gas-phase concentrations upon transport away from GL sources or at night. Net SOA yields from a specific process will be higher if that process is irreversible.

## 2.3 Experimental Procedures

Experiments were performed in Caltech’s indoor, dual  $28\text{ m}^3$  Teflon environmental chambers (Cocker et al., 2001; Keywood et al., 2004). The experimental conditions are summarized in Tables 2.1 and 2.2. Each chamber has a dedicated Differential Mobility Analyzer (DMA, TSI model 3081) coupled with a condensation nucleus counter (TSI model 3760) for measuring aerosol size distribution, and number and volume concentration. Temperature, relative humidity (RH),  $\text{O}_3$ , NO, and  $\text{NO}_x$  were continuously monitored. AS seed particles were generated by atomization of a 0.015 M aqueous AS

solution using a constant rate atomizer. Acidic seed particles were generated by atomization of a 0.015 M aqueous AS solution containing 0.015 M sulphuric acid. GL was prepared by heating a mixture of solid GL trimer dihydrate (Sigma, minimum 97%) and phosphorus pentoxide ( $P_2O_5$ ) to  $\sim 160^\circ C$  under vacuum. The monomer was collected in an  $LN_2$  trap as a yellow solid and stored overnight at  $-20^\circ C$ . Before each experiment, the frozen monomer was allowed to vaporize into a 500 mL glass bulb and introduced into the chamber using a gentle air stream. The chamber was kept at  $\sim 60\%$  RH. The concentration of an inert tracer, cyclohexane, was monitored using a gas-chromatograph with flame ionization detector (GC-FID, Agilent 6890N).

Dark experiments typically began by introducing gas-phase GL into a dark chamber and allowing the concentration to equilibrate over  $\sim 10$  h. Approximately 160 ppb<sub>v</sub> (part-per-billion by volume) of cyclohexane was also added as a tracer for dilution. Once the gas-phase GL concentration reached a steady state, AS seed was introduced, and the resulting organic growth was monitored by both the DMA and a high resolution time-of-flight AMS (HR-ToF-AMS, hereby referred to as AMS). After organic growth levelled off, the chamber air mass was diluted with clean hydrocarbon-free air to investigate the reversibility of uptake. The amount of dilution was calculated by monitoring the cyclohexane concentration with the GC-FID. In some experiments, AS seed was added first and then GL, though the results are the same.

Experiments with irradiation began similarly to dark experiments but when the addition of GL or AS seed was complete, the chamber lights were turned on. No external OH or  $NO_x$  source was added, and no dilution was performed in irradiated experiments.

Two blank experiments (Exp. 7 and 11) were conducted in which wet AS seed was atomized into a humid chamber without GL present. A negligible organic signal was measured in the absence of radiation, most likely due to background organics from the chamber walls. Under irradiation, miniscule organic growth was observed.

### 2.3.1 Teflon Filter Collection and Offline Chemical Analysis

Teflon filters (PALL Life Sciences, 47 mm diameter, 1.0  $\mu\text{m}$  pore size, teflo membrane) were collected from each experiment for offline chemical analysis. Filter sampling was initiated when the aerosol volume reached its maximum (constant) value, as determined by the DMA. Depending on the total volume concentration of aerosol in the chamber, the duration of filter sampling was 3.6–4.1 h, which resulted in  $\sim 5.1\text{--}5.8\text{ m}^3$  of total chamber air sampled. Collected filters were extracted in high-purity methanol, dried, and then reconstituted with 250  $\mu\text{L}$  of a 1:1 (v/v) solvent mixture of 0.1% acetic acid in water and 0.1% acetic acid in methanol (Surratt et al., 2008). All filter extracts were analyzed by a Waters ACQUITY ultra performance liquid chromatography (UPLC) system, coupled to a Waters LCT Premier XT time-of-flight mass spectrometer (TOFMS) equipped with an electrospray ionization (ESI) source. The ESI source was operated in both negative (–) and positive (+) ion mode; acidic GL SOA components were detected in the negative ion mode, whereas C-N compounds (e.g., imidazoles) were detected in the positive ion mode. All other operating conditions for this technique have been fully described elsewhere (Surratt et al., 2008).

Blank Teflon filters were extracted and treated in the same manner as the samples; none of the SOA products detected on the filter samples collected from the GL chamber experiments were observed in these blanks, indicating that these SOA components were not introduced during sample storage and/or preparation. Furthermore, to ensure that the SOA components observed were not an artifact formed from the collection of gaseous GL onto filter media, a blank filter was collected under dark conditions from the chamber containing a well-mixed concentration of GL ( $\sim 2\text{ ppm}_v$ ) and analyzed with UPLC/ESI-HR-TOFMS. This blank was sampled for the same duration as a sample filter. No SOA components characterized in the present study or significant contaminants were observed, consistent with the lack of observed aerosol growth in the absence of light and AS seed aerosol. All filters used for UPLC/ESI-HR-TOFMS analysis were examined within 1–2 days of the filter extraction/sample preparation. Following their initial analysis, sample extract solutions were stored at  $-20^\circ\text{C}$ . Selected samples were reanalyzed a month after initial extraction and showed no signs of degradation.

### 2.3.2 Aerodyne Aerosol Mass Spectrometer

Real-time particle mass spectra were collected continuously by the AMS, which is described in detail elsewhere (DeCarlo et al., 2006; Canagaratna et al., 2007, and references therein). The AMS switched once every minute between a high resolution “W-mode” and a lower resolution, higher sensitivity “V-mode.” The “V-mode” data were analyzed using a fragmentation table to separate out sulfate, ammonium, and organic spectra and to time-trace specific mass-to-charge ratios. “W-mode” data were analyzed using a separate high-resolution spectra toolbox known as PIKA to determine the chemical formulas contributing to distinct mass-to-charge ratios (DeCarlo et al., 2006). Since GL easily fragments to produce  $\text{CH}_2\text{O}^+$ , the fragmentation table was corrected so that the organic signal at  $m/z$  30 was equal to its total signal minus the contribution from air. The nitrate contribution was changed to approximately 1.3 times the nitrate signal at  $m/z$  46 as this was the  $m/z$  30/46 ratio during ammonium nitrate calibrations.

To determine elemental ratios, the computational toolbox known as Analytical Procedure for Elemental Separation (APES) was used. This toolbox applies the analysis procedure described in Aiken et al. (2007) to the high-resolution “W-mode data.” The particle-phase signal of  $\text{CO}^+$  and the organic contribution to  $\text{H}_x\text{O}^+$  ions were estimated as described in Aiken et al. (2008).

### 2.3.3 Madison Laser-Induced Phosphorescence Instrument

Gas-phase GL was detected with high specificity via Laser-Induced Phosphorescence (LIP) using the Madison LIP Instrument described in Huisman et al. (2008). This instrument utilizes a White-type multipass cell in a 2-pass configuration with gated photon counting and is highly sensitive, permitting specific, direct, in situ measurement of GL with a one-minute limit of detection ( $3\sigma$ ) of 6 ppt<sub>v</sub> (part-per-trillion by volume) per minute in a 32-pass configuration.

## 2.4 Results

### 2.4.1 Glyoxal Uptake in the Absence of Light

For a typical experiment, gas-phase GL was present in the chamber and equilibrated with the chamber walls prior to the introduction of AS seed particles. Organic growth began immediately upon particle addition, and reached a maximum after approximately 10 h; over this time period, sulfate and ammonium decreased due to particle wall losses. A representative unit-mass AMS spectrum is shown in Fig. 2.3. The fragments of interest to this study are summarized in Tables 2.3 and 2.4. The most significant fragments are  $m/z$  44, 58, 68, 135, 145, and 175. The observed fragments are in general accord with those observed by Liggio et al. (2005a), though certain masses such as  $m/z$  192 and 193 have lower signals in this study. Proposed precursor structures for the fragment masses marked in Fig. 2.3 are listed in Table 2.3. The fragment chemical formulae are unequivocally confirmed by the high-resolution spectra obtained in “W-mode,” verifying many of the assignments made by Liggio et al. (2005a). Masses listed in Table 2.3 which are larger than or equal to  $m/z$  77 represent ion fragments of oligomers; as an example, the high-resolution peak for  $m/z$  135 is shown in Fig. 2.4a. In the high resolution spectra, the only fragment ion found to contain both sulphur and carbon is  $m/z$  79 ( $\text{CH}_3\text{SO}_2^+$ ); however, the signal intensity is similar to that in the blank experiment (Exp. 7). Filter sample analysis did not detect any organosulfates under dark conditions in neutral (Exp. 4) or acidic seed (Fig. 2.5c, Exp. 5 and 6), as can be seen in the comparison between experiments carried out under irradiated conditions (Fig. 2.5a, Exp. 10) and experiments performed in the dark (Fig. 2.5b, Exp. 3).

After particle growth has stopped, the chamber was diluted with clean air (Exp. 1 and 3) to investigate the reversibility of GL uptake. Upon dilution, the concentrations of tracer, gas-phase GL, and particle-phase organic, sulfate, and ammonium decreased. To remove the effect of the decrease in overall particle volume due to wall loss and to dilution, the organic and several marker signals are normalized to sulfate. This normalized signal is proportional to the condensed phase concentration of each species. The normalized organic signal and GL markers at  $m/z$  58 and  $m/z$  105 decrease

after dilution by 15%–25% and 18%–30%, respectively. The gas-phase GL concentration decreased by 25%–40% of the initial concentration and the overall organic signal decreased relative to the tracer signal. Figure 2.6 shows this for a typical dilution experiment (Exp. 3).

Several fragments were observed by the AMS to have different temporal characteristics (and thus uptake kinetics) than the total organic or  $GL_n$  signal. Relatively strong signals occurred at  $m/z$  41, 68, 69, and 70. Weaker signals, approximately 5–10 times lower in magnitude, were also detected at other masses, the largest fragment occurring at  $m/z$  96. The signal at  $m/z$  68 increased immediately upon seed injection and grew steadily, even after no further change in total organic growth was observable within the uncertainty of that measurement. Furthermore, during dilution, the signal continued to increase when normalized to the sulfate signal. These compounds contribute only  $\sim 0.5\%$  of total organic mass measured by the AMS, but the sensitivity for these compounds or the  $GL_n$  has not been calibrated, and it is unlikely such a calibration can be achieved for the oligomers. Dilution has very little effect on the relative growth of  $m/z$  68, implying that the reactions are irreversible with respect to the lifetime of chamber aerosol. The high-resolution spectra obtained with the AMS in “W-mode” show unequivocally that these fragments originate from compounds containing carbon and nitrogen, as discussed below. Filter sample analysis also showed the presence of several nitrogen containing species in positive mode, including a species with  $m/z$  97.

#### 2.4.2 Glyoxal Uptake in the Presence of Light

The AMS spectra in irradiated experiments initially resembled those of dark uptake experiments, with many of the same marker fragments prominent, but then changed quickly. As under nonirradiated conditions, gaseous GL partitioned immediately to the AS seed under UV light. The organic signal increased quickly upon addition of AS aerosol, but began to decrease soon after irradiation began. Upon reaching a maximum, the GL marker signal decayed faster than wall loss and the maximum is reached earlier than in the experiments under dark conditions. No dilution was performed in the irradiated experiments. The fractional contribution of  $m/z$  44 and  $m/z$  68 increased upon irradiation (Fig. 2.7). The irradiation resulted in a temperature increase of  $\sim 5^\circ\text{C}$  and a drop in

relative humidity (see Table 2.2). As a result, the liquid water content (LWC) was lowered and the total aerosol volume decreased, which made it impossible to determine the mass of GL taken up into the aerosol from the DMA data. The fragment with  $m/z$  44 can be confidently assigned as  $\text{CO}_2^+$ , and in AMS spectra is considered an indicator of the oxidation state of organic aerosol. Its increase in irradiated experiments points to the fact that the amount of oxidized organic species is increasing in these experiments. In agreement with this, numerous highly oxidized organic species were detected via the UPLC/ESI-HR-TOFMS analysis, including glyoxylic, glycolic, and formic acids. Filter sample analysis also showed the presence of a sulphur containing compound with  $m/z$  155. No OH source was added in these experiments but a small amount of OH is potentially being produced via photolysis of GL, resulting in formation of the carboxylic acids. In one experiment, Fe was added to the seed (Exp. 9). The results closely resembled those of the other irradiated experiments (Exp. 8 and 10). Although carboxylic acids are formed, the O:C ratio of the organic fraction of the aerosol is not increasing but rather decreasing. In contrast the H:C and N:C ratios both increase in these experiments. The ammonium fraction of the aerosol is excluded in the calculation of N:C ratio.

## 2.5 Discussion

### 2.5.1 Organosulfate Formation

The fragment ions  $m/z$  145 and 175, which were previously assigned the formulas  $\text{CH}_5\text{O}_6\text{S}^+$  and  $\text{C}_2\text{H}_7\text{O}_7\text{S}^+$ , respectively by Liggio et al. (2005a), were unequivocally determined to be  $\text{C}_5\text{H}_5\text{O}_5^+$  and  $\text{C}_6\text{H}_7\text{O}_6^+$ , respectively (Fig. 2.4a and b) with the AMS in “W-mode.” The detection of these fragments demonstrates the existence of trimers or larger  $\text{GL}_n$  in the aerosol. Liggio et al. (2005a) suggested that these fragments correspond to fragmentation products of GL sulfates formed from a proposed aqueous reaction of sulfate or bisulfate with GL. If this proposed mechanism were correct, it would be the only evidence prior to the work presented here for the formation of GL sulfates in chamber aerosol resulting from GL uptake. The current study is in the unique position to unambiguously determine the chemical formulas of both fragment ions due to the employment of



the high-resolution “W-mode,” which is not possible with a quadrupole AMS. No sulfate esters were detected by the UPLC/ESI-HR-TOFMS analysis of filter samples in nonirradiated conditions with neutral or acidic seed (Fig. 2.5b and 2.5c). This evidence suggests that GL sulfate does not form in dark GL uptake experiments with AS seed.

Our results do not rule out that sulfates were formed in the study by Liggio et al. (2005b), and our irradiated experiments clearly demonstrate that organosulfates can form. Figure 2.5a shows that  $m/z$  155, which corresponds to glycolic acid sulfate ( $C_2H_3SO_6^-$ , see below), is measured in filter samples obtained during irradiated experiments (Exp. 8 and 10). The AMS did not detect this sulfate, most likely due to a high degree of fragmentation. The same organosulfate (as judged by elution time and formula)  $C_2H_3SO_6^-$  has previously been detected in filter samples from isoprene photooxidation experiments conducted in the Caltech chamber (Surratt et al., 2008) under intermediate- and high- $NO_x$  conditions, which favour GL production, but only with acidic seed. Ambient organic aerosol collected from K-puszta, Hungary (Gómez-González et al., 2008) and from the southeastern US (Surratt et al., 2008) has also been found to contain this  $C_2H_3SO_6^-$  organosulfate. In the previous work this sulfate was proposed to be GL sulfate. In all of these studies the filter extraction was performed in methanol. As sulfate is a better leaving group than methoxy, it appeared likely that the initially proposed GL sulfate would not be observed with the methanol extraction method, as it should dissociate. Thus, isomers of  $C_2H_3SO_6^-$  were investigated, and glycolic acid sulfate was chosen as a likely candidate since this sulfate should be more stable in methanol, and as a different glycolic acid ester was proposed as one of the products of the light induced experiments in the work presented here, which suggests that a pathway for glycolic acid production exists. We subsequently synthesized the glycolic acid sulfate and verified that the mass and elution time of the standard and the  $C_2H_3SO_6^-$  sulfate observed in this and previous studies were identical using UPLC/ESI-HR-TOFMS (Fig. 2.5d). This analysis shows that previous assignments of glyoxal sulfate that were obtained via filter extraction involving methanol or related solvents, such as in the chamber and ambient aerosol studies mentioned above, should be revisited as carbonyl sulfates are not stable under these conditions. However, this does not rule out the existence of carbonyl sulfates

under the conditions present in aerosol.

This is the first report of glycolic acid sulfate measured in chamber filter samples of GL uptake, and one of the few organosulfates to be positively identified in ambient aerosol. Acid catalysis has been traditionally been implicated in the formation of organosulfates. However, this study shows no sulfate formation under acidic conditions in the absence of light (Exp. 5 and 6) and recent studies have questioned this pathway for lower tropospheric conditions and instead proposed an epoxide pathway (Minerath et al., 2008; Minerath and Elrod, 2009). In contrast, the glycolic acid sulfate formation observed in this work requires a light induced pathway as it is only observed in the presence of light (Exp. 8 and 10), even in neutral seed aerosol. Although the identification of  $\text{C}_2\text{H}_3\text{SO}_6^-$  as glycolic acid sulfate reconciles the expected chemical stability to methanol extraction, it is unclear how glycolic acid or its sulfate are formed, although the increasing  $m/z$  44 marker shows that there is active oxidative chemistry occurring in the presence of UV light. However, glycolic acid is not an oxidation product of GL but rather a disproportionation product. We are currently investigating the pathway for glycolic acid sulfate formation, which is unlikely to involve an epoxide.

## 2.5.2 Carbon-Nitrogen Containing Compound Formation

Although no significant AMS fragments containing both sulphur and carbon are found, several fragments in the high-resolution spectra are found to contain nitrogen together with carbon, hydrogen and occasionally oxygen (Table 2.4). In addition, filter samples analyzed with UPLC/ESI-HR-TOFMS in positive mode showed compounds containing carbon and nitrogen (C-N compounds), listed in Table 2.4. The identification of the species corresponding to the chemical formulae listed in Table 2.4 is ongoing, but we have achieved a positive identification of three masses in the AMS spectra; the strong signals at  $m/z$  41 ( $\text{C}_2\text{H}_3\text{N}$ ) and 68 ( $\text{C}_3\text{H}_4\text{N}_2$ , Fig. 2.8a), and a weaker signal at  $m/z$  96 ( $\text{C}_4\text{H}_4\text{N}_2\text{O}$ , Fig. 2.8b). The carrier of  $m/z$  97 from the filter samples also had the formula  $\text{C}_4\text{H}_4\text{N}_2\text{O}$  (after the subtraction of a proton) in high-resolution positive mode ESI and had the same elution time as a standard of 1H-imidazole-2-carboxaldehyde (Sigma-Aldrich). The AMS fragments are also consistent with 1H-imidazole-2-carboxaldehyde. The high-resolution masses observed with

UPLC/ESI-HR-TOFMS and the AMS, the AMS fragmentation pattern and the observed elution time provide strong support for the assignment of the carrier of this signal to 1H-imidazole-2-carboxaldehyde. In further support of this finding, the general Debus mechanism for imidazole formation (see following paragraph) predicts the formation of 1H-imidazole-2-carboxaldehyde as shown in Fig. 2.9. Other C-N containing products were observed, but have not been positively identified. The production of a very stable aromatic compound such as an imidazole may be the thermodynamic driving force behind this reaction and explains why carbon-nitrogen containing fragments are observed in the AMS. This is in contrast to the case of organic nitrates, which fragment easily via loss of the nitrogen moiety.

Since no  $\text{NO}_x$  was present or added to the chamber before GL addition, the only source of labile nitrogen is ammonium from AS. Therefore, the C-N ions likely arise from fragmentation of products of a reaction between GL and ammonium. Although the ammonium ion is not a nucleophile and is not expected to react with GL, there will be a non-negligible concentration of ammonia in equilibrium with ammonium at the pH found in AS aerosol. The reaction of GL and ammonia is an established organic reaction for synthesis of imidazole and was described in 1858 (Debus, 1858). In view of recent literature describing the observation of light absorbing complexes and higher molecular weight compounds from reaction of bulk solutions containing AS and GL (Nozière et al., 2009; Shapiro et al., 2009), it is interesting to note the observations by Debus (1858). Debus (1858) describes formation of a brown solution as well as two colorless products; imidazole ( $\text{C}_3\text{H}_4\text{N}_2$ ) and  $\text{C}_6\text{H}_6\text{N}_4$ , most likely 2,2'-bi-1H-imidazole, which is available commercially as a colored compound. Thus the reaction of GL with ammonia has a long history. In addition to reaction with ammonia, the reaction of GL with AS in bulk solution is well-established. In fact, a method for reaction of GL with formaldehyde and AS in bulk aqueous solution with 69% yield has been published and patented (Schulze, 1973). The author states the yield of imidazole is surprisingly high, which could be a result of catalytic activity by ammonium (proposed recently by Nozière et al. (2009)) in addition to being a reactant, although this is complicated by the pronounced effect of anions on GL (Ip et al., 2009). A similar method for the production of 2,2'-bi-1H-imidazole in bulk aqueous solution via

reaction of GL in AS with 43–54% yield has also been published and patented (Cho et al., 2003). Thus, reaction of GL with AS in bulk solutions to form coloured compounds has a well-established history. Other studies have addressed the effect of added gas-phase ammonia (Na et al., 2006, 2007), organic amines (Angelino et al., 2001; Murphy et al., 2007; Silva et al., 2008), and amino acids (De Haan et al., 2009) on SOA formation as well as bulk phase reactions between AS and GL (Nozière et al., 2009; Shapiro et al., 2009) and amino acids and GL (De Haan et al., 2009), but to the authors’ knowledge, imidazole compounds have not been previously detected in AS seed aerosol chamber studies. The mass spectrum published by Liggio et al. (2005a) does not show a peak at  $m/z$  68. However, subsequent to the initial publication of our work, De Haan et al. (2009) identified substituted imidazole compounds formed from the reaction of GL and amino acids in both the bulk phase and in solid phase aerosols. We report the first observation of the formation of C-N containing compounds from reaction of a carbonyl in AS seed aerosol, but this finding is not surprising given the recent findings by De Haan et al. (2009) and the well established chemistry reported for bulk solutions.

Little experimental data are available on the physical properties of 1H-imidazole-2-carboxaldehyde, though it is predicted to have a vapor pressure of  $1.43 \times 10^{-3}$  torr (SciFinder Scholar, 2008). Under mildly acidic conditions, this molecule would be protonated, lowering the vapor pressure and making it a viable candidate for an SOA constituent. The  $pK_B$  of imidazole is 7, so 50% will be protonated in neutral solutions. Thus at the pH of AS ( $\sim 5$ ) most of the imidazole will be protonated and the low volatility is evidenced by the fact that the carrier of the  $m/z$  68 signal does not repartition to the gas phase in the dilution or irradiated experiments. The imidazole and other C-N compounds only contribute a small amount to the total organic mass. It is possible that reaction of other  $\alpha$ -dicarbonyls and aldehydes could increase this contribution. However, as mentioned above, some of the reaction products of GL and AS are strongly light absorbing (Shapiro et al., 2009) and even amounts that do not add significantly to SOA mass could affect aerosol optical properties. As the imidazole is formed irreversibly, it could be used as a tracer for atmospheric carbonyl–nitrogen reactivity with implications for changing aerosol optical properties.

### 2.5.3 Overall Organic Growth and Glyoxal Oligomer Formation

Analysis of the AMS spectra collected indicates strong evidence for  $GL_n$  within the aerosol (see Fig. 2.3). It is important to note that fragments with one or two carbons do not necessarily arise only from GL monomers in the particle phase. They can also be fragmentation products of larger oligomers; thus C1 and C2 fragments are a result of fragmentation of at least a monomer, C3 and C4 fragments are the result of fragmentation from at least a dimer, and so on. The GL and  $GL_n$  mass fragments stop growing in parallel with overall organic growth and show analogous behaviour to total organic growth upon dilution. Organic growth in our study reached a plateau, providing evidence for a steady-state point, which could either be due to a depletion of a reactant in an intrinsically irreversible process or because equilibrium, with a corresponding modified effective Henry's law constant, is achieved. The dilution experiments, in which the chamber air mass was diluted with GL-free air, provide key evidence that this plateau is not caused by the depletion of a reactant. The dilution process itself reduces the gas-phase GL concentration and aerosol number density and thus total aerosol volume but does not change the composition of the aerosol phase. However, if the aerosol-phase composition was achieved via equilibrium with the gas-phase GL, reduction of the gas-phase GL concentration via dilution disturbs this equilibrium. As a result the aerosol-phase organic content immediately after dilution is higher than the equilibrium value for the reduced gas-phase concentration would predict. The system will respond by repartitioning GL to the gas phase. In our dilution experiments, which reduce the gas-phase GL concentration by 25%–40% (Fig. 2.6), the organic:sulfate ratio decreases by 15%–25%, which shows that organic aerosol content decreases relative to sulfate, implying a loss of GL from the aerosol phase. This shows that GL uptake onto AS aerosol is reversible; GL will partition from the aerosol to gas phase in the event of lowered gas phase concentrations in the case of reversible uptake. The fact that the aerosol phase organic content decreased a little less than the gas-phase GL concentration is expected from the (slow) kinetics.

For the dark GL uptake experiments, only C-N compounds, GL and  $GL_n$  were identified, while no organosulfate was found. C-N compounds are clearly formed irreversibly, since no loss from the aerosol was seen upon dilution. The fact that they only contribute a small part of the organic

AMS signal and that overall organic growth as well as GL and  $GL_n$  growth are reversible, suggests strongly that overall growth is dominated by GL and  $GL_n$ . The studies by Liggio et al. (2005a,b) were conducted on timescales ( $\sim 4$  h) in which equilibrium was not yet achieved in our studies. We have therefore compared our organic growth during the first 4 h with that of Liggio et al. (2005a,b) for experiments at similar relative humidities of 49% (Liggio et al., 2005a,b) and 55% (this study) and gas-phase GL concentrations of 5.1 ppb<sub>v</sub> (Liggio et al., 2005a,b) and  $\sim 70$  ppb<sub>v</sub> (this study). The organic/sulfate ratio after 4 h in the work by Liggio et al. (2005a) is  $\sim 16$ , which is more than an order of magnitude larger than in this study ( $\sim 0.35$ ), and we expect that the difference would have been even larger if we had employed the lower GL mixing ratios of the work by Liggio et al. (2005a,b). Although the first two hours of our data can be interpreted with a linear slope, the curvature of 2-4 hrs in the study presented here shows a decreasing uptake rate in agreement with the fact that equilibrium is achieved after about 10 h. It is hard to interpret a clear curvature in the work by Liggio et al. (2005a). The average aerodynamic diameter of the seed aerosol in the study by Liggio et al. (2005a) is initially smaller, and thus the uptake rate per volume of seed aerosol is expected to be faster than in this study, but it is unlikely that this alone can explain the discrepancy. In a more recent study, Volkamer et al. (2009) showed that photochemical uptake was higher within 90 seconds than over several hours in our study and the study of Kroll et al. (2005). The presence of OH in the study by Volkamer et al. (2009) represents a significant difference, which could explain the large difference in uptake rate. However, we also currently cannot determine a particular reason why the non-irradiated studies potentially show two different types of uptake (irreversible and reversible) at different rates, information that is critical if understanding of these processes is to be applied to ambient studies.

Although the primary focus of this work are the condensed phase reactions of GL and the reversibility of uptake onto AS aerosol, effective Henry's Law values for GL were also calculated. Kroll et al. (2005) assumed a unit density of 1 g/cm<sup>3</sup> and used the seed volume to calculate aerosol GL concentrations. In this manner the authors obtained a value of  $K_{H,mod}^* = 2.6 \times 10^7$  M/atm. However, the densities of GL trimer dihydrate (in our lab) and GL aerosol derived from drying aerosolized 40%

w/w GL solutions (D. De Haan, personal communication, 2009) have since been measured. These densities were determined to be 1.67 g/cm<sup>3</sup> and 1.71 g/cm<sup>3</sup>, respectively. Therefore, the density of GL used in this work is  $\rho=1.69$  g/cm<sup>3</sup>, which is likely a lower limit due to partial molar volume effects in solution. Using this density, we calculate an effective Henry's Law value of  $3.4\times 10^7$  M/atm for the data from Kroll et al. (2005) and a value between  $4.2\times 10^7$  M/atm and  $7.0\times 10^7$  M/atm from this study. The study by Volkamer et al. (2009) used a density of  $\rho=2$  g/cm<sup>3</sup> and used the fraction of seed volume corresponding to LWC to calculate a modified GL concentration. In this manner they obtained a value of  $K_{H,mod}^{**}=1.65\times 10^8$  M/atm. Using this method and density, we calculate a value between  $1.51\times 10^8$  M/atm and  $2.52\times 10^8$  M/atm for our study, reflecting the experimental uncertainty. However, it should be noted that the two studies were conducted under different conditions, as the study Volkamer et al. (2009) had an OH source present, and thus the corresponding Henry's Law constants cannot be directly compared. More work is needed to determine the effect of GL concentration, AS and LWC on the effective Henry's Law constant of GL.

#### 2.5.4 Glyoxal Uptake under Irradiated Conditions

We present the first analysis of organic reaction products formed during irradiated GL uptake with AS seed aerosol. Within the framework of Fig. 2.1, the light induced reactions that are occurring should add additional product channels in the condensed phase, so a higher uptake would be expected under irradiated conditions. No OH source was added in our study and thus conditions are not identical to those employed by Volkamer et al. (2009). However, there is a marked difference in the fate of GL in the particle phase for the irradiated conditions compared to dark conditions in our study, even without an added OH source: an organosulfate and organic acids are formed. As discussed earlier, the organosulfate formation is a result of a light induced mechanism, as can be seen in the lack of organosulfate formed even in highly acidic aerosol under non-irradiated conditions.

The relative signal strength of  $m/z$  44, an indicator of oxidized organic aerosol in the AMS spectra, shows that a substantial amount of oxidized organics are formed over the duration of the irradiated experiments. This is supported by the organic acids found in filter sample analysis:

formic, glyoxylic and glycolic acids, the latter a disproportionation product of GL, all of which have smaller Henry's law constants than GL. The formic acid and glycolic acid are observed as an ester, a higher molecular weight condensation product. Although no OH source was added, the observation of glyoxal oxidation products strongly indicates that the irradiation resulted in radical chemistry. Whether this chemistry occurred via OH or some other radical mechanism cannot be ascertained. If oxidation to more volatile products, such as glyoxylic acid, is not significantly faster than condensation (e.g., the formic-glycolic acid ester, or oxidation to oxalic acid, which can form SOA), the net SOA yield under irradiated conditions should be higher than under dark conditions as additional product channels are available. These additional product channels also make Henry's law analysis of uptake inapplicable. In contrast to the study of Volkamer et al. (2009), which generally found increased uptake and uptake rate but had an OH source, overall organic growth was reduced under irradiated conditions in this study as compared to dark conditions. Enhanced loss of particle-phase GL in the presence of light was observed, but while it is possible that rapid oxidation to higher volatility compounds, such as formic and glyoxylic acid, and subsequent partitioning of these to the gas phase is competing with the formation of  $GL_n$  and reaction of the oxidation products to higher molecular weight compounds, it is also possible that increasing temperature upon irradiation causes significant amounts of GL to repartition to the gas phase. This is supported by the fact that the O:C ratio started to decrease once the chambers were irradiated. As the chambers heated, GL (O:C=1:1, H:C=1:1) and possibly high volatility glyoxal oxidation products are revolatilized to the gas phase, leaving behind irreversibly formed compounds such as imidazoles (O:C=1:4, N:C=1:2 and H:C=1:1) and low volatility carboxylic acids. This loss of GL, together with the lack of loss of imidazole, explains the increase in the N:C ratio and an increase in the H:C ratio, both of which are seen in these experiments. It is important to note that heating the chambers does not result in efflorescence of the aerosol, as this would trap the GL within the aerosol and increase oligomer formation (Loeffler et al., 2006), which is not observed. GL photolysis in the gas phase is also possible; however, since the walls act as a substantial reservoir of GL that is at steady state with the gas phase, this is less likely. In fact, during the irradiated GL uptake experiment shown in Fig. 2.7,



the gas-phase GL concentrations remained constant at  $\sim 150$  ppb<sub>v</sub> throughout the experiment. A quantitative comparison of SOA yields between dark and irradiated conditions is not possible for this work due to the different experimental conditions.

### 2.5.5 Implications to Ambient Aerosol

GL and other  $\alpha$ -dicarbonyls, such as methylglyoxal, are common oxidation products of both biogenic and anthropogenic VOCs. The concentration of these  $\alpha$ -dicarbonyls is typically highest during the day and thus SOA formation under irradiated conditions should be more important than under dark conditions. However, for a detailed understanding of the processes depicted in Fig. 2.1 and their contribution to SOA formation under ambient conditions, it is desirable to address these processes separately, therefore an analysis of GL uptake under both dark and irradiated conditions is helpful. While uptake and aerosol phase chemistry of GL and other  $\alpha$ -dicarbonyls may differ, understanding GL is instructive as a model for understanding the chemistry involved in other systems for model and experimental studies. Our study shows that GL uptake involves both reversible processes, such as growth via GL monomer and oligomers, and irreversible processes, such as C-N compound formation and oxidation reactions under irradiated conditions. The reversible processes are likely less relevant to ambient SOA formation as they will repartition GL to the gas phase upon decreasing GL gas-phase concentrations, such as nighttime or transport away from GL sources. However, they provide a pathway for uptake of GL into the particle phase, allowing the irreversible processes to proceed. The majority of organic growth in the chamber studies under dark conditions occurs via GL uptake with subsequent oligomer formation, but ambient GL concentrations are substantially lower (2–3 orders of magnitude), so it is less likely the organic character of the aerosol will involve multiple GL molecules such as oligomers and 1H-imidazole-2-carboxaldehyde. However, it is likely that reactions with other aldehydes will occur. Aldehydes and  $\alpha$ -dicarbonyls are ubiquitous, and the discovery of this new C-N reaction pathway allows for the potential production of many different imidazole compounds. While methylglyoxal is the most abundant  $\alpha$ -dicarbonyl, GL is likely the most important  $\alpha$ -dicarbonyl for formation of imidazoles due to the fact that the Henry's law

constant for GL is larger than that for methylglyoxal ( $K_{\text{H,aq,MGL}}^* = 3.2 \times 10^4 \text{ M/atm}$ ), and thus it partitions more strongly to aqueous aerosol. However, Matsunaga et al. (2004) detected higher levels of methylglyoxal than GL in ambient particulate matter, indicating that the high gas phase mixing ratios of methylglyoxal may make it an important contributor to SOA formation. As the underlying reasons for the large difference between  $K_{\text{H,aq}}^*$  and  $K_{\text{H,mod}}^*$  are not known, it is difficult to estimate the Henry's law constant for methylglyoxal for AS seed aerosol. Kroll et al. (2005) did not observe any organic growth for methylglyoxal, but the growth from imidazoles, which proceeds via an  $\alpha$ -dicarbonyl monomer, might have been below the detection threshold. Even small amounts of the newly discovered light absorbing compounds, in particular C-N compounds, in aerosol can influence the optical properties of the aerosol due to their strong absorptive properties (Shapiro et al., 2009). In this context it is interesting to note that Barnard et al. (2008) found enhanced absorption of "brown carbon" aerosol in Mexico City that added about 40% absorption to that of black carbon. Imidazoles are an ideal tracer for these C-N compounds, due to the ubiquitous nature of their precursors, as described above. This study suggests that methods should be developed to allow analysis of field aerosol samples with respect to this class of compound, and potentially also for compounds derived from methylglyoxal, which is typically present in higher concentrations in areas in which biogenic VOC chemistry dominates (Spaulding et al., 2003). This study also shows that irradiated conditions produce oxidation products of GL even in the absence of an added OH source. However, the monomers found in this study, such as formic acid, glycolic acid and glyoxylic acids, have lower Henry's law constants than GL and thus will not necessarily increase SOA yields. An exception would be the production of oxalic acid and higher molecular weight compounds, such as organosulfates, which would increase SOA yields.

## 2.6 Conclusions

This study provides new insights into processes that can contribute to SOA formation from GL and the degree of reversibility of these processes. Reversibility is judged with respect to the experimental

timescales, which were as long as 26 h after initiation of organic growth. We demonstrate that

1. GL does not form a sulfate (i.e. organosulfate of GL) that can be detected using methods based on filter extraction. It is likely that carbonyl sulfates are in general not stable enough to be identified with filter extraction methods. Previous assignments of such compounds should be revisited,
2.  $C_2H_3SO_6^-$ , which has been found in ambient samples, corresponds to glycolic acid sulfate. It is not formed under dark conditions with neutral or acidic AS seed aerosol and was only observed in irradiated experiments. The glycolic acid sulfate was identified by comparison with a laboratory synthesized standard,
3. carbon-nitrogen containing compounds form irreversibly with AS seed aerosol,
4. overall GL uptake and GL oligomer formation in the particle phase are reversible for neutral AS seed aerosol in the dark for the experimental conditions of this study,
5. there is clear evidence for active photochemistry for GL uptake under irradiated conditions, including formation of glyoxylic acid, glycolic acid, formic acid, and glycolic acid sulfate.

Further studies are required to evaluate imidazoles as tracers of carbonyl-ammonium chemistry that produces strongly light absorbing aerosol products. Studies are ongoing to elucidate the formation of condensed-phase oxidation products and, in particular, glycolic acid sulfate and the contribution of these compounds to SOA.

## 2.7 Acknowledgements

The authors are grateful to Tehshik Yoon for his helpful discussions about organic synthesis. This work was supported by the Camille and Henry Dreyfus Foundation, the NDSEG-ARO, the US Department of Energy grant DE-FG02-05ER63983 and US Environmental Protection Agency STAR grant RD-83374901. It has not been formally reviewed by EPA. The views expressed in this document are solely those of the authors and the EPA does not endorse any products in this publica-

tion. Development of the Madison-LIP instrument was supported by the National Science Foundation, Division of Atmospheric Sciences, Atmospheric Chemistry Program (grant 0724912), and the NDSEG-ARO. The Waters UPLC-LCT Premier XT time-of-flight mass spectrometer was purchased in 2006 with a grant from the National Science Foundation, Chemistry Research Instrumentation and Facilities Program (CHE-0541745).

## Bibliography

Aiken, A. C., DeCarlo, P. F. and Jimenez, J. L.: Elemental analysis of organic species with Electron Ionization High-Resolution Mass Spectrometry, *Anal. Chem.*, 79, 8350-8358, doi:10.1021/ac071150w, 2007.

Aiken, A. C., DeCarlo, P. F., Kroll, J. H., Worsnop, D. R., Huffman, J. A., Docherty, K., Ulbrich, I. M., Mohr, C., Kimmel, J. R., Sueper, D., Zhang, Q., Sun, Y., Trimborn, A., Northway, M., Ziemann, P. J., Canagaratna, M. R., Onasch, T. B., Alfarra, R., Prevot, A. S. H., Dommen, J., Duplissy, J., Metzger, A., Baltensperger, U. and Jimenez, J. L.: O/C and OM/OC ratios of primary, secondary, and ambient organic aerosols with High Resolution Time-of-Flight Aerosol Mass Spectrometry, *Environ. Sci. Technol.*, 42, 4478-4485, doi:10.1021/es703009q, 2008.

Angelino, S., Suess, D. T., and Prather, K. A.: Formation of aerosol particles from reactions of secondary and tertiary alkylamines: Characterization by aerosol time-of-flight mass spectrometry, *Environ. Sci. Technol.*, 35, 3130-3138, doi:10.1021/es0015444, 2001.

Barnard, J. C., Volkamer, R., and Kassianov, E. I.: Estimation of the mass absorption cross section of the organic carbon component of aerosols in the Mexico City Metropolitan Area, *Atmos. Chem. Phys.*, 8, 6665-6679, doi:10.5194/acp-8-6665-2008, 2008.

Canagaratna, M. R., Jayne, J. T., Jimenez, J. L., Allan, J. D., Alfarra, M. R., Zhang, Q., Onasch, T. B., Drewnick, F., Coe, H., Middlebrook, A., Delia, A., Williams, L. R., Trimborn, A. M., Northway, M. J., DeCarlo, P. F., Kolb, C. E., Davidovits, P., and Worsnop, D. R.: Chemical and

- microphysical characterization of ambient aerosols with the Aerodyne Aerosol Mass Spectrometer, *Mass. Spectrom. Rev.*, 26, 185–222, doi:10.1002/mas.20115, 2007.
- Carlton, A. G., Turpin, B. J., Altieri, K. E., Seitzinger, S., Reff, A., Lim, H. J., and Ervens, B.: Atmospheric oxalic acid and SOA production from glyoxal: Results of aqueous photooxidation experiments, *Atmos. Environ.*, 41, 7588–7602, doi:10.1016/j.atmosenv.2007.05.035, 2007.
- Cho, J. R., Cho, S. G., Goh, E. M. and Kim, J. K.: Procède de preparation du 2,2',-bi-1H-imidazole a partir du glyoxal ed d'un sel d'ammonium, 0304378, 2003.
- Cocker, D. R., Flagan, R. C., and Seinfeld, J. H.: State-of-the-art chamber facility for studying atmospheric aerosol chemistry, *Environ. Sci. Technol.*, 35, 2594–2601, doi:10.1021/es0019169, 2001.
- Corrigan, A. L., Hanley, S. W., and De Haan, D. O.: Uptake of glyoxal by organic and inorganic aerosol, *Environ. Sci. Technol.*, 42, 4428–4433, doi:10.1021/es7032394, 2008.
- de Gouw, J. A., Middlebrook, A. M., Warneke, C., Goldan, P. D., Kuster, W. C., Roberts, J. M., Fehsenfeld, F. C., Worsnop, D. R., Canagaratna, M. R., Pszenny, A. A. P., Keene, W. C., Marchewka, M., Bertman, S. B., and Bates, T. S.: Budget of organic carbon in a polluted atmosphere: Results from the New England air quality study in 2002, *J. Geophys. Res.-Atmos.*, 110, D16305, doi:10.1029/2004JD005623, 2005.
- De Haan, D. O., Corrigan, A. L., Smith, K. W., Stroik, D. R., Turley, J. J., Lee, F. E., Tolbert, M. A., Jimenez, J. L., Cordova, K. E. and Ferrell, G. R.: Secondary organic aerosol-forming reactions of glyoxal with amino acids, *Environ. Sci. Technol.*, 43, 2818–2824, doi:10.1021/es803534f, 2009.
- Debus, H.: Ueber die einwirkung des ammoniaks auf glyoxal, *Annalen der Chemie und Pharmacie*, 107, 199–208, doi:10.1002/jlac.18581070209, 1858.
- DeCarlo, P. F., Kimmel, J. R., Trimborn, A., Northway, M. J., Jayne, J. T., Aiken, A. C., Gonin, M., Furher, K., Horvath, T., Docherty, K. S., Worsnop, D. R. and Jimenez, J. L.: Field-deployable, high-resolution, time-of-flight aerosol mass spectrometer, *Anal. Chem.*, 78, 8281–8289, doi:10.1021/ac061249n, 2006.

- Denkenberger, K. A., Moffet, R. C., Holecek, J. C., Rebotier, T. P., and Prather, K. A.: Real-time, single-particle measurements of oligomers in aged ambient aerosol particles, *Environ. Sci. Technol.*, 41, 5439–5446, doi:10.1021/es070329l, 2007.
- Ervens, B., Carlton, A. G., Turpin, B. J., Altieri, K. E., Kreidenweis, S. M., and Feingold, G.: Secondary organic aerosol yields from cloud-processing of isoprene oxidation products, *Geophys. Res. Lett.*, 35, L02816, doi:10.1029/2007GL031828, 2008.
- Fratzke, A. R. and Reilly, P. J.: Thermodynamic and kinetic analysis of the dimerization of aqueous glyoxal, *Int. J. Chem. Kinet.*, 18, 775–789, doi:10.1002/kin.550180705, 1986.
- Fu, T. M., Jacob, D. J., Wittrock, F., Burrows, J. P., Vrekoussis, M., and Henze, D. K.: Global budgets of atmospheric glyoxal and methylglyoxal, and implications for formation of secondary organic aerosols, *J. Geophys. Res.-Atmos.*, 113, D15303, doi:10.1029/2007JD009505, 2008.
- Gómez-González, Y., Surratt, J. D., Cuyckens, F., Szmigielski, R., Vermeylen, R., Jaoui, M., Lewandowski, M., Offenberg, J. H., Kleindienst, T. E., Edney, E. O., Blockhuys, F., Van Alsenoy, C., Maenhaut, W., and Claeys, M.: Characterization of organosulfates from the photooxidation of isoprene and unsaturated fatty acids in ambient aerosol using liquid chromatography/(-) electrospray ionization mass spectrometry, *J. Mass. Spectrom.*, 43, 371–382, doi:10.1002/jms.1329, 2008.
- Gross, D. S., Galli, M. E., Kalberer, M., Prevot, A. S. H., Dommen, J., Alfarra, M. R., Duplissy, J., Gaeggeler, K., Gascho, A., Metzger, A., and Baltensperger, U.: Real-time measurement of oligomeric species in secondary organic aerosol with the aerosol time-of-flight mass spectrometer, *Anal. Chem.*, 78, 2130–2137, doi:10.1021/ac060138l, 2006.
- Hastings, W. P., Koehler, C. A., Bailey, E. L. and DeHaan, D. O.: Secondary organic aerosol formation by glyoxal hydration and oligomer formation: humidity effects and equilibrium shifts during analysis, *Environ. Sci. Technol.*, 39, 8728–8735, doi:10.1021/es050446l, 2005.
- Heald, C. L., Jacob, D. J., Park, R. J., Russell, L. M., Huebert, B. J., Seinfeld, J. H., Liao, H., and

- Weber, R. J.: A large organic aerosol source in the free troposphere missing from current models, *Geophys. Res. Lett.*, 32, L18809, doi:10.1029/2005GL023831, 2005.
- Huisman, A. J., Hottle, J. R., Coens, K. L., DiGangi, J. P., Galloway, M. M., Kammrath, A., and Keutsch, F. N.: Laser-induced phosphorescence for the in situ detection of glyoxal at part per trillion mixing ratios, *Anal. Chem.*, 80, 5884–5891, doi:10.1021/ac800407b, 2008.
- Ip, H. S. S., Huang, X. H. H. and Yu, J. Z.: Effective Henry’s law constants of glyoxal, glyoxylic acid, and glycolic acid, *Geophys. Res. Lett.*, 36, L01802, doi:10.1029/2008GL036212, 2009.
- Jang, M. S., Czoschke, N. M., Lee, S., and Kamens, R. M.: Heterogeneous atmospheric aerosol production by acid-catalyzed particle-phase reactions, *Science*, 298, 814–817, doi:10.1126/science.1075798, 2002.
- Keywood, M. D., Varutbangkul, V., Bahreini, R., Flagan, R. C., and Seinfeld, J. H.: Secondary organic aerosol formation from the ozonolysis of cycloalkenes and related compounds, *Environ. Sci. Technol.*, 38, 4157–4164, doi:10.1021/es035363o, 2004.
- Kielhorn, J., Pohlenz-Michel, C., Schmidt, S. and Mangelsdorf, I.: Concise International Chemical Assessment Document 57: Glyoxal, 57, 2004.
- Kroll, J. H., Ng, N. L., Murphy, S. M., Varutbangkul, V., Flagan, R. C., and Seinfeld, J. H.: Chamber studies of secondary organic aerosol growth by reactive uptake of simple carbonyl compounds, *J. Geophys. Res.*, 110, D23207, doi:10.1029/2005JD006004, 2005.
- Liggio, J., Li, S., and McLaren, R.: Heterogeneous reactions of glyoxal on particulate matter: Identification of acetals and sulphate esters, *Environ. Sci. Technol.*, 39, 1532–1541, doi:10.1021/es048375y, 2005a.
- Liggio, J., Li, S., and McLaren, R.: Reactive uptake of glyoxal by particulate matter, *J. Geophys. Res.*, 110, D10304, doi:10.1029/2004JD005113, 2005b.

- Loeffler, K. W., Koehler, C. A., Paul, N. M., and De Haan, D. O.: Oligomer formation in evaporating aqueous glyoxal and methyl glyoxal solutions, *Environ. Sci. Technol.*, 40, 6318–6323, doi:10.1021/es060810w, 2006.
- Matsunaga, S., Mochida, M., and Kawamura, K.: Variation on the atmospheric concentrations of biogenic carbonyl compounds and their removal processes in the Northern Forest at Moshiri, Hokkaido Island in Japan, *J. Geophys. Res.*, 109, D04302, doi:10.1029/2003JD004100, 2004.
- Minerath, E. C. and Elrod, M. J.: Assessing the potential for diol and hydroxy sulfate ester formation from the reaction of epoxides in tropospheric aerosols, *Environ. Sci. Technol.*, 43, 1386–1392, doi:10.1021/es8029076, 2009.
- Minerath, E. C., Casale, M. T. and Elrod, M. J.: Kinetics feasibility study of alcohol sulfate esterification reactions in tropospheric aerosols, *Environ. Sci. Technol.*, 42, 4410–4415, doi:10.1021/es8004333, 2008.
- Murphy, S. M., Sorooshian, A., Kroll, J. H., Ng, N. L., Chhabra, P., Tong, C., Surratt, J. D., Knipping, E., Flagan, R. C., and Seinfeld, J. H.: Secondary aerosol formation from atmospheric reactions of aliphatic amines, *Atmos. Chem. Phys.*, 7, 2313–2337, doi:10.5194/acp-7-2313-2007, 2007.
- Myriokefalitakis, S., Vrekoussis, M., Tsigaridis, K., Wittrock, F., Richter, A., Brühl, C., Volkamer, R., Burrows, J. P., and Kanakidou, M.: The influence of natural and anthropogenic secondary sources on the glyoxal global distribution, *Atmos. Chem. Phys.*, 8, 4965–4981, doi:10.5194/acp-8-4965-2008, 2008.
- Na, K., Song, C., Switzer, C., and Cocker, D. R.: Effect of ammonia on secondary organic aerosol formation from alpha-pinene ozonolysis in dry and humid conditions, *Environ. Sci. Technol.*, 41, 6096–6102, doi:10.1021/es061956y, 2007.
- Na, K., Song, C., and Cocker, D. R.: Formation of secondary organic aerosol from the reaction



- of styrene with ozone in the presence and absence of ammonia and water, *Atmos. Environ.*, 40, 1889–1900, doi:10.1016/j.atmosenv.2005.10.063, 2006.
- Nenes, A., Pandis, S. N. and Pilinis, C.: ISORROPIA: A new thermodynamic equilibrium model for multiphase multicomponent inorganic aerosols, *Aquat. Geochem.*, 4, 123–152, doi:10.1023/A:1009604003981, 1998.
- Nozière, B., Dziedzic, P. and Córdoba, A.: Products and kinetics of the liquid-phase reaction of glyoxal catalyzed by ammonium ions ( $\text{NH}_4^+$ ), *J. Phys. Chem. A*, 113, 231–237, doi:10.1021/jp8078293, 2009.
- Odum, J. R., Hoffmann, T., Bowman, F., Collins, D., Flagan, R. C., and Seinfeld, J. H.: Gas/particle partitioning and secondary organic aerosol yields, *Environ. Sci. Technol.*, 30, 2580–2585, doi:10.1021/es950943+, 1996.
- Pankow, J. F.: An absorption-model of gas-particle partitioning of organic-compounds in the atmosphere, *Atmos. Environ.*, 28, 185–188, doi:10.1016/1352-2310(94)90093-0, 1994a.
- Pankow, J. F.: An absorption-model of the gas aerosol partitioning involved in the formation of secondary organic aerosol, *Atmos. Environ.*, 28, 189–193, doi:10.1016/1352-2310(94)90094-9, 1994b.
- Reinhardt, A., Emmenegger, C., Gerrits, B., Panse, C., Dommen, J., Baltensperger, U., Zenobi, R., and Kalberer, M.: Ultrahigh mass resolution and accurate mass measurements as a tool to characterize oligomers in secondary organic aerosols, *Anal. Chem.*, 79, 4074–4082, doi:10.1021/ac062425v, 2007.
- Schweitzer, F., Magi, L., Mirabel, P., and George, C.: Uptake rate measurements of methanesulfonic acid and glyoxal by aqueous droplets, *J. Phys. Chem. A*, 102, 593–600, doi:10.1021/jp972451k, 1998.
- SciFinder Scholar: Calculated using Advanced Chemistry Development (ACD/Labs) Software V8.14 for Solaris (1994–2008 ACD/Labs), last access: 26 September 2008.

- Silva, P. J., Erupe, M. E., Price, D., Elias, J., Malloy, Q. G. J., Li, Q., Warren, B., and Cocker, D. R.: Trimethylamine as precursor to secondary organic aerosol formation via nitrate radical reaction in the atmosphere, *Environ. Sci. Technol.*, 42, 4689–4696, doi:10.1021/es703016v, 2008.
- Shapiro, E. L., Szprengiel, J., Sareen, N., Jen, C. N., Giordano, M. R. and McNeill, V. F.: Light-absorbing secondary organic material formed by glyoxal in aqueous aerosol mimics, *Atmos. Chem. Phys.*, 9, 2289–2300, doi:10.5194/acp-9-2289-2009, 2009.
- Schulze, H.: Imidazole Synthesis, 113684, 1973.
- Sorooshian, A., Varutbangkul, V., Brechtel, F. J., Ervens, B., Feingold, G., Bahreini, R., Murphy, S. M., Holloway, J. S., Atlas, E. L., Buzorius, G., Jonsson, H., Flagan, R. C., and Seinfeld, J. H.: Oxalic acid in clear and cloudy atmospheres: Analysis of data from International Consortium for Atmospheric Research on Transport and Transformation 2004, *J. Geophys. Res.-Atmos.*, 111, D23S45, doi:10.1029/2005JD006880, 2006.
- Spaulding, R. S., Schade, G. W., Goldstein, A. H., and Charles, M. J.: Characterization of secondary atmospheric photooxidation products: Evidence for biogenic and anthropogenic sources, *J. Geophys. Res.*, 108, 4247, doi:10.1029/2002JD002478, 2003.
- Surratt, J. D., Gómez-González, Y., Chan, A. W. H., Vermeylen, R., Shahgholi, M., Kleindienst, T. E., Edney, E. O., Offenberg, J. H., Lewandowski, M., Jaoui, M., Maenhaut, W., Claeys, M., Flagan, R. C., and Seinfeld, J. H.: Organosulfate formation in biogenic secondary organic aerosol, *J. Phys. Chem. A*, 112, 8345–8378, doi:10.1021/jp802310p, 2008.
- Surratt, J. D., Kroll, J. H., Kleindienst, T. E., Edney, E. O., Claeys, M., Sorooshian, A., Offenberg, J. H., Lewandowski, M., Jaoui, M., Flagan, R. C., and Seinfeld, J. H.: Evidence for organosulfates in secondary organic aerosol, *Environ. Sci. Technol.*, 41, 517–527, doi:10.1021/es062081q, 2007.
- Volkamer, R., Jimenez, J. L., San Martini, F., Dzepina, K., Zhang, Q., Salcedo, D., Molina, L. T., Worsnop, D. R., and Molina, M. J.: Secondary organic aerosol formation from an-

- thropogenic air pollution: Rapid and higher than expected, *Geophys. Res. Lett.*, **33**, L17811, doi:10.1029/2006GL026899, 2006.
- Volkamer, R., San Martini, F., Molina, L. T., Salcedo, D., Jimenez, J. L., and Molina, M. J.: A missing sink for gas-phase glyoxal in Mexico City: Formation of secondary organic aerosol, *Geophys. Res. Lett.*, **34**, L19807, doi:10.1029/2007GL030752, 2007.
- Volkamer, R., Ziemann, P. J., and Molina, M. J.: Secondary organic aerosol formation from acetylene ( $C_2H_2$ ): seed effect on SOA yields due to organic photochemistry in the aerosol aqueous phase, *Atmos. Chem. Phys.*, **9**, 1907-1928, doi:10.5194/acp-9-1907-2009, 2009.
- Whipple, E. B.: The structure of glyoxal in water, *J. Am. Chem. Soc.*, **92**, 7183-7186, doi:10.1021/ja00727a027, 1970.
- Zhang, Q., Jimenez, J. L., Canagaratna, M. R., Allan, J. D., Coe, H., Ulbrich, I., Alfarra, M. R., Takami, A., Middlebrook, A. M., Sun, Y. L., Dzepina, K., Dunlea, E., Docherty, K. S., DeCarlo, P. F., Salcedo, D., Onasch, T., Jayne, J. T., Miyoshi, T., Shimonono, A., Hatakeyama, S., Takegawa, N., Kondo, Y., Schneider, J., Drewnick, F., Borrmann, S., Weimer, S., Demerjian, K., Williams, P., Bower, K., Bahreini, R., Cottrell, L., Griffin, R. J., Rautiainen, J., Sun, J. Y., Zhang, Y. M., and Worsnop, D. R.: Ubiquity and dominance of oxygenated species in organic aerosols in anthropogenically-influenced Northern Hemisphere midlatitudes, *Geophys. Res. Lett.*, **34**, L13801, doi:10.1029/2007GL029979, 2007.
- Zhou, X. and Mopper, K.: Apparent partition coefficients of 15 carbonyl compounds between air and seawater and between air and freshwater, implications for air-sea exchange, *Environ. Sci. Technol.*, **24**, 1864-1869, doi:10.1021/es00082a013, 1990.

**Table 2.1:** Experimental conditions of dark experiments

	Seed <sup>a</sup>	[GL] <sup>b</sup> ppb <sub>v</sub>	RH	Temp K	LWC <sup>c</sup>	Seed volume <sup>d</sup> , $V$ $\mu\text{m}^3/\text{cm}^3$	$\Delta V$ $\mu\text{m}^3/\text{cm}^3$	$M_{\text{GL}}$ <sup>e</sup> $\mu\text{g}/\text{cm}^3$
1	AS	131	65%	294	43%	84.0	18.8	31.8
2	AS	67	56%	293	37%	67.0	10.7	18.1
3	AS	182	56%	293	37%	87.0	40.4	68.3
4	AS	400 <sup>f</sup>	70%	293	47%	146.0	35.0	59.2
5	AS/SA	400 <sup>f</sup>	70%	293	49%	94.0	104.0	176
6	MgSO <sub>4</sub> /SA	400 <sup>f</sup>	70%	293	67%	149.0	114.0	193
7	AS	none	70%	294	47%	77.0 <sup>g</sup>	--	--

<sup>a</sup> AS=ammonium sulfate, SA=sulphuric acid

<sup>b</sup> 20% uncertainty on gas phase glyoxal values

<sup>c</sup> Calculated using ISORROPIA (Nenes et al., 1998)

<sup>d</sup> As measured by the DMA and corrected for wall loss

<sup>e</sup> Calculated assuming  $\rho=1.69\text{ g}/\text{cm}^3$

<sup>f</sup> Estimated

<sup>g</sup> Not wall loss corrected

**Table 2.2:** Experimental conditions of irradiated experiments

Seed <sup>a</sup>	[GL] <sup>b</sup> ppbv	RH		Temp, K		LWC <sup>c</sup>		Seed volume <sup>d</sup> , V $\mu\text{m}^3/\text{cm}^3$	$\Delta V$ $\mu\text{m}^3/\text{cm}^3$
		Initial	Final	Initial, K	Final, K	Initial	Final		
8 AS	86.2	66.0%	42.6%	293.0	299.4	43.7%	28.4%	81.0	-14.0
9 AS/Fe	128	64.6%	42.5%	292.8	299.3	43.0%	28.4%	78.9	-13.5
10 AS	127	55.7%	37.9%	292.8	299.4	36.7%	25.2%	87.0	-12.0
11 AS	none	59.6%	54.7%	293.1	294.4	39.4%	36.0%	62.3 <sup>e</sup>	--

<sup>a</sup> AS=ammonium sulfate, Fe= $\text{Fe}_2(\text{SO}_4)_3$

<sup>b</sup> 20% uncertainty on gas phase glyoxal values

<sup>c</sup> Calculated using ISORROPIA (Nenes et al., 1998)

<sup>d</sup> As measured by the DMA and corrected for wall loss

<sup>e</sup> Not wall loss corrected

**Table 2.3:** GL fragments observed via AMS and suggested structures from which the fragments are formed

$m/z$	Fragment Formula	Suggested Structure
29	$\text{CHO}^+$	
58	$\text{C}_2\text{H}_2\text{O}_2^+$	
77	$\text{C}_2\text{H}_5\text{O}_3^+$	
88	$\text{C}_3\text{H}_4\text{O}_3^+$	
105	$\text{C}_3\text{H}_5\text{O}_4^+$	
117	$\text{C}_4\text{H}_5\text{O}_4^+$	
135	$\text{C}_4\text{H}_7\text{O}_5^+$	
145	$\text{C}_5\text{H}_5\text{O}_5^+$	
175	$\text{C}_6\text{H}_7\text{O}_6^+$	

**Table 2.4:** Fragments containing both carbon and nitrogen observed and suggested chemical formulas. The masses detected by UPLC/(+)ESI-TOFMS were detected in the protonated form.

	$m/z$	Fragment formula
Strong ions	41	$C_2H_3N^+$
	68	$C_3H_4N_2^+$
	69	$C_3H_3NO^+$
	70	$C_3H_4NO^+$
Weak ions	46	$CH_4NO^+$
	52	$C_3H_2N^+$
	53	$C_3H_3N^+$
	57	$C_2H_3NO^+$
	68	$C_3H_2NO^+$
	96	$C_4H_4N_2O^+$
ESI	97	$C_4H_5N_2O^+$
	115	$C_4H_7N_2O_2^+$
	129	$C_5H_9N_2O_2^+$
	159	$C_6H_{11}N_2O_3^+$
	173	$C_7H_{13}N_2O_3^+$
	184	$C_7H_{10}N_3O_3^+$

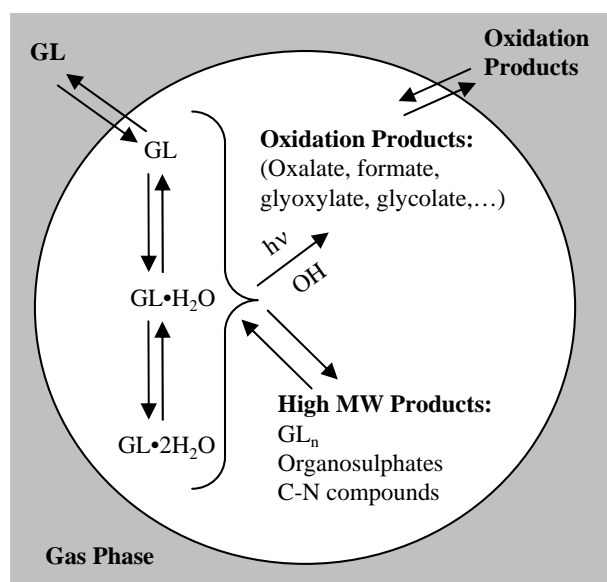


**Figure 2.1:** Processes contributing to GL uptake on AS seed aerosol. GL=GL monomer; GL·H<sub>2</sub>O=monohydrate; GL·2H<sub>2</sub>O=dihydrate; high molecular weight (MW) products include GL<sub>n</sub>, organosulfates, and carbon-nitrogen containing compounds; oxidation products include oxalate, formate, glyoxylate, and glycolate and their oxidation products.



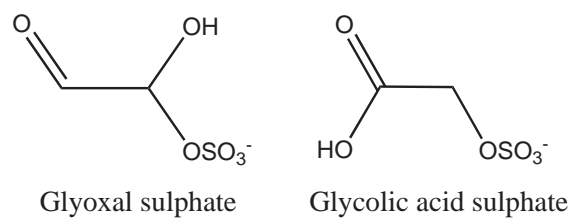


**Figure 2.2:** Proposed structures for  $m/z$  155; glyoxal sulfate and glycolic acid sulfate.

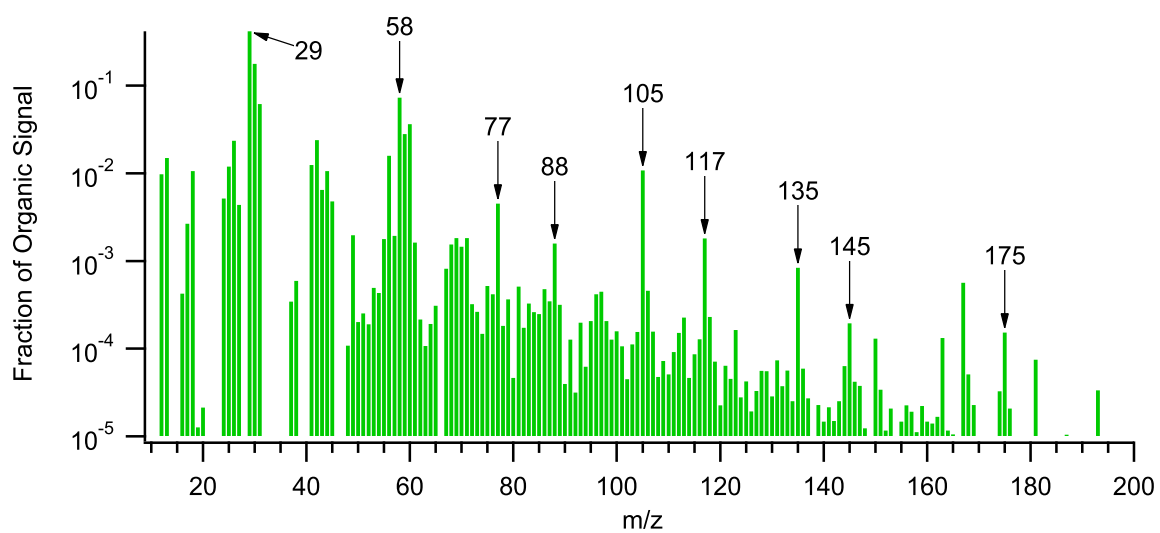


**Figure 2.3:** Representative unit-mass AMS spectrum. Distinct GL and GL oligomer marker peaks are shown. The compound from which each fragment was formed is listed in Table 2.3.

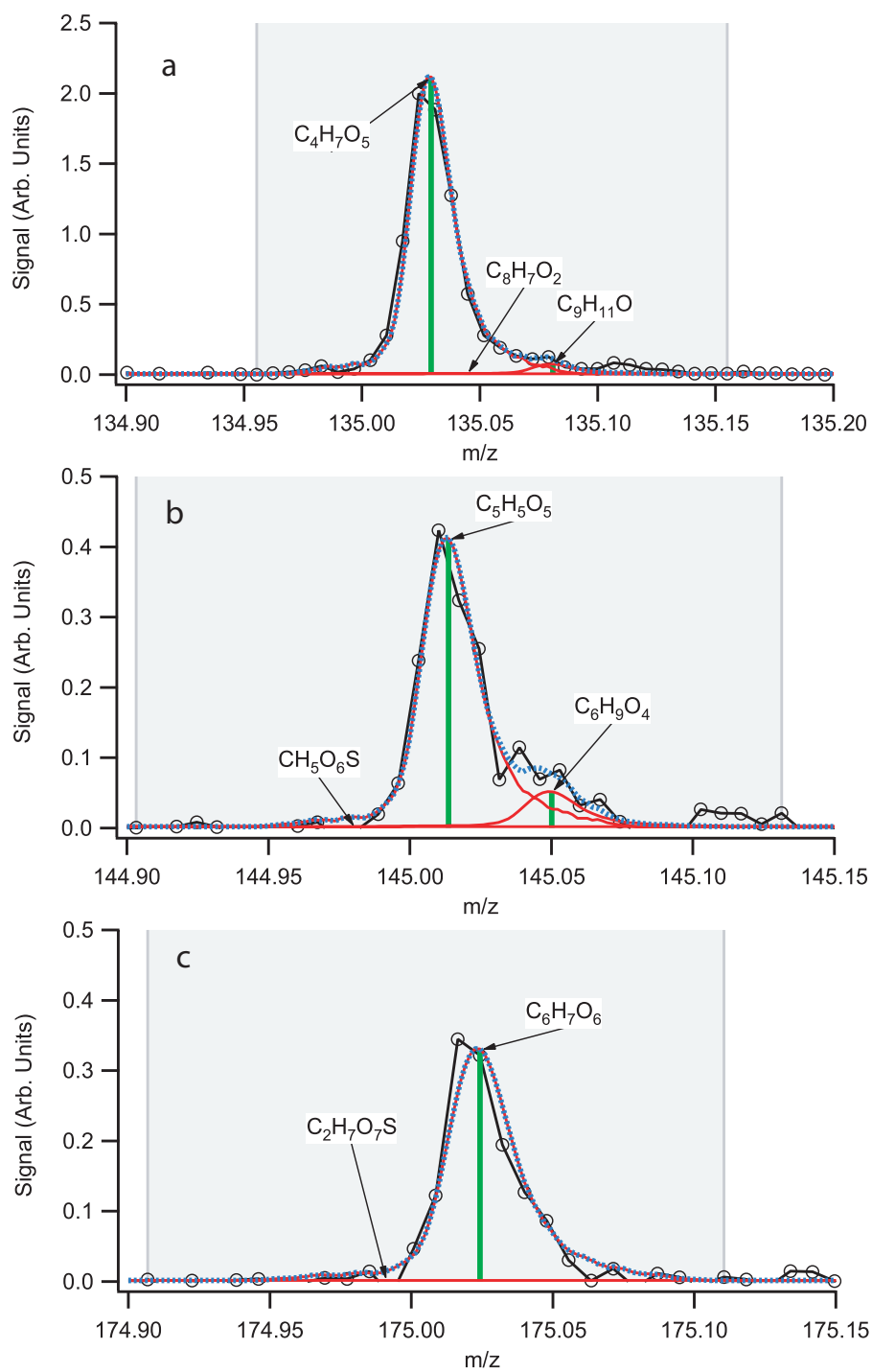


**Figure 2.4:** High-resolution (“W-mode”) AMS peaks allow unequivocal assignment of a  $C_4H_7O_5^+$  formula to the  $m/z$  135,  $C_5H_5O_5^+$  formula to the  $m/z$  145, and  $C_6H_7O_6^+$  formula to the  $m/z$  175 fragment ions.

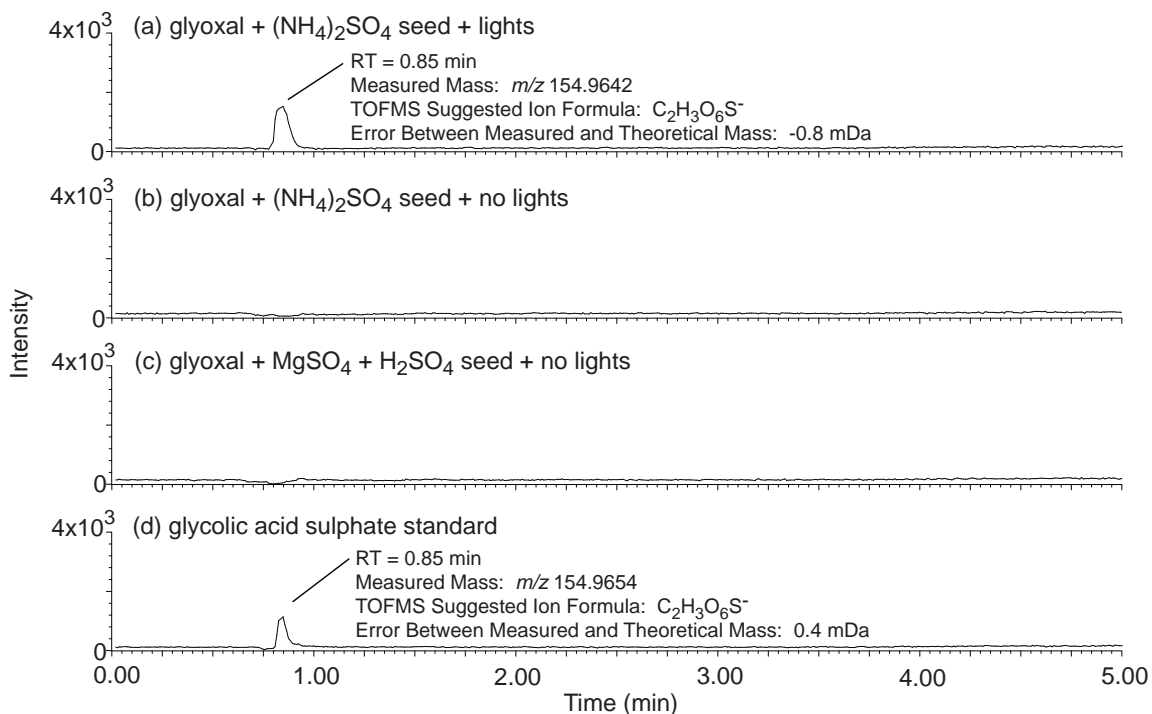


**Figure 2.5:** UPLC/ESI-TOFMS extracted ion chromatograms (EICs) of  $m/z$  155 for selected GL experiments. The comparison of these EICs reveals that glycolic acid sulfate only forms under irradiated conditions when using AS seed aerosol. Comparison of the retention time (RT) and mass ( $m/z$ ) of the compound detected in panel (a) and the glycolic acid sulfate standard, (d), unequivocally shows that glycolic acid sulfate is being formed in the presence of light, but not in neutral, (b), or acidic, (c), dark experiments.

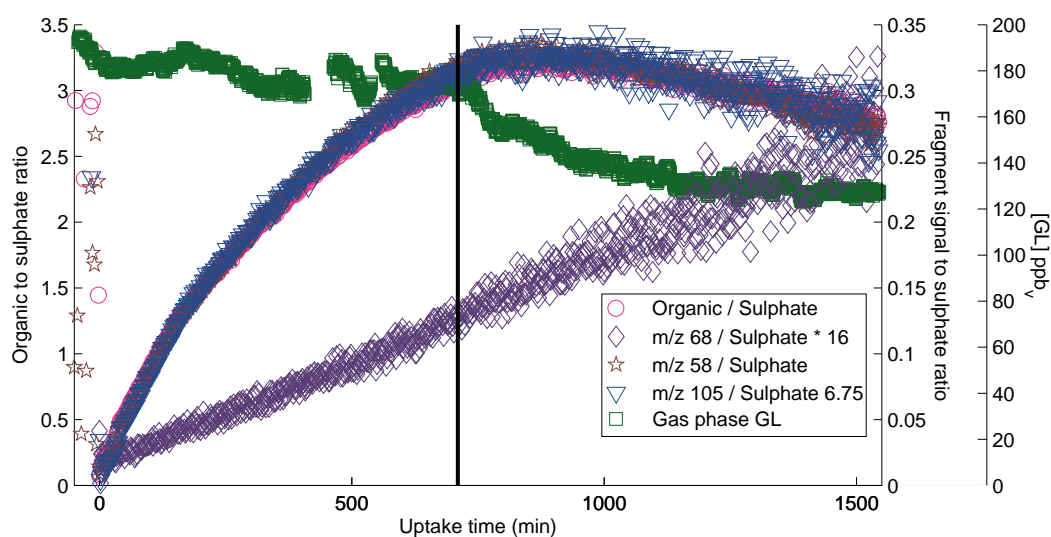


**Figure 2.6:** The time traces of total organic,  $m/z$  58, 105, and 68 fragment ions normalized by the sulfate ion signal along with gas phase GL concentrations for a dilution experiment (Exp. 3). Dilution begins at the black vertical line. Upon dilution, the normalized organic and GL ( $m/z$  58 and 105) marker signals decrease by 30%, and 17%, respectively, which is less than the 25% reduction in gas-phase GL concentrations. However, the system has clearly not equilibrated, and thus further loss of particle-phase GL is expected. In contrast to the reversible behavior of total organic and GL and GL oligomer growth, the growth of the  $m/z$  68 (imidazole) marker has markedly different characteristics, indicating irreversible uptake.

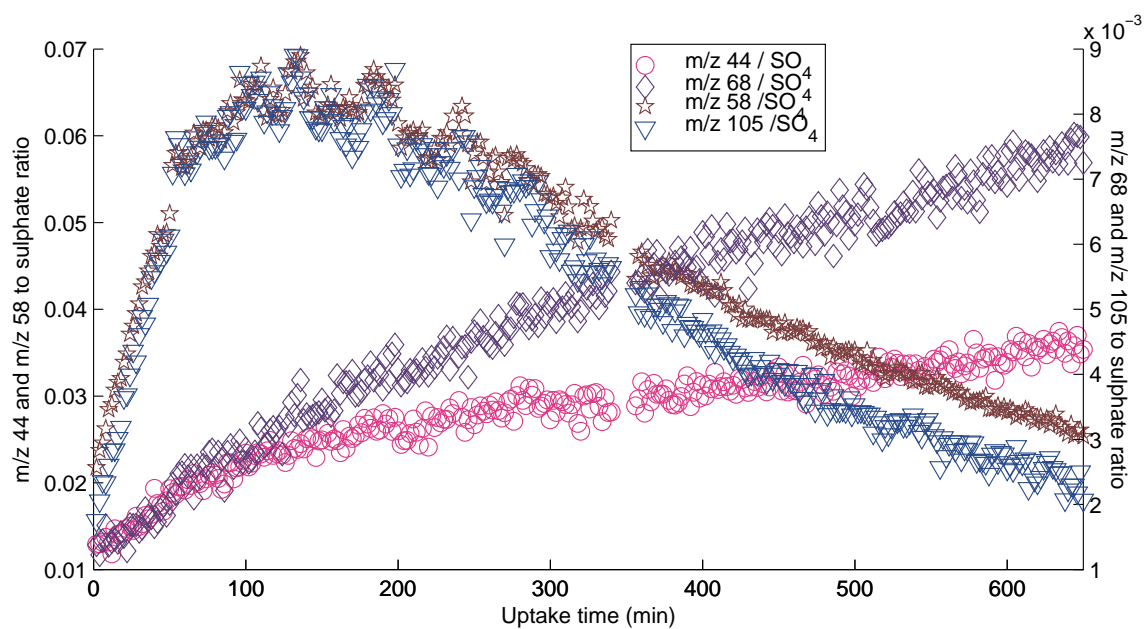


**Figure 2.7:** The sulfate normalized GL and GL oligomer marker signals  $m/z$  58 and 105 increase rapidly on introduction of seed aerosol under irradiated conditions, but decrease rapidly without any dilution taking place, which is in marked difference to the dark experiments. The  $m/z$  44, and in particular, 68 marker signals increase steadily during these experiments, indicating oxidation of the organic fraction of the aerosol and continued imidazole formation.

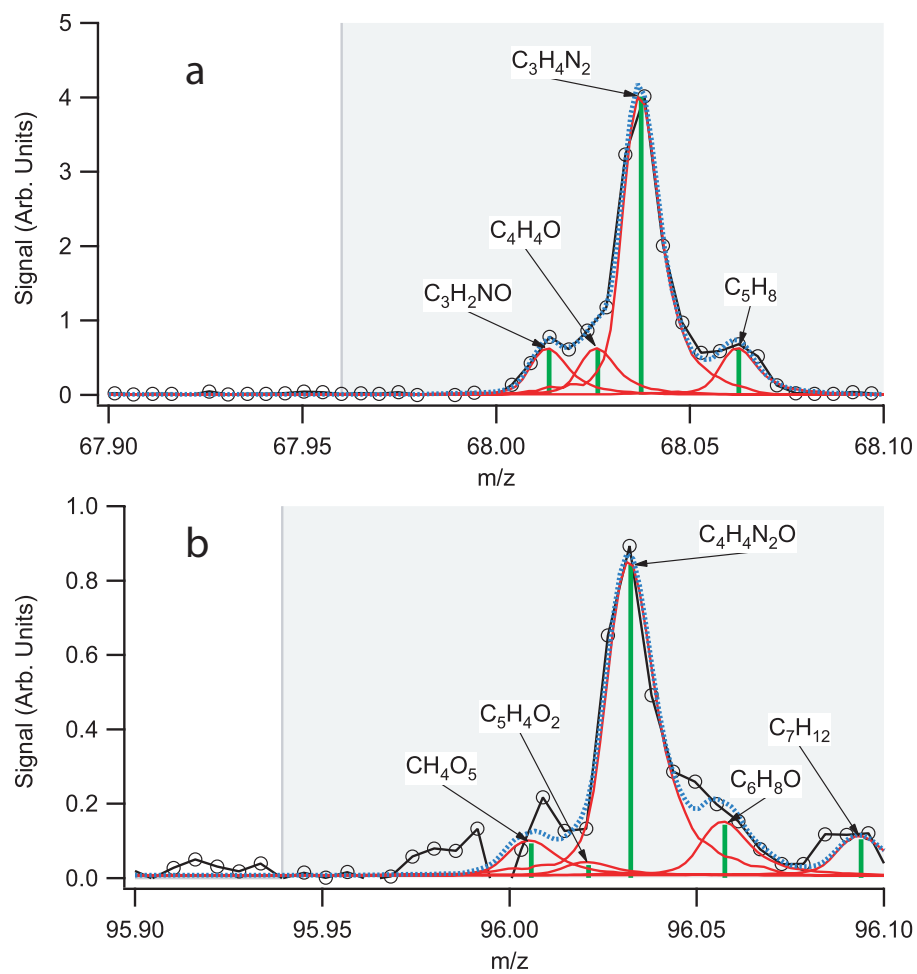


**Figure 2.8:** High-resolution (W-mode) AMS peaks allow unequivocal assignment of a  $C_3H_4N_2^+$  formula to the  $m/z$  68,  $C_4H_4N_2O^+$  formula to the  $m/z$  96 fragment ions.

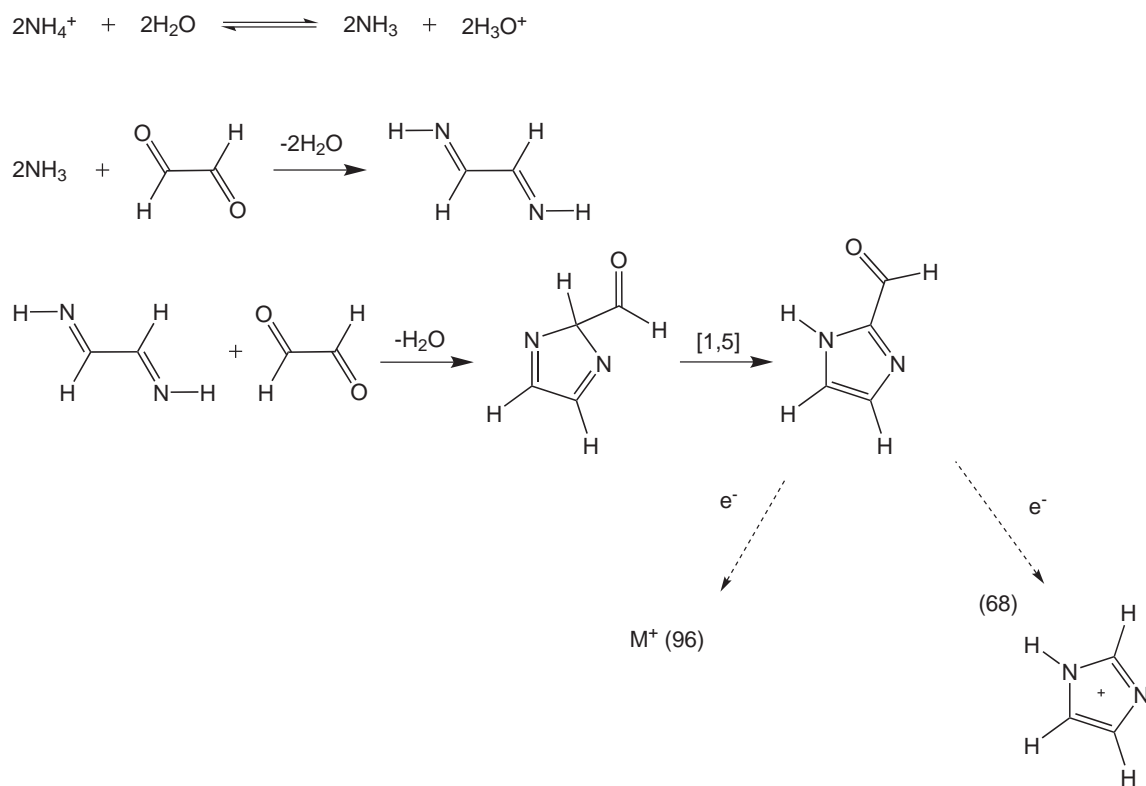


**Figure 2.9:** Proposed formation mechanism of 1H-imidazole-2-carboxaldehyde and observed  $m/z$  68 and 96 fragment ion.



## Chapter 3

# Elemental Analysis of Chamber Organic Aerosol Using an Aerodyne High-Resolution Aerosol Mass Spectrometer\*

### 3.1 Abstract

The elemental composition of laboratory chamber secondary organic aerosol (SOA) from glyoxal uptake,  $\alpha$ -pinene ozonolysis, isoprene photooxidation, single-ring aromatic photooxidation, and naphthalene photooxidation is evaluated using Aerodyne high-resolution time-of-flight mass spectrometer data. SOA O/C ratios range from 1.13 for glyoxal uptake experiments to 0.30–0.43 for  $\alpha$ -pinene ozonolysis. The elemental composition of  $\alpha$ -pinene and naphthalene SOA is also confirmed by offline mass spectrometry. The fraction of organic signal at  $m/z$  44 is generally a good measure of SOA oxygenation for  $\alpha$ -pinene/ $O_3$ , isoprene/high- $NO_x$ , and naphthalene SOA systems. The agreement between measured and estimated O/C ratios tends to get closer as the fraction of organic signal at  $m/z$  44 increases. This is in contrast to the glyoxal uptake system, in which  $m/z$  44 substantially underpredicts O/C. Although chamber SOA has generally been considered less oxygenated than ambient SOA, single-ring aromatic- and naphthalene-derived SOA can reach O/C ratios upward of 0.7, well within the range of ambient PMF component OOA, though still not as high as some ambient

---

\*Reproduced with permission from “Elemental analysis of chamber organic aerosol using an aerodyne high-resolution aerosol mass spectrometer” by P. S. Chhabra, R. C. Flagan, and J. H. Seinfeld, *Atmospheric Chemistry and Physics*, 10, 4111-4131, doi:10.5194/acp-10-4111-2010 Copyright 2010 by the Authors. CC Attribution 3.0 License.

measurements. The spectra of aromatic and isoprene-high-NO<sub>x</sub> SOA resemble that of OOA, but the spectrum of glyoxal uptake does not resemble that of any ambient organic aerosol PMF component.

## 3.2 Introduction

The chemical composition of secondary organic aerosol (SOA) from a volatile organic precursor comprises dozens of compounds owing to the variety of reaction pathways leading to semivolatile products (Hallquist et al., 2009; Kroll and Seinfeld, 2008). Offline analysis techniques can typically quantify only a portion of the wide array of compounds present in SOA. Though generally not able to provide detailed composition profiles of organic aerosol (OA), bulk, real-time mass spectrometric analysis has become an indispensable tool in chemically characterizing OA. The widely used Aerodyne quadrupole aerosol mass spectrometer (Q-AMS) uses thermal vaporization followed by electron impact ionization and a quadrupole mass analyzer to quantify the non-refractory portion of submicron aerosol mass (Jayne et al., 2000; Jimenez et al., 2003; Canagaratna et al., 2007). The original Q-AMS has been updated to improve sensitivity and time resolution by replacing the quadrupole mass spectrometer with a compact time-of-flight mass spectrometer (C-ToF-AMS) (Drewnick et al., 2005). While the C-ToF-AMS does improve the mass resolution over the Q-AMS, it still does not effectively distinguish different ions with the same nominal mass. Large gains in mass resolution were achieved when a high-resolution time-of-flight mass spectrometer (H-TOF Series, ToFwerk, Thun, Switzerland) was combined with the original AMS design (HR-ToF-AMS) (DeCarlo et al., 2006). The advantage of the HR-ToF-AMS is that it can distinguish and quantify ions with the same nominal mass but different elemental compositions, e.g., organic ions of the form, C<sub>x</sub>H<sub>y</sub><sup>+</sup>, C<sub>x</sub>H<sub>y</sub>O<sub>z</sub><sup>+</sup>, C<sub>x</sub>H<sub>y</sub>N<sub>p</sub><sup>+</sup>, and C<sub>x</sub>H<sub>y</sub>O<sub>z</sub>N<sub>p</sub><sup>+</sup>, allowing for a more detailed analysis of the elemental composition of SOA, and most importantly, its oxygen content.

DeCarlo et al. (2006) demonstrated the first application of a field-deployable HR-ToF-AMS during the MIRAGE and SOAR-1 field campaigns and found that the vast majority of the organic signal could be attributed to either C<sub>x</sub>H<sub>y</sub><sup>+</sup> or C<sub>x</sub>H<sub>y</sub>O<sub>z</sub><sup>+</sup> ions. Aiken et al. (2007) further developed HR-ToF-AMS analysis by showing that elemental ratios of OA, i.e., O/C, H/C, N/C and OM/OC,

could be estimated from the relative intensities of chemically identified ion fragments. The first detailed analyses of high-resolution data was from the MILAGRO campaign measuring ambient aerosol in and around Mexico City (DeCarlo et al., 2008; Aiken et al., 2008, 2009). Aiken et al. (2008) demonstrated the first measurements of the elemental composition of ambient OA in this field campaign and showed that the O/C ratios ranged from 0.06–0.10 for primary organic aerosol (POA) to about 0.76 for the most oxidized aerosol. Aiken et al. (2008) also showed that the fraction of the  $m/z$  44 signal to the total organic signal correlated well with O/C ratio and found it to be a good surrogate for the oxygen content of OA. DeCarlo et al. (2008) found that O/C ratios were highest in non-urban (regional) locations and that O/C could be a qualitative indicator of photochemical age. Aiken et al. (2008) performed the first positive matrix factorization (PMF) analysis on a HR-ToF-AMS data set from the MILAGRO campaign, finding that three components dominated OA: hydrocarbon-like organic aerosol (HOA, Avg. O/C=0.16), oxygenated organic aerosol (OOA, Avg. O/C=0.60) and biomass burning organic aerosol (BBOA, Avg. O/C=0.30). A fourth factor from a local source with non-negligible nitrogen content was also found (LOA, Avg. O/C=0.13 and N/C=0.06). Recently, aerosol measurements were made at the peak of Whistler Mountain during INTEX-B and the average O/C was 0.83 (Sun et al., 2009). Thermal denuder measurements of OA from SOAR-1 and MILAGRO campaigns with a HR-ToF-AMS demonstrated that aerosol volatility was inversely correlated with O/C ratio (Huffman et al., 2009).

The first series of chamber laboratory experiments to which the HR-ToF-AMS elemental analysis was applied were of SOA generated from the photooxidation of  $\alpha$ -pinene, isoprene, toluene, and gasoline vapors and ozonolysis of  $\alpha$ -pinene. Analyzing data from these experiments, Aiken et al. (2008) concluded that chamber SOA, characterized by O/C ratios from 0.27–0.42, was less oxidized than ambient OOA (at concentrations higher than ambient, as used to derive the previous generation of SOA models). For  $\alpha$ -pinene ozonolysis SOA, Shilling et al. (2009) demonstrated that the O/C ratio increased as aerosol loadings decreased, and at the lowest loadings, the mass spectrum resembled that of ambient OOA. Further work on the same system showed that a product specific volatility model could predict measured O/C ratios but overpredicted H/C ratios (Chan et al., 2009b). Mohr et al.

(2009) also used the HR-ToF-AMS to measure the degree of oxygenation of POA from meat cooking, trash burning, and vehicle exhaust and concluded that emissions from such sources could not be a substantial source of ambient OOA. Other chamber studies have used the HR-ToF-AMS to study the chemical mechanism of SOA formation from specific precursors, such as glyoxal, naphthalene, and amines (Galloway et al., 2009; Chan et al., 2009a; Kautzman et al., 2010; Malloy et al., 2009). Most recently, the HR-ToF-AMS has been used to study the heterogeneous OH oxidation of squalane particles to infer the mechanisms of OA aging (Smith et al., 2009; Kroll et al., 2009).

Ambient studies with the HR-ToF-AMS infer that much of the oxygenation of OA occurs as a result of photochemical aging of SOA, with the highest O/C ratios measured in remote regions. PMF analysis of HR-ToF-AMS data identifies similar components to those found from unit mass resolution data (Ulbrich et al., 2009; Zhang et al., 2005a,b, 2007; Lanz et al., 2007), the most common factors being HOA and OOA, which has been further subcategorized into low-volatility OOA (LV-OOA, previously known as OOA-1) and semivolatile OOA (SV-OOA, previously known as OOA-2) (Jimenez et al., 2009). LV-OOA has been characterized as aged OOA, having O/C ratios of at least 0.6 across most ambient datasets and spectra dominated by mass fragment  $\text{CO}_2^+$  at  $m/z$  44. Chamber SOA, however, generally does not exhibit as large O/C ratios as LV-OOA, at most reaching O/C ratios of SV-OOA and producing spectra with  $\text{C}_2\text{H}_3\text{O}^+$  at  $m/z$  43 as the dominant ion. In chamber investigations that use high precursor concentrations to generate SOA at aerosol loadings much higher than that of ambient OA, less oxygenated species partition into the particle phase. Additionally, chamber experiments are typically run for <24 h, which, while adequate to produce SOA from the photooxidation or ozonolysis of most SOA precursors, is still shorter than the atmospheric lifetime ( $\sim 1$  week) of ambient aerosol. Despite these limitations, chamber experiments are crucial to constraining SOA models and providing insight into the mechanisms involved in the formation and evolution of SOA (Kroll and Seinfeld, 2008). While comprehensive chamber studies of many different VOCs with the Q-AMS have been conducted (Bahreini et al., 2005), it has generally not been possible to directly compare offline speciation data to AMS data. The HR-ToF-AMS now provides the unique opportunity to make direct comparisons to offline speciation.

In this study we evaluate HR-ToF-AMS data on the elemental composition of chamber OA from a comprehensive suite of SOA systems: glyoxal uptake,  $\alpha$ -pinene ozonolysis, isoprene photooxidation, single-ring aromatic photooxidation, and naphthalene photooxidation. We compare our findings to other laboratory composition studies and identify discrepancies and sources of uncertainty. In addition, we evaluate the use of  $m/z$  44 as a surrogate for OA oxygenation. Lastly, we compare the elemental ratios measured in the chamber to those measured in ambient OA and derived from PMF analysis.

## 3.3 Experimental Section

### 3.3.1 Chamber Operation

All of the experiments analyzed here (Table 4.1) were performed in Caltech’s dual 28 m<sup>3</sup> Teflon environmental chambers (Cocker et al., 2001; Keywood et al., 2004) over the period 2007–2009. Before each experiment, the chambers were flushed for > 24 h until the particle number concentration was <100 cm<sup>3</sup> and the volume concentration was < 0.1 cm<sup>3</sup> m<sup>-3</sup>. Each chamber has a dedicated Differential Mobility Analyzer (DMA, TSI model 3081) coupled with a condensation nucleus counter (TSI model 3760) for measuring aerosol size distribution and number and volume concentration. Temperature, relative humidity (RH), ozone (O<sub>3</sub>), NO, and NO<sub>x</sub> were continuously monitored. For seeded experiments, ammonium sulfate seed particles were generated by atomization of a dilute aqueous ammonium sulfate solution using a constant rate atomizer.

For the experiments involving glyoxal, glyoxal preparation and experimental design are described by Galloway et al. (2009). Briefly, glyoxal uptake experiments begin by introducing gas-phase glyoxal into a dark, humid chamber and allowing the concentration to equilibrate over about 10 h. Approximately 160 ppb of cyclohexane was also added as a tracer for dilution. Once the gas-phase glyoxal concentration reached a steady state, ammonium sulfate seed aerosol, existing as a metastable solution, was introduced, and the resulting organic growth was monitored by both the DMA and HR-ToF-AMS. After organic growth leveled off, the chamber air mass was diluted

with clean hydrocarbon-free air to investigate the reversibility of uptake. The amount of dilution was calculated by monitoring the cyclohexane concentration with a gas-chromatograph with flame ionization detector (GC-FID, Agilent 6890N).

Ozonolysis experiments are described by Chan et al. (2009b). The effect of humidity and  $\text{H}_2\text{O}_2$  on SOA formation were tested and permuted in the four experiments. The parent hydrocarbon,  $\alpha$ -pinene (50 ppb), and an OH scavenger, cyclohexane, were introduced separately by injecting known volumes of the liquid hydrocarbon into a glass bulb, subsequently carried into the chamber by an air stream at  $5 \text{ L min}^{-1}$ . The estimated mixing ratio of cyclohexane was 37 ppm, at which the rate of cyclohexane +OH exceeds that of  $\alpha$ -pinene +OH by a factor of 100.  $\text{O}_3$  injection was stopped after the  $\text{O}_3$  concentration reached 180 ppb.

The protocol for isoprene (Kroll et al., 2006), single-ring aromatic (Ng et al., 2007), and naphthalene (Chan et al., 2009a) photooxidation experiments are described in detail in the references cited. For high- $\text{NO}_x$  experiments (initial  $[\text{NO}] > 300$  ppb), nitrous acid (HONO) was used as an OH source, at amounts between 175 and 310 ppb. Additional NO was added until the total NO mixing ratio was about 400–500 ppb. For low- $\text{NO}_x$  experiments, hydrogen peroxide ( $\text{H}_2\text{O}_2$ ) was used as an OH source.

### 3.3.2 High-Resolution Time-of-Flight Aerosol Mass Spectrometer

In all of the experiments considered here, real-time particle mass spectra were collected continuously by a HR-ToF-AMS, henceforth referred to as the AMS (Canagaratna et al., 2007; DeCarlo et al., 2006). In the mode of operation, the AMS was switched once every minute between the high-resolution “W-mode” and the lower resolution, higher sensitivity “V-mode”. The “V-mode” data were analyzed using a fragmentation table to separate sulfate, ammonium, and organic spectra and to time-trace specific mass-to-charge ratios (Allan et al., 2004). “W-mode” data were analyzed using a separate high-resolution spectra toolbox known as PIKA to determine the chemical formulas contributing to distinct mass-to-charge ( $m/z$ ) ratios (DeCarlo et al., 2006).

The AMS elemental analysis procedure exploits the properties of electron impact (EI) ionization

to determine the elemental composition of OA (Aiken et al., 2007). Briefly, the signal generated from the measured ion fragments of EI ionization is approximately proportional to the mass concentration of the initial species (Jimenez et al., 2003; Crable and Coggeshall, 1958). Because high-resolution mass spectra can determine the chemical formula of each ion fragment, the average elemental composition of all ions can be calculated. Thus the relative mass concentration  $M_X$  of a given element  $X$  is computed as follows:

$$M_X = \sum_{i=m/z_{\min}}^{m/z_{\max}} I_i \frac{m_X}{m_i} \quad (3.1)$$

where  $I_i$  is the ion signal at fragment  $i$ ,  $m_X$  is the atomic mass of element  $X$ , and  $m_i$  is the mass of singly charged fragment ion  $i$ . The elemental ratio  $X/Y$  is then

$$X/Y = \alpha_{X/Y} \frac{\frac{M_X}{m_X}}{\frac{M_Y}{m_Y}} \quad (3.2)$$

where  $\alpha_{X/Y}$  is the calibration factor for that particular ratio, determined by laboratory samples with known elemental compositions. The organic mass to organic carbon ratio OM/OC ratio is calculated as follows

$$\text{OM/OC} = \frac{12 + (16 \times \text{O/C}) + (1 \times \text{H/C}) + (14 \times \text{N/C}) + \dots}{12} \quad (3.3)$$

Aiken et al. (2007, 2008) sampled 59 different standards with the HR-ToF-AMS and determined calibration factors for O/C, H/C, and N/C and estimated uncertainties for each ratio. O/C, H/C, N/C and OM/OC ratios in the present study were computed using the computation toolbox ‘‘Analytical Procedure for Elemental Separation’’ (APES), which applies the analysis procedure as described by Aiken et al. (2007, 2008) to the W-mode data.

O/C ratios were also estimated from V-mode data using the organic signal at  $m/z$  44 (with gas-phase  $\text{CO}_2$  signal removed) as a surrogate for oxygenation in OA. Typically, the  $m/z$  44 signal arises from  $\text{CO}_2^+$  ions, which are commonly formed from the fragmentation of carboxylic acids (Takegawa et al., 2007). Aiken et al. (2008) correlated the fraction of organic signal at  $m/z$  44 to the O/C ratio

determined from high-resolution analysis and derived the following empirical relationship based on Mexico City data

$$O/C_{44}=3.82 \times f_{44} + 0.0794 \quad (3.4)$$

where  $O/C_{44}$  is the estimated O/C ratio using  $m/z$  44 as a surrogate and  $f_{44}$  is the organic signal at  $m/z$  44 divided by the total organic signal. V-mode data were chosen for the O/C estimation so as to maximize the signal to noise in the calculation; W-mode data could have been used for the O/C estimation for experiments that were not signal limited. Comparisons of  $f_{44}$  between both modes of operation produced little difference across all systems that were studied. The O/C ratio calculated from  $m/z$  44 from V-mode data will be referred to as  $O/C_{44}$ , and the O/C ratio determined from W-mode data in APES will be referred to as  $O/C_{HR}$  when the two are compared.

APES allows for special treatment of ions that may have contamination from air and allows users to include “ion families” that are traditionally considered fragments of inorganic species as part of the organic mass. The  $CO_2^+$  signal originating from ambient air  $CO_2$  is removed to determine the organic contribution of  $CO_2^+$  to  $m/z$  44. Fourier transform infrared spectroscopy measurements show the concentration of  $CO_2$  in the chamber air is nominally the same as in the atmosphere, estimated to be 370 ppm. The ion  $CO^+$  ( $m/z$  28) signal, another common fragment of organic species, tends to be overwhelmed by  $N_2^+$  from  $N_2$  in ambient air. As a result, the contribution of  $CO^+$  to the total organic signal is usually estimated as a factor of the  $CO_2^+$  organic signal. The ratios of the particle-phase signals of  $CO^+$  to  $CO_2^+$  are listed in Supplemental Table S3 and were determined from HR spectra of experiments in which the OA loading is high, for all systems except isoprene photooxidation, for which the default ratio was used. The signals from  $H_2O^+$ ,  $OH^+$ , and  $O^+$  in the particulate organic mass may suffer interference from gas-phase  $H_2O$ , and their organic contributions are estimated as suggested in Aiken et al. (2008). For all experiments, ions in the “OH family” that are not  $H_2O^+$ ,  $OH^+$ , and  $O^+$  are added as part of the organic mass; however, their inclusion turns out to be negligible to the O/C and H/C calculations.

Particulate nitrogen signals were observed in high- $NO_x$  photooxidation experiments, mostly originating from  $NO^+$  and  $NO_2^+$  ions. In ambient studies, these ions usually result from the fragmenta-



tion of inorganic nitrates in the particle phase. Although gas-phase nitric acid is produced from the OH+NO<sub>2</sub> reaction, at low chamber humidities, nitric acid is not expected to partition appreciably into the particle phase. Thus, the signals of NO<sup>+</sup> and NO<sub>2</sub><sup>+</sup> ions, termed as “NO Family” ions, are included as part of the organic mass in high-NO<sub>x</sub> photooxidation experiments to estimate the contribution of nitrogen from organonitrate compounds.

## 3.4 Results

Table 3.2 lists the average elemental ratios and estimated uncertainties at the time of the peak O/C ratio for each experimental system. Aerosol produced from glyoxal uptake exhibits the largest average O/C and OM/OC at 1.13 and 2.68, respectively, and  $\alpha$ -pinene-O<sub>3</sub> SOA has the smallest average O/C and OM/OC at 0.43 and 1.70, respectively. SOA from all OH-photooxidation experiments exhibits intermediate O/C and OM/OC values ranging from 0.57 to 0.74 and 1.89 to 2.15. Values of N/C are essentially zero for low-NO<sub>x</sub> experiments and do not exceed 0.08 for high-NO<sub>x</sub> experiments. Values of H/C vary from 1.39 to 1.64 for all systems except naphthalene-OH, which is 0.89 on average. Time trends of O/C, H/C and OM/OC ratios for systems with the same VOC and NO<sub>x</sub> conditions largely overlap, illustrating that elemental ratios tend to be a function of the extent of conversion of the parent hydrocarbon. OM/OC follows the same time dependence as O/C, as oxygen is the only major source of SOA mass other than carbon.

### 3.4.1 SOA from Reactive Uptake of Glyoxal

Recently, glyoxal has received attention as being a possible ambient SOA precursor. It has been estimated that glyoxal could contribute to at least 15% of the SOA formation in Mexico City (Volkamer et al., 2007) and has been implicated in SOA formation from the photooxidation of acetylene (Volkamer et al., 2009). As we will show, the O/C ratio of glyoxal-SOA determined in the laboratory is the largest of any system we consider. Dzepina et al. (2009) modelled SOA formation in Mexico City, including glyoxal SOA, as well as updated aromatic SOA yields and SOA from primary semivolatile and intermediate volatility species. To evaluate the model, they compared the

predicted O/C ratios to those measured in Mexico City; assuming an O/C ratio of 0.37 for aromatic SOA (Aiken et al., 2008), the model underpredicts the oxygen content of the ambient aerosol. When glyoxal is included as an SOA constituent and assumed to have an O/C of 1.0, the modelled SOA O/C is in much closer agreement with ambient measurements (while the assumed O/C of glyoxal is close to what we will report below, the O/C assumed for aromatic SOA is considerably lower than that measured).

Figure 3.1 displays the time dependence of OM/OC, H/C, O/C, and N/C ratios during the three glyoxal uptake experiments. At the onset of uptake, O/C and OM/OC rise sharply, reaching values of 1.13 and 2.68, respectively, the largest of these ratios of all the systems studied. This is not unexpected as pure glyoxal itself has an O/C of 1 and OM/OC of 2.42, the highest of all the VOCs investigated. In aqueous solution, the two aldehyde groups of glyoxal can be hydrated, adding two H<sub>2</sub>O molecules. Also, glyoxal can polymerize to aldols and acetals, removing H<sub>2</sub>O (Whipple, 1970; Fratzke and Reilly, 1986; Loeffler et al., 2006). Thus, the O/C of aqueous-phase glyoxal can be as high as 2, H/C as high as 3, and OM/OC as high as 3.92. The measured ratios lay between these bounds, suggesting that both hydration and polymerization processes are occurring in the wet ammonium sulfate seed.

One can estimate the extent of polymerization based on the elemental composition measured by the AMS. Assuming that free glyoxal in the particle phase is hydrated twice, C<sub>2</sub>H<sub>2</sub>O<sub>2</sub> · 2H<sub>2</sub>O, and that oligomerization produces straight chain acetals, for every monomer unit added to the chain, two water molecules are lost. Thus, a glyoxal oligomer will have the formula C<sub>2n</sub>O<sub>2n+2</sub>H<sub>2n+4</sub> where  $n$  is the number of glyoxal subunits. On this basis, one gets O/C=( $n+1$ )/ $n$ , H/C=( $n+2$ )/ $n$ , and OM/OC=( $29n+18$ )/ $12n$ . Using the elemental values in Table 3.2 and solving for  $n$ , the number of glyoxal subunits ranges from 4 to 8. Kua et al. (2008) performed DFT calculations to study the aqueous phase hydration and oligomerization of glyoxal and found that the dioxolane ring dimer (C<sub>4</sub>H<sub>8</sub>O<sub>6</sub>, O/C=1.5, H/C=2, OM/OC=3.2) is the preferred thermodynamic form for oligomerization and that the hydrated trimer (C<sub>6</sub>H<sub>10</sub>O<sub>8</sub>, O/C=1.3, H/C=1.7, OM/OC=2.9) is the oligomer endpoint. These structures imply a smaller extent of oligomerization than suggested by the AMS

elemental ratios. The AMS analysis technique may be underestimating the organic oxygen in the glyoxal/ $(\text{NH}_4)_2\text{SO}_4(\text{aq})$  system but is within the reported measurement uncertainty of about 31%.

Figure 3.2a shows the contribution of each  $m/z$  to the elemental composition of the organic mass at the peak of organic growth. About 56% of the signal comes from  $\text{CHO}^+$ ,  $\text{CH}_2\text{O}^+$ , and  $\text{CH}_3\text{O}^+$  fragments at  $m/z$  29-31, with smaller contributions from  $\text{CH}_3\text{O}_2^+$ ,  $\text{C}_2\text{H}_2\text{O}_2^+$ ,  $\text{C}_2\text{H}_3\text{O}_2^+$ , and  $\text{C}_2\text{H}_4\text{O}_2^+$ . Together, these ions represent the bulk of the oxygen signal in the AMS spectra. As identified by Galloway et al. (2009), other distinct fragments that appear in the spectrum,  $\text{C}_4\text{H}_7\text{O}_5^+$ ,  $\text{C}_5\text{H}_5\text{O}_5^+$ , and  $\text{C}_6\text{H}_7\text{O}_6^+$ , suggest the existence of oligomers of at least  $n=3$ . About 1% of the total AMS signal can be attributed to nitrogen-containing organic fragments resulting from the reaction of glyoxal with ammonium, producing imidazoles (Galloway et al., 2009). Signals from the fragmentation of these compounds result in a measured N/C ratio for this system of about 0.01. This is possibly an underestimate of the organic nitrogen signal as imidazoles may fragment into  $\text{NH}_x^+$  ions. These ions are part of the “NH family” of ions and were not included as part of the organic signal since they are the primary fragments of ammonium in the ammonium sulfate seed.

After organic growth by glyoxal uptake had ceased in experiments 1 and 2, the chamber was diluted with clean air to investigate the reversibility of glyoxal uptake. As shown in Fig. 3.1, aerosol O/C decreases slowly after dilution, H/C stays approximately constant, and N/C increases gradually. The AMS organic signal and glyoxal markers decrease relative to sulfate during dilution, showing that glyoxal can repartition to the gas phase and that uptake is reversible (Galloway et al., 2009). Also, markers for N-containing compounds presumably formed from the reaction of glyoxal and ammonium, such as 1H-imidazole-2-carboxaldehyde ( $\text{C}_4\text{H}_4\text{N}_2\text{O}$ , O/C=0.25, H/C=1, N/C=0.5), increase relative to sulfate. These N-containing compounds are formed as ammonia replaces  $\text{H}_2\text{O}$  as part of the organic phase.

### 3.4.2 $\alpha$ -pinene Ozonolysis SOA

The elemental and OM/OC ratios for the four  $\alpha$ -pinene/ $\text{O}_3$  SOA experiments evaluated here are similar so only data from experiment 4 are discussed. Figure 3.3 shows the evolution of OM/OC,

H/C and O/C ratios of the SOA for experiment 4. The earliest aerosol formed has an O/C ratio of 0.50, which decreases throughout the experiment to approximately 0.30, close to the O/C ratio reported by Aiken et al. (2008) for this system. The H/C ratio increases from about 1.3 to 1.5. These ratios are in good agreement with the high-resolution AMS measurements of Shilling et al. (2009). This behavior has been explained by increased partitioning of less oxidized semivolatile compounds as the mass of partitioning medium grows (Shilling et al., 2009; Chan et al., 2009b). There is no substantial difference in SOA elemental composition between humid and dry experiments and experiments with and without H<sub>2</sub>O<sub>2</sub>.

$\alpha$ -Pinene ozonolysis has served as a canonical SOA system for which the particle-phase composition of  $\alpha$ -pinene SOA has been investigated in numerous studies (Yu et al., 1999; Jang and Kamens, 1999; Glasius et al., 2000; Koch et al., 2000; Iinuma et al., 2004; Gao et al., 2004). Using a denuder/filter pack sampling system and derivatization with GC-MS detection, Yu et al. (1999) were able to identify >90% of the aerosol composition by mass at the molecular level. Using the molar yields reported in Yu et al. (1999), we calculate the aerosol-phase elemental ratios for their  $\alpha$ -pinene/O<sub>3</sub> experiments as shown in Supplemental Table S4. The composition analysis yields an O/C range of 0.34–0.36 and an H/C range of 1.56–1.58, which are very close to the AMS measured values. Using the Nanoaerosol Mass Spectrometer, Tolocka et al. (2006) determined the aerosol products of  $\alpha$ -pinene/O<sub>3</sub> to have an O/C ratio of 0.37 to 0.4 for nucleated particles 30 and 50 nm in diameter. Reinhardt et al. (2007) used filter sampling in conjunction with electrospray ionization mass spectrometry to determine O/C ratios of 0.4 to 0.6. In contrast to Yu et al. (1999), using an iodometric-spectrophotometric technique, Docherty et al. (2005) estimated that nearly half of the SOA mass formed in  $\alpha$ -pinene ozonolysis comprised organic peroxides. Suggested compounds, such as peroxy pinalic acid (O/C=0.44) and peroxy pinic acid (O/C=0.56), generally have higher O/C ratios than those measured by Yu et al. (1999) but still close to the range measured in this study. A comparison of the elemental analyses in this work and others is given in Table 3.3.

Important ions in the  $\alpha$ -pinene/O<sub>3</sub> system are noted in Fig. 3.2b, with the largest contribution to the total organic signal coming from C<sub>2</sub>H<sub>3</sub>O<sup>+</sup> ( $m/z$  43) and the largest contribution to oxygen

coming from  $\text{CO}_2^+$  ( $m/z$  44) at the peak of organic loading. Other prominent peaks reported by Shilling et al. (2009) are also observed. Over the course of the experiments evaluated here, the contribution of  $m/z$  44 to the organic signal decreases from approximately 11% to 6–7% as the organic mass increases.

### 3.4.3 Isoprene SOA

#### 3.4.3.1 Low- $\text{NO}_x$

Figure 3.4 tracks the organic growth, isoprene decay, and elemental ratios for experiment 10, the longest duration experiment conducted under low- $\text{NO}_x$  conditions. The SOA mass peaks soon after the onset of irradiation but then decreases rapidly. Kroll et al. (2006) suggested that the rapid loss in organic mass could be attributed to photolysis of semivolatile or condensed-phase hydroperoxides, as the decay occurred only under irradiation and only in a low- $\text{NO}_x$  environment. This hypothesis was supported by Surratt et al. (2006) who found, using iodometric-spectrophotometric measurements, that the contribution of organic peroxides decreased from 59% of the total SOA mass to 26% over the 12 h duration.

For low- $\text{NO}_x$  isoprene SOA, the O/C ratio is approximately 0.60 at the onset of photooxidation, decreasing gradually to 0.50 in the longest duration experiment. The H/C ratio starts at approximately 1.2, increases to 1.6, and then steadily decreases to 1.45. Using offline filter analyses, several classes of compounds have been identified as constituents of SOA from the photooxidation of isoprene under low- $\text{NO}_x$  conditions with ammonium sulfate seed, including dihydroxydihydroperoxides (O/C=1.2, H/C=2.4), epoxydiols (O/C=0.6, H/C=2),  $\text{C}_5$ -alkene triols (O/C=0.6, H/C=2), 2-methyltetrols (O/C=0.8, H/C=2.4), and hydroxyl sulfate esters (O/C=1.4, H/C=2.4, S/C=0.2) (Claeys et al., 2004; Wang et al., 2005; Surratt et al., 2006, 2007; Gómez-González et al., 2008; Surratt et al., 2010). Oligomers of 2-methyltetrols and hydroxy sulfate esters have also been measured (Surratt et al., 2006, 2008). An O/C value of 0.6 is consistent with SOA consisting of epoxydiols and  $\text{C}_5$ -alkene triols. However, numerous studies have reported peroxides and 2-methyltetrols as major constituents as well, both having higher degrees of oxygenation. Tetrol dimers and sulfate

esters will also have O/C ratios higher than 0.6. Therefore, the expected particle-phase composition of isoprene-OH SOA has higher O/C and H/C ratios than those measured by the AMS, reasons for which will be discussed in Sect. 4.2. However, the slow decay of the O/C ratio over time could reflect the photolysis of hydroxyhydroperoxide compounds or reaction with OH radicals (Lee et al., 2000). Photolysis would split the peroxy bond, releasing an OH radical. The subsequent alkoxy radical would then react with O<sub>2</sub> to form an aldehyde and HO<sub>2</sub>. Reaction with OH would abstract a hydrogen leaving an alkoxy peroxy radical which could then further decompose. Overall these processes have the potential to deplete both oxygen and hydrogen relative to carbon, reducing their elemental ratios.

The time dependence of the H/C ratio is consistent with the effects of two different processes. H/C rises quickly to a peak at about 200 min into the experiment, coinciding with the peak of SOA growth. The increasing amount of OA provides a medium for continued partitioning of semivolatile species with a higher H/C ratio into the particle phase. This effect is also seen in the H/C ratio of  $\alpha$ -pinene ozonolysis SOA. However, as noted earlier, with continued irradiation, peroxide compounds could photolyze or react with OH, causing the H/C ratio to decrease. The decrease in H/C and O/C ratios could also be explained by oligomerization, as H<sub>2</sub>O is lost through condensation reactions.

The spectrum of low-NO<sub>x</sub> isoprene SOA changes throughout irradiation time reflecting the continued processing of the SOA, consistent with the observed rapid decay in organic aerosol mass. At the peak of aerosol growth about 85% of the organic signal occurs for  $m/z \leq 45$ . The strongest signals occur at COH<sup>+</sup> and C<sub>2</sub>H<sub>3</sub>O<sup>+</sup>, representing approximately 30% of the organic signal as displayed in Fig. 3.5a, with most of the oxygen content coming from COH<sup>+</sup>. The spectrum changes considerably after 20 h of irradiation with the contribution of the organic signal decreasing to 75% for  $m/z \leq 45$  and contributions of  $m/z > 100$  increasing. Mass fragment CO<sub>2</sub><sup>+</sup> also becomes the dominant contributor of oxygen to the SOA. Unit-mass resolution AMS data from Surratt et al. (2006) indicate an increasing signal at  $m/z > 200$  over the course of the experiment, suggesting oligomerization even as organic mass is decreasing. The authors of this previous study also proposed  $m/z$  91 as an AMS tracer ion for peroxides, as the ion reaches its peak signal earlier than that of organics and decreases

faster than wall loss. The high-resolution study here confirms the existence of their ion assignment of  $C_3H_7O_3^+$ , though it also occurs with  $C_7H_7^+$  (see Supplemental Material).

### 3.4.3.2 High-NO<sub>x</sub>

Under high-NO<sub>x</sub> conditions, isoprene SOA is characterized by O/C atomic ratios generally higher than those of low-NO<sub>x</sub> experiments. As illustrated in Fig. 3.6, H/C, O/C and OM/OC ratios quickly plateau to 1.46, 0.62, and 2.00, respectively, and do not change over the course of the experiments. The N/C ratio, however, peaks early at approximately 0.05 and decreases thereafter. Figure 3.7 compares the organic growth and isoprene decay to the O/C ratio, and the gas-phase NO and NO<sub>2</sub> concentrations to the N/C ratio for experiment 12, conducted under high-NO<sub>x</sub> conditions. In contrast to low-NO<sub>x</sub> experiments, as the isoprene concentration drops, organic mass grows to a plateau about 4 h after irradiation begins. After organic growth levels out, additional HONO is added to convert any existing gas-phase intermediates such as methacrolein and peroxy methacryl nitrate (MPAN) (Surratt et al., 2010); additional SOA is formed but no change in elemental composition is observed.

Previous work has established that the main constituents of SOA derived from isoprene photooxidation under high-NO<sub>x</sub> conditions are 2-methylglyceric acid (O/C=1, H/C=2), the hydroxynitrate of 2-methylglyceric acid (O/C=1.75, H/C=1.75, N/C=0.25), and their corresponding oligoesters (Surratt et al., 2006, 2010; Szmigielski et al., 2007) from detailed offline chemical analyses of filter samples. These compounds have been estimated to represent approximately 20% of the SOA mass (Surratt et al., 2006). Thus the AMS elemental ratios are below those that would be expected from offline filter analysis. Even if one considers the linear oligomerization of 2-methylglyceric acid by esterification, which will reduce the O/C and H/C ratios by removing H<sub>2</sub>O, the O/C ratio will not fall below 0.75 and the H/C ratio will not fall below 1.5.

SOA derived from isoprene photooxidation under high-NO<sub>x</sub> conditions also has non-negligible nitrogen content. The nitrogen is likely organic in nature as the gas-phase concentration of NO<sub>2</sub> remains high throughout the experiment (Fig. 3.7), and recent work has shown that a major route

to form isoprene-SOA under high-NO<sub>x</sub> conditions occurs through the reaction of the methacrolein peroxy radical with NO<sub>2</sub> to form MPAN (Surratt et al., 2010). Aerosol-phase compounds containing nitrogen are presumably the hydroxynitrate of 2-methylglyceric acid or nitroxypolyols, which fragment in the AMS forming NO<sup>+</sup> and NO<sub>2</sub><sup>+</sup> ions (Fig. 3.5b). While the addition of extra HONO produces more SOA, it does not alter the elemental ratios, and continued irradiation led to no measurable aerosol processing (Fig. 3.7). If the aerosol-phase nitrogen resulted from the uptake of HNO<sub>3</sub>, one would expect a jump in the N/C ratio with the second addition of HONO, just as in the beginning of the experiment. The N/C ratio decreases throughout the experiment, which could be the result of hydrolysis of the aerosol-phase organonitrates to form volatile nitric acid (Sato, 2008), or photolysis to form an alkoxy radical and NO<sub>2</sub> (Renbaum and Smith, 2009; Roberts and Fajer, 1989). The steady oxygen and hydrogen content of the isoprene high-NO<sub>x</sub> SOA is supported by the relatively constant HR spectra. In contrast to the low-NO<sub>x</sub> isoprene SOA spectrum (Fig. 3.5a), much of the oxygen in the high-NO<sub>x</sub> AMS spectrum comes from CO<sub>2</sub><sup>+</sup>.

### 3.4.4 Single-Ring Aromatic SOA

Figure 3.8 shows the O/C, H/C, N/C and OM/OC ratios for single-ringed aromatic SOA experiments (i.e., *m*-xylene and toluene). Maximum O/C ratios ranged from 0.60 to 0.73. Toluene SOA under high-NO<sub>x</sub> conditions achieves an O/C of about 0.7. Low-NO<sub>x</sub> experiments begin with low O/C values that increase with continued irradiation. The O/C of high-NO<sub>x</sub> SOA increases with continued irradiation as well, albeit more slowly. The N/C ratio of high-NO<sub>x</sub> SOA peaks at 0.10 shortly after irradiation begins, but decreases gradually throughout the experiment.

While numerous studies have investigated the chemical composition of SOA from toluene photooxidation, as well as other aliphatic aromatic compounds, usually in the presence of NO<sub>x</sub>, quantification of particle-phase organic species has proved difficult (Hamilton et al., 2005; Sato et al., 2007). Kalberer et al. (2004) found that a large fraction of the SOA formed from trimethylbenzene was oligomeric; proposed polymer structures lead to an O/C ratio of 1.0, and peaks from LDI-MS spectra have O/C ratios ranging from 0.7 to 1.6. For the same system, Fisseha et al. (2004) found



that organic acids constitute 20% to 45% of the organic mass. If one considers the small organic acids quantified by Fisseha et al. (2004), O/C ratios would range from 1 to 2, substantially higher than those measured in the experiments surveyed here. Furthermore, aromatic photooxidation yields considerable amounts of glyoxal, methylglyoxal, and other multifunctional carbonyls that, if incorporated into the SOA, would produce high O/C ratios (Bloss et al., 2005; Hamilton et al., 2005, 2003; Kalberer et al., 2004). However, with the number of less oxygenated compounds measured, including aromatic ring-retaining compounds, unsaturated acids, ketones and aldehydes (Sato et al., 2007; Hamilton et al., 2005; Jang and Kamens, 2001), the measured O/C could accurately represent the oxygen content of the SOA formed.

AMS data indicate that *m*-xylene-derived SOA has a lower O/C ratio than that of toluene SOA. This is likely due to the presence of the second methyl group in *m*-xylene. For both NO<sub>x</sub> conditions and hydrocarbons, the O/C ratio continues to increase over the course of oxidation, indicating continued oxidation of the aerosol even after the organic loading has peaked. This prolonged processing, perhaps as a result of OH oxidation of unsaturated compounds in the particle phase or of vapor-phase semivolatile species, leads to a greater contribution of CO<sub>2</sub><sup>+</sup> to the organic signal in each experiment. The SOA from both high-NO<sub>x</sub> experiments had similar N/C ratios. Under high-NO<sub>x</sub> conditions, organic nitrogen is expected as evidenced by the presence of nitroaromatics (Hamilton et al., 2005; Sato et al., 2007; Jang and Kamens, 2001). Compounds, like nitrocresols and nitrotoluenes, form from the reaction of the OH-aromatic adduct with NO<sub>2</sub>, which under high-NO<sub>x</sub> conditions has the same concentration profile as in Fig. 3.8. N/C decreasing could reflect the continued photooxidation of these compounds in the gas or particle phases.

At the peak of SOA growth, toluene SOA exhibits similar spectra regardless of NO<sub>x</sub> level (Fig. 3.9), except for the existence of the NO<sup>+</sup> and NO<sub>2</sub><sup>+</sup> ions in high-NO<sub>x</sub> spectra. Mass fragment CO<sub>2</sub><sup>+</sup> contributes nearly the same amount to the organic signal as C<sub>2</sub>H<sub>3</sub>O<sup>+</sup> in toluene experiments. Conversely, C<sub>2</sub>H<sub>3</sub>O<sup>+</sup> is the dominant ion in *m*-xylene SOA spectra, representing 19% of the organic signal in low-NO<sub>x</sub> conditions and 15% in high-NO<sub>x</sub> conditions (Fig. 3.9). In both systems, the fraction of CO<sub>2</sub><sup>+</sup> increases with continued irradiation with *f*<sub>44</sub> ranging from 10%–13% for toluene SOA

and 8%–10% for *m*-xylene SOA. These ranges of  $f_{44}$  values were also observed by Sato et al. (2010).

### 3.4.5 Naphthalene SOA

Figures 3.11 and 3.12 show the elemental ratios for SOA derived from naphthalene photooxidation at high- and low- $\text{NO}_x$  conditions, respectively. O/C ratios under low- $\text{NO}_x$  conditions decrease sharply to 0.30 early in the experiments, but then increase to above 0.70 in the longest experiment. H/C ratios decrease from approximately 1.0 to 0.9. O/C and H/C ratios for high- $\text{NO}_x$  experiments exhibit similar characteristics; O/C ratios start from about 0.35 at the beginning of irradiation and then increase steadily to 0.60 in the longest experiment, but no initial decrease occurred. H/C ratios decrease from 1.0 to approximately 0.8. N/C profiles under high- $\text{NO}_x$  conditions resemble those of isoprene and aromatic high- $\text{NO}_x$  systems, starting high at 0.10 and decreasing with continued irradiation. Figure 3.14 show the spectra for SOA derived under both  $\text{NO}_x$  levels.

The elemental values measured by the AMS are close to those determined in a comprehensive study of naphthalene photooxidation by Kautzman et al. (2010), who characterized, from detailed offline chemical analyses of filter samples, 68% and 53% of the SOA mass under low- $\text{NO}_x$  and high- $\text{NO}_x$  conditions, respectively. Acidic species and peroxides represented a major portion of the SOA in both  $\text{NO}_x$  regimes, and nitrogen-containing constituents were 3% of the total SOA mass formed under high- $\text{NO}_x$  conditions. The O/C and H/C ratios calculated in that study were 0.50 and 0.82 under low- $\text{NO}_x$  conditions and 0.48 and 0.83 under high- $\text{NO}_x$  conditions. The N/C ratios measured by the AMS varied from 0.02 to 0.10 for SOA formed at high- $\text{NO}_x$  conditions, in good agreement with Kautzman et al. (2010), as they estimate a lower bound estimate of N/C to be 0.04 from filter techniques.

Under low- $\text{NO}_x$  conditions, O/C values descend slightly within the first hour of irradiation, which is likely a result of less oxygenated species partitioning into the growing organic phase. This phenomenon is not observed in the high- $\text{NO}_x$  case, presumably because the high rates of oxidation and aerosol growth obscure this effect. As in the single-ringed aromatic experiments, the O/C ratio of naphthalene-derived SOA increases well after the organic mass has reached a maximum in both

NO<sub>x</sub> regimes (Fig. 3.13). This behavior is consistent with continued OH oxidation of semivolatile species, since most of the gas- and aerosol-phase species still retain aromaticity and unsaturation that are susceptible to oxidation by OH. Under high-NO<sub>x</sub> conditions, the rapid decline of N/C could be explained by photolysis of nitrogen containing compounds (Atkinson et al., 1989; Kautzman et al., 2010).

## 3.5 Discussion

### 3.5.1 Overall Trends in O/C Ratios from Laboratory Chamber-Generated SOA

Of the VOCs studied here, glyoxal is unique because no oxidant initiates SOA formation. Based solely on its vapor pressure, glyoxal, the smallest dicarbonyl, would not be expected to produce SOA. Due to its ability to hydrate and polymerize, however, glyoxal has a large effective Henry's law constant (Loeffler et al., 2006; Ip et al., 2009). These properties, along with its small carbon number, lead to the largest O/C of any system studied here and a measured O/C ratio greater than 1.

Although  $\alpha$ -pinene along with naphthalene has the highest carbon number, it produced the least oxygenated SOA. This is because, with 10 carbons,  $\alpha$ -pinene has only one double bond that is the only active site for ozone reaction. The lack of subsequent ozonolysis reactions limit oxygenation to first-generation products, primarily consisting of oxocarboxylic acids, dicarboxylic acids, and hydroxyl pinonic acid (Yu et al., 1999). This is supported by the chamber AMS data reported by Ng et al. (2006), which shows that the SOA chemistry is virtually constant over time. AMS elemental analysis confirms this as O/C and H/C ratios remain unchanged after semivolatile partitioning has reached equilibrium.

Like single-ringed aromatic SOA, the O/C ratios of naphthalene SOA increase with irradiation time, surpassing 0.7 for the longest low-NO<sub>x</sub> experiments. The aromaticity of naphthalene, toluene, and *m*-xylene allow for multiple oxidation steps through ring opening and bicyclic peroxy radical

routes (Kautzman et al., 2010; Bloss et al., 2005; Alvarez et al., 2007). The different rates of O/C ratio growth between high- and low-NO<sub>x</sub> conditions can be explained by the source of OH radicals. Under high-NO<sub>x</sub> conditions, the rapid photolysis of HONO yields high concentrations of OH radicals ( $\sim 3 \times 10^7$  molecules cm<sup>-3</sup>) at the onset of irradiation, which promptly generates SOA. SOA growth slows once HONO is consumed and OH radicals are produced through NO<sub>x</sub>/HO<sub>x</sub> cycling. Thus, under high-NO<sub>x</sub> conditions, O/C ratios for naphthalene and single-ringed aromatic SOA start high, and then increase slowly afterward, as depicted in Fig. 3.13. Under low-NO<sub>x</sub> conditions, ppm levels of H<sub>2</sub>O<sub>2</sub> are needed to reach an adequate OH concentration and OH levels are lower ( $\sim 3 \times 10^6$  molecules cm<sup>-3</sup>) but more constant throughout the experiment. O/C ratios of the earliest formed low-NO<sub>x</sub> SOA are lower than in the high-NO<sub>x</sub> case, but grow steadily throughout.

Of the five carbons of isoprene, four are subject to OH attack, leading to higher O/C ratios than SOA from  $\alpha$ -pinene ozonolysis. Isoprene photooxidation yields very different SOA products depending on the NO<sub>x</sub> level. Under low-NO<sub>x</sub> conditions, isoprene photooxidation products consist predominantly of polyols and peroxides (Surratt et al., 2006, 2010). These compounds initially give isoprene-SOA high O/C values, but due to photolysis or oligomerization reactions, the O/C ratio decreases. This behavior is in contrast to the behavior of single-ringed aromatic and naphthalene-SOA, in which the O/C ratios tend to increase with time. SOA from isoprene photooxidation under high-NO<sub>x</sub> conditions is predominantly comprised of 2-methylglyceric acid and its corresponding oligoesters (Surratt et al., 2006, 2010; Szmigielski et al., 2007). However, O/C and H/C ratios remain constant over the course of oxidation.

Table 3.3 lists the O/C values of various laboratory SOA systems as determined by different mass spectrometry methods. As in this study, Aiken et al. (2008) used the AMS to measure the elemental composition of chamber SOA in several systems; the O/C values of SOA from the photooxidation of comparable VOCs tend to be higher in the experiments considered in the present study. The exact reason for this disparity is unclear but could be a result of several factors, including differences in OH sources, amounts of organic mass, and extents of reaction. Other studies of monoterpene-derived SOA tend to yield similar O/C values. Although only O/C ratios are presented in Table 3.3,

measured OM/OC ratios are similar to those found in other studies as well (Kleindienst et al., 2007, 2009).

### 3.5.2 Comparisons with Offline Analytical Techniques

The elemental ratios measured by the HR-ToF-AMS can be compared to those of compounds detected by offline analytical techniques, such as coupled chromatography/mass spectrometry of filter extractions. For systems for which the majority of the SOA mass can be quantified by offline advanced analytical techniques, the elemental composition of both measurement techniques can be compared and validated. For  $\alpha$ -pinene/O<sub>3</sub> and naphthalene photooxidation SOA, a substantial portion of the total organic mass has been identified and quantified by coupled gas or liquid chromatography/mass spectrometry (GC/MS or LC/MS) methods and iodometric-spectrophotometric techniques (Yu et al., 1999; Docherty et al., 2005; Kautzman et al., 2010). The discrepancy between the  $\alpha$ -pinene ozonolysis products measured by Yu et al. (1999) and Docherty et al. (2005) could be due to the reactive nature of organic peroxides which decompose to the products measured by gas chromatography. However, the elemental ratios of the products suggested by Docherty et al. (2005) and the mole-weighted calculations of H/C, O/C and N/C ratios of the quantified species in Yu et al. (1999) are very close to the measured elemental composition of the HR-ToF-AMS. In contrast, quantification of many of the particle-phase constituents of isoprene, toluene, and *m*-xylene photooxidation in both NO<sub>x</sub> regimes has been difficult to achieve. For isoprene photooxidation, Surratt et al. (2006) were able to quantify roughly 20% of the SOA mass formed under high-NO<sub>x</sub> conditions and 30% under low-NO<sub>x</sub> conditions. These measurements, however, have associated uncertainties. Because exact standards were not available, acidic species formed under high-NO<sub>x</sub> conditions were quantified using surrogate standards. In addition, peroxides formed under low-NO<sub>x</sub> conditions were quantified using a surrogate with a molecular weight close to the average molecular weight determined from mass spectrometry techniques. Quantification of compounds in aromatic SOA has been difficult as well, though much of the mass has been attributed to small organic acids (Kalberer et al., 2004; Fisseha et al., 2004). Despite the lack of mass closure, the elemental ratios

determined by the HR-ToF-AMS can be compared to the compounds identified from these speciation studies. As noted earlier, the AMS-derived O/C ratios of isoprene and aromatic SOA tend to be lower than those of representative compounds identified by coupled chromatography/mass spectrometry. One possible reason for this difference is the extensive oligomerization present in the particle phase of both systems. Isoprene-SOA formed under both low- and high-NO<sub>x</sub> conditions has been found to form high-MW compounds, either by oligomerization or organosulfate formation (Surratt et al., 2006, 2007, 2010; Szmigielski et al., 2007). For example, Surratt et al. (2006) estimated that 2-methylglyceric acid and its corresponding oligoesters comprise 22–34% of the high-NO<sub>x</sub> SOA mass. In addition, Kalberer et al. (2004) found that about 50% of the trimethylbenzene SOA mass was oligomeric, possibly from the particle-phase reactions of small acids (Fisseha et al., 2004). Esterification, aldol condensation, and hemiacetal/acetal formation reactions have been implicated in producing oligomers. Esterification and aldol condensation reactions, however, release H<sub>2</sub>O which can evaporate to the gas-phase which may occur under low RH conditions. Through VTDMA measurements, Dommen et al. (2006) found that under dry conditions, isoprene SOA volatility is suppressed, implying an enhancement of oligomerization at lower relative humidity. Removal of H<sub>2</sub>O will give lower O/C and H/C ratios measured by the AMS when compared to the monomers measured through chromatography. Substantial oligomerization has also been observed in  $\alpha$ -pinene/O<sub>3</sub> SOA by Gao et al. (2004); however, the relatively low oxygenation of the SOA likely restrains condensation reactions. Thus the O/C ratios of the first generation SOA products are a good representation of the bulk SOA as measured by the AMS. Kautzman et al. (2010) observed no oligomerization in naphthalene-SOA, hence condensation reactions are likely non-existent which allows the elemental ratios measured by the AMS to likely represent the individual species detected through filter sampling. Artifacts of chromatographic separation may also lead to a bias in the detection of oligomers (Hallquist et al., 2009). Because of the reversibility of condensation reactions, oligomers can hydrolyze, increasing the oxygenation of the species detected. Double-bonds can also hydrate, further increasing the O/C ratio of detected compounds. Further work is needed in characterizing the extent of oligomerization in SOA.

### 3.5.3 Uncertainty in the AMS Elemental Analysis

Uncertainties in the AMS elemental analysis method contributing to discrepancies in elemental ratios arise from two main sources: variations in the ionization and fragmentation of compounds in the AMS and errors in analysis of high-resolution mass spectra. To first order, the efficiency with which a molecule is ionized is proportional to the mass of the molecule. However, variations in the efficiencies at which fragment ions are detected occur due to the identity and structure of the molecule being ionized. For instance, uncorrected O/C measurements tend to be biased low due to the propensity of oxygen-containing fragments to be neutral and therefore undetected (Aiken et al., 2007). As a result, the raw measurement of elemental ratios requires calibration factors derived from the analysis of laboratory standards. The uncertainty stated in Aiken et al. (2008) represents the average absolute value of the relative error of the individual data points with respect to the regression between measured elemental ratios and true elemental ratios of the laboratory standards. The uncertainty estimates for O/C, H/C, N/C, and OM/OC are 31%, 10%, 22%, and 6%, respectively. Since the uncertainty is an average for pure standards, Aiken et al. (2008) suggest it represents an upper bound to the uncertainty of measurements of complex mixtures of organic aerosol. Many of those standards are large alkanols and alkanolic acids or aromatic species, which are quite similar to the compounds detected in  $\alpha$ -pinene and naphthalene SOA. By contrast, few of the standards have structures similar to the species found in glyoxal, isoprene, and aromatic SOA such as polyols, peroxides, small organic acids, or larger oligoesters. Thus the calibration factor for an individual compound or class of species like glyoxal may be very different than those determined by Aiken et al. (2008). For instance the O/C calibration factor for glyoxal is likely within a factor of two of the Aiken factor since the upperbound O/C is likely 2 (O/C of hydrated glyoxal monomer), and the average measurement is 1.13. As more standards become available or as methods to measure hard to sample species are developed, the calibration factors should be revised to reflect ambient OA.

Recent studies have investigated the ability of AMS elemental analysis methods to measure the elemental composition of organonitrates. Farmer et al. (2010) studied AMS high-resolution

measurements of organonitrate standards and mixtures and found that most of the nitrogen signal originates from  $\text{NO}_x^+$  ions. Elemental analysis of these standards underestimated the O/C, H/C, and N/C ratios though usually within the aforementioned uncertainties. Farmer et al. (2010) found that the underestimation in O/C was approximately equivalent to assuming that the AMS detects all oxygen except the oxygen in the  $\text{NO}_2$  group. In the systems considered here, the effect of the inclusion of NO family ions to the O/C measurement varies across VOC type. Inclusion of these ions increases the measured O/C of *m*-xylene SOA formed under high- $\text{NO}_x$  conditions by approximately 20%, the largest contribution for all systems investigated. In a separate study, Rollins et al. (2010) synthesized four organonitrates similar in structure to oxidation products of common atmospheric VOCs and measured them with an AMS. It was found that while nitrogen was detected at a higher efficiency than previous standards, oxygen was detected at a much lower efficiency than Aiken et al. (2008). Therefore, both studies suggest that the O/C ratios measured for high- $\text{NO}_x$  photooxidation experiments are biased low partly because of the inability of the AMS to efficiently detect oxygen in an organic nitrate group. Rollins et al. (2010) estimated a correction to measured O/C ratios as follows:

$$\left(\frac{O}{C}\right)_{\text{true}} = \left(\frac{O}{C}\right)_{\text{rep}} + 1.5 \left(\frac{N}{C}\right)_{\text{rep}} \quad (3.5)$$

where “true” corresponds to the actual elemental ratio of the aerosol, and “rep” corresponds to ratios determined using traditional correction factors. Given that the maximum N/C ratios for high- $\text{NO}_x$  photooxidation systems in this study vary from 0.06 to 0.10, the additional correction to O/C ratios ranges from 0.09 to 0.15. While this is not enough to account for the disparity between measured AMS O/C ratios and those of identified SOA species from high- $\text{NO}_x$  isoprene experiments, it does provide an explanation as to why AMS O/C measurements might be biased low.

Apart from ionization and fragmentation variations, errors in the analysis of high-resolution mass spectra can also contribute to the uncertainty of measured elemental ratios. For instance, it is crucial that the  $m/z$  calibration and peak shapes determined from a high-resolution dataset are accurate. Small deviations in the parameters for either of those determinations can lead to significant errors in the relative ratios of ion signals with the same mass-to-charge ratio or the erroneous existence of



ions that lie near other ions with large signals. This becomes especially important at low organic loadings and when analyzing relatively lower resolution V-mode data. Across all systems studied here, elemental analysis of V-mode data consistently produced lower O/C ratios than that of W-mode data by 2% to 27% when the same set of ions were used. This disparity is almost completely due to an imperfect peak shape at  $\text{N}_2^+$  producing artificially large contributions for nearby  $\text{C}_2\text{H}_4^+$  at  $m/z$  28. In W-mode, these ions are significantly resolved so that their peaks do not interfere, and the removal of  $\text{C}_2\text{H}_4^+$  from V-mode data allows for near agreement of O/C ratios between both modes of operation. It is recommended that the  $\text{C}_2\text{H}_4^+$  be removed or estimated when performing elemental analysis of V-mode data.

Inclusion of various ions whose signals might not completely be due to organic aerosol mass may also add to measurement uncertainty. For instance, it is possible that the default treatment of  $\text{O}^+$ ,  $\text{OH}^+$  and  $\text{H}_2\text{O}^+$  ions may be inappropriate for glyoxal-SOA. The glyoxal uptake experiments were carried out at relative humidities of at least 60% so as to produce moist ammonium sulfate seed aerosol. Particle-phase water plays an integral role in promoting uptake and oligomerization through hydration, likely leading to larger organic signals at  $\text{O}^+$ ,  $\text{OH}^+$  and  $\text{H}_2\text{O}^+$ . The contributions of these ions are based on the  $\text{CO}_2^+$  organic signal, which is very low for glyoxal-SOA, possibly contributing to an underestimate of H/C and O/C ratios. Underestimates in elemental ratios may also be a result of the exclusion of “NH family” ions and “SO family” ions. These ions were not included as part of the organic mass because most of their signals could be attributed to ammonium sulfate seed aerosol. Yet, various studies have shown that inorganic constituents of aerosol may react with organics to form new species (Hallquist et al., 2009). For example, Galloway et al. (2009) demonstrated the formation of reduced nitrogen-containing compounds, particularly imidazoles, from a proposed reaction of ammonium and glyoxal while organonitrate standards have been shown to produce  $\text{NH}_x^+$  fragments (Rollins et al., 2010). Other studies have observed organosulfates ( $\text{R-OSO}_3$ ), organonitrates, and nitrated organosulfates in SOA produced from the photooxidation of isoprene in the presence of ammonium sulfate seed (Surratt et al., 2006, 2007, 2010). Kautzman et al. (2010) observed hydroxybenzene sulfonic acid in naphthalene SOA in both high and low- $\text{NO}_x$

regimes and most recent investigations of organosulfate standards show that these compounds tend to fragment into SO family ions (Farmer et al., 2010). Thus exclusion of these ions will negatively bias N/C, H/C, O/C, and S/C values. S/C ratios were considered zero, as no sulfur-containing ions were measured apart from SO family ions.

### 3.5.4 AMS Marker Ions and SOA Oxygenation

Analysis of the elemental contributions of different AMS marker ions can provide insight into the possible bulk chemistry occurring in the particle phase. In the oxidative systems studied here ( $\alpha$ -pinene, isoprene, single-ring aromatics, and naphthalene), the ions  $\text{C}_2\text{H}_3\text{O}^+$  and  $\text{CO}_2^+$  at  $m/z$  43 and 44, respectively, contribute strongly to the oxygen content of the formed SOA. In past AMS studies,  $\text{C}_2\text{H}_3\text{O}^+$  is prominent in freshly oxidized SOA while  $\text{CO}_2^+$  appears strongly in the spectra of aged OA and laboratory standards of organic acids (Takegawa et al., 2007; Zhang et al., 2005a, 2007; Ulbrich et al., 2009). The spectra presented in the current experiments support these general observations, as the  $\text{C}_2\text{H}_3\text{O}^+$  signal is relatively prominent early in the experiments but its fraction of the total organic signal decreases as that of  $\text{CO}_2^+$  increases. In a recent study by Kroll et al. (2009) of heterogeneously oxidized squalane particles, the initial increase of  $\text{C}_2\text{H}_3\text{O}^+$  signal was associated with functionalization reactions, those that add oxygen to the carbon chain. With further oxidation, the  $\text{CO}_2^+$  signal increased, which was associated with fragmentation reactions, those associated with C-C bond scission and subsequent loss of relatively small carbon fragments. It is likely that such processes are occurring, either heterogeneously or in the gas phase, in the systems evaluated here, especially for the single-ring aromatic and naphthalene systems where the O/C ratio continues to increase even as the total particulate volume decreases (Fig. 3.13 for example). Although time-dependent densities were not measured, and wall losses may contribute to the declining particulate volume, it is likely that the continued O/C increase is occurring through fragmentation reactions that are removing carbon from the particle phase. More study is needed to elucidate the contributions of functionalization and fragmentation pathways of SOA.

Recently Aiken et al. (2008) derived a correlation (Eqn. 3.4) between  $f_{44}$ , the fraction of organic

signal at  $m/z$  44 and the O/C measured from the elemental analysis method. Using this correlation, we can evaluate the extent to which  $f_{44}$  captures the relative oxygenation of SOA formed in chamber studies. This correlation along with ambient Mexico City data and data from the systems evaluated here are shown in Fig. 3.15. For most oxidant/precursor systems,  $O/C_{44}$  mimics the overall trend of  $O/C_{HR}$  well. For the  $\alpha$ -pinene/ $O_3$ , isoprene/high- $NO_x$ , and naphthalene SOA systems, the close correspondence of  $O/C_{44}$  and  $O/C_{HR}$  results because  $CO_2^+$  provides much of the oxygen signal in the spectra. For the single ring aromatic systems,  $O/C_{44}$  is consistently below  $O/C_{HR}$  but trends with it. For the isoprene/low- $NO_x$  system,  $O/C_{44}$  underestimates  $O/C_{HR}$  by 50% early in the oxidation, but then increases to meet  $O/C_{HR}$ . For these systems, other mass fragments, especially  $m/z$  43 ( $C_2H_3O^+$ ), contribute a large part of the oxygen content. As the contribution of  $m/z$  44 grows in these experiments,  $O/C_{44}$  becomes a better surrogate for  $O/C_{HR}$ . Glyoxal-SOA is a special case because  $CO_2^+$  represents less than 1% of the total organic signal. Although hydrated glyoxal and its oligomers are highly oxygenated, they do not contain acid groups that can easily fragment into  $CO_2^+$ . Thus  $m/z$  44 is a poor surrogate for estimating the oxygen content of glyoxal SOA. In general,  $m/z$  44 adequately represents the oxygenation of SOA in different oxidative systems, especially for more aged SOA, and for SOA where  $m/z$  44 has the largest contribution to the spectral signal. In the ambient atmosphere,  $m/z$  44 and the correlation determined by Aiken et al. (2008) may better reflect the oxygen content of SOA because ambient SOA represents a very large mixture of compounds from many different VOCs whereas chamber SOA is relatively more homogeneous.

### 3.6 Comparison of Chamber and Ambient Elemental Ratios and Spectra

Figure 3.16 shows the range of O/C ratios determined from the set of chamber experiments evaluated here, as compared with ambient O/C measurements of Mexico City SOA. Chamber SOA O/C ratios are plotted as a function of precursor carbon number, and the bars represent the maximum range of O/C values observed for each VOC precursor. The dotted lines represent the average O/C values for

different sampling times and areas in Mexico City (Aiken et al., 2008), showing that the O/C ratios increase with photochemical age. The shaded regions depict the range of O/C ratios commonly attributed to the different PMF components found for various ambient data sets (Aiken et al., 2008, 2009; Ulbrich et al., 2009; Zhang et al., 2005a,b, 2007), including oxygenated organic aerosol (OOA), biomass burning organic aerosol (BBOA), and hydrocarbon-like organic aerosol (HOA). These ranges and factors are not definite for all ambient data sets but typify the oxygenation domains for commonly derived PMF factors. Often, the OOA is found to consist of two factors: the LV-OOA PMF component is considered to represent aged organic aerosol with a higher O/C ratio than SV-OOA which is considered to represent relatively fresh SOA.

While one might expect SOA O/C ratios to decrease as the carbon number of the precursor system increases, individual differences in elemental composition depend greatly on the identity of the precursor and mechanism, and the duration of oxidation. In the experiments surveyed here, photooxidation of aromatic precursor systems (toluene, *m*-xylene, and naphthalene) produces SOA that achieves higher O/C ratios than the biogenic systems (isoprene photooxidation and  $\alpha$ -pinene ozonolysis). While this is not necessarily representative of ambient SOA formation, it does provide context to compare the SOA O/C ratios measured in ambient atmosphere to those from chamber experiments. Previous studies have noted that AMS mass spectra of chamber data do not exhibit as much oxidation as the OOA mass spectrum, with the possible exception of SOA derived from aromatic precursors (Zhang et al., 2005a; Bahreini et al., 2005). The laboratory data evaluated here show that for photooxidation-SOA, O/C ratios of at least 0.5 are achieved, an oxidation state comparable to that of SV-OOA. Aromatic and naphthalene photooxidation yield SOA that increases in O/C ratios throughout the experiments, regardless of NO<sub>x</sub> condition, reaching upwards of 0.7, well into what might be considered as the oxygenation state of LV-OOA. Generally chamber studies do not reach the highest O/C ratios observed in remote OA, which can approach unity (DeCarlo et al., 2008). This emphasizes the need to devise chamber experiments that achieve sufficient timescales to achieve the OH exposure needed to form the most oxygenated SOA (Hallquist et al., 2009).

In addition to elemental composition, comparisons between PMF component spectra and cham-

ber spectra from the AMS can provide insight into the extent to which chamber systems represent ambient SOA. The typical HOA spectrum is identified by its  $C_nH_{2n+1}^+$  and  $C_nH_{2n-1}^+$  ion series, characteristic of hydrocarbon spectra. On the other hand, the OOA spectrum is distinguished by a strong peak at  $m/z$  44 ( $CO_2^+$ ) and relatively little signal at  $m/z > 55$ . In its subclasses, SV-OOA has a prominent  $m/z$  43 ( $C_2H_3O^+$ ) signal, and LV-OOA has a dominant  $m/z$  44 signal. Of the systems surveyed here, aromatic (toluene, *m*-xylene, and naphthalene) and isoprene high- $NO_x$  spectra most resemble that of OOA, with prominent contributions at  $C_2H_3O^+$  and  $CO_2^+$  and relatively small signals at higher mass-to-charge ratios. Naphthalene spectra best resemble LV-OOA with a dominant  $m/z$  44 signal; they do, however, have fairly sizable signals at hydrocarbon-like ions, likely from the fragmentation of a retained aromatic ring. The spectra of *m*-xylene, toluene and isoprene-high- $NO_x$  resemble that of SV-OOA with strong contributions at  $C_2H_3O^+$ . The steady increase of  $f_{44}$  throughout the duration of single-ring aromatic photooxidation suggests that with continued irradiation the spectra will look more like that of LV-OOA. Consistent with measured O/C ratios, the spectrum of SOA from  $\alpha$ -pinene ozonolysis is the least oxidized; along with a prominent  $C_2H_3O^+$  contribution, the spectrum shown in Fig. 3.2b has considerable signals of hydrocarbon-like ions in series similar to that of HOA. One should note that the organic loadings for the  $\alpha$ -pinene system were relatively large, and that at smaller loadings the spectrum will be more similar to that of OOA (Shilling et al., 2009). Interestingly, the spectrum of the most oxidized system, glyoxal uptake, least resembles the spectra of previously identified PMF components. The dominant  $CHO^+$  ion and other notable ions that exist in the valleys of typical ions series, such as  $CH_3O_2^+$  and  $C_2H_2O_2^+$ , in the glyoxal-SOA spectrum suggest that if glyoxal uptake is occurring to a significant extent in ambient systems, these ions would be prominent in ambient spectra; they do appear in OOA spectra (Aiken et al., 2009, Sup. Matl.) but not at the percent of the total spectral signal observed here. If reactive uptake of glyoxal occurs substantially in ambient SOA, its contribution to AMS spectra may be obscured by the presence of other species or by its participation in particle-phase reactions.

The work here presents high resolution AMS data of a canonical ensemble of chamber SOA systems. While not representing the most oxidized ambient SOA, the spectra and elemental composition

measurements of the surveyed systems could provide a basis for linking chamber data to ambient measurements and understanding ambient PMF factors, especially the SV-OOA component. However, more work is needed to correlate AMS spectra with molecular structure, and experiments need to be devised that can reach the oxidation states achieved in ambient systems to further interpret the the full transformation of VOCs to OOA.

### 3.7 Acknowledgements

This work was supported by the US Department of Energy Biological and Environmental Research grant DE-FG02-05ER63983, US Environmental Protection Agency STAR grant RD-83374901, and US NSF grant ATM-0432377. It has not been formally reviewed by EPA. The views expressed in this document are solely those of the authors and the EPA does not endorse any products in this publication. The authors would like to thank Arthur Chan, Jason Surratt and Nga Lee Ng for helpful discussions and Man Nin Chan for analysis of filter samples. Edited by: J.-L. Jimenez

### Bibliography

- Aiken, A. C., DeCarlo, P. F., and Jimenez, J. L.: Elemental analysis of organic species with electron ionization high-resolution mass spectrometry, *Anal. Chem.*, 79, 8350–8358, doi:10.1021/Ac071150w, 2007.
- Aiken, A. C., Decarlo, P. F., Kroll, J. H., Worsnop, D. R., Huffman, J. A., Docherty, K. S., Ulbrich, I. M., Mohr, C., Kimmel, J. R., Sueper, D., Sun, Y., Zhang, Q., Trimborn, A., Northway, M., Ziemann, P. J., Canagaratna, M. R., Onasch, T. B., Alfarra, M. R., Prevot, A. S. H., Dommen, J., Duplissy, J., Metzger, A., Baltensperger, U., and Jimenez, J. L.: O/C and OM/OC ratios of primary, secondary, and ambient organic aerosols with high-resolution time-of-flight aerosol mass spectrometry, *Environ. Sci. Technol.*, 42, 4478–4485, doi:10.1021/Es703009q, 2008.
- Aiken, A. C., Salcedo, D., Cubison, M. J., Huffman, J. A., DeCarlo, P. F., Ulbrich, I. M., Docherty, K. S., Sueper, D., Kimmel, J. R., Worsnop, D. R., Trimborn, A., Northway, M., Stone, E. A.,

- Schauer, J. J., Volkamer, R. M., Fortner, E., de Foy, B., Wang, J., Laskin, A., Shutthanandan, V., Zheng, J., Zhang, R., Gaffney, J., Marley, N. A., Paredes-Miranda, G., Arnott, W. P., Molina, L. T., Sosa, G., and Jimenez, J. L.: Mexico City aerosol analysis during MILAGRO using high resolution aerosol mass spectrometry at the urban supersite (T0) - Part 1: Fine particle composition and organic source apportionment, *Atmos. Chem. Phys.*, 9, 6633–6653, doi:10.5194/acp-9-6633-2009 2009.
- Allan, J. D., Delia, A. E., Coe, H., Bower, K. N., Alfarra, M. R., Jimenez, J. L., Middlebrook, A. M., Drewnick, F., Onasch, T. B., Canagaratna, M. R., Jayne, J. T., and Worsnop, D. R.: A generalised method for the extraction of chemically resolved mass spectra from aerodyne aerosol mass spectrometer data, *J. Aerosol Sci.*, 35, 909–922, doi:10.1016/j.jaerosci.2004.02.007, 2004.
- Alvarez, E. G., Viidanoja, J., Munoz, A., Wirtz, K., and Hjorth, J.: Experimental confirmation of the dicarbonyl route in the photo-oxidation of toluene and benzene, *Environ. Sci. Technol.*, 41, 8362–8369, doi:10.1021/Es0713274, 2007.
- Atkinson, R., Aschmann, S. M., Arey, J., Zielinska, B., and Schuetzle, D.: Gas-phase atmospheric chemistry of 1-Nitronaphthalene and 2-Nitronaphthalene and 1,4-Naphthoquinone, *Atmos. Environ.*, 23, 2679–2690, doi:10.1016/0004-6981(89)90548-9, 1989.
- Bahreini, R., Keywood, M. D., Ng, N. L., Varutbangkul, V., Gao, S., Flagan, R. C., Seinfeld, J. H., Worsnop, D. R., and Jimenez, J. L.: Measurements of secondary organic aerosol from oxidation of cycloalkenes, terpenes, and *m*-xylene using an Aerodyne aerosol mass spectrometer, *Environ. Sci. Technol.*, 39, 5674–5688, doi:10.1021/Es048061a, 2005.
- Bloss, C., Wagner, V., Jenkin, M. E., Volkamer, R., Bloss, W. J., Lee, J. D., Heard, D. E., Wirtz, K., Martin-Reviejo, M., Rea, G., Wenger, J. C., and Pilling, M. J.: Development of a detailed chemical mechanism (MCMv3.1) for the atmospheric oxidation of aromatic hydrocarbons, *Atmos. Chem. Phys.*, 5, 641–664, doi:10.5194/acp-5-641-2005, 2005.
- Canagaratna, M. R., Jayne, J. T., Jimenez, J. L., Allan, J. D., Alfarra, M. R., Zhang, Q.,

- Onasch, T. B., Drewnick, F., Coe, H., Middlebrook, A., Delia, A., Williams, L. R., Trimborn, A. M., Northway, M. J., DeCarlo, P. F., Kolb, C. E., Davidovits, P., and Worsnop, D. R.: Chemical and microphysical characterization of ambient aerosols with the aerodyne aerosol mass spectrometer, *Mass Spectrom. Rev.*, 26, 185–222, doi:10.1002/Mas.20115, 2007.
- Chan, A. W. H., Kautzman, K. E., Chhabra, P. S., Surratt, J. D., Chan, M. N., Crouse, J. D., Kürten, A., Wennberg, P. O., Flagan, R. C., and Seinfeld, J. H.: Secondary organic aerosol formation from photooxidation of naphthalene and alkylnaphthalenes: implications for oxidation of intermediate volatility organic compounds (IVOCs), *Atmos. Chem. Phys.*, 9, 3049–3060, doi:10.5194/acp-9-3049-2009, 2009a.
- Chan, M. N., Chan, A. W. H., Chhabra, P. S., Surratt, J. D., and Seinfeld, J. H.: Modeling of secondary organic aerosol yields from laboratory chamber data, *Atmos. Chem. Phys.*, 9, 5669–5680, doi:10.5194/acp-9-5669-2009, 2009b.
- Claeys, M., Graham, B., Vas, G., Wang, W., Vermeylen, R., Pashynska, V., Cafmeyer, J., Guyon, P., Andreae, M. O., Artaxo, P., and Maenhaut, W.: Formation of secondary organic aerosols through photooxidation of isoprene, *Science*, 303, 1173–1176, doi:10.1126/science.1092805, 2004.
- Cocker, D. R., Flagan, R. C., and Seinfeld, J. H.: State-of-the-art chamber facility for studying atmospheric aerosol chemistry, *Environ. Sci. Technol.*, 35, 2594–2601, doi:10.1021/Es0019169, 2001.
- Crabbe, G. F. and Coggeshall, N. D.: Application of total ionization principles to mass spectrometric analysis, *Anal. Chem.*, 30, 310–313, doi:10.1021/ac60135a001, 1958.
- DeCarlo, P. F., Kimmel, J. R., Trimborn, A., Northway, M. J., Jayne, J. T., Aiken, A. C., Gonin, M., Fuhrer, K., Horvath, T., Docherty, K. S., Worsnop, D. R., and Jimenez, J. L.: Field-deployable, high-resolution, time-of-flight aerosol mass spectrometer, *Anal. Chem.*, 78, 8281–8289, doi:10.1021/Ac061249n, 2006.
- DeCarlo, P. F., Dunlea, E. J., Kimmel, J. R., Aiken, A. C., Sueper, D., Crouse, J., Wennberg,



- P. O., Emmons, L., Shinozuka, Y., Clarke, A., Zhou, J., Tomlinson, J., Collins, D. R., Knapp, D., Weinheimer, A. J., Montzka, D. D., Campos, T., and Jimenez, J. L.: Fast airborne aerosol size and chemistry measurements above Mexico City and Central Mexico during the MILAGRO campaign, *Atmos. Chem. Phys.*, 8, 4027–4048, doi:10.5194/acp-8-4027-2008, 2008.
- Docherty, K. S., Wu, W., Lim, Y. B., and Ziemann, P. J.: Contributions of organic peroxides to secondary aerosol formed from reactions of monoterpenes with O<sub>3</sub>, *Environ. Sci. Technol.*, 39, doi:10.1021/es050228s, 4049–4059, 2005.
- Dommen, J., Metzger, A., Duplissy, J., Kalberer, M., Alfarra, M. R., Gascho, A., Weingartner, E., Prevot, A. S. H., Verheggen, B., and Baltensperger, U.: Laboratory observation of oligomers in the aerosol from isoprene/NO<sub>x</sub> photooxidation, *Geophys. Res. Lett.*, 33, L13805, doi:10.1029/2006gl026523, 2006.
- Drewnick, F., Hings, S. S., DeCarlo, P., Jayne, J. T., Gonin, M., Fuhrer, K., Weimer, S., Jimenez, J. L., Demerjian, K. L., Borrmann, S., and Worsnop, D. R.: A new time-of-flight aerosol mass spectrometer (TOF-AMS) – instrument description and first field deployment, *Aerosol Sci. Tech.*, 39, 637–658, doi:10.1080/02786820500182040, 2005.
- Dzepina, K., Volkamer, R. M., Madronich, S., Tulet, P., Ulbrich, I. M., Zhang, Q., Cappa, C. D., Ziemann, P. J., and Jimenez, J. L.: Evaluation of recently-proposed secondary organic aerosol models for a case study in Mexico City, *Atmos. Chem. Phys.*, 9, 5681–5709, doi:10.5194/acp-9-5681-2009 2009.
- Farmer, D. K., Matsunaga, A., Docherty, K. S., Surratt, J. D., Seinfeld, J. H., Ziemann, P. J., and Jimenez, J. L.: Response of an aerosol mass spectrometer to organonitrates and organosulfates and implications for atmospheric chemistry, *Proc. Natl. Acad. Sci.*, doi:10.1073/pnas.0912340107, 2010.
- Fisseha, R., Dommen, J., Sax, M., Paulsen, D., Kalberer, M., Maurer, R., Hofler, F., Weingartner, E., and Baltensperger, U.: Identification of organic acids in secondary organic aerosol

- and the corresponding gas phase from chamber experiments, *Anal. Chem.*, 76, 6535–6540, doi:10.1021/Ac048975f, 2004.
- Fratzke, A. R. and Reilly, P. J.: Thermodynamic and kinetic-analysis of the dimerization of aqueous glyoxal, *Int. J. Chem. Kinet.*, 18, 775–789, doi:10.1002/kin.550180705, 1986.
- Galloway, M. M., Chhabra, P. S., Chan, A. W. H., Surratt, J. D., Flagan, R. C., Seinfeld, J. H., and Keutsch, F. N.: Glyoxal uptake on ammonium sulphate seed aerosol: reaction products and reversibility of uptake under dark and irradiated conditions, *Atmos. Chem. Phys.*, 9, 3331–3345, doi:10.5194/acp-9-3331-2009, 2009.
- Gao, S., Keywood, M., Ng, N. L., Surratt, J., Varutbangkul, V., Bahreini, R., Flagan, R. C., and Seinfeld, J. H.: Low-molecular-weight and oligomeric components in secondary organic aerosol from the ozonolysis of cycloalkenes and alpha-pinene, *J. Phys. Chem. A*, 108, 10147–10164, doi:10.1021/Jp047466e, 2004.
- Glasius, M., Lahaniati, M., Calogirou, A., Di Bella, D., Jensen, N. R., Hjorth, J., Kotzias, D., and Larsen, B. R.: Carboxylic acids in secondary aerosols from oxidation of cyclic monoterpenes by ozone, *Environ. Sci. Technol.*, 34, 1001–1010, doi:10.1021/es990445r, 2000.
- Gómez-González, Y., Surratt, J. D., Cuyckens, F., Szmigielski, R., Vermeylen, R., Jaoui, M., Lewandowski, M., Offenberg, J. H., Kleindienst, T. E., Edney, E. O., Blockhuys, F., Van Alsenoy, C., Maenhaut, W., and Claeys, M.: Characterization of organosulfates from the photooxidation of isoprene and unsaturated fatty acids in ambient aerosol using liquid chromatography/(-) electrospray ionization mass spectrometry, *J. Mass Spectrom.*, 43, 371–382, doi:10.1002/Jms.1329, 2008.
- Hallquist, M., Wenger, J. C., Baltensperger, U., Rudich, Y., Simpson, D., Claeys, M., Dommen, J., Donahue, N. M., George, C., Goldstein, A. H., Hamilton, J. F., Herrmann, H., Hoffmann, T., Iinuma, Y., Jang, M., Jenkin, M. E., Jimenez, J. L., Kiendler-Scharr, A., Maenhaut, W., McFiggans, G., Mentel, T. F., Monod, A., Prévôt, A. S. H., Seinfeld, J. H., Surratt, J. D.,

- Szmigielski, R., and Wildt, J.: The formation, properties and impact of secondary organic aerosol: current and emerging issues, *Atmos. Chem. Phys.*, 9, 5155–5235, doi:10.5194/acp-9-5155-2009, 2009.
- Hamilton, J. F., Lewis, A. C., Bloss, C., Wagner, V., Henderson, A. P., Golding, B. T., Wirtz, K., Martin-Reviejo, M., and Pilling, M. J.: Measurements of photo-oxidation products from the reaction of a series of alkyl-benzenes with hydroxyl radicals during EXACT using comprehensive gas chromatography, *Atmos. Chem. Phys.*, 3, 1999–2014, doi:10.5194/acp-3-1999-2003, 2003.
- Hamilton, J. F., Webb, P. J., Lewis, A. C., and Reviejo, M. M.: Quantifying small molecules in secondary organic aerosol formed during the photo-oxidation of toluene with hydroxyl radicals, *Atmos. Environ.*, 39, 7263–7275, doi:10.1016/j.atmosenv.2005.09.006, 2005.
- Heaton, K. J., Dreyfus, M. A., Wang, S., and Johnston, M. V.: Oligomers in the early stage of biogenic secondary organic aerosol formation and growth, *Environ. Sci. Technol.*, 41, 6129–6136, doi:10.1021/Es070314n, 2007.
- Huffman, J. A., Docherty, K. S., Mohr, C., Cubison, M. J., Ulbrich, I. M., Ziemann, P. J., Onasch, T. B., and Jimenez, J. L.: Chemically-resolved volatility measurements of organic aerosol from different sources, *Environ. Sci. Technol.*, 43, 5351–5357, doi:10.1021/Es803539d, 2009.
- Iinuma, Y., Boge, O., Gnauk, T., and Herrmann, H.: Aerosol-chamber study of the alpha-pinene/O<sub>3</sub> reaction: influence of particle acidity on aerosol yields and products, *Atmos. Environ.*, 38, 761–773, doi:10.1016/j.atmosenv.2003.10.015, 2004.
- Ip, H. S. S., Huang, X. H. H., and Yu, J. Z.: Effective Henry's law constants of glyoxal, glyoxylic acid, and glycolic acid, *Geophys. Res. Lett.*, 36, L01802, doi:10.1029/2008gl036212, 2009.
- Jang, M. and Kamens, R. M.: Newly characterized products and composition of secondary aerosols from the reaction of alpha-pinene with ozone, *Atmos. Environ.*, 33, 459–474, doi:10.1016/S1352-2310(98)00222-2, 1999.

- Jang, M. S. and Kamens, R. M.: Characterization of secondary aerosol from the photooxidation of toluene in the presence of  $\text{NO}_x$  and 1-propene, *Environ. Sci. Technol.*, 35, 3626–3639, doi:10.1021/Es010676+, 2001.
- Jayne, J. T., Leard, D. C., Zhang, X. F., Davidovits, P., Smith, K. A., Kolb, C. E., and Worsnop, D. R.: Development of an aerosol mass spectrometer for size and composition analysis of submicron particles, *Aerosol Sci. Tech.*, 33, 49–70, 2000.
- Jimenez, J. L., Jayne, J. T., Shi, Q., Kolb, C. E., Worsnop, D. R., Yourshaw, I., Seinfeld, J. H., Flagan, R. C., Zhang, X. F., Smith, K. A., Morris, J. W., and Davidovits, P.: Ambient aerosol sampling using the Aerodyne Aerosol Mass Spectrometer, *J. Geophys. Res.-Atmos.*, 108(D7), 8425, doi:10.1029/2001jd001213, 2003.
- Jimenez, J. L., Canagaratna, M. R., Donahue, N. M., Prevot, A. S. H., Zhang, Q., Kroll, J. H., Decarlo, P. F., Allan, J. D., Coe, H., Ng, N. L., Aiken, A. C., Docherty, K. D., Ulbrich, I. M., Grieshop, A. P., Robinson, A. L., Duplissy, J., Smith, J. D., Wilson, K. R., Lanz, V. A., Hueglin, C., Sun, Y. L., Tian, J., Laaksonen, A., Raatikainen, T., Rautiainen, J., Vaattovaara, P., Ehn, M., Kulmala, M., Tomlinson, J. M., Collins, D. R., Cubison, M. J., Dunlea, E. J., Huffman, J. A., Onasch, T. B., Alfarra, M. R., Williams, P. I., Bower, K., Kondo, Y., Schneider, J., Drewnick, F., Borrmann, S., Weimer, S., Demerjian, K., Salcedo, D., Cottrell, L., Griffin, R., Takami, A., Miyoshi, T., Hatakeyama, S., Shimono, A., Sun, J. Y., Zhang, Y. M., Dzepina, K., Kimmel, J. R., Sueper, D., Jayne, J. T., Herndon, S. C., Trimborn, A. M., Williams, L. R., Wood, E. C., Kolb, C. E., Middlebrook, A. M., Baltensperger, U., and Worsnop, D. R.: Evolution of organic aerosols in the atmosphere, *Science*, 326(5959), 1525–1529, doi:10.1126/science.1180353, 2009.
- Kalberer, M., Paulsen, D., Sax, M., Steinbacher, M., Dommen, J., Prevot, A. S. H., Fisseha, R., Weingartner, E., Frankevich, V., Zenobi, R., and Baltensperger, U.: Identification of polymers as major components of atmospheric organic aerosols, *Science*, 303, 1659–1662, doi:10.1126/science.1092185, 2004.

- Kautzman, K. E., Surratt, J. D., Chan, M. N., Chan, A. W. H., Hersey, S. P., Chhabra, P. S., Dalleska, N. F., Wennberg, P. O., Flagan, R. C., and Seinfeld, J. H.: Chemical composition of gas- and aerosol-phase products from the photooxidation of naphthalene, *J. Phys. Chem. A*, 114(2), 913–934, doi:10.1021/jp908530s, 2010.
- Keywood, M. D., Kroll, J. H., Varutbangkul, V., Bahreini, R., Flagan, R. C., and Seinfeld, J. H.: Secondary organic aerosol formation from cyclohexene ozonolysis: effect of OH scavenger and the role of radical chemistry, *Environ. Sci. Technol.*, 38, 3343–3350, doi:10.1021/Es049725j, 2004.
- Kleindienst, T. E., Jaoui, M., Lewandowski, M., Offenberg, J. H., Lewis, C. W., Bhave, P. V., and Edney, E. O.: Estimates of the contributions of biogenic and anthropogenic hydrocarbons to secondary organic aerosol at a southeastern US location, *Atmos. Env.*, 41, 8288–8300, doi:10.1016/j.atmosenv.2007.06.045, 2007.
- Kleindienst, T. E., Lewandowski, M., Offenberg, J. H., Jaoui, M., Edney, E. O.: The formation of secondary organic aerosol from the isoprene + OH reaction in the absence of  $\text{NO}_x$ , *Atmos. Chem. Phys.*, 9, 6541–6558, doi:10.5194/acp-9-6541-2009, 2009.
- Koch, S., Winterhalter, R., Uherek, E., Kolloff, A., Neeb, P., and Moortgat, G. K.: Formation of new particles in the gas-phase ozonolysis of monoterpenes, *Atmos. Environ.*, 34, 4031–4042, doi:10.1016/S1352-2310(00)00133-3, 2000.
- Kroll, J. H. and Seinfeld, J. H.: Chemistry of secondary organic aerosol: Formation and evolution of low-volatility organics in the atmosphere, *Atmos. Environ.*, 42, 3593–3624, doi:10.1016/j.atmosenv.2008.01.003, 2008.
- Kroll, J. H., Ng, N. L., Murphy, S. M., Flagan, R. C., and Seinfeld, J. H.: Secondary organic aerosol formation from isoprene photooxidation, *Environ. Sci. Technol.*, 40, 1869–1877, doi:10.1021/Es0524301, 2006.
- Kroll, J. H., Smith, J. D., Che, D. L., Kessler, S. H., Worsnop, D. R., and Wilson, K. R.: Measure-

- ment of fragmentation and functionalization pathways in the heterogeneous oxidation of oxidized organic aerosol, *Phys. Chem. Chem. Phys.*, 11, 8005–8014, doi:10.1039/B905289e, 2009.
- Kua, J., Hanley, S. W., and De Haan, D. O.: Thermodynamics and kinetics of glyoxal dimer formation: a computational study, *J. Phys. Chem. A*, 112, 66–72, doi:10.1021/Jp076573g, 2008.
- Lanz, V. A., Alfarra, M. R., Baltensperger, U., Buchmann, B., Hueglin, C., and Prévôt, A. S. H.: Source apportionment of submicron organic aerosols at an urban site by factor analytical modelling of aerosol mass spectra, *Atmos. Chem. Phys.*, 7, 1503–1522, doi:10.5194/acp-7-1503-2007, 2007.
- Lee, M. H., Heikes, B. G., and O’Sullivan, D. W.: Hydrogen peroxide and organic hydroperoxide in the troposphere: a review, *Atmos. Environ.*, 34, 3475–3494, doi:10.1016/S1352-2310(99)00432-X, 2000.
- Loeffler, K. W., Koehler, C. A., Paul, N. M., and De Haan, D. O.: Oligomer formation in evaporating aqueous glyoxal and methyl glyoxal solutions, *Environ. Sci. Technol.*, 40, 6318–6323, doi:10.1021/Es060810w, 2006.
- Malloy, Q. G. J., Li Qi, , Warren, B., Cocker III, D. R., Erupe, M. E., and Silva, P. J.: Secondary organic aerosol formation from primary aliphatic amines with  $\text{NO}_3$  radical, *Atmos. Chem. Phys.*, 9, 2051–2060, doi:10.5194/acp-9-2051-2009, 2009.
- Mohr, C., Huffman, J. A., Cubison, M. J., Aiken, A. C., Docherty, K. S., Kimmel, J. R., Ulbricht, I. M., Hannigan, M., and Jimenez, J. L.: Characterization of primary organic aerosol emissions from meat cooking, trash burning, and motor vehicles with high-resolution aerosol mass spectrometry and comparison with ambient and chamber observations, *Environ. Sci. Technol.*, 43, 2443–2449, doi:10.1021/Es8011518, 2009.
- Ng, N. L., Kroll, J. H., Keywood, M. D., Bahreini, R., Varutbangkul, V., Flagan, R. C., Seinfeld, J. H., Lee, A., and Goldstein, A. H.: Contribution of first- versus second-generation products to secondary organic aerosols formed in the oxidation of biogenic hydrocarbons, *Environ. Sci. Technol.*, 40, 2283–2297, doi:10.1021/Es052269u, 2006.

- Ng, N. L., Kroll, J. H., Chan, A. W. H., Chhabra, P. S., Flagan, R. C., and Seinfeld, J. H.: Secondary organic aerosol formation from m-xylene, toluene, and benzene, *Atmos. Chem. Phys.*, 7, 3909–3922, doi:10.5194/acp-7-3909-2007, 2007.
- Reinhardt, A., Emmenegger, C., Gerrits, B., Panse, C., Dommen, J., Baltensperger, U., Zenobi, R., and Kalberer, M.: Ultrahigh mass resolution and accurate mass measurements as a tool to characterize oligomers in secondary organic aerosols, *Anal. Chem.*, 79, 4074–4082, doi:10.1021/Ac062425v, 2007.
- Renbaum, L. H. and Smith, G. D.: Organic nitrate formation in the radical-initiated oxidation of model aerosol particles in the presence of  $\text{NO}_x$ , *Phys. Chem. Chem. Phys.*, 11, 8040–8047, doi:10.1039/B909239k, 2009.
- Roberts, J. M. and Fajer, R. W.: UV absorption cross-sections of organic nitrates of potential atmospheric importance and estimation of atmospheric lifetimes, *Environ. Sci. Technol.*, 23, 945–951, doi:10.1021/es00066a003, 1989.
- Rollins, A. W., Fry, J. L., Hunter, J. F., Kroll, J. H., Worsnop, D. R., Singaram, S. W., and Cohen, R. C.: Elemental analysis of aerosol organic nitrates with electron ionization high-resolution mass spectrometry, *Atmos. Chem. Phys.*, 3, 301–310, doi:10.5194/amt-3-301-2010, 2010.
- Sato, K.: Detection of nitrooxypolyols in secondary organic aerosol formed from the photooxidation of conjugated dienes under high- $\text{NO}_x$  conditions, *Atmos. Environ.*, 42, 6851–6861, doi:10.1016/j.atmosenv.2008.05.010, 2008.
- Sato, K., Hatakeyama, S., and Imamura, T.: Secondary organic aerosol formation during the photooxidation of toluene:  $\text{NO}_x$  dependence of chemical composition, *J. Phys. Chem. A*, 111, 9796–9808, doi:10.1021/Jp071419f, 2007.
- Sato, K., Takami, A., Isozaki, T., Hikida, T., Shimono, A., and Imamura, T.: Mass spectrometric study of secondary organic aerosol formed from the photo-oxidation of aromatic hydrocarbons, *Atmos. Environ.*, 44, 1080–1087, doi:10.1016/j.atmosenv.2009.12.013, 2010.

- Shilling, J. E., Chen, Q., King, S. M., Rosenoern, T., Kroll, J. H., Worsnop, D. R., DeCarlo, P. F., Aiken, A. C., Sueper, D., Jimenez, J. L., and Martin, S. T.: Loading-dependent elemental composition of  $\alpha$ -pinene SOA particles, *Atmos. Chem. Phys.*, 9, 771–782, doi:10.5194/acp-9-771-2009, 2009.
- Smith, J. D., Kroll, J. H., Cappa, C. D., Che, D. L., Liu, C. L., Ahmed, M., Leone, S. R., Worsnop, D. R., and Wilson, K. R.: The heterogeneous reaction of hydroxyl radicals with sub-micron squalane particles: a model system for understanding the oxidative aging of ambient aerosols, *Atmos. Chem. Phys.*, 9, 3209–3222, doi:10.5194/acp-9-3209-2009, 2009.
- Sun, Y., Zhang, Q., Macdonald, A. M., Hayden, K., Li, S. M., Liggio, J., Liu, P. S. K., Anlauf, K. G., Leitch, W. R., Steffen, A., Cubison, M., Worsnop, D. R., van Donkelaar, A., and Martin, R. V.: Size-resolved aerosol chemistry on Whistler Mountain, Canada with a high-resolution aerosol mass spectrometer during INTEX-B, *Atmos. Chem. Phys.*, 9, 3095–3111, doi:10.5194/acp-9-3095-2009, 2009.
- Surratt, J. D., Murphy, S. M., Kroll, J. H., Ng, N. L., Hildebrandt, L., Sorooshian, A., Szmigielski, R., Vermeylen, R., Maenhaut, W., Claeys, M., Flagan, R. C., and Seinfeld, J. H.: Chemical composition of secondary organic aerosol formed from the photooxidation of isoprene, *J. Phys. Chem. A*, 110, 9665–9690, doi:10.1021/Jp061734m, 2006.
- Surratt, J. D., Lewandowski, M., Offenberg, J. H., Jaoui, M., Kleindienst, T. E., Edney, E. O., and Seinfeld, J. H.: Effect of acidity on secondary organic aerosol formation from isoprene, *Environ. Sci. Technol.*, 41, 5363–5369, doi:10.1021/Es0704176, 2007.
- Surratt, J. D., Gómez-González, Y., Chan, A. W. H., Vermeylen, R., Shahgholi, M., Kleindienst, T. E., Edney, E. O., Offenberg, J. H., Lewandowski, M., Jaoui, M., Maenhaut, W., Claeys, M., Flagan, R. C., and Seinfeld, J. H.: Organosulfate formation in biogenic secondary organic aerosol, *J. Phys. Chem. A*, 112, 8345–8378, doi:10.1021/jp802310p, 2008.
- Surratt, J. D., Chan, A. W. H., Eddingsaas, N. C., Chan, M. N., Loza, C. L., Kwan, A. J.,



- Hersey, S. P., Flagan, R. C., Wennberg, P. O., and Seinfeld, J. H.: Reactive intermediates revealed in secondary organic aerosol formation from isoprene, *Proc. Natl. Acad. Sci.*, 107(15), 6640–6645, doi:10.1073/pnas.0911114107, 2010.
- Szmigielski, R., Surratt, J. D., Vermeylen, R., Szmigielska, K., Kroll, J. H., Ng, N. L., Murphy, S. M., Sorooshian, A., Seinfeld, J. H., and Claeys, M.: Characterization of 2-methylglyceric acid oligomers in secondary organic aerosol formed from the photooxidation of isoprene using trimethylsilylation and gas chromatography/ion trap mass spectrometry, *J. Mass Spectrom.*, 42, 101–116, doi:10.1002/Jms.1146, 2007.
- Takegawa, N., Miyakawa, T., Kawamura, K., and Kondo, Y.: Contribution of selected dicarboxylic and omega-oxocarboxylic acids in ambient aerosol to the  $m/z$  44 signal of an aerodyne aerosol mass spectrometer, *Aerosol Sci. Tech.*, 41, 418–437, doi:10.1080/02786820701203215, 2007.
- Tolocka, M. P., Heaton, K. J., Dreyfus, M. A., Wang, S. Y., Zordan, C. A., Saul, T. D., and Johnston, M. V.: Chemistry of particle inception and growth during  $\alpha$ -pinene ozonolysis, *Environ. Sci. Technol.*, 40, 1843–1848, doi:10.1021/Es051926f, 2006.
- Ulbrich, I. M., Canagaratna, M. R., Zhang, Q., Worsnop, D. R., and Jimenez, J. L.: Interpretation of organic components from Positive Matrix Factorization of aerosol mass spectrometric data, *Atmos. Chem. Phys.*, 9, 2891–2918, doi:10.5194/acp-9-2891-2009, 2009.
- Volkamer, R., Martini, F. S., Molina, L. T., Salcedo, D., Jimenez, J. L., and Molina, M. J.: A missing sink for gas-phase glyoxal in Mexico City: formation of secondary organic aerosol, *Geophys. Res. Lett.*, 34, L13805, doi:10.1029/2007gl030752, 2007.
- Volkamer, R., Ziemann, P. J., and Molina, M. J.: Secondary Organic Aerosol Formation from Acetylene ( $C_2H_2$ ): seed effect on SOA yields due to organic photochemistry in the aerosol aqueous phase, *Atmos. Chem. Phys.*, 9, 1907–1928, doi:10.5194/acp-9-1907-2009, 2009.
- Walser, M. L., Desyaterik, Y., Laskin, J., Laskin, A., and Nizkorodov, S. A.: High-resolution mass

- spectrometric analysis of secondary organic aerosol produced by ozonation of limonene, *Phys. Chem. Chem. Phys.*, 10, 1009–1022, doi:10.1039/B712620d, 2008.
- Wang, W., Kourtchev, I., Graham, B., Cafmeyer, J., Maenhaut, W., and Claeys, M.: Characterization of oxygenated derivatives of isoprene related to 2-methyltetrols in Amazonian aerosols using trimethylsilylation and gas chromatography/ion trap mass spectrometry, *Rapid Commun. Mass Sp.*, 19, 1343–1351, doi:10.1002/Rcm.1940, 2005.
- Whipple, E. B.: Structure of glyoxal in water, *J. Am. Chem. Soc.*, 92, 7183, doi:10.1021/ja00727a027, 1970.
- Yu, J. Z., Cocker, D. R., Griffin, R. J., Flagan, R. C., and Seinfeld, J. H.: Gas-phase ozone oxidation of monoterpenes: gaseous and particulate products, *J. Atmos. Chem.*, 34, 207–258, doi:10.1023/A:1006254930583, 1999.
- Zhang, Q., Alfarra, M. R., Worsnop, D. R., Allan, J. D., Coe, H., Canagaratna, M. R., and Jimenez, J. L.: Deconvolution and quantification of hydrocarbon-like and oxygenated organic aerosols based on aerosol mass spectrometry, *Environ. Sci. Technol.*, 39, 4938–4952, doi:10.1021/Es048568l, 2005a.
- Zhang, Q., Worsnop, D. R., Canagaratna, M. R., and Jimenez, J. L.: Hydrocarbon-like and oxygenated organic aerosols in Pittsburgh: insights into sources and processes of organic aerosols, *Atmos. Chem. Phys.*, 5, 3289–3311, doi:10.5194/acp-5-3289-2005, 2005b.
- Zhang, Q., Jimenez, J. L., Canagaratna, M. R., Allan, J. D., Coe, H., Ulbrich, I., Alfarra, M. R., Takami, A., Middlebrook, A. M., Sun, Y. L., Dzepina, K., Dunlea, E., Docherty, K., DeCarlo, P. F., Salcedo, D., Onasch, T., Jayne, J. T., Miyoshi, T., Shimojo, A., Hatakeyama, S., Takegawa, N., Kondo, Y., Schneider, J., Drewnick, F., Borrmann, S., Weimer, S., Demerjian, K., Williams, P., Bower, K., Bahreini, R., Cottrell, L., Griffin, R. J., Rautiainen, J., Sun, J. Y., Zhang, Y. M., and Worsnop, D. R.: Ubiquity and dominance of oxygenated species in organic aerosols in anthropogenically-influenced Northern Hemisphere midlatitudes, *Geophys. Res. Lett.*, 34, L13801, doi:10.1029/2007gl029979, 2007.

Table 3.1: Experimental conditions and results

Expt.#	VOC System	Experiment Type	RH (%)	[NO] <sub>0</sub> (ppb)	[NO <sub>2</sub> ] <sub>0</sub> (ppb)	VOC Reacted (ppb)	Seed Vol. (μm <sup>3</sup> cm <sup>-3</sup> )	ΔM <sub>0</sub> (Max) <sup>d</sup> (μg m <sup>-3</sup> )
1	glyoxal uptake	humid	67	<det <sup>a</sup>	<5	131 <sup>b</sup>	84	31.80
2	glyoxal uptake	humid	60	<det <sup>a</sup>	<det <sup>a</sup>	182 <sup>b</sup>	87	68.30
3	glyoxal uptake	humid	70	<det <sup>a</sup>	<det <sup>a</sup>	NA	NA	NA
4	α-pinene+O <sub>3</sub>	no H <sub>2</sub> O <sub>2</sub> , dry	5.4	<det <sup>a</sup>	<det <sup>a</sup>	50 <sup>c</sup>	12.45	56.84
5	α-pinene+O <sub>3</sub>	no H <sub>2</sub> O <sub>2</sub> , humid	66	<det <sup>a</sup>	<det <sup>a</sup>	50 <sup>c</sup>	20.00	83.30
6	α-pinene+O <sub>3</sub>	H <sub>2</sub> O <sub>2</sub> , dry	7.2	<det <sup>a</sup>	<det <sup>a</sup>	50 <sup>c</sup>	11.59	121.00
7	α-pinene+O <sub>3</sub>	H <sub>2</sub> O <sub>2</sub> , humid	72.3	<det <sup>a</sup>	<det <sup>a</sup>	50 <sup>c</sup>	27.38	183.22
8	isoprene+OH	low-NO <sub>x</sub>	5.2	<det <sup>a</sup>	<det <sup>a</sup>	49	16.23	3.71
9	isoprene+OH	low-NO <sub>x</sub>	5.3	<det <sup>a</sup>	<det <sup>a</sup>	49	NA	7.00
10	isoprene+OH	lowNO <sub>x</sub>	<10	<det <sup>a</sup>	<det <sup>a</sup>	91	10.54	10.47
11	isoprene+OH	high-NO <sub>x</sub>	<10	518	374	81	11.00	1.35
12	isoprene+OH	high-NO <sub>x</sub>	<10	536	400	267	11.73	4.27
13	isoprene+OH	high-NO <sub>x</sub>	<10	591	434	286	13.80	11.83
14	toluene+OH	low-NO <sub>x</sub>	<10	<det <sup>a</sup>	<det <sup>a</sup>	112	10.86	141.45
15	toluene+OH	high-NO <sub>x</sub>	<10	583	423	136	9.32	50.26
16	<i>m</i> -xylene+OH	low-NO <sub>x</sub>	<10	<det <sup>a</sup>	<det <sup>a</sup>	114	9.78	190.40
17	<i>m</i> -xylene+OH	high-NO <sub>x</sub>	<10	501	538	200	9.34	52.04
18	naphthalene+OH	low-NO <sub>x</sub>	7.8	<det <sup>a</sup>	<det <sup>a</sup>	5 <sup>c</sup>	10.64	12.15
19	naphthalene+OH	low-NO <sub>x</sub>	13.9	<det <sup>a</sup>	<det <sup>a</sup>	12	24.52	44.91
20	naphthalene+OH	low-NO <sub>x</sub> , nucleation	8.1	<det <sup>a</sup>	<det <sup>a</sup>	15 <sup>c</sup>	0.00	47.17
21	naphthalene+OH	low-NO <sub>x</sub>	8.3	<det <sup>a</sup>	<det <sup>a</sup>	20 <sup>c</sup>	10.48	53.12
22	naphthalene+OH	low-NO <sub>x</sub>	9.9	<det <sup>a</sup>	<det <sup>a</sup>	63	12.98	201.75
23	naphthalene+OH	high-NO <sub>x</sub>	7.7	415	272	5 <sup>c</sup>	12.25	5.90
24	naphthalene+OH	high-NO <sub>x</sub>	6.3	431	370	25 <sup>c</sup>	12.82	39.02
25	naphthalene+OH	high-NO <sub>x</sub> , nucleation	<10	422	222	350 <sup>c</sup>	0.00	39.26
26	naphthalene+OH	high-NO <sub>x</sub>	5.9	401	166	40	14.67	75.43

<sup>a</sup> Below the detection limit of the measurement

<sup>b</sup> Equilibrium concentration

<sup>c</sup> Approximate initial concentration

<sup>d</sup> Mass loadings are calculated by multiplying the change in DMA volume by an estimated density. Estimated densities of glyoxal, α-pinene, isoprene, single-ringed aromatics, and naphthalene SOA were taken from Galloway et al. (2009); Bahreini et al. (2005); Kroll et al. (2006); Ng et al. (2007); Chan et al. (2009a), respectively.

**Table 3.2:** Elemental composition of each SOA system. Values represent the average ratio for each experiment at the time of maximum O/C. Uncertainty estimates reflect the measurement uncertainty as determined by Aiken et al. (2008).

VOC System	O/C (max)	H/C	N/C	OM/OC	
glyoxal uptake	1.13±0.35	1.54±0.15	0.01±0.0022	2.68±0.16	
$\alpha$ -pinene+O <sub>3</sub>	0.43±0.13	1.47±0.15	0.00±0	1.70±0.10	
isoprene+OH	0.61±0.19	1.55±0.16	0.02±0.0044	1.96±0.12	
	low-NO <sub>x</sub>	0.59±0.18	1.64±0.16	0.00±0	1.92±0.12
	high-NO <sub>x</sub>	0.62±0.19	1.46±0.15	0.04±0.0088	2.00±0.12
aromatics+OH	0.68±0.21	1.44±0.14	0.04±0.0088	2.07±0.12	
	<i>m</i> -xylene, high-NO <sub>x</sub>	0.66±0.20	1.48±0.15	0.08±0.017	2.09±0.13
	<i>m</i> -xylene, low-NO <sub>x</sub>	0.60±0.19	1.54±0.15	0.00±0	1.93±0.12
	toluene, high-NO <sub>x</sub>	0.72±0.22	1.38±0.14	0.07±0.14	2.15±0.13
	toluene, low-NO <sub>x</sub>	0.74±0.23	1.39±0.14	0.00±0	2.10±0.13
naphthalene+OH	0.62±0.19	0.89±0.09	0.02±0.0044	1.93±0.12	
	low-NO <sub>x</sub>	0.66±0.20	0.88±0.09	0.00±0	1.96±0.12
	high-NO <sub>x</sub>	0.57±0.18	0.90±0.09	0.04±0.0088	1.89±0.11

**Table 3.3:** O/C ratios of various laboratory SOA systems

System	O/C Ratio	Method	Reference
glyoxal uptake	1.13	HR-ToF-AMS	This Study
$\alpha$ -pinene+O <sub>3</sub>	0.30–0.43	HR-ToF-AMS	This Study
	0.29–0.45	HR-ToF-AMS	Shilling et al. (2009)
	0.27	HR-ToF-AMS	Aiken et al. (2008)
	0.4–0.6	ESI-FTICR-MS	Reinhardt et al. (2007)
	0.37–0.4	NAMS	Tolocka et al. (2006)
$\beta$ -pinene+O <sub>3</sub>	0.45	NAMS	Heaton et al. (2007)
$\Delta^3$ -carene+O <sub>3</sub>	0.43	NAMS	Heaton et al. (2007)
limonene+O <sub>3</sub>	0.45	NAMS	Heaton et al. (2007)
	0.43–0.50	ESI-MS (Orbitrap)	Walser et al. (2008)
sabinene+O <sub>3</sub>	0.37	NAMS	Heaton et al. (2007)
$\alpha$ -pinene+NO <sub>x</sub>	0.39	HR-ToF-AMS	Aiken et al. (2008)
isoprene+OH	0.41	HR-ToF-AMS	Aiken et al. (2008)
	0.50–0.62	HR-ToF-AMS	This Study
toluene+OH	0.43	HR-ToF-AMS	Aiken et al. (2008)
	0.50–0.74	HR-ToF-AMS	This Study
<i>m</i> -xylene+OH	0.50–0.66	HR-ToF-AMS	This Study
naphthalene+OH	0.30–0.74	HR-ToF-AMS	This Study

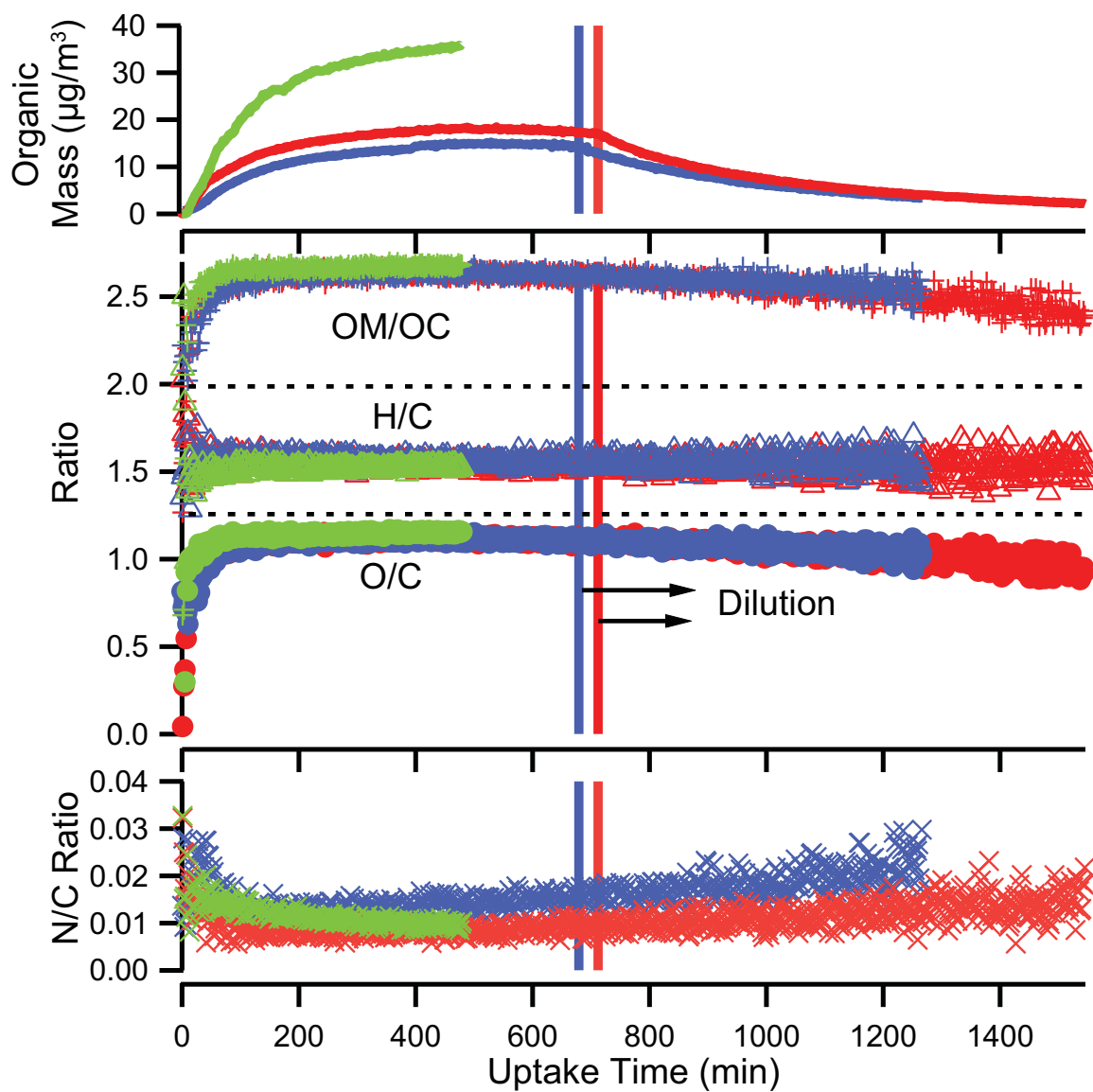


**Figure 3.1:** Experimental profile of AMS organic mass (not corrected for collection efficiency), elemental ratios and OM/OC for glyoxal uptake experiments. Experiment 1 is in blue, 2 in red and 3 in green. Dotted lines are provided to visually separate different ratios.

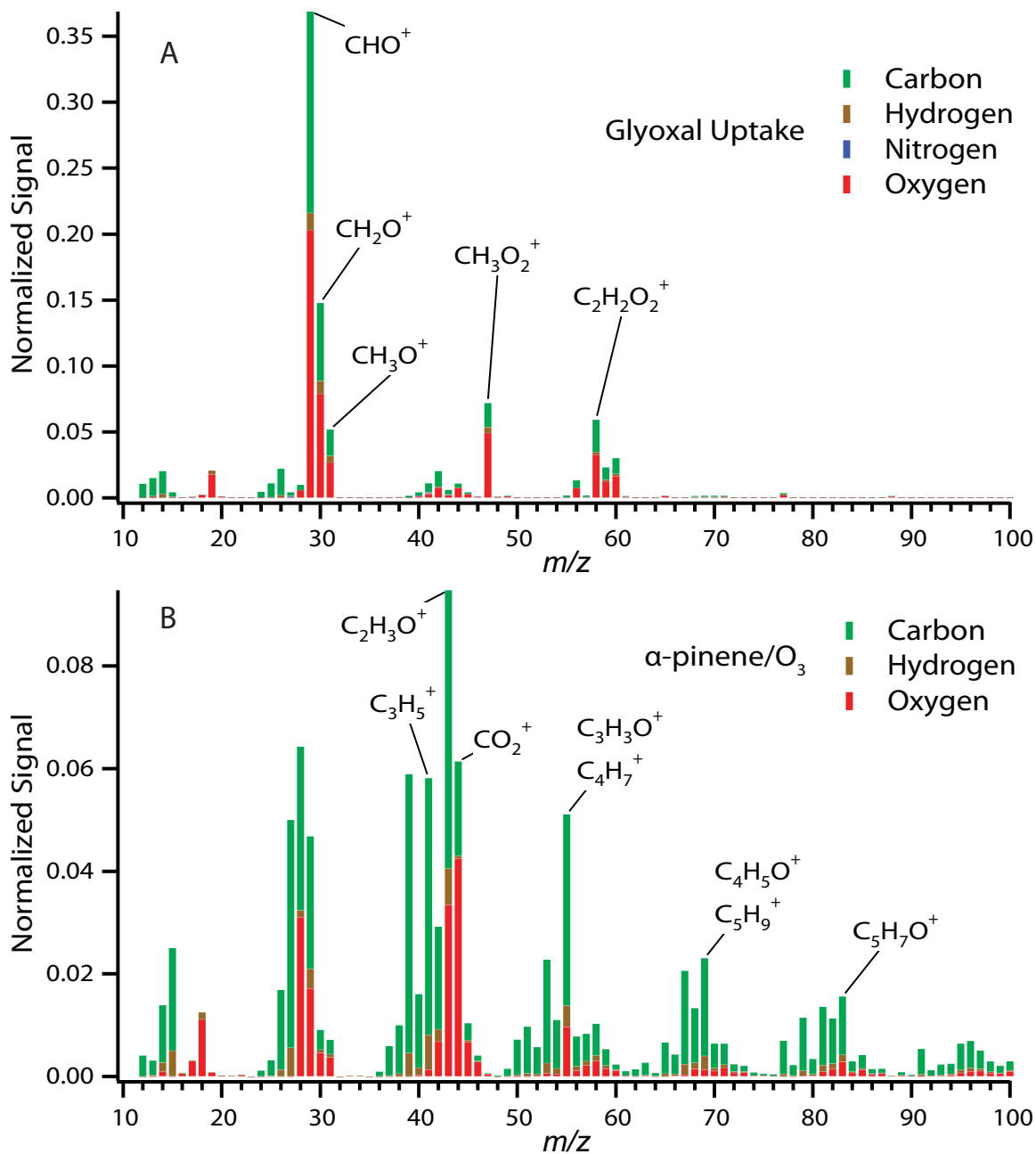


**Figure 3.2:** High-resolution mass spectra of glyoxal (A) and  $\alpha$ -pinene (B) SOA with elemental contributions to each mass-to-charge ratio shown. Spectra are taken at the peak of SOA growth.

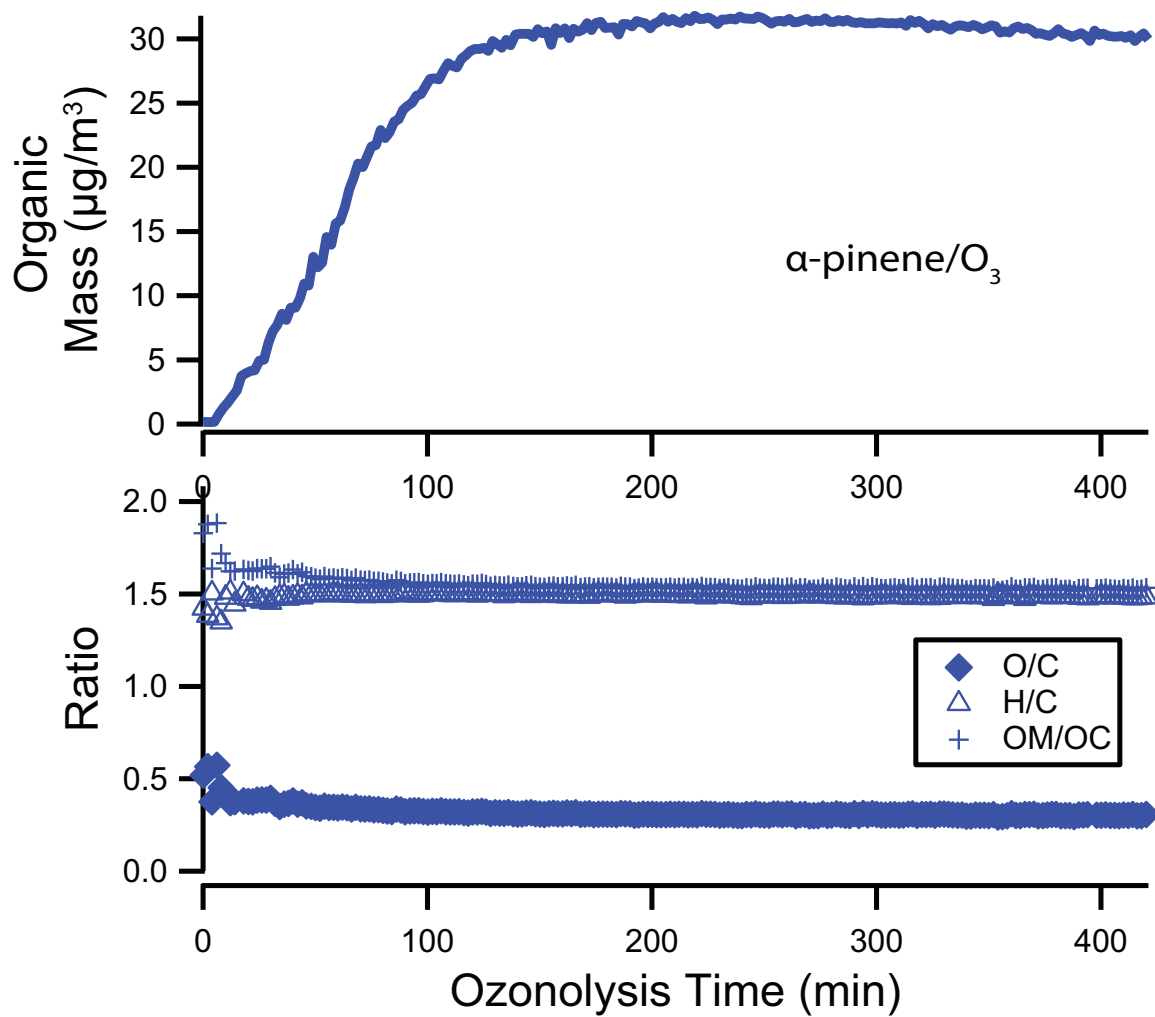


**Figure 3.3:** AMS organic mass (not corrected for collection efficiency) O/C, H/C and OM/OC ratios for a typical  $\alpha$ -pinene ozonolysis experiment (Experiment 4).



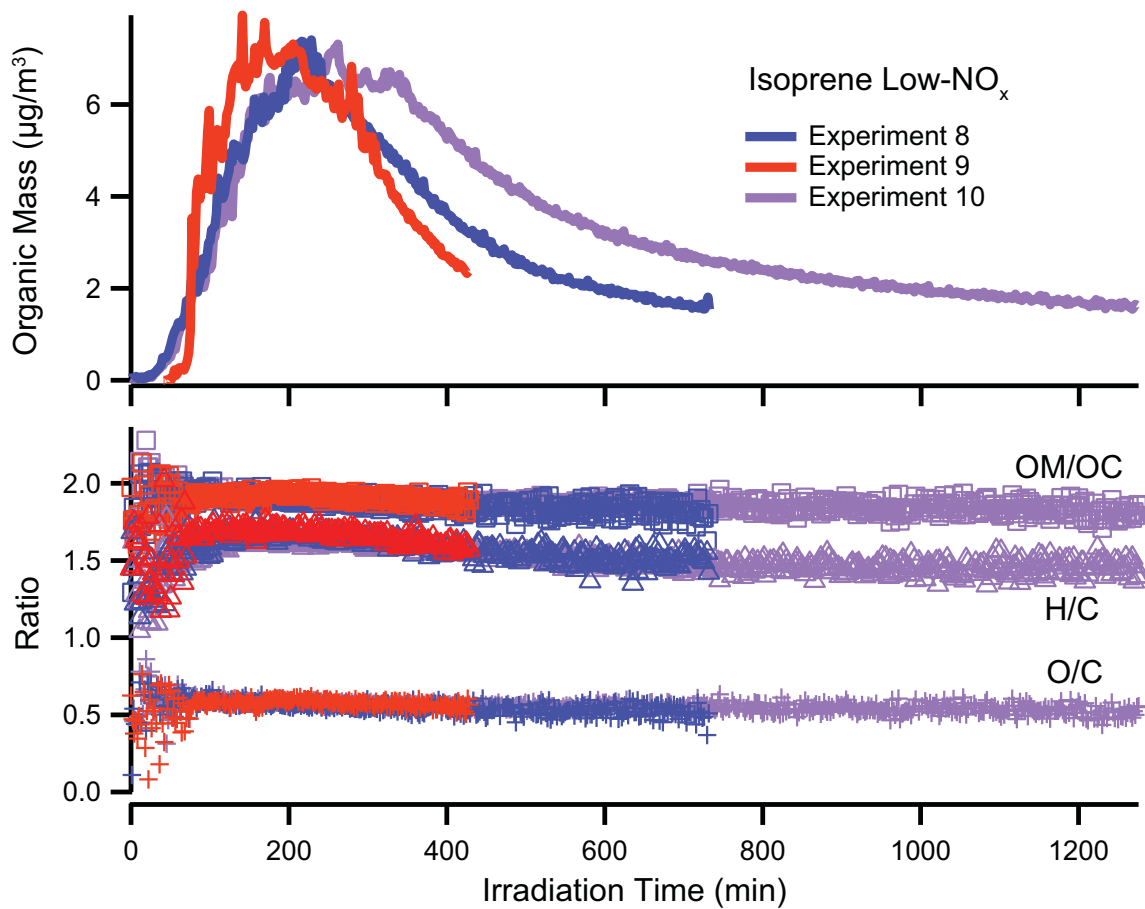


**Figure 3.4:** Top Panel: AMS organic mass loading (not corrected for collection efficiency) for isoprene low- $\text{NO}_x$  experiments. Bottom Panel: O/C, H/C and OM/OC ratios of isoprene SOA formed under low- $\text{NO}_x$  conditions. Experiment 8 is in blue, 9 in red, and 10 in purple.

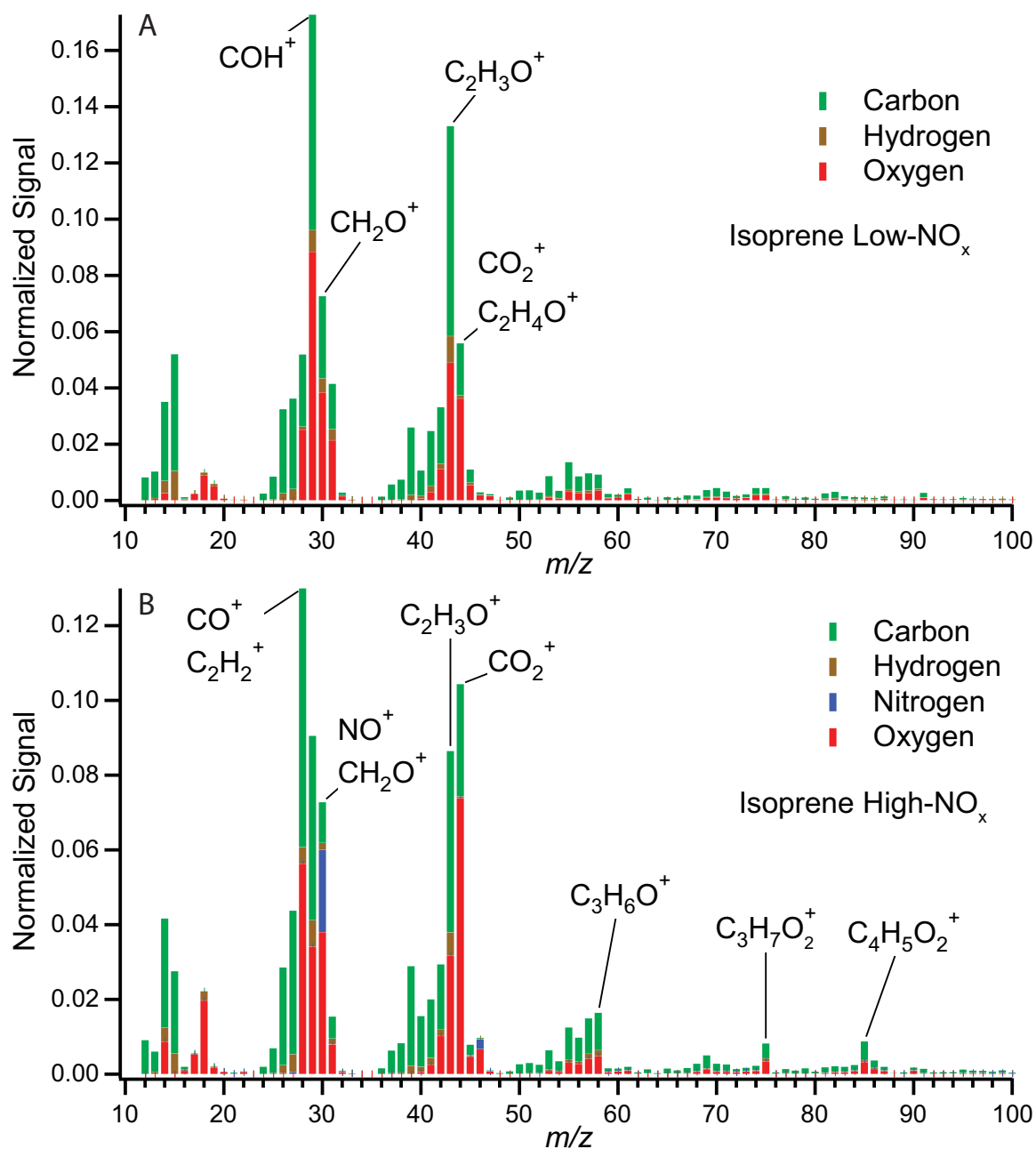


**Figure 3.5:** High-resolution mass spectra of isoprene SOA formed under low- $\text{NO}_x$  (A) and high- $\text{NO}_x$  (B) conditions with elemental contributions to each mass-to-charge ratio shown. Spectra are taken at the peak of SOA growth.

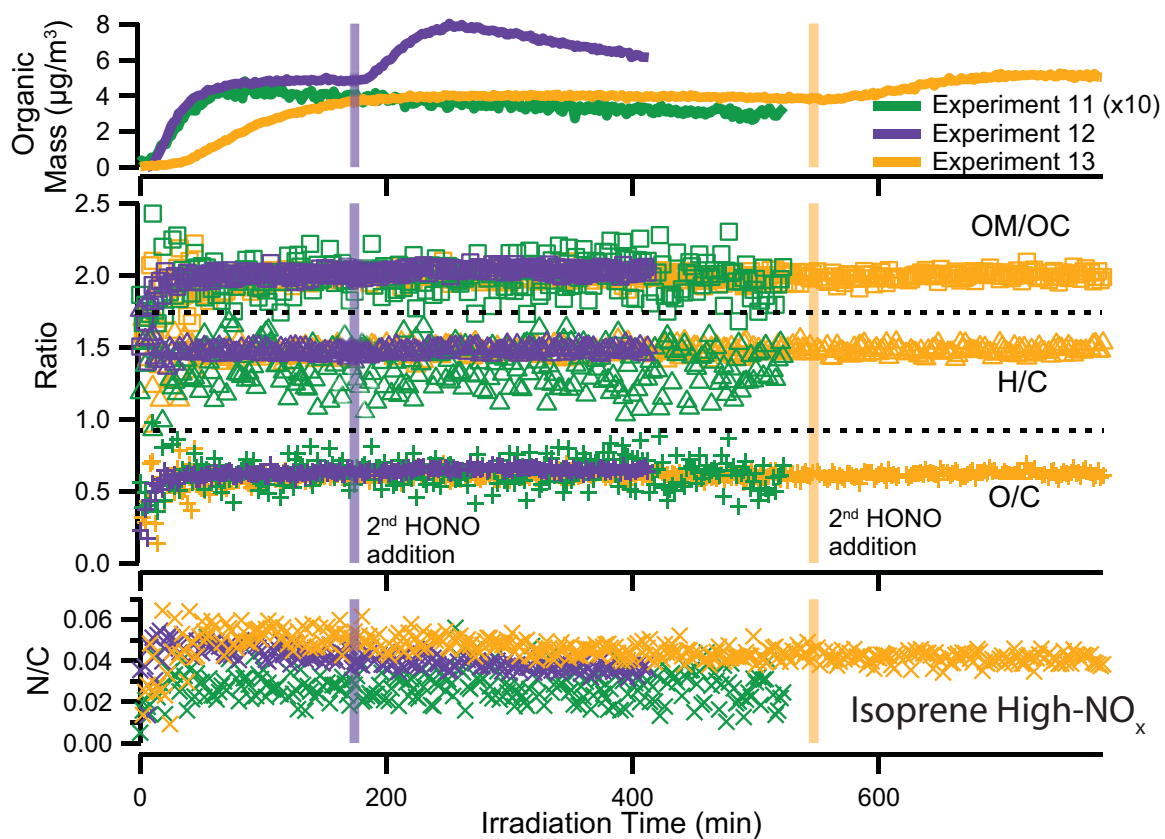


**Figure 3.6:** AMS organic mass (not corrected for collection efficiency), elemental ratios, and OM/OC for isoprene high-NO<sub>x</sub> experiments. Experiment 11 is in green, 12 in purple, and 13 in orange. Dotted lines are provided to visually separate different ratios.

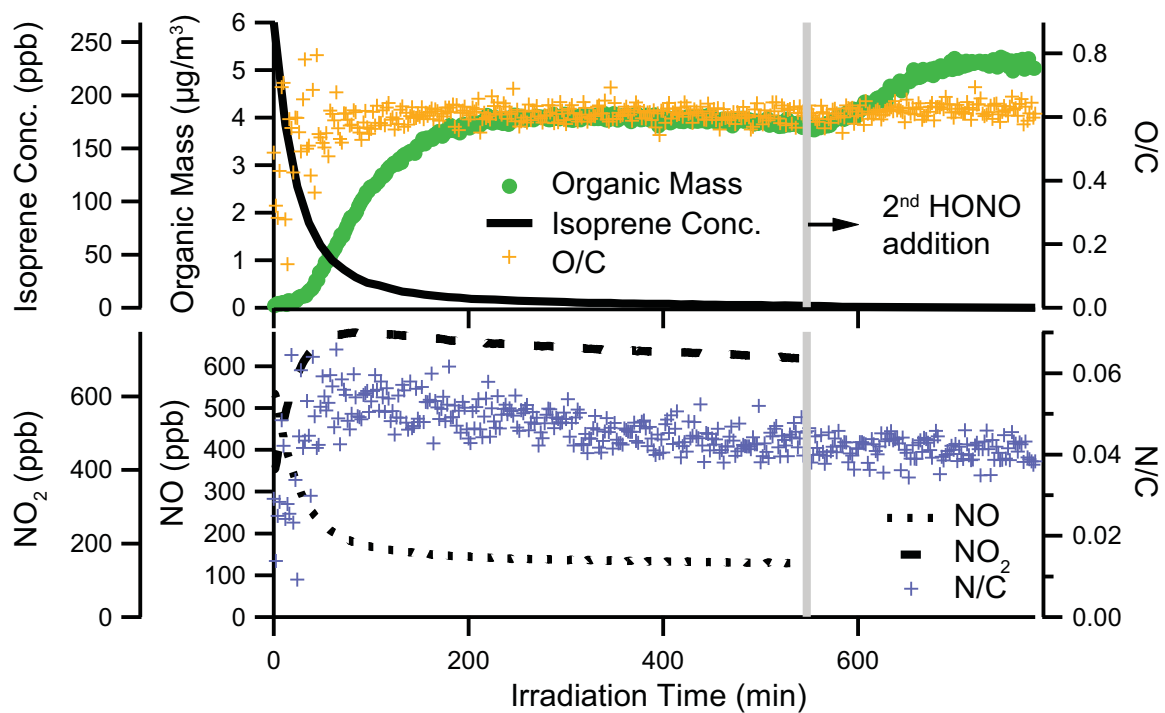


**Figure 3.7:** Top panel: Time dependence of AMS organic mass (not corrected for collection efficiency), O/C ratio, and isoprene concentration for Experiment 12. Bottom panel: Time dependence of NO, NO<sub>2</sub>, and N/C ratio for Experiment 12. A second addition of HONO at about 550 min after the start of the experiment is marked.

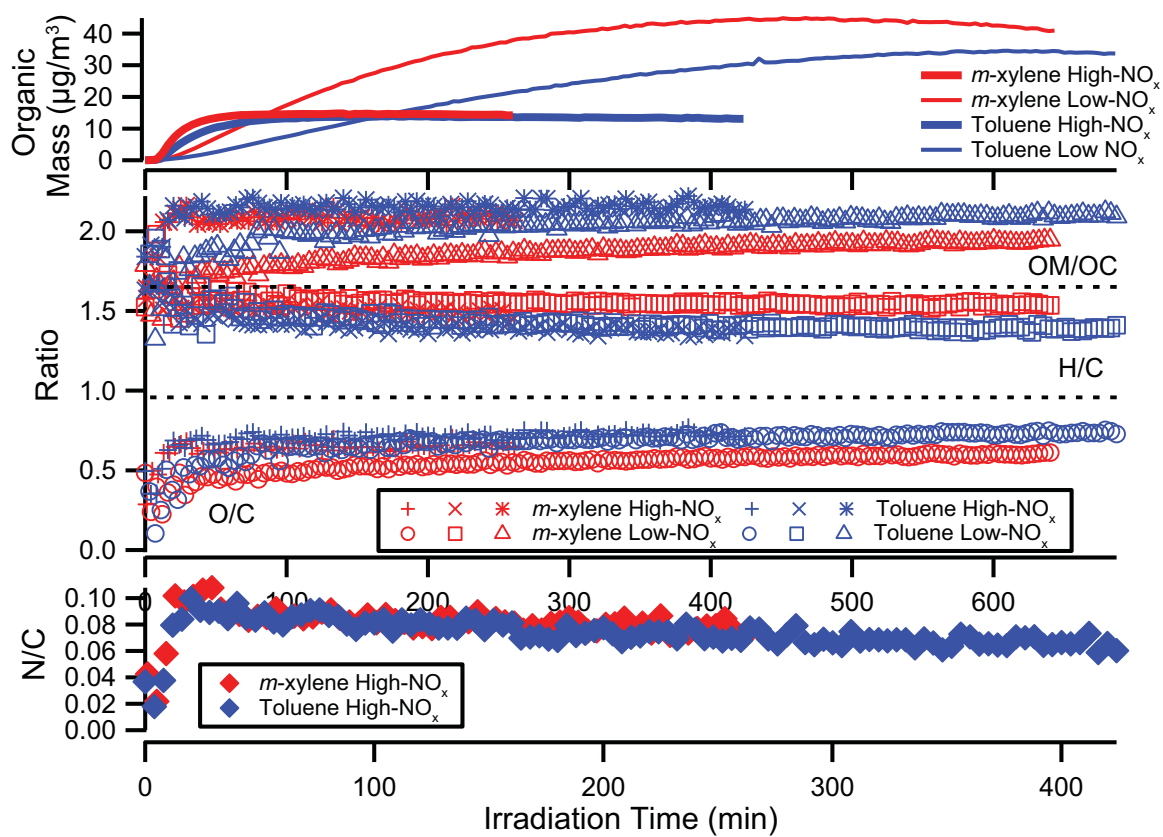


**Figure 3.8:** AMS organic mass (not corrected for collection efficiency), elemental ratios, and OM/OC for single-ring aromatic experiments. Dotted lines are provided to visually separate different ratios.

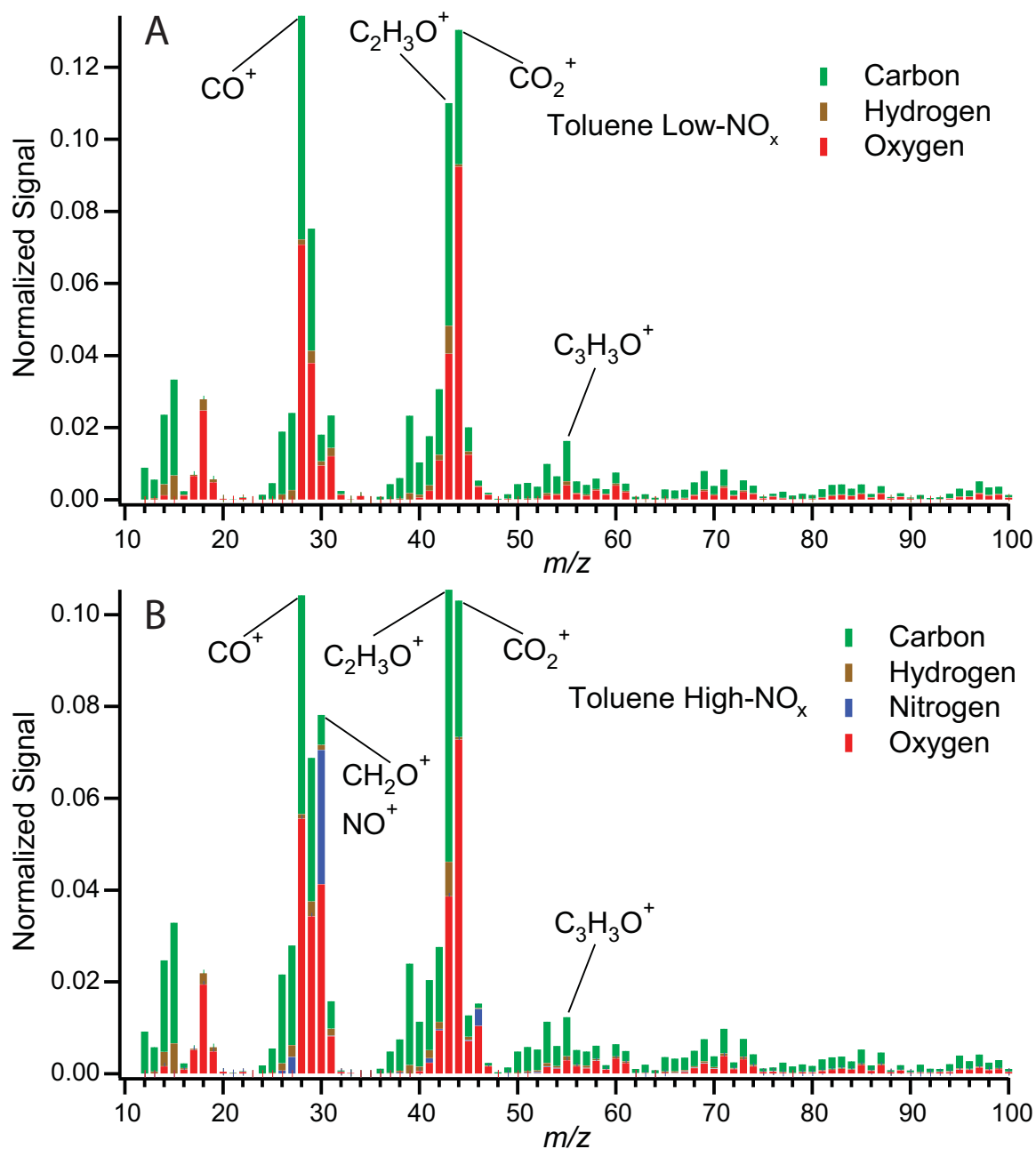


**Figure 3.9:** High-resolution mass spectra of toluene SOA formed under low-NO<sub>x</sub> (A) and high-NO<sub>x</sub> (B) conditions with elemental contributions to each mass-to-charge ratio shown. Spectra are taken at the peak of SOA growth.

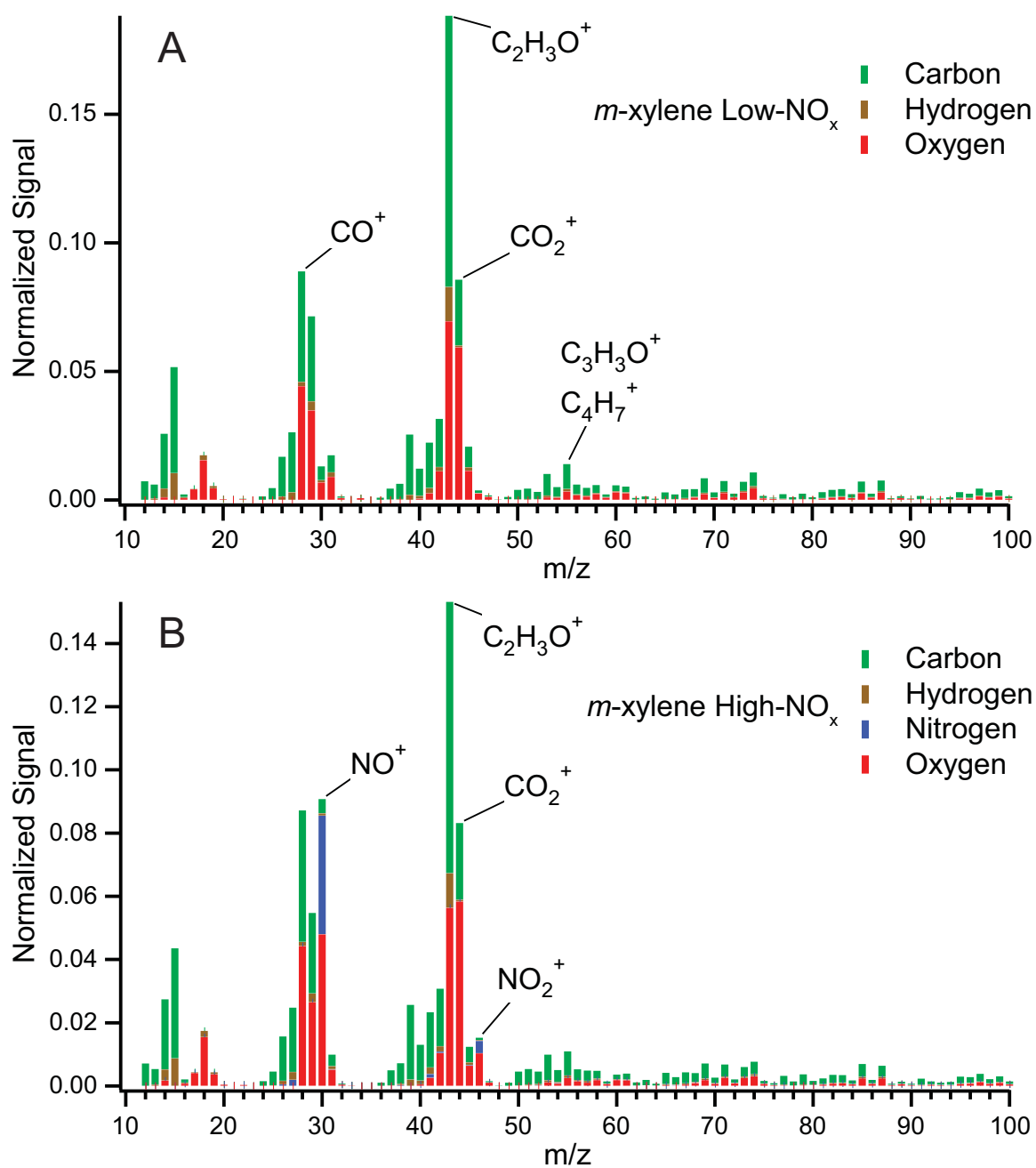


**Figure 3.10:** High-resolution mass spectra of  $m$ -xylene SOA formed under low- $\text{NO}_x$  (A) and high- $\text{NO}_x$  (B) conditions with elemental contributions to each mass-to-charge ratio shown. Spectra were taken at the peak of SOA growth.

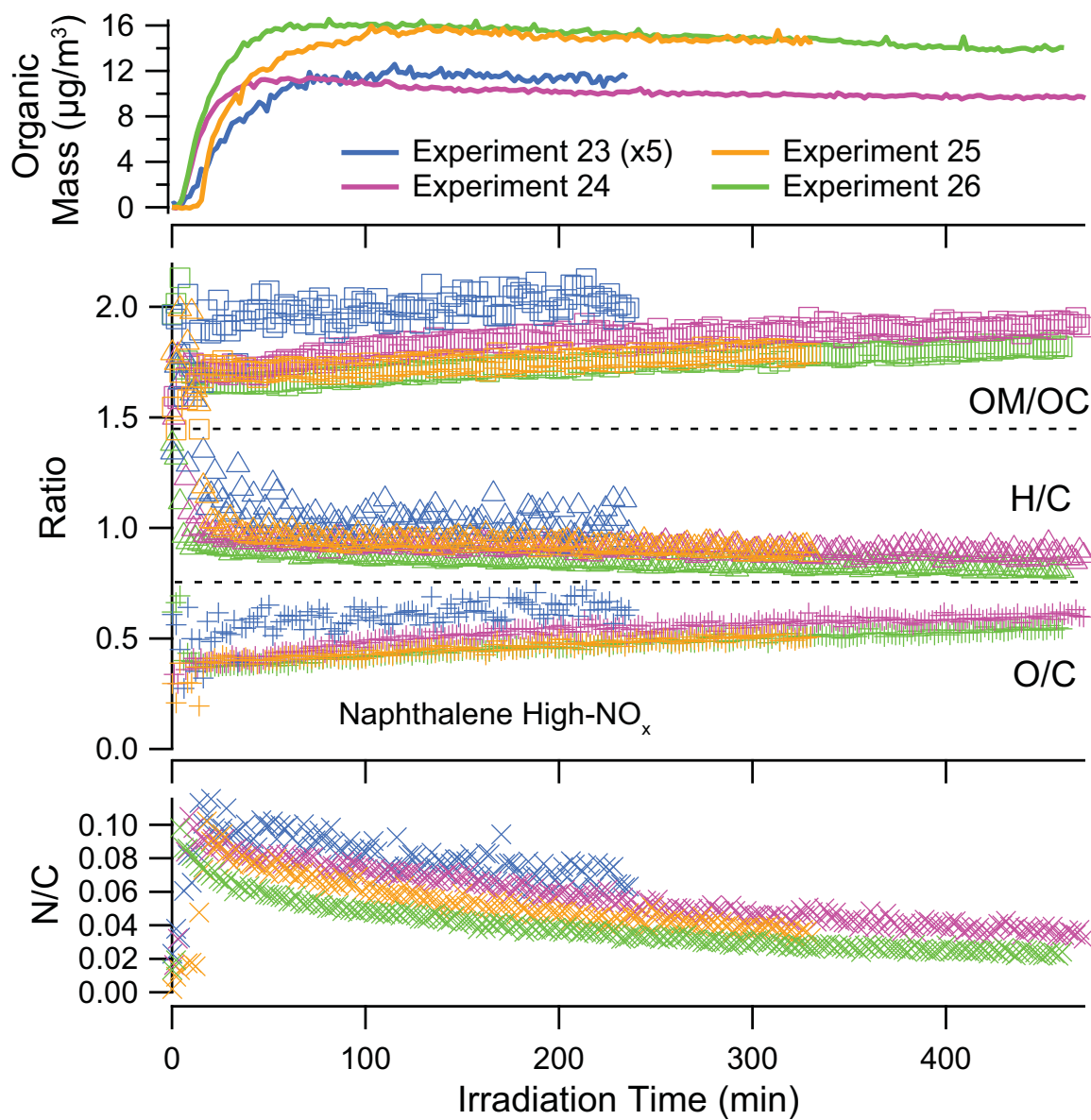


**Figure 3.11:** Organic mass (not corrected for collection efficiency), elemental ratios, and OM/OC for naphthalene high-NO<sub>x</sub> experiments. Experiment 23 is in blue, 24 in pink, 25 in orange and 26 in green. Dotted lines are provided to visually separate different ratios.



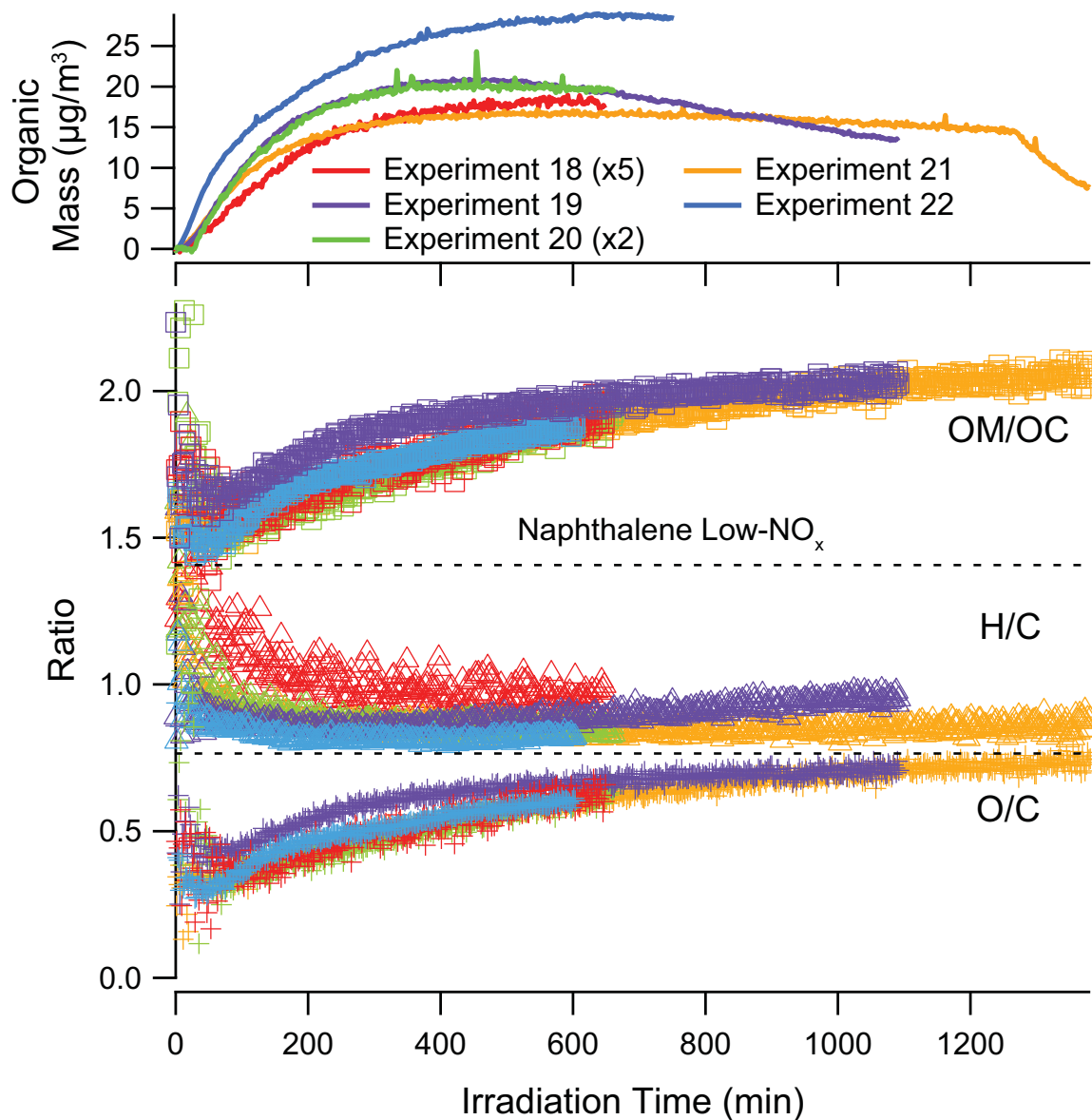


**Figure 3.12:** AMS organic mass (not corrected for collection efficiency), elemental ratios, and OM/OC for naphthalene low- $\text{NO}_x$  experiments. Experiment 18 is in red, 19 in purple, 20 in green, 21 in orange, and 22 in blue. Dotted lines are provided to visually separate different ratios.

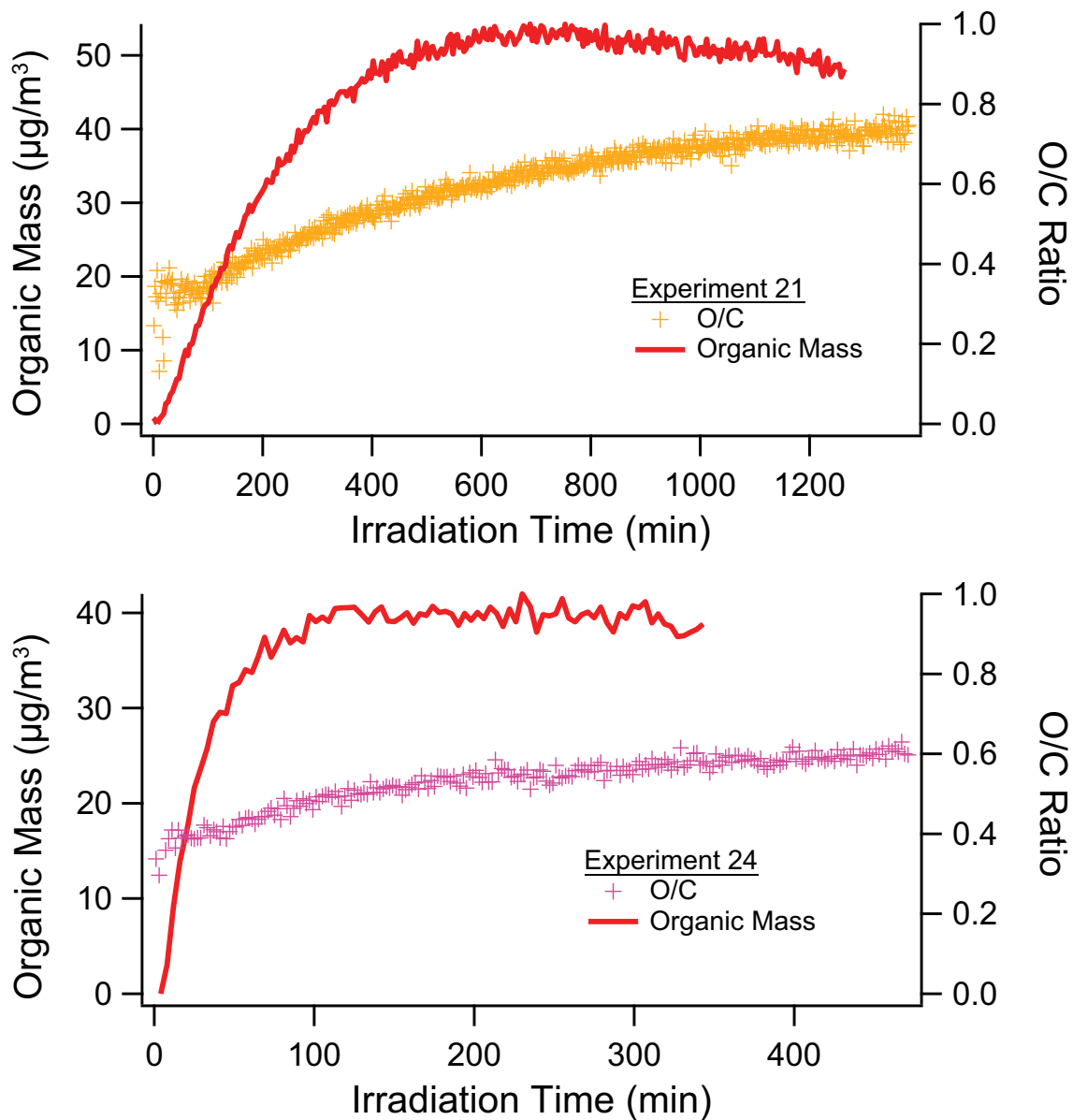


**Figure 3.13:** Organic mass and O/C ratio as a function of time for typical naphthalene photooxidation experiments under low-NO<sub>x</sub> (Experiment 21, Top) and high-NO<sub>x</sub> (Experiment 24, Bottom) conditions. Mass loadings are calculated by multiplying the change in DMA volume by an estimated density (Chan et al., 2009a).

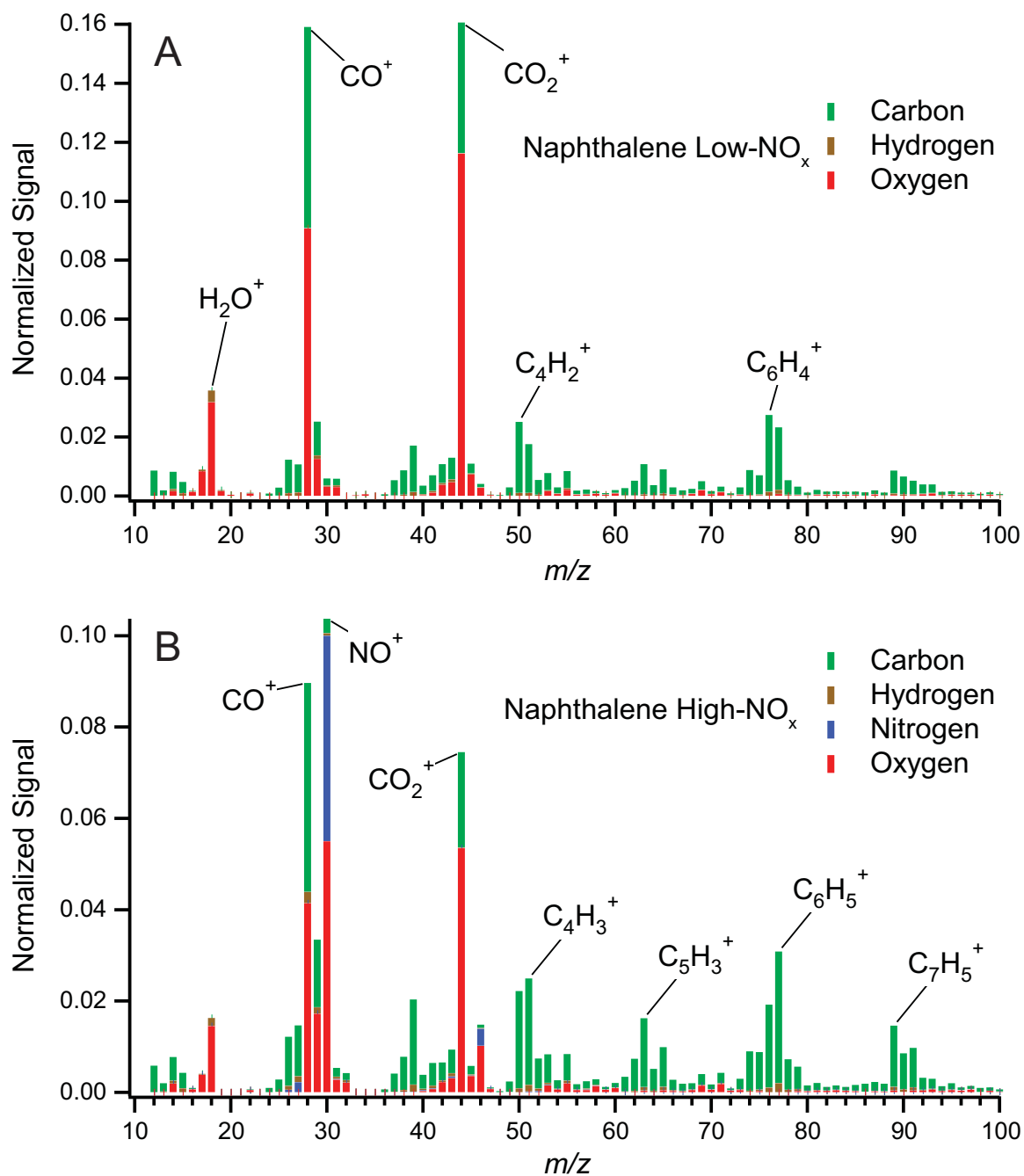


**Figure 3.14:** High-resolution mass spectra of naphthalene-SOA formed under low-NO<sub>x</sub> (A) and high-NO<sub>x</sub> (B) conditions with elemental contributions to each mass-to-charge ratio shown. Spectra were taken at the peak of SOA growth.

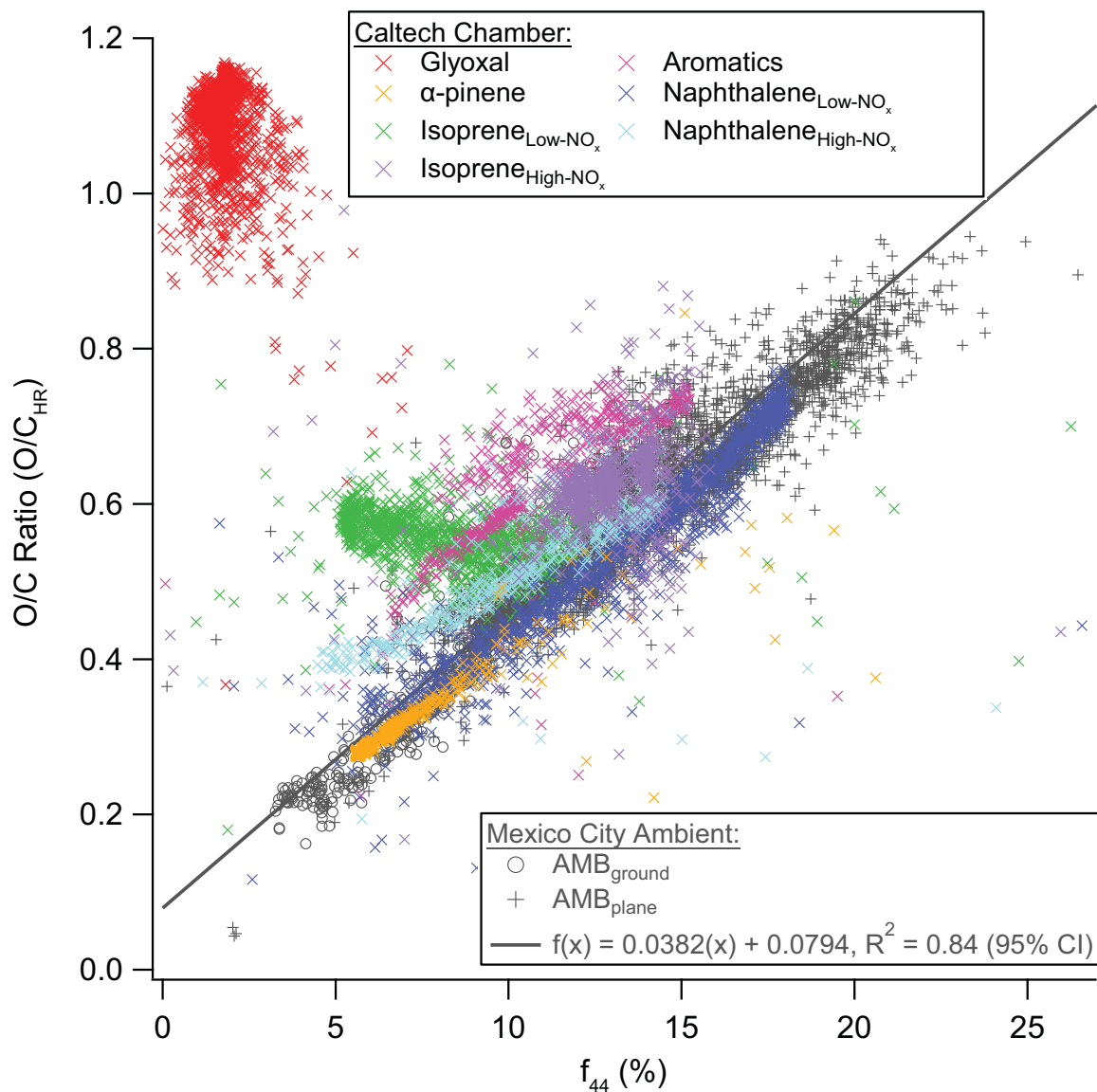


**Figure 3.15:**  $O/C_{HR}$  vs.  $f_{44}$  for ambient Mexico City OA (Aiken et al., 2008, Fig. 4) and chamber OA. The solid line represents the correlation derived from ambient data. Experiments 19, 22, and 26 are not shown for simplicity.

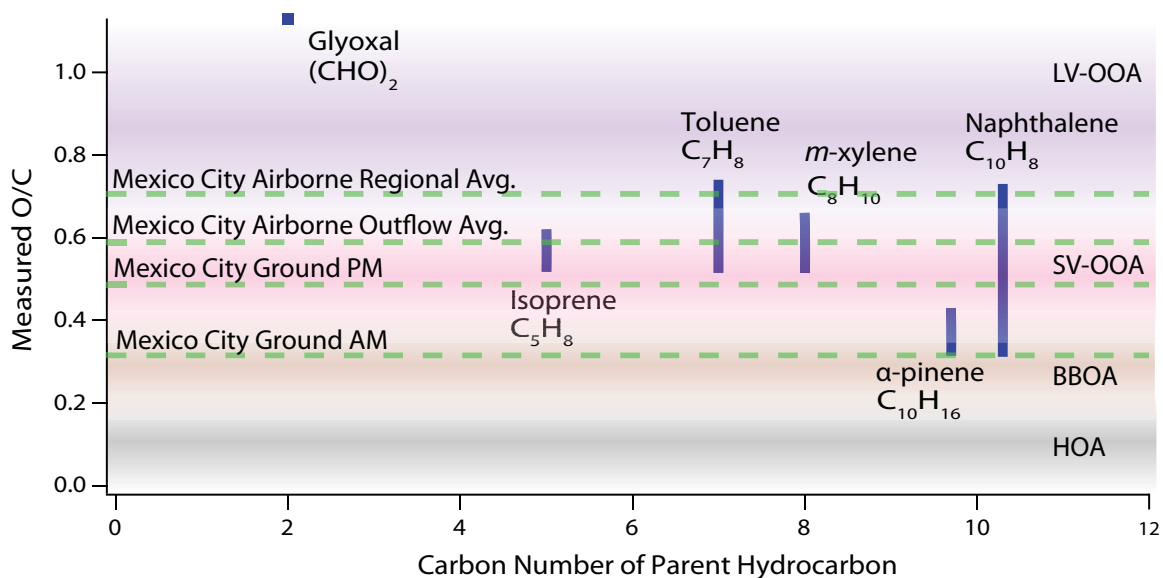


**Figure 3.16:** O/C ratios for ambient Mexico City organic aerosol (Aiken et al., 2008), typical AMS components derived from positive matrix factorization (PMF) (Aiken et al., 2008, 2009; Ulbrich et al., 2009; Zhang et al., 2005b), and chamber SOA as a function of precursor carbon number. Ranges for each precursor represent the total O/C range achieved in the experiments surveyed here. Shaded regions represent the typically prescribed O/C ranges for AMS PMF components and can vary depending on the ambient data set.

## Chapter 4

# Elemental Composition and Oxidation of Chamber Organic Aerosol\*

### 4.1 Abstract

Recently, graphical representations of aerosol mass spectrometer (AMS) spectra and elemental composition have been developed to explain the oxidative and aging processes of secondary organic aerosol (SOA). It has been shown previously that oxygenated organic aerosol (OOA) components from ambient and laboratory data fall within a triangular region in the  $f_{44}$  vs.  $f_{43}$  space, where  $f_{44}$  and  $f_{43}$  are the ratios of the organic signal at  $m/z$  44 and 43 to the total organic signal, respectively; we refer to this model as the “triangle plot.” Alternatively, the Van Krevelen diagram has been used to describe the evolution of functional groups in SOA. In this study we investigate the variability of SOA formed in chamber experiments from twelve different precursors in both “triangle plot” and Van Krevelen domains. Spectral and elemental data from the high-resolution Aerodyne aerosol mass spectrometer are compared to offline species identification analysis and FTIR filter analysis to better understand the changes in functional and elemental composition inherent in SOA formation and aging. We find that SOA formed under high- and low- $\text{NO}_x$  conditions occupy similar areas in the “triangle plot” and Van Krevelen diagram and that SOA generated from already

---

\*Reproduced with permission from “Elemental composition and oxidation of chamber organic aerosol” by P. S. Chhabra, N. L. Ng, M. R. Canagaratna, A. L. Corrigan, L. M. Russell, D. R. Worsnop, R. C. Flagan, and J. H. Seinfeld, *Atmospheric Chemistry and Physics Discussions*, 11, 10305-10342, doi:10.5194/acpd-11-10305-2011, Copyright 2011 by the Authors. CC Attribution 3.0 License.

oxidized precursors starts higher on the “triangle plot.” As SOA ages, it migrates toward the top of the triangle, suggesting higher organic acid content and decreased mass spectral variability. The most oxidized SOA come from the photooxidation of methoxyphenol precursors which yielded SOA O/C ratios near unity.  $\alpha$ -pinene ozonolysis and naphthalene photooxidation SOA systems have had the highest degree of mass closure in previous chemical characterization studies and also show the best agreement between AMS elemental composition measurements and elemental composition of identified species. In general, compared to their respective unsaturated SOA precursors, the elemental composition of chamber SOA follows a slope shallower than  $-1$  on the Van Krevelen diagram. From the spectra of SOA studied here, we are able to reproduce the triangular region originally constructed with ambient OOA components with chamber aerosol showing that SOA becomes more chemically similar as it ages. Ambient data in the middle of the triangle represent the ensemble average of many different SOA precursors, ages, and oxidative processes.

## 4.2 Introduction

Organic compounds comprise a significant fraction of ambient submicron aerosol mass (Zhang et al., 2007; Jimenez et al., 2009) with numerous sources and atmospheric processes contributing to their chemical complexity (Hallquist et al., 2009). Secondary organic aerosol (SOA) forms from the gas-phase oxidation of a number of anthropogenic and biogenic volatile organic compounds (VOCs) (Kroll and Seinfeld, 2008; Robinson et al., 2007; Lim et al., 2010; Donahue et al., 2009; Goldstein and Galbally, 2007; De Gouw and Jimenez, 2009). Although typically only a portion of the multitude of compounds present in SOA can be identified on a molecular level, on-line instruments like the Aerodyne Aerosol Mass Spectrometer (AMS) (Jayne et al., 2000) can provide bulk, chemical characterization in real-time.

Recently, two important methods using AMS data to characterize the chemical nature of OA have been proposed. Heald et al. (2010) applied the Van Krevelen diagram to the bulk elemental composition of ambient and laboratory OA formed under a wide range of reaction conditions. Previous investigations have used the Van Krevelen diagram to map individual masses identified

by high resolution electrospray ionization mass spectrometry (ESI-MS), but not for OA as a whole (Reinhardt et al., 2007; Walser et al., 2008; Bateman et al., 2009). Originally developed to describe the elemental composition of coal, the Van Krevelen diagram has axes of hydrogen to carbon (H/C) molar ratios and oxygen to carbon (O/C) molar ratios. Changes in functionality of OA are traced in this space along a line of a particular slope. For instance, when an aliphatic functionality is replaced by a carbonyl functionality, the resulting line on a Van Krevelen has a slope of  $-2$ . Substituting aliphatic to alcohol or peroxide functionality produces a line with a slope of zero. Addition of carboxylic acids or hydroxycarbonyls gives a  $-1$  slope. Hydration or condensation reactions follow a line with a slope of  $+2$ . Heald et al. (2010) found that bulk OA elemental ratios from both laboratory and ambient atmospheres occupy a tight range on the Van Krevelen diagram with a slope of  $-1$ , implying that OA aging involves, on average, the addition of carboxylic acids or equal amounts of alcohol and carbonyl functionalities.

Ng et al. (2010) used positive matrix factorization techniques (Zhang et al., 2005; Lanz et al., 2007; Ulbrich et al., 2009) and compiled the factor analysis for 43 Northern Hemisphere AMS datasets of OA. They found that at most sites AMS spectra can be separated into oxygenated OA (OOA) and hydrocarbon-like OA (HOA) components (Zhang et al., 2007). For many datasets, OOA was further subcategorized into low-volatility OOA (LV-OOA) and semi-volatile OOA (SV-OOA) (Jimenez et al., 2009). LV-OOA has been described as aged OOA, with spectra dominated by mass fragment  $\text{CO}_2^+$  at  $m/z$  44, and SV-OOA, described as “fresh” OOA with an intense signal at  $\text{C}_2\text{H}_3\text{O}^+$  at  $m/z$  43 as well. Mass fragment  $\text{CO}_2^+$  has been considered a marker ion for organic acids in OA, as it is known to form from the thermal decarboxylation of many different oxo-, di-, and polycarboxylic acids (Alfarra, 2004; Aiken et al., 2007; Takegawa et al., 2007; Duplissy et al., 2011). Fragment ion  $\text{C}_2\text{H}_3\text{O}^+$ , conversely, has been hypothesized to form from non-acid oxygen-containing organic compounds. Since  $m/z$  43 and 44 are the dominant ions in SV- and LV-OOA spectra and represent different functionalities, Ng et al. (2010) plotted  $f_{44}$  vs.  $f_{43}$  for all OOA spectra from different sites, where  $f_{44}$  and  $f_{43}$  are the ratios of  $m/z$  44 and  $m/z$  43 to the total OA signal in the spectrum, respectively. Ng et al. (2010) found that the OOA components clustered into a



triangular region with wide variability across  $f_{43}$  at low values of  $f_{44}$  that narrows as  $f_{44}$  increases. As a consequence, LV-OOA data tend to group in the top half of the “triangle plot” and SV-OOA in the lower half. Ng et al. (2010) concluded that OOA components become more similar in terms of oxidation state with increasing photochemical age, regardless of source. The most oxidized spectra tend to resemble that of fulvic acid.

Chamber experiments have long been the gold standard to determine SOA formation mechanisms and to constrain the chemistry and yields of SOA. The studies of both Chhabra et al. (2010) and Ng et al. (2010) found, however, that SOA from chamber studies typically does not reach the degree of oxygenation of ambient LV-OOA. For example, Heald et al. (2010) presented data from Shilling et al. (2009), in which the most oxidized SOA from  $\alpha$ -pinene ozonolysis has an O/C of approximately 0.4, whereas SOA from the MILAGRO (Mexico City) campaign (Aiken et al., 2009) surpasses 0.6. Ng et al. (2010) noted that most laboratory chamber data fall into the lower half of the “triangle plot”, showing that laboratory OA is closer to SV-OOA than LV-OOA. Like SV-OOA, chamber SOA has high variability in  $f_{43}$ , likely a result of the variety of precursors, oxidants, and other experimental variables. In chamber investigations in which SOA is generated at total organic loadings higher than those of ambient OA, more volatile, less oxygenated species partition into the particle phase than would at lower aerosol loadings. Additionally, chamber experiments are typically carried out for less than  $\sim 24$  h, shorter than the atmospheric lifetime ( $\sim 1$  week) of ambient aerosol, and therefore not accessing further oxidation that might be occurring over this extended timescale. A comprehensive study by Chhabra et al. (2010) compared the elemental composition of five different chamber systems and found that single-ring aromatic- and naphthalene-derived SOA can reach O/C ratios upward of 0.7, approaching those of ambient measurements, and thus emphasizing the importance of OH exposure and precursor identity on SOA oxidation state.

In this study, we build on the previous investigation of Chhabra et al. (2010) by exploring the variability of chamber SOA in both Van Krevelen and “triangle plot” spaces. In addition to the systems studied in Chhabra et al. (2010) (glyoxal uptake,  $\alpha$ -pinene ozonolysis, isoprene photooxidation, single-ring aromatic photooxidation, and naphthalene photooxidation), we present high-resolution

time-of-flight AMS (HR-ToF-AMS) spectra and elemental composition of chamber SOA from  $\alpha$ -pinene photooxidation, methoxyphenol photooxidation, and unsaturated aldehyde photooxidation. Structures for each of the twelve precursors are shown in Fig. 4.1. We compare the elemental composition as measured by the AMS to molecular species identified by off-line methods for each SOA system as well as FTIR measurements of  $\alpha$ -pinene photooxidation and guaiacol photooxidation SOA. The goal of this work is to assess the extent to which SOA molecular and functional group composition analyses support the overall analysis of SOA formation and aging as represented in the Van Krevelen and “triangle plot” spaces.

## 4.3 Experimental Section

### 4.3.1 Chamber Operation

Chamber operation and experimental methods for glyoxal uptake,  $\alpha$ -pinene ozonolysis, single-ringed aromatic, isoprene, and naphthalene photooxidation experiments are described in Chhabra et al. (2010). Experimental methods for  $\alpha$ -pinene, methoxyphenol, and aldehyde photooxidation were nearly identical and are described in detail in Chan et al. (2010). In experiments in which methyl nitrite ( $\text{CH}_3\text{ONO}$ ) was used as the OH precursor,  $\text{CH}_3\text{ONO}$  was vaporized into an evacuated 500 mL glass bulb and introduced into the chamber with an air stream of  $5 \text{ L min}^{-1}$ . The mixing ratio of  $\text{CH}_3\text{ONO}$  injected was estimated to be 200-400 ppb, based on the vapor pressure in the glass bulb measured using a capacitance manometer (MKS). Experimental conditions for each system are summarized in Table 4.1. All experiments were performed in the Caltech dual  $28 \text{ m}^3$  Teflon laboratory chambers (Cocker et al., 2001; Keywood et al., 2004) over the period 2007–2010. A Differential Mobility Analyzer (DMA, TSI model 3081) coupled with a condensation nucleus counter (TSI model 3760) measured aerosol size distribution and number concentration. Temperature, relative humidity (RH), ozone ( $\text{O}_3$ ), NO, and  $\text{NO}_x$  were continuously monitored. For seeded experiments, ammonium sulfate seed particles were generated by atomization of a dilute aqueous ammonium sulfate solution using a constant rate atomizer.

### 4.3.2 High-Resolution Time-of-Flight Aerosol Mass Spectrometer

HR-ToF-AMS (Canagaratna et al., 2007; DeCarlo et al., 2006) spectra were analyzed as described in Chhabra et al. (2010). Briefly, in the mode of operation, the AMS was switched once every minute between the high-resolution “W-mode” and the lower resolution, higher sensitivity “V-mode”. The “V-mode” data were analyzed using a fragmentation table to separate sulfate, ammonium, and organic spectra and to time-trace specific mass-to-charge ratios (Allan et al., 2004). “W-mode” data were analyzed using a separate high-resolution spectra toolbox known as PIKA to determine the chemical formulas contributing to distinct mass-to-charge ( $m/z$ ) ratios (DeCarlo et al., 2006). “V-mode” data were used in “triangle plots” and “W-mode” data were used in Van Krevelen diagrams.

Default values were used for the  $\text{CO}_2^+$  signal originating from chamber air as FTIR measurements showed the concentration of  $\text{CO}_2$  in the chamber air is nominally the same as that in the atmosphere. Ratios of the particle-phase signals of  $\text{CO}^+$  to  $\text{CO}_2^+$  were determined to be close to 1 (Supplement) for most experiments so this value was used for all experiments except those of glyoxal uptake for which a value of 5 was used. The signals from  $\text{H}_2\text{O}^+$ ,  $\text{OH}^+$ , and  $\text{O}^+$  in the particulate organic mass may suffer interference from gas-phase  $\text{H}_2\text{O}$ , and their organic contributions were estimated as suggested in Aiken et al. (2008). Particulate nitrogen signals were observed in high- $\text{NO}_x$  photooxidation experiments, originating mostly from  $\text{NO}^+$  and  $\text{NO}_2^+$  ions. Although gas-phase nitric acid is produced from the  $\text{OH} + \text{NO}_2$  reaction, at low chamber humidities nitric acid is not expected to partition appreciably into the particle phase. Thus, the signals of  $\text{NO}^+$  and  $\text{NO}_2^+$  ions were included as part of the organic mass in high- $\text{NO}_x$  photooxidation experiments.

### 4.3.3 Fourier Transform Infrared Spectroscopy (FTIR)

Samples for FTIR analysis were collected on Teflon filters (Pall Inc., Ann Arbor, MI, 37 mm diameter, 1.0  $\mu\text{m}$  pore size, teflo membrane), following the collection, storage, analysis, and peak-fitting techniques described by Russell et al. (2009). Specifically, a Bruker Tensor 27 FTIR Spectrometer with a DTGS detector (Bruker, Waltham, MA) was used to scan filters before and after sample collection; samples were frozen during transport and storage to reduce evaporative loss of organ-

ics and reaction. An automated algorithm was used for subtracting Teflon (using the pre-scanned spectra) and ammonium, baselining, peak-fitting, and error estimation (Russell et al., 2009). Mass concentrations of alkane, carboxylic acid, hydroxyl, amine, non-acid carbonyl, organonitrate, alkene, and aromatic functional groups were quantified using previously reported algorithms and standards (Russell et al., 2009; Day et al., 2010).

FTIR O/C and H/C ratios were determined from measured organic bond absorbances by calculating the estimated moles of oxygen, carbon, and hydrogen associated with each measured bond and its associated functional group (Russell et al., 2009; Russell, 2003). Since alkene groups were below detection, an upper bound was considered to be their detection limit, and a lower bound was considered zero. The degree of saturation for other functional groups was weighted by the saturation in the reactants ( $\alpha$ -pinene and guaiacol). Hydrogen associated with amine groups was omitted since it is assumed that any ammonium is part of the inorganic seed rather than SOA. To account for oxygen and carbon associated methoxy, hydroperoxy, and nitro groups that are obscured by the use of Teflon substrates, the upper bound O/C ratio for guaiacol was incremented by 3O:7C, equivalent to one methoxy group and one hydroperoxy or nitro group (typical groups found in low- and high-NO<sub>x</sub>) to guaiacol's seven carbon structure. No ether groups are expected for  $\alpha$ -pinene products.

## 4.4 Results

Elemental composition and high resolution-spectra of SOA derived from  $\alpha$ -pinene ozonolysis, glyoxal uptake into seed aerosol, and single-ring aromatic, isoprene, and naphthalene photooxidation have been described in detail in Chhabra et al. (2010). Tabulated elemental ratios and high-resolution spectra for  $\alpha$ -pinene, methoxyphenol, and unsaturated aldehyde photooxidation SOA are provided in the Supplement. High-resolution spectra for SOA formed under similar conditions for each parent organic were identical; thus, one experiment for each system is presented. Uncertainty in AMS elemental analysis and offline speciation is discussed in detail in Chhabra et al. (2010).

#### 4.4.1 $\alpha$ -pinene SOA

Figure 4.2 illustrates the “triangle plot” (Panel A) and Van Krevelen diagram (Panels B and C) for SOA derived from  $\alpha$ -pinene ozonolysis and photooxidation. The time progression of each system is illustrated in Panel A with open and closed circles representing the beginning and end of each experiment, respectively. Consistent with previous studies (Chhabra et al., 2010; Shilling et al., 2009), as the SOA mass formed by  $\alpha$ -pinene ozonolysis increases, the O/C ratio and  $f_{44}$  decrease, behavior that is a result of increased partitioning of less oxidized semivolatile compounds into a growing OA medium. Oxygen-to-carbon ratios for  $\alpha$ -pinene photooxidation SOA are approximately the same as those of ozonolysis SOA, however H/C ratios are slightly higher at 1.6. Similar to  $\alpha$ -pinene ozonolysis SOA, the O/C ratios of photooxidation SOA under both  $\text{NO}_x$  conditions decrease as OA mass increases, behavior manifested in the Van Krevelen diagram but more readily apparent in the “triangle plot” with decreases in  $f_{44}$  and increases in  $f_{43}$ . In contrast to ozonolysis SOA, however, photooxidation processes eventually overtake semivolatile partitioning and the oxidation state of photooxidation SOA increases, represented by increases in  $f_{44}$  (Ng et al., 2010). Toward the end of  $\alpha$ -pinene photooxidation experiments, data in Panel A tend to migrate toward the top of the “triangle plot”.

The elemental composition of identified compounds in  $\alpha$ -pinene SOA are also shown on the Van Krevelen diagrams in Fig. 4.2 (Panels B and C). Chhabra et al. (2010) found close agreement between the bulk elemental ratios measured by the AMS and those of compounds detected by offline GC-MS by Yu et al. (1999), who were able to identify >90% of the  $\alpha$ -pinene ozonolysis SOA mass. The species identified by Yu et al. (1999) are represented in Panel B by gray squares and show close agreement to AMS data. Peroxypinic acid, represented by the blue square, is a product of  $\alpha$ -pinene ozonolysis proposed by Docherty et al. (2005) and is an approximate O/C upper bound. Similar elemental compositions to those measured by the AMS have also been measured by other methods (Tolocka et al., 2006; Reinhardt et al., 2007). Many of the same products identified in  $\alpha$ -pinene ozonolysis SOA have been identified in photooxidation SOA (Panel C) by Jaoui and Kamens (2001) (black circles), who determined that particle-phase products accounted for approximately 20% of

the reacted carbon; therefore there is close agreement between AMS elemental composition and that of identified products. Tri-carboxylic acid species (pink circle) observed in ambient aerosol filter samples have been proposed as photooxidation products of  $\alpha$ -pinene (Szmigielski et al., 2007), though it is unlikely the  $\alpha$ -pinene photooxidation experiments achieved OH exposures high enough to form these highly oxygenated species in substantial concentrations.

The crosses in Panel C of Fig. 4.2 represent the estimated ranges of H/C and O/C ratios of  $\alpha$ -pinene SOA as measured by FTIR filter analysis. The lower bound elemental measurements for both SOA systems agree well with measured AMS O/C and H/C ratios and those of identified products suggesting that undetectable alkene signal is significant to the H/C calculation. Functional group analysis shows substantial mass contributions of alkane and acid groups, consistent with the structures illustrated in Panel C.

#### 4.4.2 Isoprene SOA

The triangle and Van Krevelen plots for isoprene-photooxidation SOA appear in Fig. 4.3. The Van Krevelen diagram (Panel B) illustrates that the SOA elemental composition does not change appreciably over the course of the oxidation or at different  $\text{NO}_x$  concentrations (Chhabra et al., 2010). However,  $f_{44}$  increases as  $f_{43}$  decreases over the course of the experiment for both  $\text{NO}_x$  conditions (Panel A), suggesting that organic acid content increases with continued oxidation. High- $\text{NO}_x$  spectra also display higher  $f_{44}$  values than low- $\text{NO}_x$  spectra, consistent with filter measurements identifying methylglyceric acid oligomers as the dominant species in high- $\text{NO}_x$  SOA and non-acid methyltetrols as the dominant species in low- $\text{NO}_x$  SOA. Panel A shows that data for both systems migrate to the top of the triangle with continued photooxidation.

The main species and classes of compounds identified in isoprene SOA under both high- $\text{NO}_x$  and low- $\text{NO}_x$  conditions are shown in Fig. 4.3, Panel B (Surratt et al., 2010; Gomez-Gonzalez et al., 2008; Szmigielski et al., 2007; Surratt et al., 2007, 2006; Claeys et al., 2004; Wang et al., 2005). Surratt et al. (2006) found that under low- $\text{NO}_x$  conditions,  $\sim 25$ – $30\%$  of the SOA mass in seeded experiments is organic peroxides, and under high- $\text{NO}_x$  conditions, oligomers comprise  $\sim 22\%$ – $34\%$

of the SOA mass. Oligomerization of both methyltetrols and methylglyceric acid (or peroxides and nitrates thereof) results in the loss of water, especially under low RH conditions and therefore leads to lower H/C and O/C ratios. Products resulting from the linear oligomerization of 2-methyltetrol, 2-methylglyceric acid, and 2-methylglyceric acid nitrate are shown in Fig. 4.3, Panel B with the oligomerization limits denoted with circles. The locations of the circles highlight the importance of oligomerization in the isoprene system by suggesting that the elemental composition measured by the AMS represents that of highly oligomerized compounds rather than individual monomers or dimers; even better agreement between oligomers and AMS data is possible if one considers crosslinked oligomerization and other dehydration reactions. This observation is consistent with Dommen et al. (2006) who, based on volatility tandem differential mobility analyzer (VTDMA) measurements, found that under lower humidities isoprene SOA volatility is suppressed, suggesting the effect of oligomerization.

#### 4.4.3 Single-Ring Aromatic SOA

Figure 4.4 presents both diagrams for toluene and *m*-xylene photooxidation SOA. Like isoprene and  $\alpha$ -pinene photooxidation SOA, toluene and *m*-xylene SOA spectra sit on the right side of the triangle and migrate upwards, likely representing an increase in organic acid content and a decrease in non-acid oxygenates, possibly unsaturated carbonyls. This is consistent with studies showing small organic acids as a major aromatic SOA product (Fisseha et al., 2004). Increasing SOA oxygenation is also apparent in the Van Krevelen diagram as the AMS data show decreasing H/C ratios and increasing O/C ratios with continued oxidation. In addition, both plots show that *m*-xylene SOA is less oxidized than toluene SOA due to the presence of the second methyl group in *m*-xylene.

Structures of identified SOA products from toluene photooxidation are indicated in the Van Krevelen diagram Fig. 4.4, (Panel B). Despite numerous studies investigating the aerosol composition of aromatic SOA, substantial mass closure has been difficult to achieve. For instance Forstner et al. (1997) studied the molecular composition of SOA formed from the photooxidation of several aromatic compounds and could quantify only 15–30% of the aerosol mass. In subsequent studies, typically

1% of toluene SOA could be identified (Hamilton et al., 2005; Sato et al., 2007). A study by Fisseha et al. (2004) determined 20–45% of SOA from trimethylbenzene photooxidation were small organic acids. The uncertainty in the composition of aromatic SOA is illustrated by the wide spread of SOA products around the AMS data and the absence of a clear representative compound or process explaining the measured elemental composition. AMS measurements indicate SOA that is less oxidized than the indicated compounds would suggest. The presence of unsaturated carbonyls or aromatic-ring retaining species in the particle phase along with oligomerization may serve to limit O/C ratios.

#### 4.4.4 Naphthalene SOA

Figure 4.5 presents the Van Krevelen and “triangle plots” for naphthalene photooxidation SOA. In contrast to the preceding SOA systems, naphthalene AMS data lie to the left of the “triangle plot” and migrate straight upwards (Panel A), consistent with elemental AMS measurements on the Van Krevelen diagram which show increasing O/C ratios (Panel B). The aromaticity of naphthalene allows for multiple oxidation pathways, including bicyclic peroxy radical and ring-opening routes that lead to substantial organic acid yields. Kautzman et al. (2009) determined that about 16% of SOA formed under high-NO<sub>x</sub> conditions and 33% of SOA formed under low-NO<sub>x</sub> conditions are organic acids. Higher organic acid concentrations under low-NO<sub>x</sub> conditions are also consistent with AMS data which exhibit higher  $f_{44}$  values and O/C ratios than those of high-NO<sub>x</sub> data, likely a result of higher OH exposures (Chhabra et al., 2010).

Structures of SOA products identified by Kautzman et al. (2009) in naphthalene SOA and their elemental compositions are presented in Fig. 4.5, Panel B. Kautzman et al. (2009) were able to chemically characterize 53–68% of the SOA mass and Chhabra et al. (2010) found close agreement between the elemental ratios of compounds identified and bulk ratios determined by AMS analysis. Oxygen-to-carbon ratios of identified species also span a range similar to that of AMS measurements of low-NO<sub>x</sub> SOA, evidence of continuous aging.



#### 4.4.5 Phenol and Methoxyphenol SOA

Phenol and methoxyphenol compounds have been investigated as they are semivolatile species formed from the pyrolysis of lignin, the dominant process in biomass burning. Hawthorne et al. (1992) found that phenols and methoxyphenols accounted for forming 21% and 45% of aerosol mass from wood smoke, respectively. Like naphthalene SOA, phenol and methoxyphenol SOA lie to the left of the “triangle” with the highest  $f_{44}$  values of any precursor studied (Fig. 4.6A). Similarly, O/C ratios of methoxyphenols range from 0.8 to 1.0; syringol SOA achieves the highest O/C ratios measured for any chamber aerosol precursor system. The O/C values measured here are in close agreement with those of compounds formed in aqueous reactions of phenolic compounds (Sun et al., 2010). Addition of methoxy groups to the phenol ring increases the H/C but tends to lead to decreases of the  $f_{44}$  of the resulting SOA. The presence of methoxy groups, while increasing the bulk oxygenation of SOA, may be retained in the SOA and inhibit acid formation.

Structures of identified SOA products from guaiacol photooxidation are indicated in the Van Krevelen diagram (Fig. 4.6, Panel B). AMS measured elemental compositions of SOA formed under high- and low- $\text{NO}_x$  regimes agree well with those of compounds formed under low- $\text{NO}_x$  conditions but have higher H/C ratios than those of compounds formed under high- $\text{NO}_x$ . It is possible that the UPLC-MS technique is biased to detect the high- $\text{NO}_x$  compounds shown, compounds with lower H/C ratios.

The crosses in Panel B of Fig. 4.6 represent the estimated ranges of H/C and O/C ratios of guaiacol SOA as measured by FTIR filter analysis. The best agreement between FTIR and AMS data occurs at the upper bound O/C calculation which could imply that the nitro, hydroperoxy, or methoxy groups that the FTIR analysis is not able to measure account for at least some of the oxygen present in the SOA.

#### 4.4.6 Unsaturated Aldehyde SOA

Aldehydes are widely formed in the atmospheric oxidation of SOA precursors; methacrolein is a gas-phase product of the high- $\text{NO}_x$  photooxidation of isoprene. Recent studies have shown that

aldehydes are important intermediates to SOA formation and sensitive to NO and NO<sub>2</sub> concentrations (Chan et al., 2010; Surratt et al., 2010). The “triangle plot” and Van Krevelen Diagram for SOA formed from the high-NO<sub>x</sub> photooxidation of methacrolein, acrolein, and crotonaldehyde are given in Fig. 4.7. As shown in Fig. 4.1, crotonaldehyde and methacrolein are structural isomers of each other while acrolein lacks the additional methyl group. SOA from all three precursors cluster high in the “triangle plot” with acrolein having the highest  $f_{44}$  values. Such high oxidation states are likely due to carboxylic acids and esters contributing a larger fraction of the OA mass. This is consistent with acrolein SOA exhibiting the highest O/C ratios ( $\sim 0.8$ ) of the three systems. SOA from methacrolein photooxidation has higher  $f_{43}$  values than that of crotonaldehyde SOA, implying that the position of the methyl group on the oligomeric chain affects fragmentation in the AMS, but does not change the elemental composition of the SOA substantially.

Oligomers identified in crotonaldehyde and acrolein SOA are depicted in Fig. 4.7, Panel B. The monomers and oligomers formed from methacrolein photooxidation are the same as those of high-NO<sub>x</sub> isoprene SOA (Surratt et al., 2010). Like isoprene SOA, the addition of each monomer to the oligomeric chain results in the loss of a water molecule. The elemental composition of the limit of a linear oligomer is represented by a circle and approaches the AMS measurement suggesting that the AMS measurement is that of a highly esterified compound rather than individual monomers. The lower O/C ratios measured by the AMS is likely due to the inability of the AMS to efficiently detect oxygen in an organic nitrate group (Farmer et al., 2010; Rollins et al., 2010).

#### 4.4.7 SOA from Reactive Uptake of Glyoxal

The reactive uptake of glyoxal onto ammonium sulfate aerosol and the elemental composition of its OA have been described in previous investigations (Galloway et al., 2009; Chhabra et al., 2010). Glyoxal OA exhibits high O/C ratios due to its high oxygen content and its ability to hydrate and polymerize in the aerosol phase (Fig. 4.8, Panel B). Despite a high measured O/C ratio, glyoxal OA sits on the bottom left of the “triangle plot”, a result of insignificant signals at  $m/z$  43 and 44. Most of the oxygen signal in glyoxal OA spectra resides in  $m/z$  29 (CHO<sup>+</sup>), 30 (CH<sub>2</sub>O<sup>+</sup>), 31 (CH<sub>3</sub>O<sup>+</sup>),

and 47 ( $\text{CH}_3\text{O}_2^+$ ) (Chhabra et al., 2010).

Structures proposed to form in the aqueous particle phase are shown in Panel B. Hydrated glyoxal has the highest O/C and H/C values; with consecutive additions of glyoxal, water is removed and the oligomer follows a dehydration route with a limit at the same elemental composition of glyoxal itself. Also shown on the Van Krevelen plot is 1H-imidazole-2-carboxaldehyde, a compound formed from the reaction of glyoxal with ammonium (Chhabra et al., 2010). The AMS elemental composition measurement lies roughly in the middle of the wide range spanned by the proposed species. Further work is needed in characterizing glyoxal OA, its interaction with inorganic species, and the extent of its oligomerization in SOA.

## 4.5 Discussion and Conclusions

We investigate two different analysis methods (“triangle plot” and Van Krevelen diagram) for representing the general processes of formation and aging of SOA. Figure 4.9 summarizes SOA data in a “triangle plot” and Van Krevelen diagram for the variety of laboratory systems studied. Despite the variety of experimental conditions, differences in oxidative conditions have relatively little effect on the spectral identity and elemental composition of SOA as measured by the AMS compared to the identity of the SOA precursor. Most SOA formed under high- and low- $\text{NO}_x$  conditions occupy similar areas in the “triangle plot” and Van Krevelen diagram. Typically, chemical characterizations of SOA find significant concentrations of peroxides under low- $\text{NO}_x$  conditions and organic nitrates under high- $\text{NO}_x$  conditions. However, it is likely that these differences in functionality do not lead to substantial differences in  $f_{43}$  and  $f_{44}$  and the elemental composition as the underlying chemical structure of SOA remains relatively unchanged. All individual photooxidation systems, apart from the aldehydes that are not large enough to support continued oxidation, also show that AMS spectra head toward the top of the “triangle plot” as they age, consistent with an increase in O/C ratios in the Van Krevelen diagram. Evidence from other AMS studies suggest that this movement toward the top of the “triangle plot” is representative of an increase in organic acids (Alfarra, 2004; Aiken et al., 2007; Takegawa et al., 2007; Duplissy et al., 2011).

We find close agreement between the  $f_{43}$  and  $f_{44}$  values presented in Ng et al. (2010) and those presented here for the traditional set of SOA systems: single-ringed aromatic,  $\alpha$ -pinene, and isoprene SOA. These SOA systems cluster in the lower half of the “triangle plot” indicating relatively low oxygen content and a high degree of mass spectral variation, similar to SV-OOA components. The additional SOA precursors studied here exhibit more mass spectral variation and show that highly oxidized OA with similar O/C ratios to LV-OOA can be formed in a laboratory chamber. The most oxidized SOA formed in the systems studied here results from the photooxidation of already oxidized VOCs, methoxyphenols and unsaturated aldehydes, suggesting that OH exposure is the limiting variable in SOA oxidation. Starting with an oxidized SOA precursor gives SOA a “head start” to the oxidative aging process, a phenomenon apparent when comparing the methacrolein and isoprene high-NO<sub>x</sub> systems. Methacrolein, a gas-phase product and major SOA intermediate of isoprene photooxidation under high-NO<sub>x</sub> conditions, yields SOA with  $f_{43}$  and  $f_{44}$  values just beyond those of the isoprene SOA range. It is likely that methacrolein SOA formed under high-NO<sub>x</sub> does not occupy the same space of high-NO<sub>x</sub> isoprene SOA because high-NO<sub>x</sub> isoprene SOA could also contain products of low-NO<sub>x</sub> photooxidation, thereby lowering it in the “triangle plot.” In the extreme case, methoxyphenols are subject to multiple oxidation steps on an already oxidized compound, leading to O/C ratios that approach unity. Although containing aromatic functionality, both methoxyphenols and naphthalene generate SOA spectra that group on the left side of the “triangle plot” while *m*-xylene and toluene generate SOA spectra that group on the right side. Similarly, Ng et al. (2010) found that benzene SOA spectra sit on the left side of the “triangle plot” and 1, 3, 5-trimethylbenzene SOA spectra sit on the right. It is likely that functionality on the aromatic ring of the SOA precursor affects the fragmentation of the resultant SOA. Specifically, electron donating groups like  $-\text{CH}_3$  on the aromatic ring yield SOA spectra with high  $f_{43}$  values while electron withdrawing groups like  $-\text{OH}$  and  $-\text{OCH}_3$  or the lack of functionality on the aromatic ring yield SOA spectra with low  $f_{43}$  values.

The Van Krevelen diagrams of the elemental composition of individual SOA systems reveal that elemental ratios measured by the AMS agree most closely with SOA systems for which the

greatest degree of mass closure has been achieved. Yu et al. (1999) were able to speciate >90% of the  $\alpha$ -pinene ozonolysis aerosol composition by mass, and Kautzman et al. (2009) were able to speciate 53–68% of the SOA formed from naphthalene photooxidation, the two systems with the closest agreement between measured elemental ratios and identified compounds. The diagrams also illustrate that highly oligomerized compounds may dominate, in particular, SOA systems such as isoprene and unsaturated aldehyde photooxidation. Conversely, in systems for which mass closure has been difficult, such as single-ringed aromatics, AMS and filter data do not agree. This may be due to poorly characterized processes occurring in the particle phase such as oligomerization or dehydration or measurement artifacts (Chhabra et al., 2010).

From a variety of ambient and laboratory measurements, Heald et al. (2010) found that atmospheric OA occupy a narrow range in the Van Krevelen diagram following a line with slope of  $-1$  implying the addition of carboxylic acids or equal amounts of hydroxy and carbonyl functional groups on average to a saturated carbon chain. From Fig. 4.9, Panel B, for the set of compounds studied here the slope is shallower than  $-1$  if one considers a y-intercept within the range of SOA precursors. In the systems studied here, most SOA precursors do not resemble a saturated chain, and many have cyclic chains, alkene, or aromatic groups. This allows for oxidation of the precursor without substantial loss of hydrogen, leading to a slope shallower than  $-1$ , even with the addition of carbonyl and acid groups. Aging pathways on the Van Krevelen diagram are likely to be different for different precursor species like isoprene and  $\alpha$ -pinene and for different precursor classes like biogenic and anthropogenic VOCs. Recently Ng et al. (2011) developed a parameterization to transform ambient OOA components in the “triangle plot” directly onto the Van Krevelen space. The transformed ambient “VK-triangle” (shown in Fig. 4.9, Panel B) is consistent with the chamber data and also yields a slope shallower than  $-1$ .

Figure 4.9, Panel A shows that precursor structure and functionality determine the SOA “starting point” on the “triangle plot” and that the path taken is largely dependent on identity of the SOA precursor. Ng et al. (2010) showed that as SOA photochemically ages, and becomes more oxidized, spectral uniqueness is lost and SOA on the “triangle plot” becomes chemically similar.

Panel A supports this model with SOA converging at the pinnacle of the triangle which corresponds to an oxidation state ( $\overline{OS}_C \approx 2 \times O/C - H/C$ ) (Kroll et al., 2011) of around 1 (Ng et al., 2011; Kroll et al., 2011). Panel A also shows that with a finite set of SOA precursors, one can essentially recreate the “triangle plot” as originally created by Ng et al. (2010). The SOA spectra represented on the boundaries of the triangle do not mean that they are not representative of ambient spectral components. Rather this SOA represents AMS spectral extremes. Thus, ambient spectra and components falling within the triangle represent the ensemble average of many different SOA precursors and oxidative processes that mix spatially and temporally, and as SOA becomes more oxidized, it loses its source history. Indeed more chamber experiments would help to more fully characterize the “triangle plot” space. High-resolution analysis with species identification can more accurately assign functional groups to individual ions in the AMS spectra. Molecular level chemical characterization of SOA will also be useful in comparison to AMS elemental measurements, especially in systems for which mass closure has been difficult.

## 4.6 Acknowledgements

This work was supported by the US Department of Energy Biological and Environmental Research grant DE-FG02-05ER63983, US Environmental Protection Agency STAR grant RD-83374901, and US NSF grant ATM-0432377. It has not been formally reviewed by EPA. The views expressed in this document are solely those of the authors and the EPA does not endorse any products in this publication. The authors would like to thank Christine Loza for SOA yield analysis and Man Nin Chan, Lindsay Yee, and Katherine Schilling for guaiacol filter analysis. The authors would also like to thank Satoshi Takahama for helpful discussions on FTIR analysis.

## Bibliography

Aiken, A. C., DeCarlo, P. F., and Jimenez, J. L.: Elemental analysis of organic species with electron ionization high-resolution mass spectrometry, *Anal. Chem.*, 79, 8350–8358,

doi:10.1021/Ac071150w, 2007.

Aiken, A. C., Decarlo, P. F., Kroll, J. H., Worsnop, D. R., Huffman, J. A., Docherty, K. S., Ulbrich, I. M., Mohr, C., Kimmel, J. R., Sueper, D., Sun, Y., Zhang, Q., Trimborn, A., Northway, M., Ziemann, P. J., Canagaratna, M. R., Onasch, T. B., Alfarra, M. R., Prevot, A. S. H., Dommen, J., Duplissy, J., Metzger, A., Baltensperger, U., and Jimenez, J. L.: O/C and OM/OC ratios of primary, secondary, and ambient organic aerosols with high-resolution time-of-flight aerosol mass spectrometry, *Environ. Sci. Technol.*, 42, 4478–4485, doi:10.1021/Es703009q, 2008.

Aiken, A. C., Salcedo, D., Cubison, M. J., Huffman, J. A., DeCarlo, P. F., Ulbrich, I. M., Docherty, K. S., Sueper, D., Kimmel, J. R., Worsnop, D. R., Trimborn, A., Northway, M., Stone, E. A., Schauer, J. J., Volkamer, R. M., Fortner, E., de Foy, B., Wang, J., Laskin, A., Shutthanandan, V., Zheng, J., Zhang, R., Gaffney, J., Marley, N. A., Paredes-Miranda, G., Arnott, W. P., Molina, L. T., Sosa, G., and Jimenez, J. L.: Mexico City aerosol analysis during MILAGRO using high resolution aerosol mass spectrometry at the urban supersite (T0) Part 1: Fine particle composition and organic source apportionment, *Atmos. Chem. Phys.*, 9, 6633–6653, doi:10.5194/acp-9-6633-2009, 2009.

Alfarra, M. R.: Insights into the atmospheric organic aerosols using an aerosol mass spectrometer, Ph.D. thesis, University of Manchester, Manchester, UK, 2004.

Allan, J. D., Delia, A. E., Coe, H., Bower, K. N., Alfarra, M. R., Jimenez, J. L., Middlebrook, A. M., Drewnick, F., Onasch, T. B., Canagaratna, M. R., Jayne, J. T., and Worsnop, D. R.: A generalised method for the extraction of chemically resolved mass spectra from aerodyne aerosol mass spectrometer data, *J. Aerosol Sci.*, 35, 909–922, doi:10.1016/j.jaerosci.2004.02.007, 2004.

Bahreini, R., Keywood, M. D., Ng, N. L., Varutbangkul, V., Gao, S., Flagan, R. C., Seinfeld, J. H., Worsnop, D. R., and Jimenez, J. L.: Measurements of secondary organic aerosol from oxidation of cycloalkenes, terpenes, and m-xylene using an Aerodyne aerosol mass spectrometer, *Environ. Sci. Technol.*, 39, 5674–5688, doi:10.1021/Es048061a, 2005.

- Bateman, A. P., Nizkorodov, S. A., Laskin, J., and Laskin, A.: Time-resolved molecular characterization of limonene/ozonol aerosol using high-resolution electrospray ionization mass spectrometry, *PCCP*, 11, 7931–7942, doi:10.1039/B905288g, 2009.
- Bloss, C., Wagner, V., Jenkin, M. E., Volkamer, R., Bloss, W. J., Lee, J. D., Heard, D. E., Wirtz, K., Martin-Reviejo, M., Rea, G., Wenger, J. C., and Pilling, M. J.: Development of a detailed chemical mechanism (MCMv3.1) for the atmospheric oxidation of aromatic hydrocarbons, *Atmos. Chem. Phys.*, 5, 641–664, doi:10.5194/acp-5-641-2005, 2005.
- Canagaratna, M. R., Jayne, J. T., Jimenez, J. L., Allan, J. D., Alfarra, M. R., Zhang, Q., Onasch, T. B., Drewnick, F., Coe, H., Middlebrook, A., Delia, A., Williams, L. R., Trimborn, A. M., Northway, M. J., DeCarlo, P. F., Kolb, C. E., Davidovits, P., and Worsnop, D. R.: Chemical and microphysical characterization of ambient aerosols with the aerodyne aerosol mass spectrometer, *Mass Spectrom. Rev.*, 26, 185–222, doi:10.1002/Mas.20115, 2007.
- Chan, A. W. H., Kautzman, K. E., Chhabra, P. S., Surratt, J. D., Chan, M. N., Crouse, J. D., Kurten, A., Wennberg, P. O., Flagan, R. C., and Seinfeld, J. H.: Secondary organic aerosol formation from photooxidation of naphthalene and alkylnaphthalenes: implications for oxidation of intermediate volatility organic compounds (IVOCs), *Atmos. Chem. Phys.*, 9, 3049–3060, doi:10.5194/acp-9-3049-2009, 2009.
- Chan, A. W. H., Chan, M. N., Surratt, J. D., Chhabra, P. S., Loza, C. L., Crouse, J. D., Yee, L. D., Flagan, R. C., Wennberg, P. O., and Seinfeld, J. H.: Role of aldehyde chemistry and NO<sub>x</sub> concentrations in secondary organic aerosol formation, *Atmos. Chem. Phys.*, 10, 7169–7188, doi:10.5194/acp-10-7169-2010, 2010.
- Chhabra, P. S., Flagan, R. C., and Seinfeld, J. H.: Elemental analysis of chamber organic aerosol using an aerodyne high-resolution aerosol mass spectrometer, *Atmos. Chem. Phys.*, 10, 4111–4131, doi:10.5194/acp-10-4111-2010, 2010.
- Claeys, M., Graham, B., Vas, G., Wang, W., Vermeylen, R., Pashynska, V., Cafmeyer, J., Guyon,



- P., Andreae, M. O., Artaxo, P., and Maenhaut, W.: Formation of secondary organic aerosols through photooxidation of isoprene, *Science*, 303, 1173–1176, doi:10.1126/science.1092805, 2004.
- Cocker, D. R., Flagan, R. C., and Seinfeld, J. H.: State-of-the-art chamber facility for studying atmospheric aerosol chemistry, *Environ. Sci. Technol.*, 35, 2594–2601, doi:10.1021/Es0019169, 2001.
- Day, D. A., Liu, S., Russell, L. M., and Ziemann, P. J.: Organonitrate group concentrations in submicron particles with high nitrate and organic fractions in coastal southern California, *Atmos. Environ.*, 44, 1970–1979, doi:10.1016/j.atmosenv.2010.02.045, 2010.
- De Gouw, J. and Jimenez, J. L.: Organic Aerosols in the Earth’s Atmosphere, *Environ. Sci. Technol.*, 43, 7614–7618, doi:10.1021/Es9006004, 2009.
- DeCarlo, P. F., Kimmel, J. R., Trimborn, A., Northway, M. J., Jayne, J. T., Aiken, A. C., Gonin, M., Fuhrer, K., Horvath, T., Docherty, K. S., Worsnop, D. R., and Jimenez, J. L.: Field-deployable, high-resolution, time-of-flight aerosol mass spectrometer, *Anal. Chem.*, 78, 8281–8289, doi:10.1021/Ac061249n, 2006.
- Docherty, K. S., Wu, W., Lim, Y. B., and Ziemann, P. J.: Contributions of organic peroxides to secondary aerosol formed from reactions of monoterpenes with O<sub>3</sub>, *Environ. Sci. Technol.*, 39, 4049–4059, doi:10.1021/Es050228s, 2005.
- Dommen, J., Metzger, A., Duplissy, J., Kalberer, M., Alfarra, M. R., Gascho, A., Weingartner, E., Prevot, A. S. H., Verheggen, B., and Baltensperger, U.: Laboratory observation of oligomers in the aerosol from isoprene/NO<sub>x</sub> photooxidation, *Geophys. Res. Lett.*, 33, doi:10.1029/2006gl026523, 2006.
- Donahue, N. M., Robinson, A. L., and Pandis, S. N.: Atmospheric organic particulate matter: From smoke to secondary organic aerosol, *Atmos. Environ.*, 43, 94–106, doi:10.1016/j.atmosenv.2008.09.055, 2009.

- Duplissy, J., DeCarlo, P. F., Dommen, J., Alfarra, M. R., Metzger, A., Barmapadimos, I., Prevot, A. S. H., Weingartner, E., Tritscher, T., Gysel, M., Aiken, A. C., Jimenez, J. L., Canagaratna, M. R., Worsnop, D. R., Collins, D. R., Tomlinson, J., and Baltensperger, U.: Relating hygroscopicity and composition of organic aerosol particulate matter, *Atmos. Chem. Phys.*, 11, 1155–1165, doi:10.5194/acp-11-1155-2011, 2011.
- Farmer, D. K., Matsunaga, A., Docherty, K. S., Surratt, J. D., Seinfeld, J. H., Ziemann, P. J., and Jimenez, J. L.: Response of an aerosol mass spectrometer to organonitrates and organosulfates and implications for atmospheric chemistry, *P. Natl. Acad. Sci. USA*, 107, 6670–6675, doi:10.1073/pnas.0912340107, 2010.
- Fisseha, R., Dommen, J., Sax, M., Paulsen, D., Kalberer, M., Maurer, R., Hofler, F., Weingartner, E., and Baltensperger, U.: Identification of organic acids in secondary organic aerosol and the corresponding gas phase from chamber experiments, *Anal. Chem.*, 76, 6535–6540, doi:10.1021/Ac048975f, 2004.
- Forstner, H. J. L., Flagan, R. C., and Seinfeld, J. H.: Secondary organic aerosol from the photooxidation of aromatic hydrocarbons: Molecular composition, *Environ. Sci. Technol.*, 31, 1345–1358, doi:10.1021/es9605376, 1997.
- Galloway, M. M., Chhabra, P. S., Chan, A. W. H., Surratt, J. D., Flagan, R. C., Seinfeld, J. H., and Keutsch, F. N.: Glyoxal uptake on ammonium sulphate seed aerosol: reaction products and reversibility of uptake under dark and irradiated conditions, *Atmos. Chem. Phys.*, 9, 3331–3345, doi:10.5194/acp-9-3331-2009, 2009.
- Goldstein, A. H. and Galbally, I. E.: Known and unexplored organic constituents in the earth's atmosphere, *Environ. Sci. Technol.*, 41, 1514–1521, doi:10.1021/es072476p, 2007.
- Gomez-Gonzalez, Y., Surratt, J. D., Cuyckens, F., Szmigielski, R., Vermeylen, R., Jaoui, M., Lewandowski, M., Offenberg, J. H., Kleindienst, T. E., Edney, E. O., Blockhuys, F., Van Alsenoy, C., Maenhaut, W., and Claeys, M.: Characterization of organosulfates from the photooxidation

- of isoprene and unsaturated fatty acids in ambient aerosol using liquid chromatography/(-) electrospray ionization mass spectrometry, *J. Mass Spectrom.*, **43**, 371–382, doi:10.1002/Jms.1329, 2008.
- Hallquist, M., Wenger, J. C., Baltensperger, U., Rudich, Y., Simpson, D., Claeys, M., Dommen, J., Donahue, N. M., George, C., Goldstein, A. H., Hamilton, J. F., Herrmann, H., Hoffmann, T., Iinuma, Y., Jang, M., Jenkin, M. E., Jimenez, J. L., Kiendler-Scharr, A., Maenhaut, W., McFiggans, G., Mentel, T. F., Monod, A., Prevot, A. S. H., Seinfeld, J. H., Surratt, J. D., Szmigielski, R., and Wildt, J.: The formation, properties and impact of secondary organic aerosol: current and emerging issues, *Atmos. Chem. Phys.*, **9**, 5155–5236, doi:10.5194/acp-9-5155-2009, 2009.
- Hamilton, J. F., Webb, P. J., Lewis, A. C., and Reviejo, M. M.: Quantifying small molecules in secondary organic aerosol formed during the photo-oxidation of toluene with hydroxyl radicals, *Atmos. Environ.*, **39**, 7263–7275, doi:10.1016/j.atmosenv.2005.09.006, 2005.
- Hawthorne, S. B., Miller, D. J., Langenfeld, J. J., and Krieger, M. S.: Pm-10 High-Volume Collection and Quantitation of Semivolatile and Nonvolatile Phenols, Methoxylated Phenols, Alkanes, and Polycyclic Aromatic-Hydrocarbons from Winter Urban Air and Their Relationship to Wood Smoke Emissions, *Environ. Sci. Technol.*, **26**, 2251–2262, doi:10.1021/es00035a026, 1992.
- Heald, C. L., Kroll, J. H., Jimenez, J. L., Docherty, K. S., DeCarlo, P. F., Aiken, A. C., Chen, Q., Martin, S. T., Farmer, D. K., and Artaxo, P.: A simplified description of the evolution of organic aerosol composition in the atmosphere, *Geophys. Res. Lett.*, **37**, L08803, doi:10.1029/2010gl042737, 2010.
- Jang, M. S. and Kamens, R. M.: Characterization of secondary aerosol from the photooxidation of toluene in the presence of NO<sub>x</sub> and 1-propene, *Environ. Sci. Technol.*, **35**, 3626–3639, doi:10.1021/Es010676+, 2001.
- Jaoui, M. and Kamens, R. M.: Mass balance of gaseous and particulate products analysis from alpha-

- pinene/NO<sub>x</sub>/air in the presence of natural sunlight, *J. Geophys. Res.-Atmos.*, 106, 12541–12558, doi:10.1029/2001JD900005, 2001.
- Jayne, J. T., Leard, D. C., Zhang, X. F., Davidovits, P., Smith, K. A., Kolb, C. E., and Worsnop, D. R.: Development of an aerosol mass spectrometer for size and composition analysis of submicron particles, *Aerosol Sci. Technol.*, 33, 49–70, doi:10.1080/027868200410840, 2000.
- Jimenez, J. L., Canagaratna, M. R., Donahue, N. M., Prevot, A. S. H., Zhang, Q., Kroll, J. H., DeCarlo, P. F., Allan, J. D., Coe, H., Ng, N. L., Aiken, A. C., Docherty, K. S., Ulbrich, I. M., Grieshop, A. P., Robinson, A. L., Duplissy, J., Smith, J. D., Wilson, K. R., Lanz, V. A., Hueglin, C., Sun, Y. L., Tian, J., Laaksonen, A., Raatikainen, T., Rautiainen, J., Vaattovaara, P., Ehn, M., Kulmala, M., Tomlinson, J. M., Collins, D. R., Cubison, M. J., E., Dunlea, J., Huffman, J. A., Onasch, T. B., Alfarra, M. R., Williams, P. I., Bower, K., Kondo, Y., Schneider, J., Drewnick, F., Borrmann, S., Weimer, S., Demerjian, K., Salcedo, D., Cottrell, L., Griffin, R., Takami, A., Miyoshi, T., Hatakeyama, S., Shimono, A., Sun, J. Y., Zhang, Y. M., Dzepina, K., Kimmel, J. R., Sueper, D., Jayne, J. T., Herndon, S. C., Trimborn, A. M., Williams, L. R., Wood, E. C., Middlebrook, A. M., Kolb, C. E., Baltensperger, U., and Worsnop, D. R.: Evolution of Organic Aerosols in the Atmosphere, *Science*, 326, 1525–1529, doi:10.1126/science.1180353, 2009.
- Kautzman, K. E., Surratt, J. D., Chan, M. N., Chan, A. W. H., Hersey, S. P., Chhabra, P. S., Dalleska, N. F., Wennberg, P. O., Flagan, R. C., and Seinfeld, J. H.: Chemical Composition of Gas- and Aerosol-Phase Products from the Photooxidation of Naphthalene, *J. Phys. Chem. A*, 114, 913–934, doi:10.1021/jp908530s, 2009.
- Keyword, M. D., Kroll, J. H., Varutbangkul, V., Bahreini, R., Flagan, R. C., and Seinfeld, J. H.: Secondary organic aerosol formation from cyclohexene ozonolysis: Effect of OH scavenger and the role of radical chemistry, *Environ. Sci. Technol.*, 38, 3343–3350, doi:10.1021/Es049725j, 2004.
- Kroll, J. H. and Seinfeld, J. H.: Chemistry of secondary organic aerosol: Formation and evolution of low-volatility organics in the atmosphere, *Atmos. Environ.*, 42, 3593–3624, doi:10.1016/j.atmosenv.2008.01.003, 2008.

- Kroll, J. H., Ng, N. L., Murphy, S. M., Flagan, R. C., and Seinfeld, J. H.: Secondary organic aerosol formation from isoprene photooxidation, *Environ. Sci. Technol.*, 40, 1869–1877, doi:10.1021/Es0524301, 2006.
- Kroll, J. H., Donahue, N. M., Jimenez, J. L., Kessler, S. H., Canagaratna, M. R., Wilson, K. R., Altieri, K. E., Mazzoleni, L. R., Wozniak, A. S., Bluhm, H., Mysak, E. R., Smith, J. D., Kolb, C. E., and Worsnop, D. R.: Carbon oxidation state as a metric for describing the chemistry of atmospheric organic aerosol, *Nat Chem*, 3, 133–139, doi:10.1038/Nchem.948, 2011.
- Kua, J., Hanley, S. W., and De Haan, D. O.: Thermodynamics and kinetics of glyoxal dimer formation: A computational study, *J. Phys. Chem. A*, 112, 66–72, doi:10.1021/Jp076573g, 2008.
- Lanz, V. A., Alfarra, M. R., Baltensperger, U., Buchmann, B., Hueglin, C., and Prevot, A. S. H.: Source apportionment of submicron organic aerosols at an urban site by factor analytical modelling of aerosol mass spectra, *Atmos. Chem. Phys.*, 7, 1503–1522, doi:10.5194/acp-7-1503-2007, 2007.
- Lim, Y. B., Tan, Y., Perri, M. J., Seitzinger, S. P., and Turpin, B. J.: Aqueous chemistry and its role in secondary organic aerosol (SOA) formation, *Atmos. Chem. Phys.*, 10, 10521–10539, doi:10.5194/acp-10-10521-2010, 2010.
- Loeffler, K. W., Koehler, C. A., Paul, N. M., and De Haan, D. O.: Oligomer formation in evaporating aqueous glyoxal and methyl glyoxal solutions, *Environ. Sci. Technol.*, 40, 6318–6323, doi:10.1021/Es060810w, 2006.
- Ng, N. L., Kroll, J. H., Chan, A. W. H., Chhabra, P. S., Flagan, R. C., and Seinfeld, J. H.: Secondary organic aerosol formation from m-xylene, toluene, and benzene, *Atmos. Chem. Phys.*, 7, 3909–3922, doi:10.5194/acp-7-3909-2007, 2007.
- Ng, N. L., Canagaratna, M. R., Zhang, Q., Jimenez, J. L., Tian, J., Ulbrich, I. M., Kroll, J. H., Docherty, K. S., Chhabra, P. S., Bahreini, R., Murphy, S. M., Seinfeld, J. H., Hildebrandt, L., Donahue, N. M., DeCarlo, P. F., Lanz, V. A., Prevot, A. S. H., Dinar, E., Rudich, Y., and Worsnop, D. R.: Organic aerosol components observed in Northern Hemispheric datasets from

- Aerosol Mass Spectrometry, *Atmos. Chem. Phys.*, 10, 4625–4641, doi:10.5194/acp-10-4625-2010, 2010.
- Ng, N. L., Canagaratna, M. R., Jimenez, J. L., Chhabra, P. S., Seinfeld, J. H., and Worsnop, D. R.: Changes in organic aerosol composition with aging inferred from aerosol mass spectra, *Atmos. Chem. Phys. Discuss.*, 11, 7095–7112, doi:10.5194/acpd-11-7095-2011, 2011.
- Reinhardt, A., Emmenegger, C., Gerrits, B., Panse, C., Dommen, J., Baltensperger, U., Zenobi, R., and Kalberer, M.: Ultrahigh mass resolution and accurate mass measurements as a tool to characterize oligomers in secondary organic aerosols, *Anal. Chem.*, 79, 4074–4082, doi:10.1021/Ac062425v, 2007.
- Robinson, A. L., Donahue, N. M., Shrivastava, M. K., Weitkamp, E. A., Sage, A. M., Grieshop, A. P., Lane, T. E., Pierce, J. R., and Pandis, S. N.: Rethinking organic aerosols: Semivolatile emissions and photochemical aging, *Science*, 315, 1259–1262, doi:10.1126/science.1133061, 2007.
- Rollins, A. W., Fry, J. L., Hunter, J. F., Kroll, J. H., Worsnop, D. R., Singaram, S. W., and Cohen, R. C.: Elemental analysis of aerosol organic nitrates with electron ionization high-resolution mass spectrometry, *Atmos. Meas. Tech.*, 3, 301–310, doi:10.5194/amt-3-301-2010, 2010.
- Russell, L. M.: Aerosol organic-mass-to-organic-carbon ratio measurements, *Environ. Sci. Technol.*, 37, 2982–2987, doi:10.1021/Es026123w, 2003.
- Russell, L. M., Takahama, S., Liu, S., Hawkins, L. N., Covert, D. S., Quinn, P. K., and Bates, T. S.: Oxygenated fraction and mass of organic aerosol from direct emission and atmospheric processing measured on the R/V Ronald Brown during TEXAQS/GoMACCS 2006, *J. Geophys. Res.-Atmos.*, 114, doi:10.1029/2008jd011275, 2009.
- Sato, K., Hatakeyama, S., and Imamura, T.: Secondary organic aerosol formation during the photooxidation of toluene: NO<sub>x</sub> dependence of chemical composition, *J. Phys. Chem. A*, 111, 9796–9808, doi:10.1021/Jp071419f, 2007.

- Shilling, J. E., Chen, Q., King, S. M., Rosenoern, T., Kroll, J. H., Worsnop, D. R., DeCarlo, P. F., Aiken, A. C., Sueper, D., Jimenez, J. L., and Martin, S. T.: Loading-dependent elemental composition of alpha-pinene SOA particles, *Atmos. Chem. Phys.*, 9, 771–782, doi:10.5194/acp-9-771-2009, 2009.
- Sun, Y. L., Zhang, Q., Anastasio, C., and Sun, J.: Insights into secondary organic aerosol formed via aqueous-phase reactions of phenolic compounds based on high resolution mass spectrometry, *Atmos. Chem. Phys.*, 10, 4809–4822, doi:10.5194/acp-10-4809-2010, 2010.
- Surratt, J. D., Murphy, S. M., Kroll, J. H., Ng, N. L., Hildebrandt, L., Sorooshian, A., Szmigielski, R., Vermeylen, R., Maenhaut, W., Claeys, M., Flagan, R. C., and Seinfeld, J. H.: Chemical composition of secondary organic aerosol formed from the photooxidation of isoprene, *J. Phys. Chem. A*, 110, 9665–9690, doi:10.1021/Jp061734m, 2006.
- Surratt, J. D., Lewandowski, M., Offenberg, J. H., Jaoui, M., Kleindienst, T. E., Edney, E. O., and Seinfeld, J. H.: Effect of acidity on secondary organic aerosol formation from isoprene, *Environ. Sci. Technol.*, 41, 5363–5369, doi:10.1021/Es0704176, 2007.
- Surratt, J. D., Chan, A. W. H., Eddingsaas, N. C., Chan, M. N., Loza, C. L., Kwan, A. J., Hersey, S. P., Flagan, R. C., Wennberg, P. O., and Seinfeld, J. H.: Reactive intermediates revealed in secondary organic aerosol formation from isoprene, *P Natl Acad Sci USA*, 107, 6640–6645, doi:10.1073/pnas.0911114107, 2010.
- Szmigielski, R., Surratt, J. D., Vermeylen, R., Szmigielska, K., Kroll, J. H., Ng, N. L., Murphy, S. M., Sorooshian, A., Seinfeld, J. H., and Claeys, M.: Characterization of 2-methylglyceric acid oligomers in secondary organic aerosol formed from the photooxidation of isoprene using trimethylsilylation and gas chromatography/ion trap mass spectrometry, *J. Mass Spectrom.*, 42, 101–116, doi:10.1002/Jms.1146, 2007.
- Takegawa, N., Miyakawa, T., Kawamura, K., and Kondo, Y.: Contribution of selected dicarboxylic and omega-oxocarboxylic acids in ambient aerosol to the  $m/z$  44 signal of an aerodyne aerosol mass spectrometer, *Aerosol Sci. Technol.*, 41, 418–437, doi:10.1080/02786820701203215, 2007.

- Tolocka, M. P., Heaton, K. J., Dreyfus, M. A., Wang, S. Y., Zordan, C. A., Saul, T. D., and Johnston, M. V.: Chemistry of particle inception and growth during alpha-pinene ozonolysis, *Environ. Sci. Technol.*, 40, 1843–1848, doi:10.1021/Es051926f, 2006.
- Ulbrich, I. M., Canagaratna, M. R., Zhang, Q., Worsnop, D. R., and Jimenez, J. L.: Interpretation of organic components from Positive Matrix Factorization of aerosol mass spectrometric data, *Atmos. Chem. Phys.*, 9, 2891–2918, doi:10.5194/acp-9-2891-2009, 2009.
- Walser, M. L., Desyaterik, Y., Laskin, J., Laskin, A., and Nizkorodov, S. A.: High-resolution mass spectrometric analysis of secondary organic aerosol produced by ozonation of limonene, *PCCP*, 10, 1009–1022, doi:10.1039/B712620d, 2008.
- Wang, W., Kourtchev, I., Graham, B., Cafmeyer, J., Maenhaut, W., and Claeys, M.: Characterization of oxygenated derivatives of isoprene related to 2-methyltetrols in Amazonian aerosols using trimethylsilylation and gas chromatography/ion trap mass spectrometry, *Rapid Commun. Mass Spectrom.*, 19, 1343–1351, doi:10.1002/Rcm.1940, 2005.
- Yu, J. Z., Cocker, D. R., Griffin, R. J., Flagan, R. C., and Seinfeld, J. H.: Gas-phase ozone oxidation of monoterpenes: Gaseous and particulate products, *J. Atmos. Chem.*, 34, 207–258, doi:10.1023/A:1006254930583, 1999.
- Zhang, Q., Alfarra, M. R., Worsnop, D. R., Allan, J. D., Coe, H., Canagaratna, M. R., and Jimenez, J. L.: Deconvolution and quantification of hydrocarbon-like and oxygenated organic aerosols based on aerosol mass spectrometry, *Environ. Sci. Technol.*, 39, 4938–4952, doi:10.1021/Es048568l, 2005.
- Zhang, Q., Jimenez, J. L., Canagaratna, M. R., Allan, J. D., Coe, H., Ulbrich, I., Alfarra, M. R., Takami, A., Middlebrook, A. M., Sun, Y. L., Dzepina, K., Dunlea, E., Docherty, K., DeCarlo, P. F., Salcedo, D., Onasch, T., Jayne, J. T., Miyoshi, T., Shimono, A., Hatakeyama, S., Takegawa, N., Kondo, Y., Schneider, J., Drewnick, F., Borrmann, S., Weimer, S., Demerjian, K., Williams, P., Bower, K., Bahreini, R., Cottrell, L., Griffin, R. J., Rautiainen, J., Sun, J. Y., Zhang, Y. M., and Worsnop, D. R.: Ubiquity and dominance of oxygenated species in organic aerosols in



anthropogenically-influenced Northern Hemisphere midlatitudes, *Geophys. Res. Lett.*, 34, L13801, doi:10.1029/2007gl029979, 2007.

**Table 4.1:** Experimental conditions and results

Expt.#	VOC System	Experiment Type	RH (%)	[NO] <sub>0</sub> (ppb)	[NO <sub>2</sub> ] <sub>0</sub> (ppb)	VOC Reacted (ppb)	Seed Vol. (μm <sup>3</sup> cm <sup>-3</sup> )	ΔM <sub>0</sub> (Max) <sup>d</sup> (μg m <sup>-3</sup> )
1	glyoxal uptake	humid	60	<det <sup>a</sup>	<det <sup>a</sup>	182 <sup>b</sup>	87	68.3
2	α-pinene + O <sub>3</sub>	ozonolysis	5.4	<det <sup>a</sup>	<det <sup>a</sup>	50 <sup>c</sup>	12.5	56.8
3	α-pinene + OH	low NO <sub>x</sub>	4.2	<det <sup>a</sup>	<det <sup>a</sup>	46	13.7	63.9
4	α-pinene + OH	high NO <sub>x</sub>	4.9	447	400	47	15.4	53.7
5	isoprene + OH	low NO <sub>x</sub>	5.2	<det <sup>a</sup>	<det <sup>a</sup>	49	16.2	3.7
6	isoprene + OH	high NO <sub>x</sub>	< 10	536	400	267	11.7	4.3
7	toluene + OH	low NO <sub>x</sub>	< 10	<det <sup>a</sup>	<det <sup>a</sup>	112	10.9	141.5
8	toluene + OH	high NO <sub>x</sub>	< 10	583	423	136	9.3	50.3
9	<i>m</i> -xylene + OH	low NO <sub>x</sub>	< 10	<det <sup>a</sup>	<det <sup>a</sup>	114	9.8	190.4
10	<i>m</i> -xylene + OH	high NO <sub>x</sub>	< 10	501	538	200	9.3	52.0
11	naphthalene + OH	low NO <sub>x</sub>	8.3	<det <sup>a</sup>	<det <sup>a</sup>	20 <sup>c</sup>	10.5	53.1
12	naphthalene + OH	high NO <sub>x</sub>	6.3	431	370	25 <sup>c</sup>	12.8	39.0
13	phenol + OH	low NO <sub>x</sub> , nucleation	4.9	<det <sup>a</sup>	<det <sup>a</sup>	21	0.1	30.5
14	phenol + OH	high NO <sub>x</sub> , nucleation	3.7	332	545	19	0.0	24.8
15	guaiacol + OH	low NO <sub>x</sub>	5.7	<det <sup>a</sup>	<det <sup>a</sup>	6	16.3	11.9
16	guaiacol + OH	high NO <sub>x</sub>	4.8	267	427	7	12.6	12.8
17	syringol + OH	low NO <sub>x</sub>	3.7	<det <sup>a</sup>	<det <sup>a</sup>	108	10.8	228
18	syringol + OH	high NO <sub>x</sub> , nucleation	3.7	238	508	50	0.0	34.8
19	acrolein + OH	high NO <sub>x</sub>	7.2	215	389	412	13.2	21.3
20	methacrolein + OH	high NO <sub>x</sub>	9.3	725	368	186	11.4	10.1
21	crotonaldehyde + OH	high NO <sub>x</sub>	9.0	215	370	252	12.1	14.0

<sup>a</sup> Below the detection limit of the measurement.

<sup>b</sup> Equilibrium concentration.

<sup>c</sup> Approximate initial concentration.

<sup>d</sup> Mass loadings are calculated by multiplying the change in DMA volume by an estimated density. Estimated densities of glyoxal, α-pinene, isoprene (and unsaturated aldehydes), single-ringed aromatics, naphthalene, and methoxyphenol SOA were taken from Galloway et al. (2009); Bahreini et al. (2005); Kroll et al. (2006); Ng et al. (2007); Chan et al. (2009) respectively.

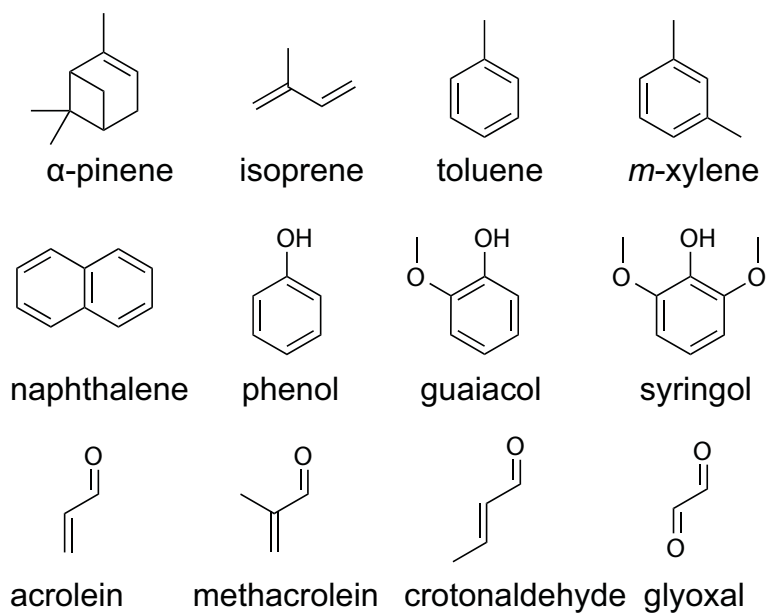


**Figure 4.1:** Structures of the SOA precursors presented in this study.

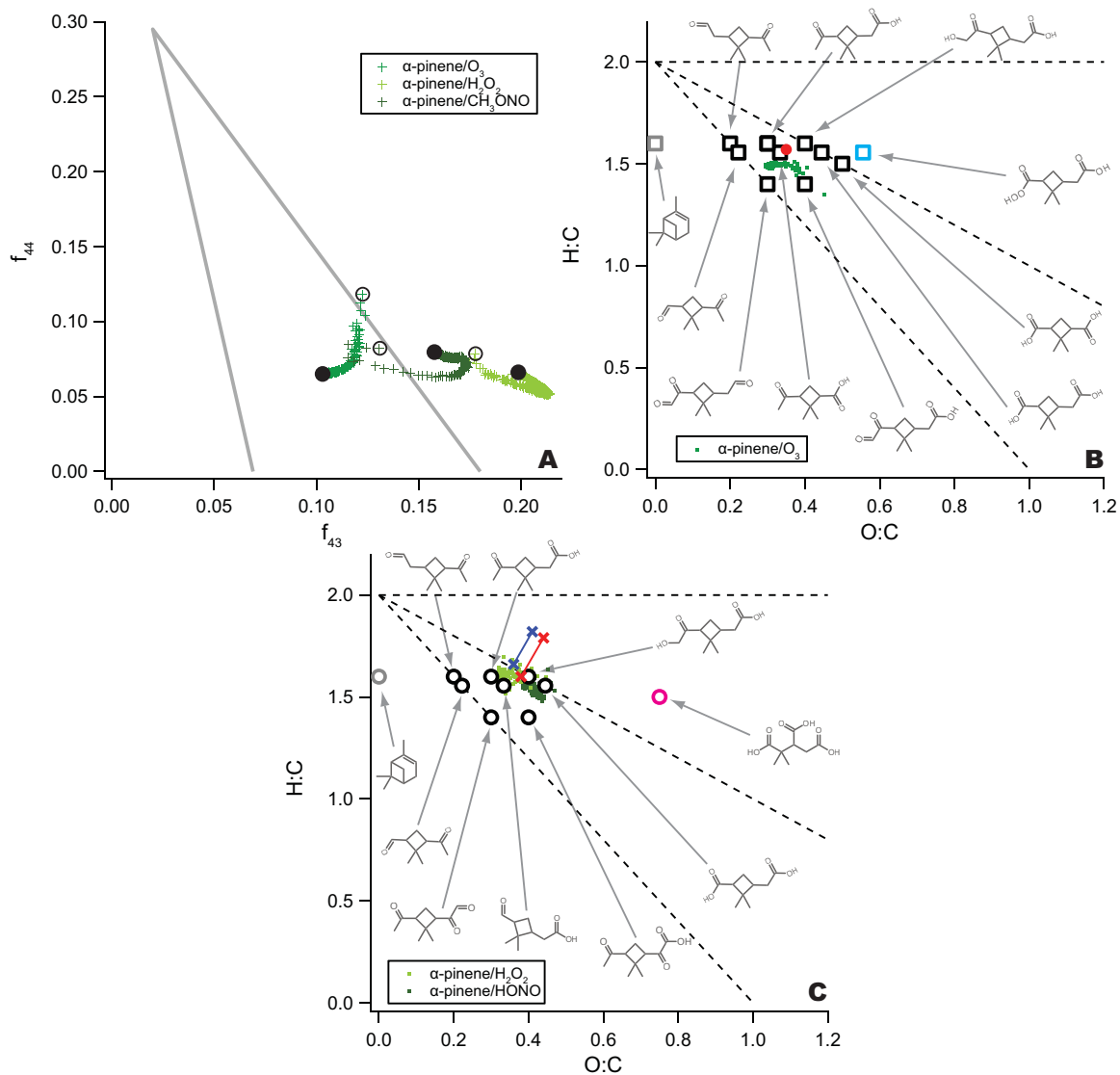


**Figure 4.2:** (A) Triangle plot for  $\alpha$ -pinene SOA formed from ozonolysis and high- and low- $NO_x$  photooxidation. Here and in subsequent figures, the outline of the triangle (Ng et al., 2010) is shown in gray. Open and closed black circles represent the beginning and end of the experiments, respectively. (B) Van Krevelen diagram for SOA formed from  $\alpha$ -pinene ozonolysis.  $\alpha$ -pinene and SOA products identified by Yu et al. (1999) represented by gray and black boxes respectively. The molar weighted average of the elemental ratios of identified SOA products is represented by the red circle (Chhabra et al., 2010). The blue square denotes peroxypinic acid, a product of  $\alpha$ -pinene ozonolysis proposed by Docherty et al. (2005). Here and in subsequent figures, lines with slopes of 0,  $-1$  and  $-2$  are represented by dashed lines. (C) Van Krevelen diagram for SOA formed from the high- and low- $NO_x$  photooxidation of  $\alpha$ -pinene.  $\alpha$ -pinene is represented by a gray square, and SOA products identified by Jaoui and Kamens (2001) and Szmigielski et al. (2007) are represented by black and pink circles, respectively. Ranges of elemental ratios as measured by FTIR data are represented by red (low- $NO_x$ ) and blue (high- $NO_x$ ) crosses.

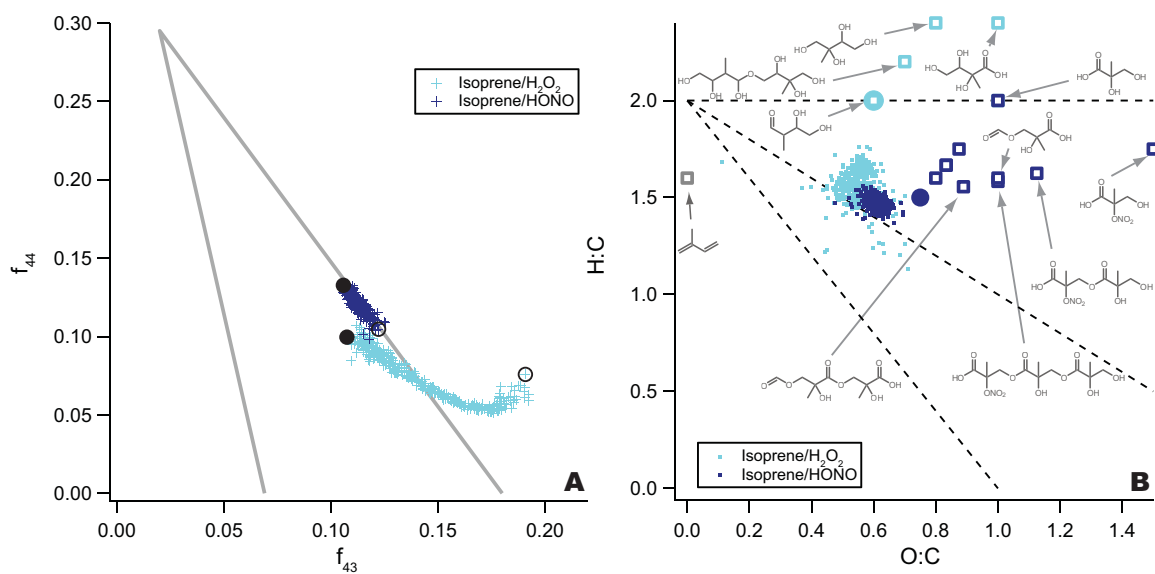


**Figure 4.3:** (A) Triangle plot for SOA formed from photooxidation of isoprene under low- and high- $NO_x$  conditions. Open and closed black circles represent the beginning and end of the experiments, respectively. (B) Van Krevelen diagram for SOA formed from photooxidation of isoprene under low- and high- $NO_x$  conditions. Identified SOA products of each  $NO_x$  condition are presented in blue boxes of the corresponding color (Surratt et al., 2006; Claeys et al., 2004; Wang et al., 2005; Surratt et al., 2007; Gomez-Gonzalez et al., 2008). Surratt et al. (2006) found that under low- $NO_x$  conditions,  $\sim 25\%$ – $30\%$  of the SOA mass in seeded experiments is organic peroxides, and under high- $NO_x$  conditions, oligomers comprise  $\sim 22\%$ – $34\%$  of the SOA mass. Oligomeric limits for each  $NO_x$  condition are represented by circles.

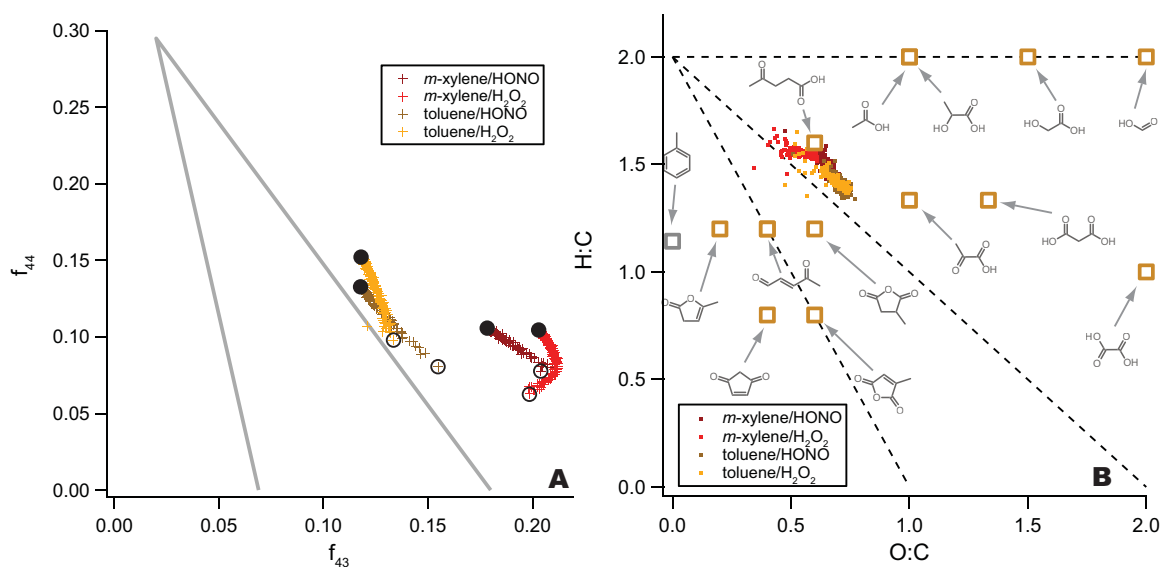


**Figure 4.4:** (A) Triangle plot for SOA formed from photooxidation of toluene and *m*-xylene under low- and high-NO<sub>x</sub> conditions. Open and closed black circles represent the beginning and end of the experiments, respectively. (B) Van Krevelen diagram for SOA formed from photooxidation of toluene and *m*-xylene under low- and high-NO<sub>x</sub> conditions. Identified toluene-SOA products are presented in tan boxes (Sato et al., 2007; Hamilton et al., 2005; Bloss et al., 2005; Fisseha et al., 2004; Jang and Kamens, 2001). Substantial mass closure has been difficult to achieve in molecular characterization studies.



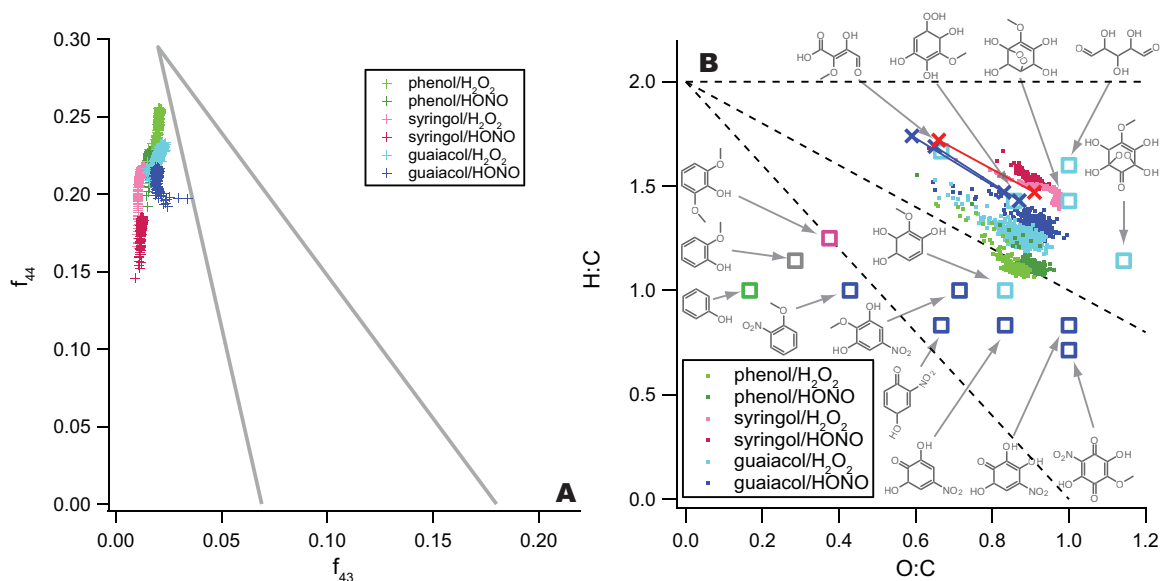


**Figure 4.6:** (A) Triangle plot for SOA formed from photooxidation of phenol, guaiacol, and syringol under low- and high- $NO_x$  conditions. Experiment progression is from bottom to top. (B) Van Krevelen diagram for SOA formed from photooxidation of phenol, guaiacol, and syringol under low- and high- $NO_x$  conditions. Identified guaiacol-SOA products of high- and low- $NO_x$  conditions are presented dark and light blue boxes respectively. Ranges of elemental ratios as measured by FTIR data are represented by red (low- $NO_x$ ) and blue (high- $NO_x$ ) crosses. Quantification of molecular species in methoxyphenol SOA systems has not yet been accomplished.



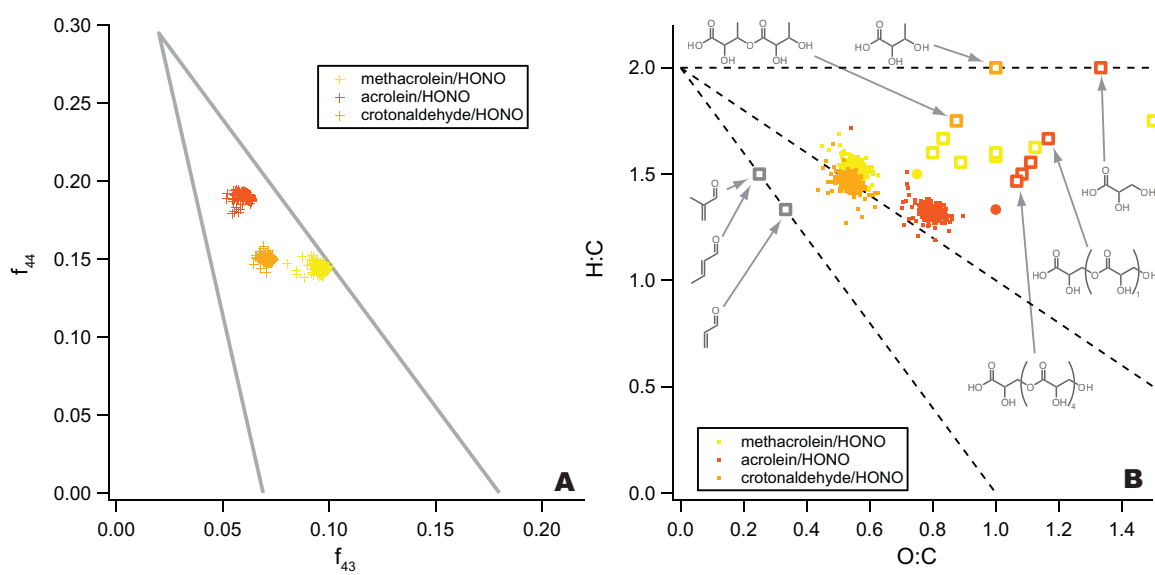


**Figure 4.7:** (A) Triangle plot for SOA formed from photooxidation of methacrolein, acrolein, and crotonaldehyde. (B) Van Krevelen diagram for SOA formed from photooxidation of methacrolein, acrolein, and crotonaldehyde. Identified SOA products of each system are presented in boxes of the corresponding color (Chan et al., 2010). Oligomeric limits for each system condition are represented by circles.

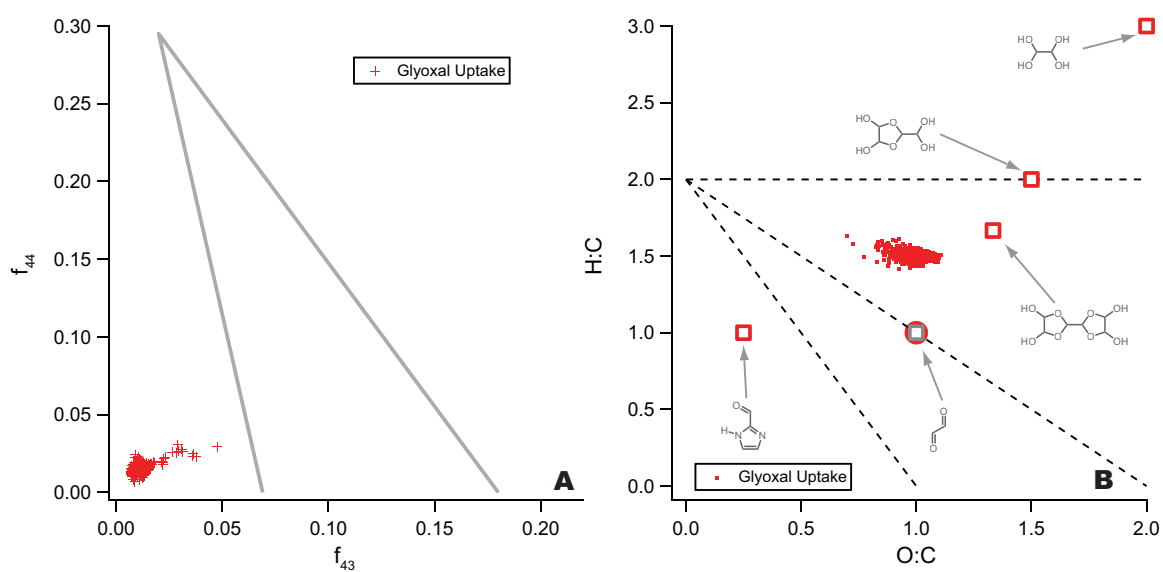


**Figure 4.8:** (A) Triangle plot for SOA formed from reactive uptake of glyoxal onto wet ammonium sulfate aerosol. (B) Van Krevelen diagram for SOA formed from the uptake of glyoxal onto wet ammonium sulfate aerosol. Proposed SOA products are presented in boxes (Galloway et al., 2009; Kua et al., 2008; Loeffler et al., 2006). Oligomeric limits for glyoxal oligomerization condition is represented by a circle.

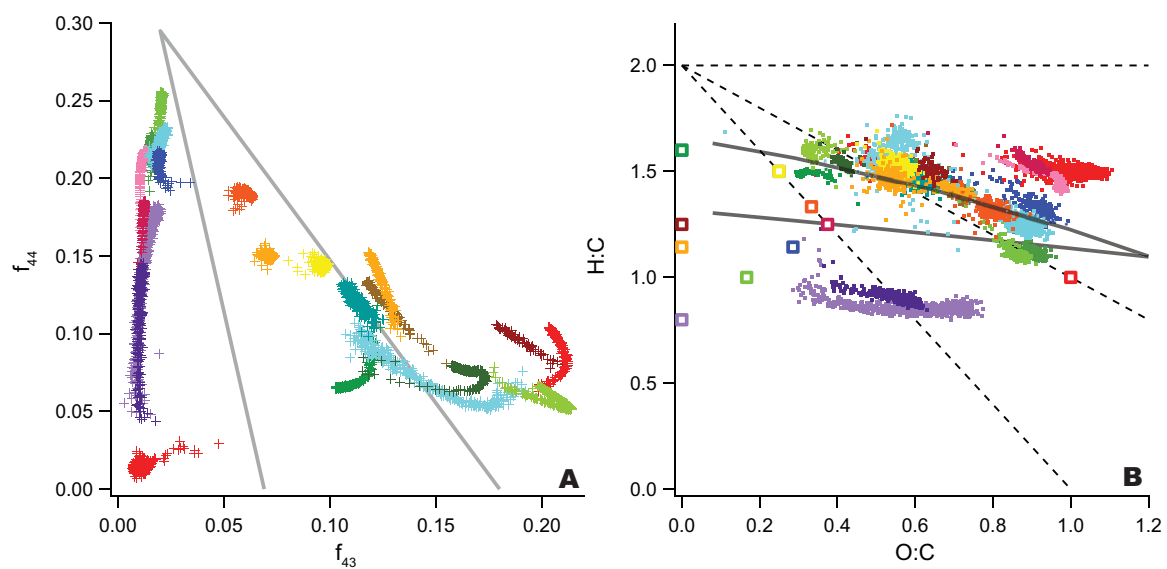


**Figure 4.9:** (A) Triangle plot for all SOA systems (B) Van Krevelen diagram for all SOA systems. SOA precursors are represented by corresponding colored boxes. The “VK-triangle” parameterization developed by Ng et al. (2011) is represented by solid gray curves.

## Chapter 5

# Conclusions

Ambient SOA represents the complex confluence of many different precursors and processes that mix spatially and temporally. Chamber experiments attempt to isolate specific variables to simplify these processes and elucidate SOA formation mechanisms. While generally unable to give compound specific measurements in organic aerosol mixtures, the AMS has become important in bulk characterization of OA. With the addition of a high-resolution mass spectrometer to the original AMS design, the HR-ToF-AMS can now provide chemical formulas of measured ions; the additional information now allows for the estimation of the elemental composition (i.e. oxygen content) of SOA. This thesis presents the analysis of HR-ToF-AMS data of chamber experiments to understand the chemistry behind SOA formation from a variety of precursors.

Glyoxal is produced by a wide variety of biogenic and anthropogenic VOCs, many of which are SOA precursors, and is considered a tracer for SOA formation. Chapter 2 examines the uptake processes onto wet ammonium sulfate seed aerosol using a variety of instrumentation in dark conditions and in the presence of light. Organic fragments from glyoxal dimers and trimers are observed within the aerosol under dark and irradiated conditions. Analysis of HR-ToF-AMS spectra provides evidence for irreversible formation of carbon-nitrogen (C-N) compounds in the aerosol such as 1H-imidazole-2-carboxaldehyde. Carboxylic acids and organic esters are also identified within the aerosol. An organosulfate, which had been previously assigned as glyoxal sulfate in ambient samples and chamber studies of isoprene oxidation, was observed only in the irradiated experiments. Comparison with a laboratory synthesized standard and chemical considerations strongly suggest that this organosulfate is glycolic acid sulfate, an isomer of the previously proposed glyoxal sulfate. More study is required to determine the rates and relevance of such particle phase reactions; ambient glyoxal concentrations are substantially lower than those in the chamber experiment (2–3 orders of magnitude), so it is less likely the organic character of ambient aerosol will involve multiple glyoxal molecules such as oligomers and 1H-imidazole-2-carboxaldehyde. However, reactions between glyoxal and other aldehydes are likely occur and these should be identified. The newly identified imidazoles are light-absorbing species, and thus have may have a large influence on the optical properties of organic aerosols which should be investigated.

Chapters 3 and 4 investigate the elemental composition and oxidation of a variety of chamber SOA systems as measured by a HR-ToF-AMS. Chapter 3 in particular shows that the fraction of organic signal at  $m/z$  44 is generally a good measure of SOA oxygenation and that measured and estimated O/C ratios tend to converge as the fraction of organic signal at  $m/z$  44 increases. Chapter 4 expands on the set of SOA precursors presented in chapter 3 and presents HR-ToF-AMS data in both “triangle plot” and Van Krevelen spaces. SOA formed under high- and low-NO<sub>x</sub> conditions occupy similar areas in the “triangle plot” and Van Krevelen diagram and SOA generated from already oxidized precursors starts higher on the “triangle plot.” The most oxidized SOA come from the photooxidation of methoxyphenol precursors which yielded SOA O/C ratios near unity.  $\alpha$ -pinene ozonolysis and naphthalene photooxidation SOA systems have had the highest degree of mass closure in previous chemical characterization studies and also show the best agreement between AMS elemental composition measurements and elemental composition of identified species. From the spectra of chamber SOA, we are able to reproduce the triangular region originally constructed with ambient OOA showing that SOA becomes more chemically similar as it ages.

Chapter 3 discusses the uncertainties inherent in AMS elemental analysis. More work should be done to further quantify the error in elemental analysis. As more standards become available or as methods to measure hard to sample species are developed, the calibration factors of AMS elemental analysis should be revised to reflect ambient OA. Chapter 3 also compares ambient PMF component spectra and elemental composition to those measured in chamber experiments. Previous studies have noted that AMS mass spectra of chamber data do not exhibit as much oxidation as the OOA mass spectrum. While chapters 3 and 4 show that O/C ratios comparable to that of LV-OOA can be achieved, there is a need to devise chamber experiments that reach OH exposures needed to form the most oxygenated SOA. In addition more chamber experiments are needed more fully characterize the “triangle plot” space. Molecular level chemical characterization of SOA will also be useful in comparison to AMS elemental measurements, especially in systems for which mass closure has been difficult.

## Appendix A

# Supplementary Material for “Elemental Analysis of Chamber Organic Aerosol Using an Aerodyne High-Resolution Aerosol Mass Spectrometer”\*

---

\*Reproduced with permission from “Elemental analysis of chamber organic aerosol using an aerodyne high-resolution aerosol mass spectrometer” by P. S. Chhabra, R. C. Flagan, and J. H. Seinfeld, *Atmospheric Chemistry and Physics*, 10, 4111–4131, doi:10.5194/acp-10-4111-2010 Copyright 2010 by the Authors. CC Attribution 3.0 License.

**Table 1:** Calibration factors and estimated uncertainties for O/C, H/C, N/C and OM/OC as determined by Aiken et al. (2008)

Ratio	Calibration Factor	Measurement Uncertainty
O/C	0.75	31%
H/C	0.91	10%
N/C	0.96	22%
OM/OC	-	6%



**Table 2:** Ratios of particle-phase signals of  $\text{CO}^+$  to  $\text{CO}_2^+$ .

System	Organic $\text{CO}^+/\text{CO}_2^+$ Estimate
$\alpha$ -pinene/ $\text{O}_3$	0.98
Glyoxal Uptake	5.00
Isoprene/OH	1.00
Aromatic/OH	1.03
Naphthalene/OH	1.17

**Table 3:** O/C and H/C ratios of  $\alpha$ -pinene ozonolysis SOA determined from offline by Yu et al. (1999, Table XI)

Product Name	Formula	Molar Yield		
		6-9-98a	6-9-98b	6-17-98a
Pinic acid	$C_9H_{14}O_4$	1.8	3.9	2.8
Norpinic acid	$C_8H_{12}O_4$	0.08	0.09	0.05
Hydroxy pinonaldehydes	$C_{10}H_{16}O_3$	2.4	1.1	2
Pinonic acid	$C_{10}H_{16}O_3$	1.7	1.6	1.3
Norpinonic acid and isomers	$C_9H_{14}O_3$	2.1	4.8	2.8
Pinonaldehyde	$C_{10}H_{16}O_2$	0.8	0.3	0.9
Norpinonaldehyde	$C_9H_{14}O_2$	0.1	0.2	0.2
Hydroxy pinonic acid	$C_{10}H_{14}O_4$	2.1	1.3	2.1
A13	$C_{10}H_{16}O_3$	0.08	0.12	0.1
A14	$C_{10}H_{14}O_3$	0.55	0.48	0.8
	<b>O/C</b>	<b>0.34</b>	<b>0.36</b>	<b>0.35</b>
	<b>H/C</b>	<b>1.58</b>	<b>1.56</b>	<b>1.57</b>

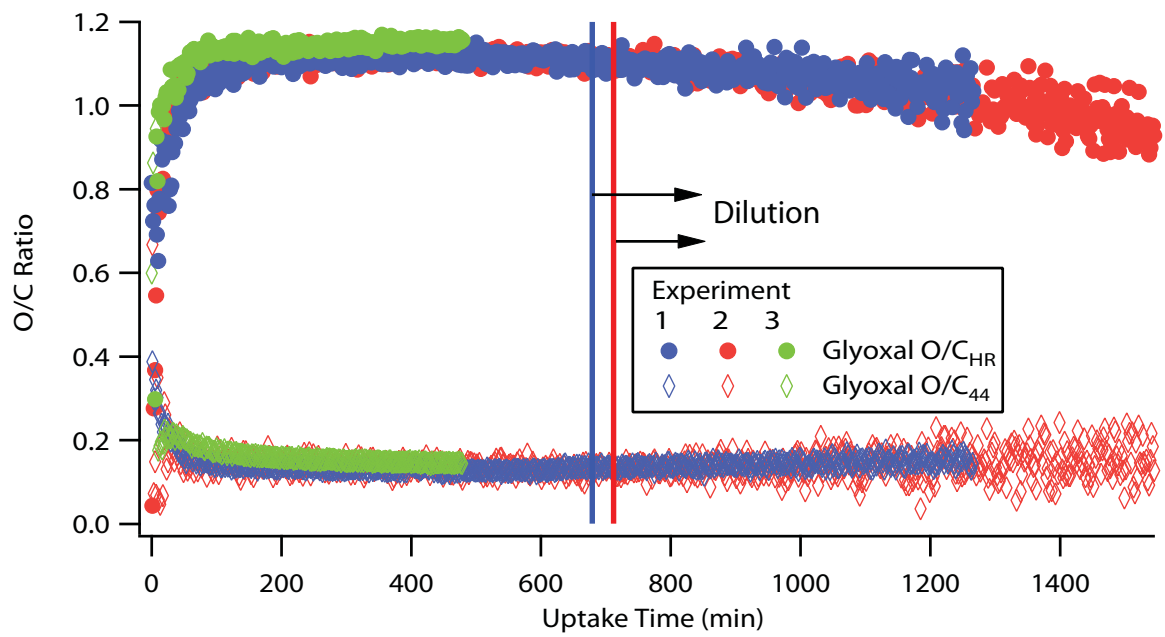


**Figure 1:**  $O/C_{HR}$  and  $O/C_{44}$  for glyoxal uptake SOA.

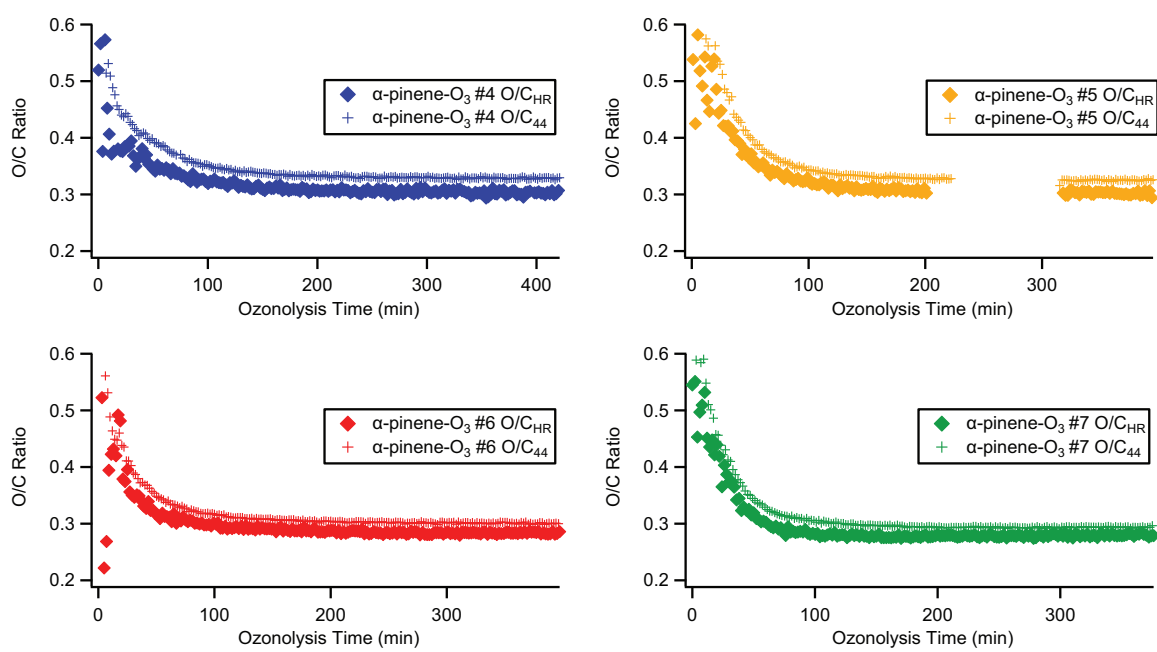


**Figure 2:**  $O/C_{HR}$  and  $O/C_{44}$  for  $\alpha$ -pinene ozonolysis SOA.

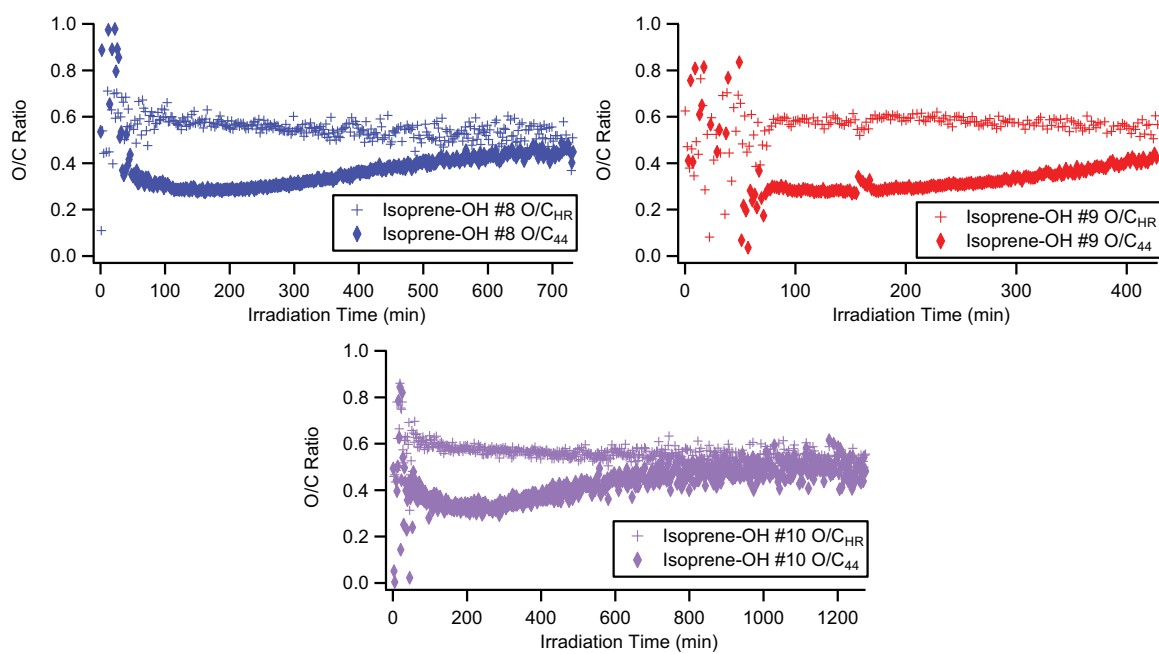


**Figure 3:**  $O/C_{HR}$  and  $O/C_{44}$  for isoprene SOA formed under low- $NO_x$  conditions.

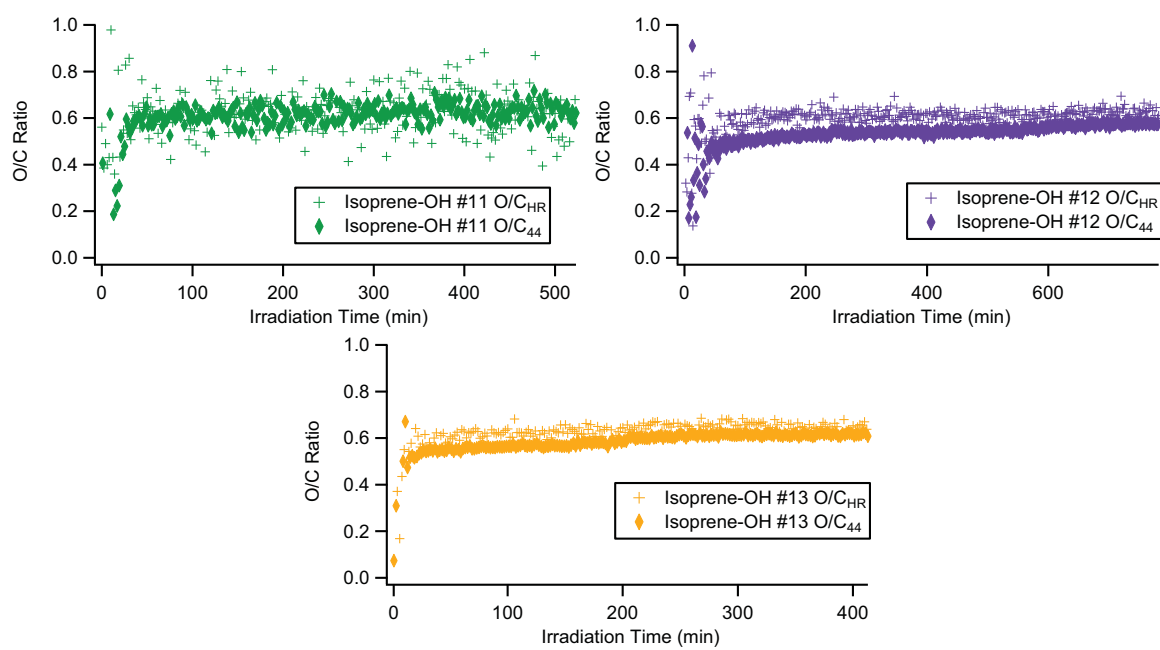


**Figure 4:**  $O/C_{HR}$  and  $O/C_{44}$  for isoprene SOA formed under high- $NO_x$  conditions.

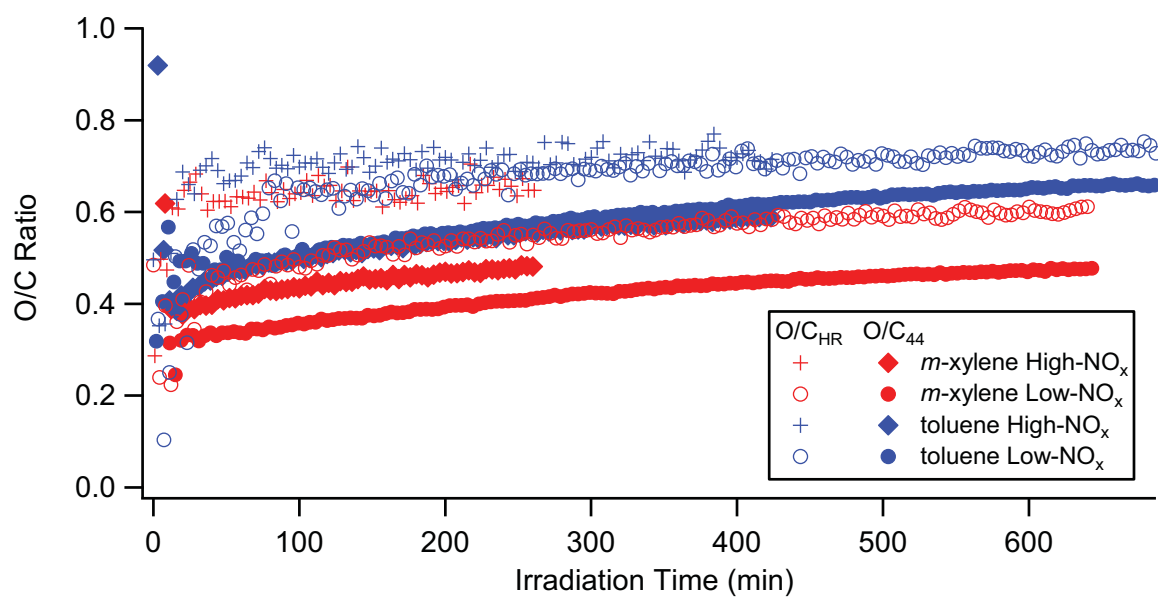


**Figure 5:**  $O/C_{HR}$  and  $O/C_{44}$  for single-ring aromatic SOA.

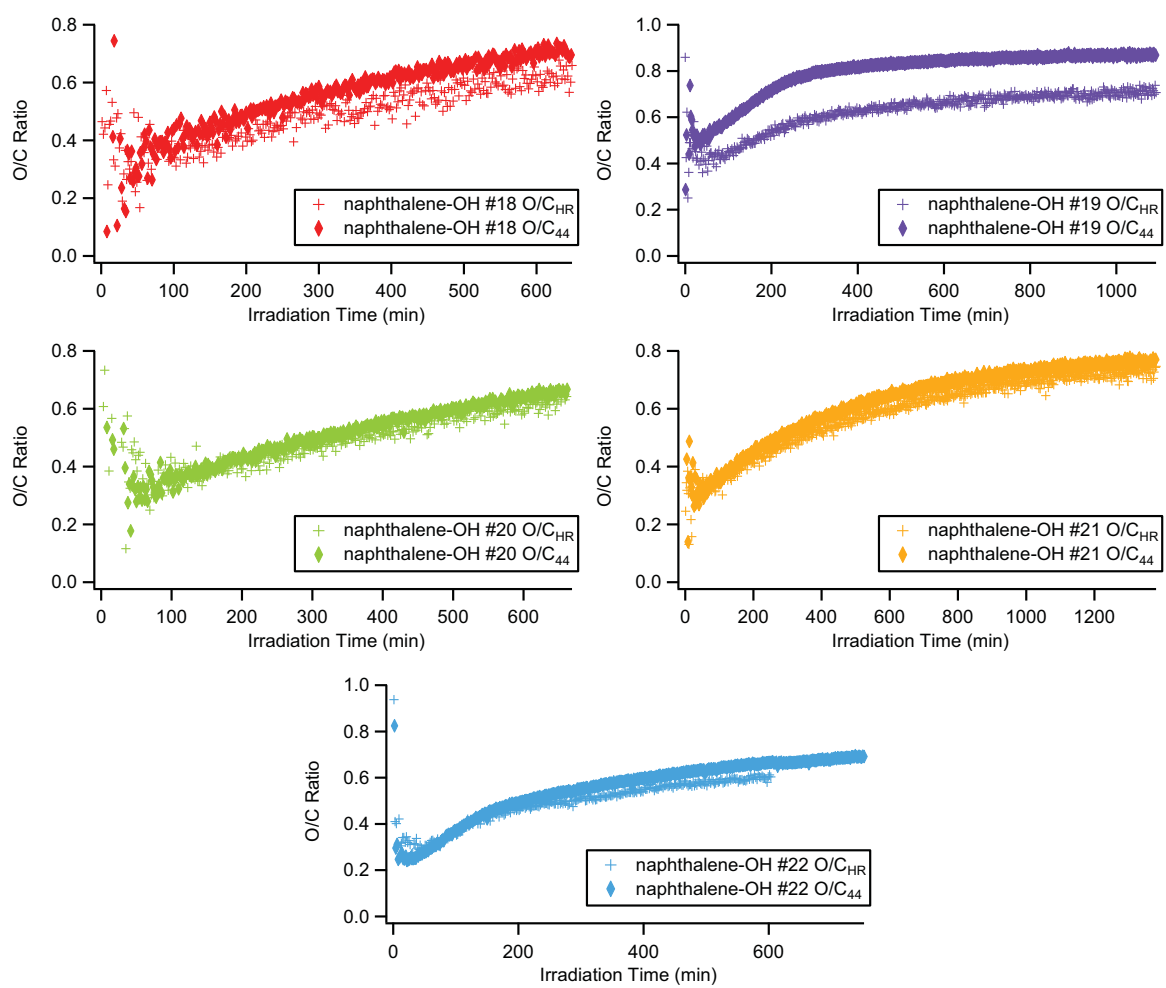


**Figure 6:**  $O/C_{HR}$  and  $O/C_{44}$  for naphthalene SOA formed under low- $NO_x$  conditions.



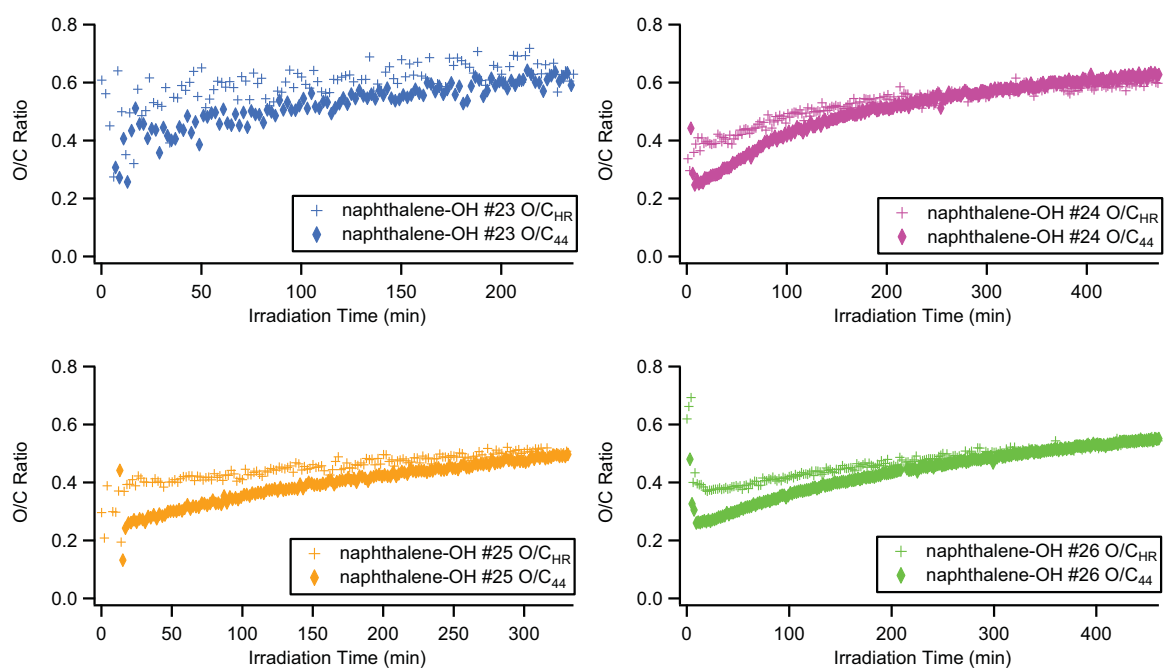


**Figure 7:**  $O/C_{HR}$  and  $O/C_{44}$  for naphthalene SOA formed under high- $NO_x$  conditions.

## Bibliography

Aiken, A. C., Decarlo, P. F., Kroll, J. H., Worsnop, D. R., Huffman, J. A., Docherty, K. S., Ulbrich, I. M., Mohr, C., Kimmel, J. R., Sueper, D., Sun, Y., Zhang, Q., Trimborn, A., Northway, M., Ziemann, P. J., Canagaratna, M. R., Onasch, T. B., Alfarra, M. R., Prevot, A. S. H., Dommen, J., Duplissy, J., Metzger, A., Baltensperger, U., and Jimenez, J. L.: O/C and OM/OC ratios of primary, secondary, and ambient organic aerosols with high-resolution time-of-flight aerosol mass spectrometry, *Environ. Sci. Technol.*, 42, 4478–4485, doi:10.1021/Es703009q, 2008.

Yu, J. Z., Cocker, D. R., Griffin, R. J., Flagan, R. C., and Seinfeld, J. H.: Gas-phase ozone oxidation of monoterpenes: Gaseous and particulate products, *J. Atmos. Chem.*, 34, 207–258, doi:10.1023/A:1006254930583, 1999.

## Appendix B

# Supplementary Material for “Elemental Composition and Oxidation of Chamber Organic Aerosol”\*

---

\*Reproduced with permission from “Elemental composition and oxidation of chamber organic aerosol” by P. S. Chhabra, N. L. Ng, M. R. Canagaratna, A. L. Corrigan, L. M. Russell, D. R. Worsnop, R. C. Flagan, and J. H. Seinfeld, *Atmospheric Chemistry and Physics Discussions*, 11, 10305–10342, doi:10.5194/acpd-11-10305-2011, Copyright 2011 by the Authors. CC Attribution 3.0 License.

**Table 1:** Average ratios of particle phase signals of  $\text{CO}^+$  to  $\text{CO}_2^+$ . Ratios were determined from high-resolution spectra that had adequate separation of the  $\text{CO}^+$  and  $\text{N}_2^+$  ions, typically from experiments with high organic loadings. The average values found are close to the default value of 1.0 in the AMS High-Resolution Fragmentation Table and in agreement with other studies (Zhang et al., 2005; Takegawa et al., 2007) so this default value was used for all experiments in this study.

SOA Precursor	$\text{CO}^+/\text{CO}_2^+$
glyoxal uptake	5.6 <sup>a</sup>
$\alpha$ -pinene <sup>b</sup>	0.9
toluene	1.1
<i>m</i> -xylene	1.3
isoprene	1.3
naphthalene	1.2
phenol	0.9
guaiacol	1.0
syringol	1.1
acrolein	ND <sup>c</sup>
methacrolein	ND <sup>c</sup>
crotonaldehyde	ND <sup>c</sup>

<sup>a</sup>A value of 5.0 was used for  $\text{CO}^+/\text{CO}_2^+$  in glyoxal uptake experiments presented in this study.

<sup>b</sup>Includes both ozonolysis and photooxidation experiments.

<sup>c</sup>Not Determined.  $\text{CO}^+$  could not be adequately separated from  $\text{N}_2^+$  to determine a ratio accurately.

**Table 2:** Elemental composition of SOA system. Values represent the average ratio for each experiment at the time of maximum O/C.

VOC System	O/C (max)	H/C	N/C	OM/OC	
glyoxal uptake <sup>a</sup>	1.13	1.54	0.01	2.68	
$\alpha$ -pinene + O <sub>3</sub> <sup>a</sup>	0.43	1.47	0.00	1.70	
$\alpha$ -pinene + OH	0.41	1.57	0.02	1.70	
	low-NO <sub>x</sub>	0.40	1.62	0.00	1.67
	high-NO <sub>x</sub>	0.42	1.51	0.03	1.73
isoprene + OH <sup>a</sup>	0.61	1.55	0.02	1.96	
	low-NO <sub>x</sub>	0.59	1.64	0.00	1.92
	high-NO <sub>x</sub>	0.62	1.46	0.04	2.00
aromatics + OH <sup>a</sup>	0.68	1.44	0.04	2.07	
	<i>m</i> -xylene, high-NO <sub>x</sub>	0.66	1.48	0.08	2.09
	<i>m</i> -xylene, low-NO <sub>x</sub>	0.60	1.54	0.00	1.93
	toluene, high-NO <sub>x</sub>	0.72	1.38	0.07	2.15
	toluene, low-NO <sub>x</sub>	0.74	1.39	0.00	2.10
naphthalene + OH <sup>a</sup>	0.62	0.89	0.02	1.93	
	low-NO <sub>x</sub>	0.66	0.88	0.00	1.96
	high-NO <sub>x</sub>	0.57	0.90	0.04	1.89
phenol + OH	0.90	1.11	0.03	2.32	
	low-NO <sub>x</sub>	0.88	1.10	0.00	2.26
	high-NO <sub>x</sub>	0.92	1.12	0.05	2.38
guaiacol + OH	0.92	1.28	0.03	2.37	
	low-NO <sub>x</sub>	0.89	1.26	0.00	2.30
	high-NO <sub>x</sub>	0.94	1.30	0.06	2.43
syringol + OH	0.95	1.47	0.02	2.41	
	low-NO <sub>x</sub>	0.97	1.41	0.00	2.41
	high-NO <sub>x</sub>	0.93	1.52	0.03	2.41
acrolein + OH	0.79	1.31	0.03	2.20	
methacrolein + OH	0.54	1.53	0.02	1.87	
crotonaldehyde + OH	0.56	1.45	0.01	1.88	

<sup>a</sup>Values first reported in Chhabra et al. (2010).

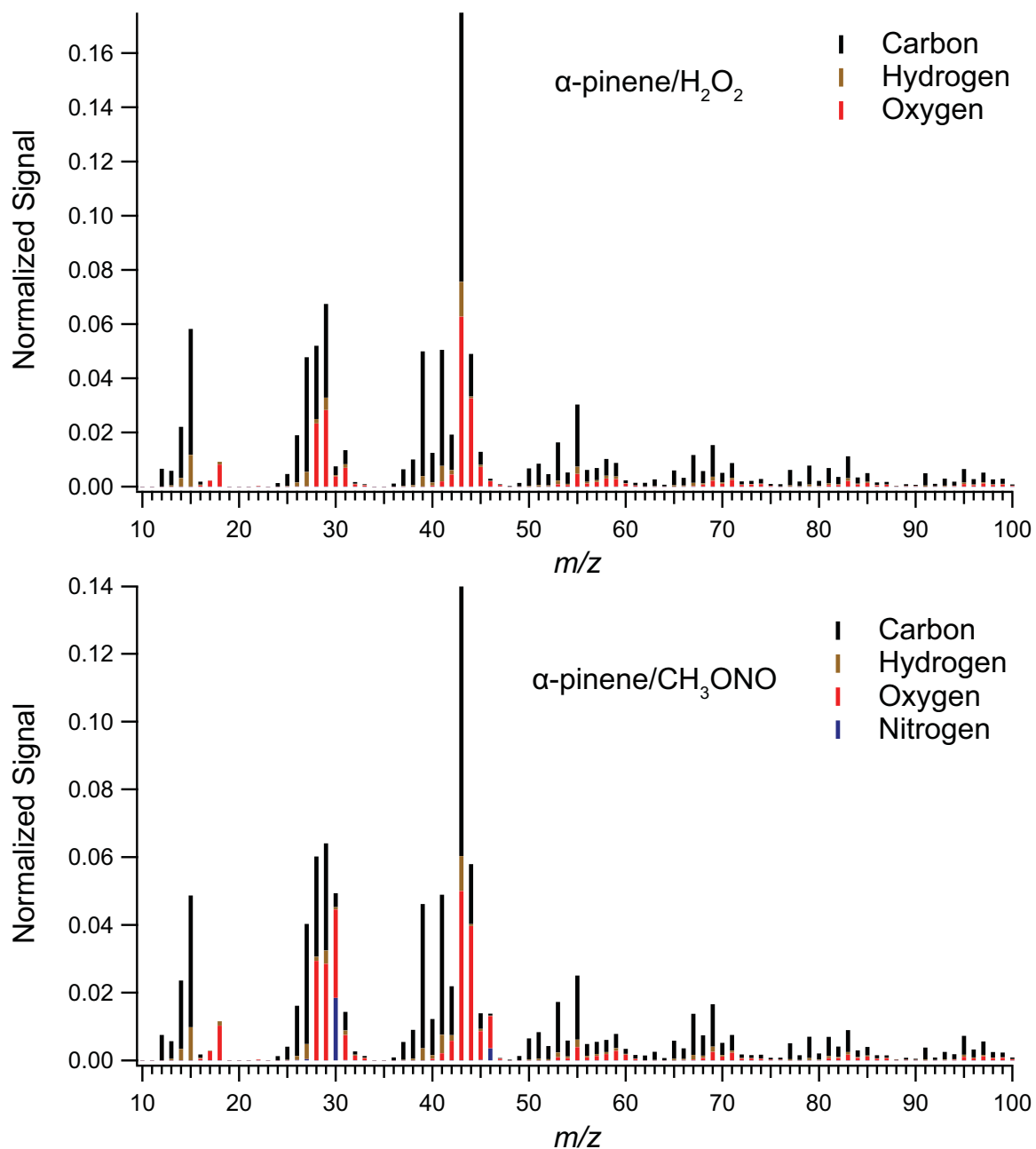


**Figure 1:** High-resolution spectra of  $\alpha$ -pinene photooxidation SOA formed under high- and low-NO<sub>x</sub> conditions.

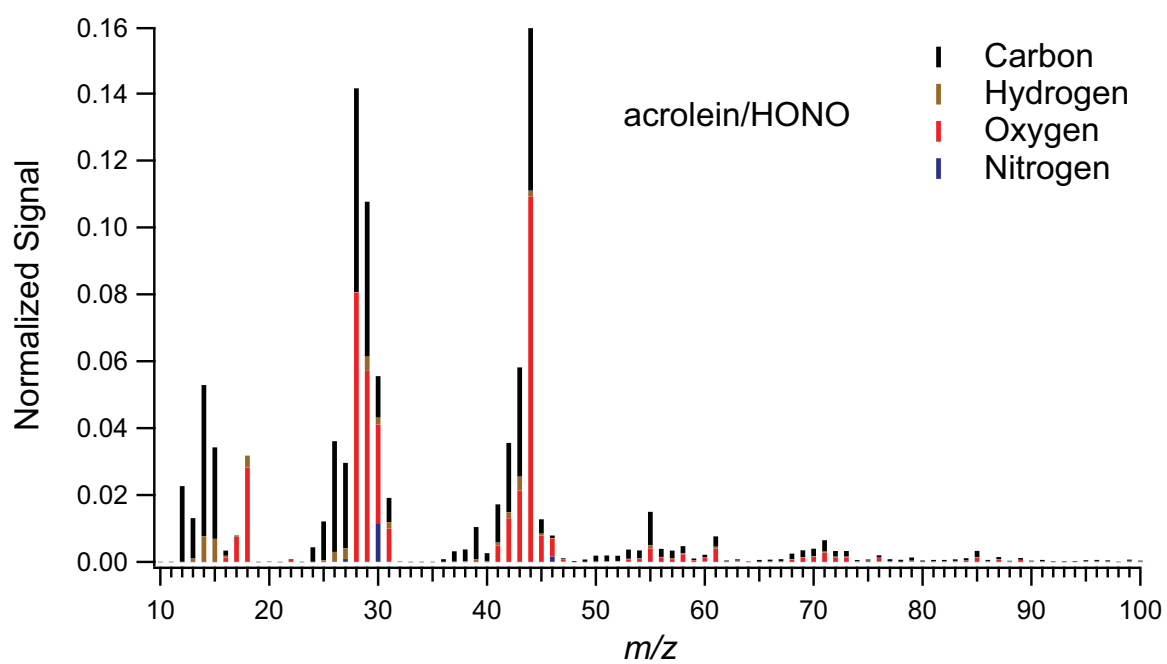


**Figure 2:** High-resolution spectra of acrolein photooxidation SOA.

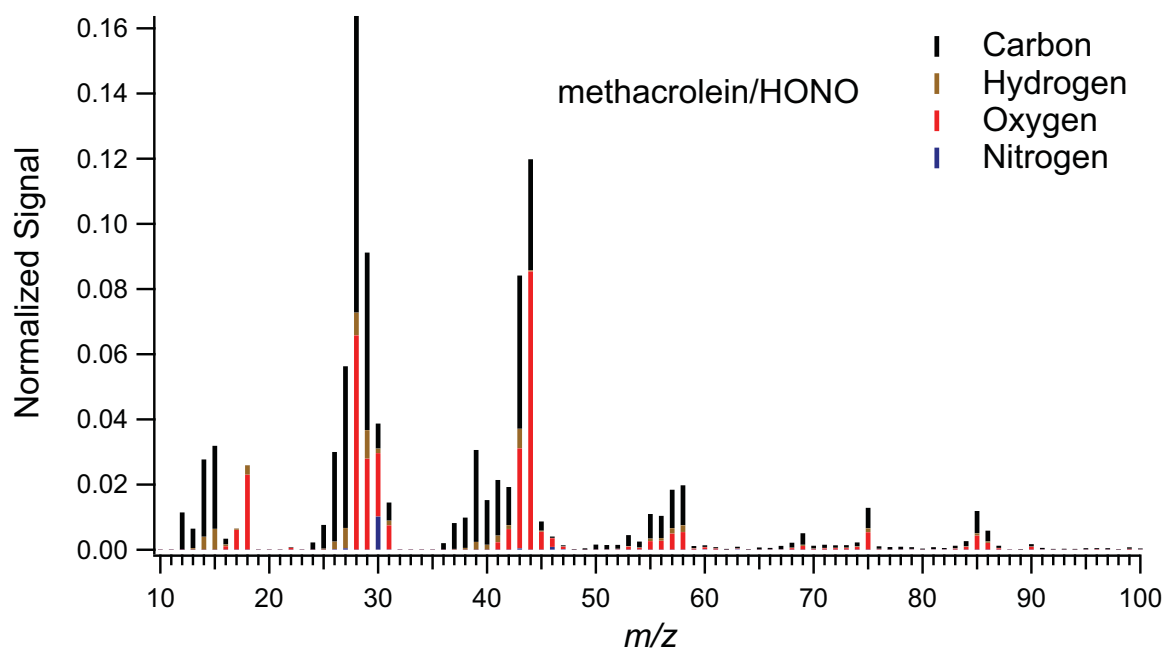


**Figure 3:** High-resolution spectra of methacrolein photooxidation SOA.



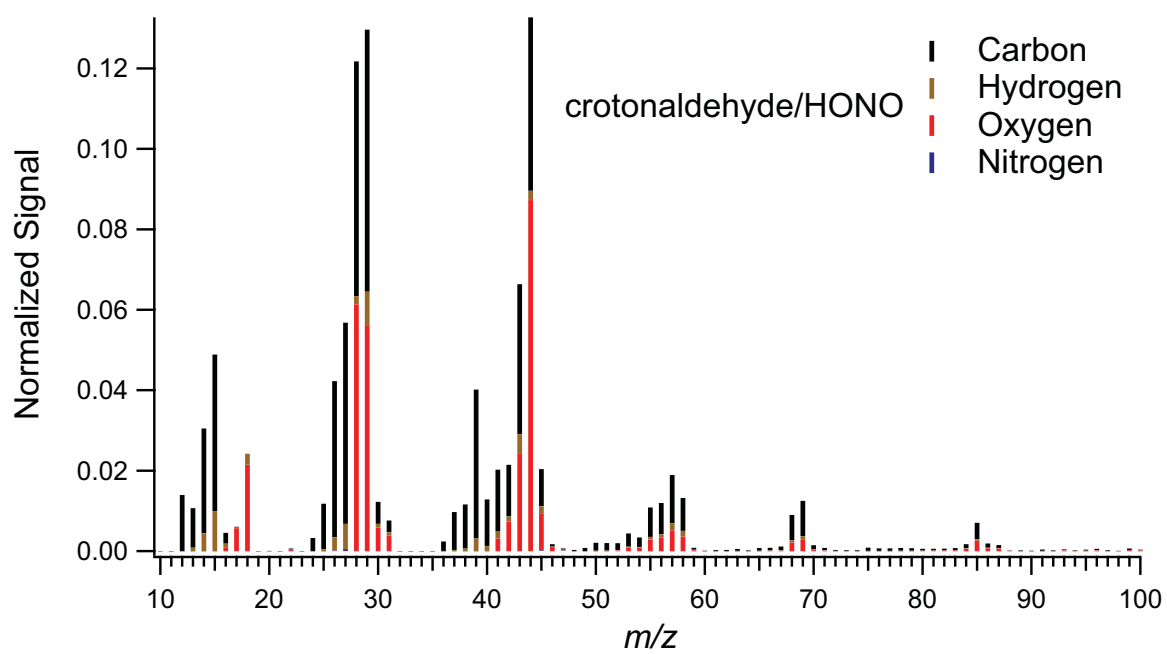


**Figure 4:** High-resolution spectra of crotonaldehyde photooxidation SOA.

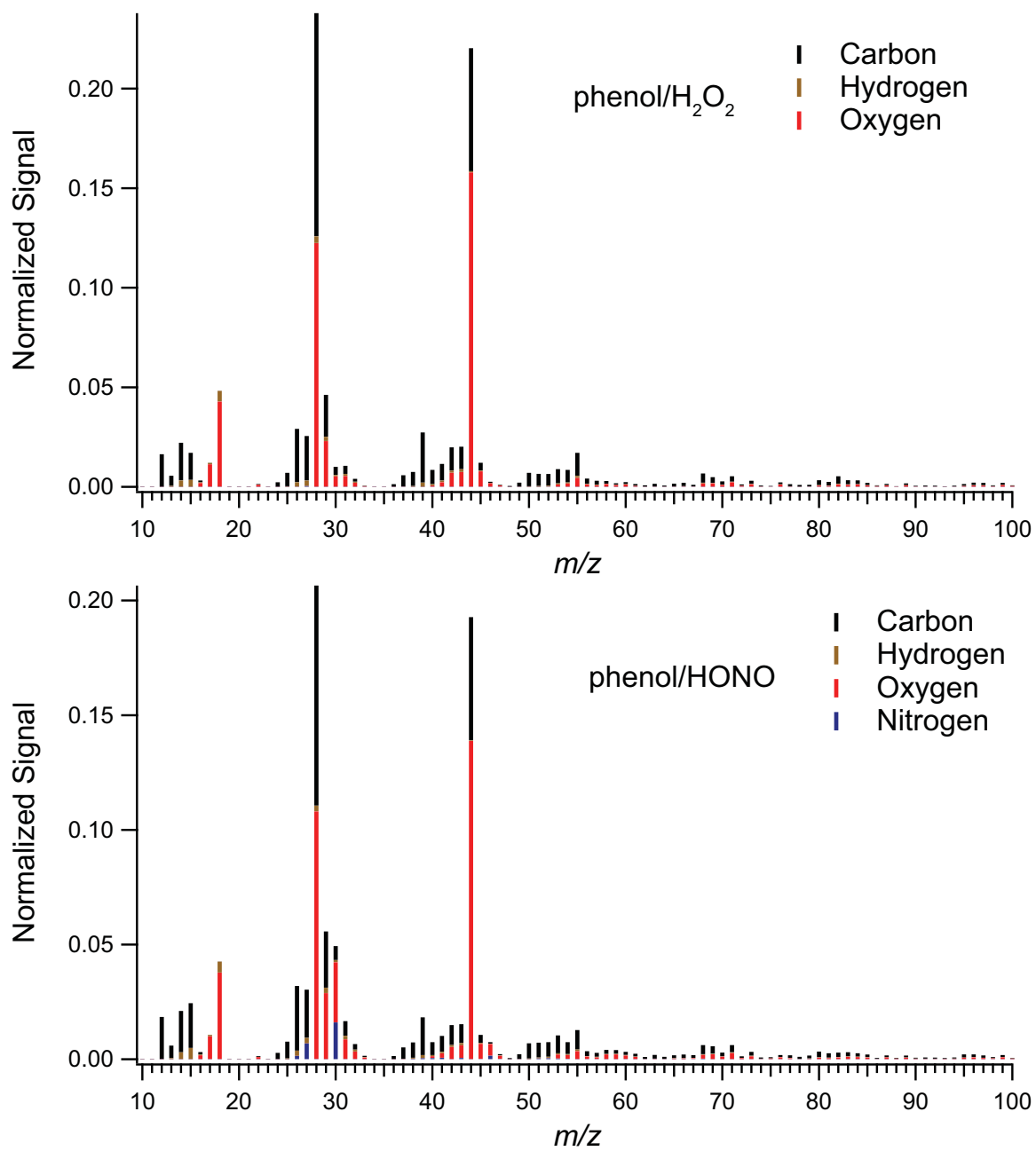


**Figure 5:** High-resolution spectra of phenol photooxidation SOA under high- and low-NO<sub>x</sub>.

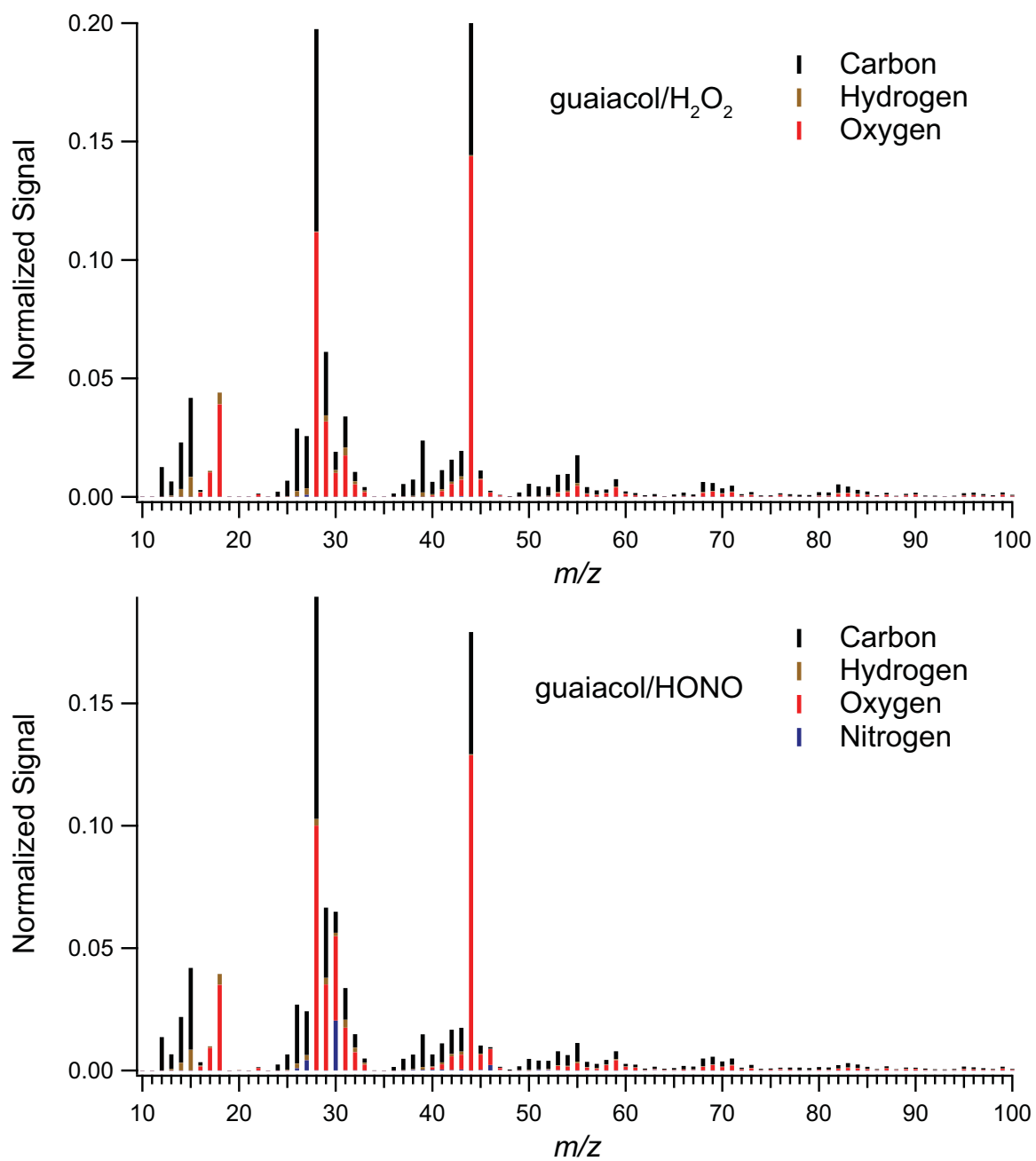


**Figure 6:** High-resolution spectra of guaiacol photooxidation SOA under high- and low-NO<sub>x</sub>.

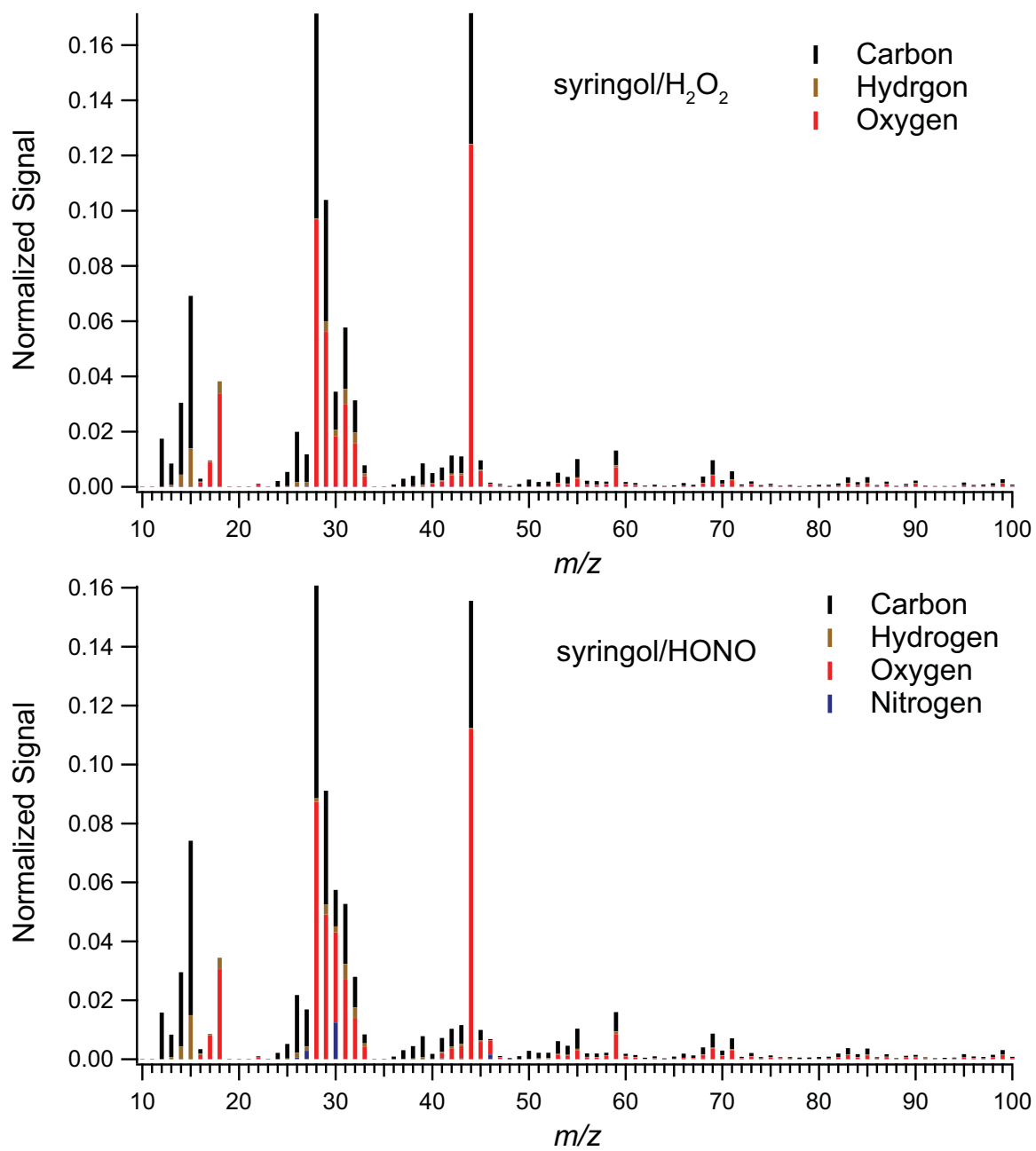


**Figure 7:** High-resolution spectra of syringol photooxidation SOA under high- and low-NO<sub>x</sub>.

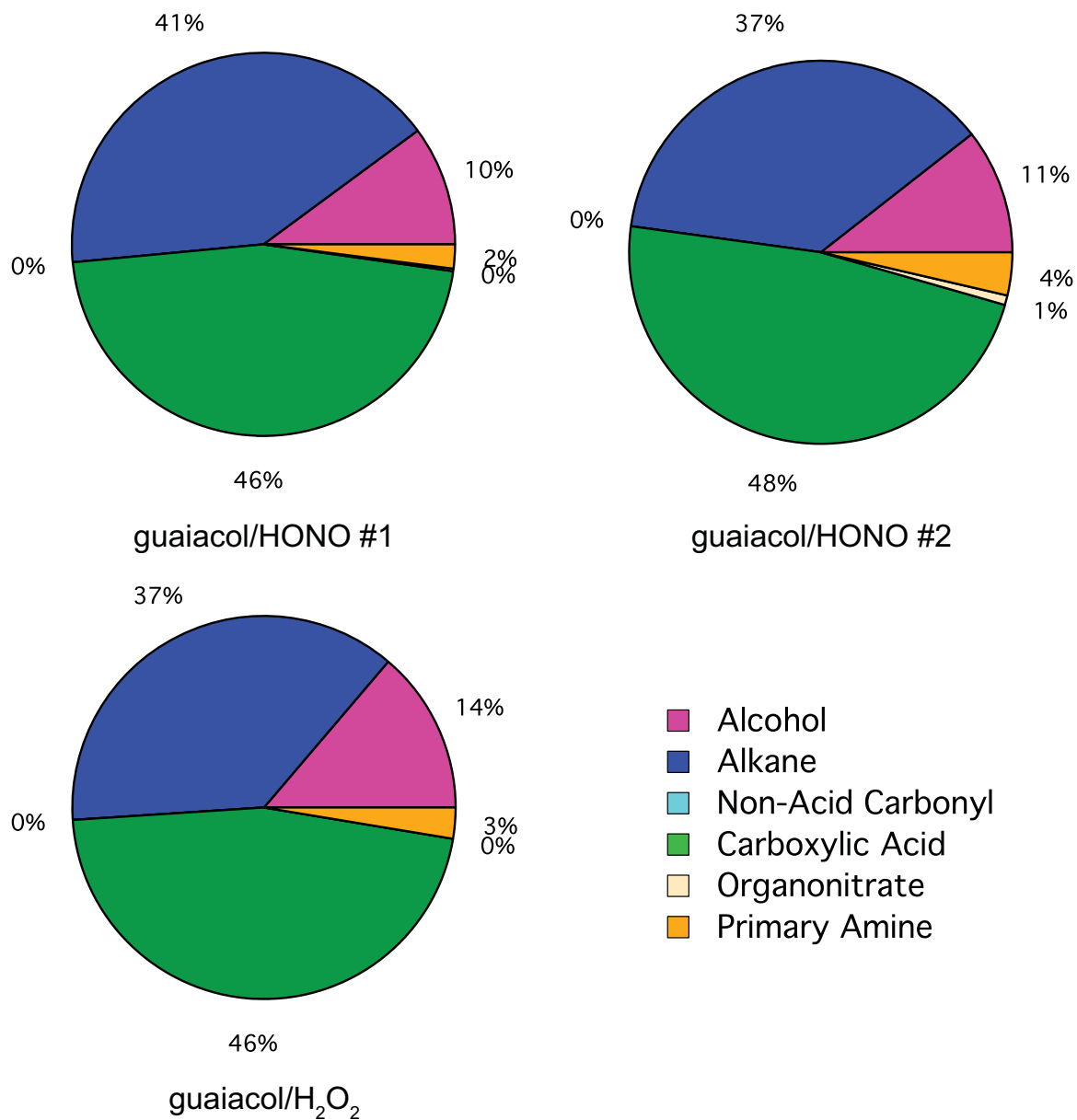


**Figure 8:** Average composition by mass of guaiacol photooxidation SOA as measured by FTIR analysis.

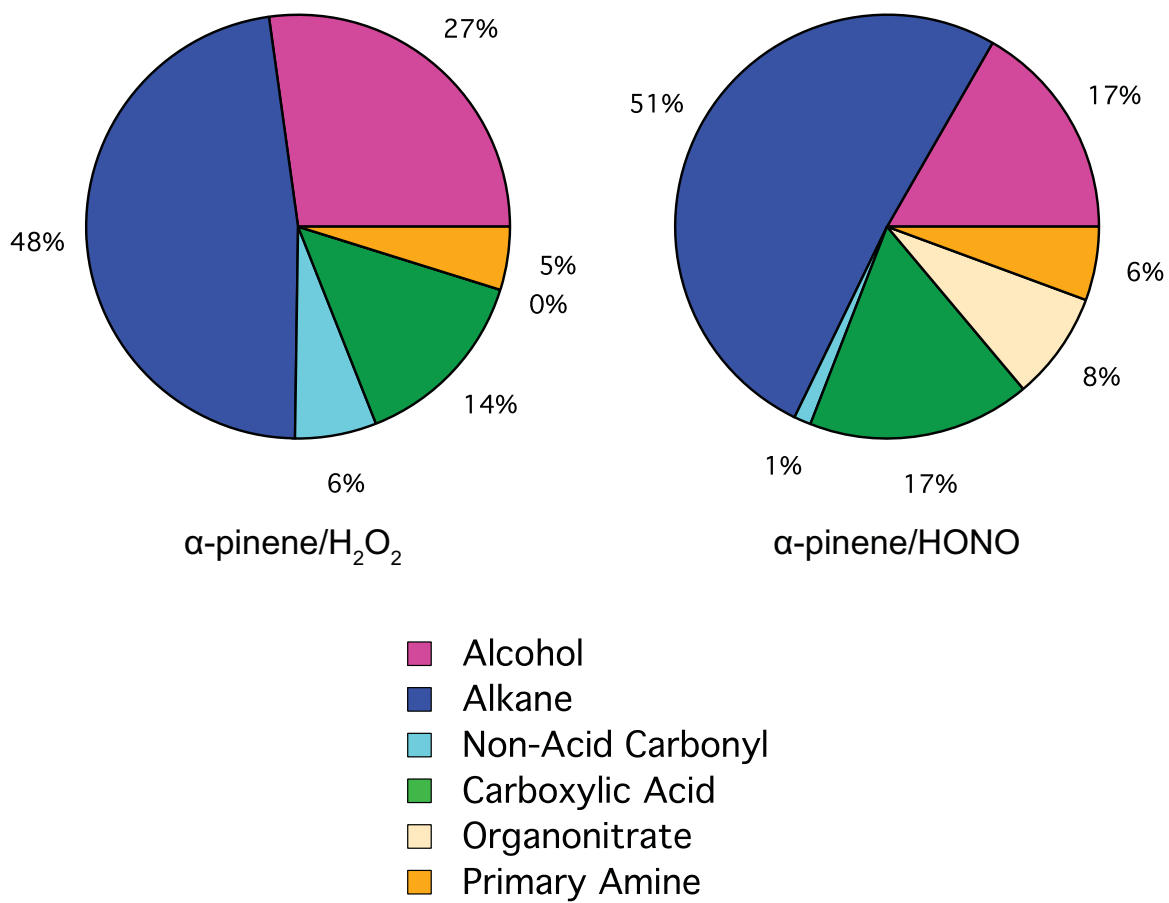


**Figure 9:** Average composition by mass of  $\alpha$ -pinene photooxidation SOA as measured by FTIR analysis.

## Bibliography

- Chhabra, P. S., Flagan, R. C., and Seinfeld, J. H.: Elemental analysis of chamber organic aerosol using an aerodyne high-resolution aerosol mass spectrometer, *Atmos. Chem. Phys.*, 10, 4111–4131, doi:10.5194/acp-10-4111-2010, 2010.
- Takegawa, N., Miyakawa, T., Kawamura, K., and Kondo, Y.: Contribution of selected dicarboxylic and omega-oxocarboxylic acids in ambient aerosol to the  $m/z$  44 signal of an aerodyne aerosol mass spectrometer, *Aerosol Sci. Technol.*, 41, 418–437, doi:10.1080/02786820701203215, 2007.
- Zhang, Q., Alfarra, M. R., Worsnop, D. R., Allan, J. D., Coe, H., Canagaratna, M. R., and Jimenez, J. L.: Deconvolution and quantification of hydrocarbon-like and oxygenated organic aerosols based on aerosol mass spectrometry, *Environ. Sci. Technol.*, 39, 4938–4952, doi:10.1021/Es048568l, 2005.

## Appendix C

# Changes in Organic Aerosol Composition with Aging Inferred from Aerosol Mass Spectra\*

---

\*Reproduced with permission from “Changes in organic aerosol composition with aging inferred from aerosol mass spectra” by N. L. Ng, M. R. Canagaratna, J. L. Jimenez, P. S. Chhabra, J. H. Seinfeld, and D. R. Worsnop *Atmospheric Chemistry and Physics Discussions*, 11, 7095–7112, doi:10.5194/acpd-11-7095-2011, Copyright 2011 by the Authors. CC Attribution 3.0 License.



This discussion paper is/has been under review for the journal Atmospheric Chemistry and Physics (ACP). Please refer to the corresponding final paper in ACP if available.

## Changes in organic aerosol composition with aging inferred from aerosol mass spectra

N. L. Ng<sup>1</sup>, M. R. Canagaratna<sup>1</sup>, J. L. Jimenez<sup>2,3</sup>, P. S. Chhabra<sup>4</sup>, J. H. Seinfeld<sup>4</sup>, and D. R. Worsnop<sup>1</sup>

<sup>1</sup>Aerodyne Research, Inc. Billerica, MA, USA

<sup>2</sup>Department of Chemistry and Biochemistry, University of Colorado, Boulder, CO, USA

<sup>3</sup>CIRES, University of Colorado, Boulder, CO, USA

<sup>4</sup>Department of Chemical Engineering, California Institute of Technology, Pasadena, CA, USA

Received: 23 February 2011 – Accepted: 23 February 2011 – Published: 2 March 2011

Correspondence to: M. R. Canagaratna (mrcana@aerodyne.com)

Published by Copernicus Publications on behalf of the European Geosciences Union.

7095

### Abstract

Organic aerosols (OA) can be separated with factor analysis of aerosol mass spectrometer (AMS) data into hydrocarbon-like OA (HOA) and oxygenated OA (OOA). We develop a new method to parameterize H:C of OOA in terms of  $f_{43}$  (ratio of  $m/z$  43, mostly  $C_2H_3O^+$ , to total signal in the component mass spectrum). Such parameterization allows the transformation of large database of ambient OOA components from the  $f_{44}$  (mostly  $CO_2^+$ , likely from acid groups) vs.  $f_{43}$  space ("triangle plot") (Ng et al., 2010) into the Van Krevelen diagram (H:C vs. O:C). Heald et al. (2010) suggested that the bulk composition of OA line up in the Van Krevelen diagram with a slope  $\sim -1$ ; such slope can potentially arise from the physical mixing of HOA and OOA, and/or from chemical aging of these components. In this study, we find that the OOA components from all sites occupy an area in the Van Krevelen space, with the evolution of OOA following a shallower slope of  $\sim -0.5$ , consistent with the additions of both acid and alcohol functional groups without fragmentation, and/or the addition of acid groups with C-C bond breakage. The importance of acid formation in OOA evolution is consistent with increasing  $f_{44}$  in the triangle plot with photochemical age. These results provide a framework for linking the bulk aerosol chemical composition evolution to molecular-level studies.

### 1 Introduction

The study of organic aerosols (OA) in the atmosphere is challenging due to the large number of molecular species involved and the continuous evolution of OA concentration, composition, and properties (Jimenez et al., 2009). Recently, simplified ways of characterizing the aging of OA in the atmosphere from aerosol mass spectrometer (AMS) datasets have been identified (Ng et al., 2010; Heald et al., 2010). Ng et al. (2010) analyzed OA components determined from positive matrix factorization (PMF) analysis of 43 AMS datasets in the Northern Hemisphere (unit mass

7096

resolution mass spectra, UMR, and high resolution, HR). At most sites, OA could be separated into hydrocarbon-like OA (HOA) and oxygenated OA (OOA), and sometimes other primary components. OOA is a good surrogate for SOA under most conditions (Jimenez et al., 2009) and can be further deconvolved into semi-volatile OOA (SV-OOA) and low-volatility OOA (LV-OOA). OA evolution is characterized in terms of the changing intensities of the two most dominant oxygen-containing ions in the OOA spectra,  $m/z44$  (mostly  $\text{CO}_2^+$  in ambient data) and  $m/z43$  (mostly  $\text{C}_2\text{H}_3\text{O}^+$ ). The ion  $m/z44$  is thought to be due mostly to acids (Duplissy et al., 2011) or acid-derived species, such as esters. The  $m/z43$  ion is predominantly due to non-acid oxygenates. Both acid and non-acid oxygenates have been observed in ambient OA (Russell et al., 2011; Decesari et al., 2007). When  $f_{44}$  (ratio of  $m/z44$  to total signal in the component spectrum) is plotted against  $f_{43}$  (defined similarly), all OA components fall within a triangular space (Fig. 1, hereafter referred to as the "triangle plot"). The HOA components have  $f_{44} < 0.05$ ; SV-OOA and LV-OOA components concentrate in the lower and upper halves of the triangle, respectively. The  $m/z43$  fragment is mainly  $\text{C}_2\text{H}_3\text{O}^+$  for the OOA components, and  $\text{C}_3\text{H}_7^+$  for the HOA components. The base of the triangle encompasses the variability in HOA and SV-OOA composition. This range decreases with increasing  $f_{44}$  (O:C ratio), suggesting that the aerosols become more chemically similar with increasing aging, largely independent of the initial source of the material (Jimenez et al., 2009; Ng et al., 2010). Most SOA produced in the laboratory cluster on the lower half of the triangle, indicating that they are not as oxidized as ambient LV-OOA (Ng et al., 2010).

Heald et al. (2010) characterized the evolution of bulk OA composition using the Van Krevelen diagram (H:C vs. O:C) (Van Krevelen, 1950). In this approach, high resolution mass spectra were analyzed to obtain bulk H:C and O:C values (Aiken et al., 2007; Aiken et al., 2008). HR-AMS field datasets and laboratory studies occupy a narrow range when plotted in the Van Krevelen diagram. The authors reported that all the data cluster along a line with slope  $\sim -1$ , consistent with simultaneous increases in carbonyl and alcohol moieties, either in separate carbons or due to the addition of

7097

carboxylic acid groups. It is suggested that the aerosol composition moves along this line with increased aging (Heald et al., 2010).

In this work, we link the complementary information of the triangle plot and the Van Krevelen diagram to provide further understanding of atmospheric OA evolution. The triangle plot provides an empirical way of viewing all new AMS data in the context of available data for characterizing aerosol aging; data obtained from both UMR (such as the Q-AMS and the recently developed Aerosol Chemical Speciation Monitor, ACSM, (Ng et al., 2011)) and HR instruments can be readily plotted in real time in this space. With detailed data processing of HR-AMS data, the added chemical insight contained in the Van Krevelen diagram provides information on the mechanism of evolution of OA composition.

### 1.1 Methods: parameterization of H:C vs. $f_{43}$

In order to map data from the triangle plot ( $f_{44}$  vs.  $f_{43}$ ) onto the Van Krevelen diagram (H:C vs. O:C), both H:C and O:C must be parameterized using UMR data. Aiken et al. (2008) showed that O:C of ambient OA can be estimated from  $f_{44}$  through a linear parameterization. In this work, we obtain an analogous parameterization of H:C in terms of  $f_{43}$  (Fig. 2) for SOA/OOA, using OOA components obtained from PMF analysis of HR-AMS ambient datasets (Docherty et al., 2008; Aiken et al., 2009; DeCarlo et al., 2010; Huang et al., 2010a, b; Sun et al., 2011) and SOA formed in laboratory studies (Chhabra et al., 2010; 2011, Massoli et al., 2010). All the data shown are HR, in which H:C is determined explicitly by elemental analysis. As these are OOA/SOA data,  $f_{43}$  in Fig. 2 is dominated by the oxygenated fragment at  $m/z43$ , i.e.,  $\text{C}_2\text{H}_3\text{O}^+$ . The laboratory studies include both chamber (Chhabra et al., 2010, 2011) and flow tube experiments (Massoli et al., 2010), encompassing a wide range of precursors (anthropogenic and biogenic) and degree of oxidation (hours to  $\sim 2$  weeks of photooxidation). The data are fitted to a polynomial function. The y-intercept is constrained to an H:C of 1.0, which corresponds to aromatic SOA precursors which often have the lowest H:C values. We caution that this parameterization is only valid for

7098

0.05 <  $f_{43}$  ( $C_2H_3O^+$ ) < 0.25 and  $f_{44}$  > 0.06 (Fig. S1). These ranges overlap well with all the ambient OOA components in the triangle plot (Fig. 1). It appears that the HOA and other OA components (local OA (LOA), biomass burning OA (BBOA), cooking OA (COA)) where  $C_3H_7^+$  contributes >~20% of  $m/z$ 43 may require a separate parameterization (Fig. S2) and warrants future investigation.

## 2 Results and discussion

### 2.1 Field measurements

The OOA components in the triangle plot are transformed into the Van Krevelen diagram using the parameterization, and the results are shown in Fig. 3. The left and right sides of the triangle plot become the bottom and top lines in the Van Krevelen diagram, respectively. The light green points are SV-OOA which has lower O:C, while the dark green data are LV-OOA which has higher O:C. We refer to Fig. 3 as the "VK-triangle" diagram. Histograms showing the distribution of the estimated H:C ratios and the carbon oxidation states ( $\overline{OS}_C \approx 2 O/C - H/C$ ) (Kroll et al., 2011) observed across multiple sites are shown in Fig. 4b and c, respectively. Carbon oxidation state is found to be a useful metric for describing the chemistry of atmospheric organic aerosol (Kroll et al., 2011). The variation in  $f_{43}$  of the SV-OOA components in the triangle plot is still preserved in the VK-triangle diagram, with SV-OOA components spanning a range of H:C ratios. Possible reasons for the range of observed H:C ratios include the different SOA precursor mixes and chemical pathways of SOA formation. For instance, the chamber data from photooxidation of methyl chavicol ( $C_{10}H_{12}O$ ) and linalool ( $C_{10}H_{18}O$ ) span the base of the triangle plot (Fig. 1); these data roughly define the intercepts of the two lines that made up the VK-triangle, which is consistent with the H:C ratios of the precursor hydrocarbon (i.e. H:C = 1.2 for methyl chavicol, H:C = 1.8 for linalool).

7099

There are two observations from this VK-triangle diagram that differ from those in Heald et al. (2010): (1) Most data points in Heald et al. (2010) cluster around the line with the  $-1$  slope, with only some points at high O:C showing a lower slope of  $\sim -0.8$ . In Fig. 3, however, the data points span a larger region in the diagram; (2) on average, the transition from SV-OOA to LV-OOA follows a line with a slope that is shallower than  $-1$  ( $\sim -0.5$ ). Only four HR OOA components were available at the time of Heald et al. (2010), which may explain why these features are not clear in that study.

Other than Mexico City (flight and ground) (Aiken et al., 2009; DeCarlo et al., 2010), the OA components from other HR datasets (Riverside, Queens NY, China PRD, Beijing) (Docherty et al., 2008, Sun et al., 2011; Huang et al., 2010a, 2010b) have also become available recently. The OA components from all these sites and the results from the heterogeneous oxidation of squalane (Kroll et al., 2009) are shown in Fig. 5. The OOA components from these HR datasets mostly fall into the VK-triangle region defined by the UMR data while the HOA components and the squalane data are outside the VK-triangle region. As most data in Heald et al. (2010) represent the average OA composition at each site, the observed slope of  $\sim -1$  in their study can arise from a combination of physical mixing of HOA and OOA components, and/or chemical evolution of these components. The HOA, SV-OOA, and LV-OOA components from Riverside are highlighted in Fig. 5. It is clear that once the total OA is deconvolved into these components, the evolution of SV-OOA to LV-OOA follows a shallower slope. The differences in primary OA components (HOA, LOA, BBOA, COA) likely reflect some atmospheric evolution, but are not easily interpreted since they also likely represent differences in the initially emitted POA. However, the squalane data suggest that the initial heterogeneous oxidation of POA species may follow a steeper slope, consistent with carbonyl group addition. This corresponds to the horizontal movement of the squalane data across the triangle plot (Fig. 1), with larger increase in  $f_{43}$  due to non-acid oxygenates (such as carbonyls) and relatively smaller increase in  $f_{44}$  (acids). Freshly formed SOA, represented by SV-OOA, evolves in a different way, with a shallower slope of  $\sim -0.5$ . It is possible that further aging of oxidized HOA which has

7100

reached the SV-OOA region of the VK-triangle may also proceed with the shallower slope, as hinted by the change in slope of the evolution of squalane oxidation products in Fig. 5. However, this is not definitive from the available ambient data.

A slope of  $\sim -0.5$  in the Van Krevelen diagram can be explained by at least two systematic OA chemical transformations mechanisms. If the functional group addition occurs on a  $\text{CH}_2$  group without C-C bond breakage, this slope can be caused by e.g., the addition of 3 OH groups and 1 C=O group, or the addition of 2 OH groups and 1 COOH group. A movement to the right (increase in O:C) with the gentler slope ( $\sim -0.5$ ) in the Van Krevelen diagram is equivalent to a movement up the triangle plot (increase in  $f_{44}$ ). Since  $m/z44$  is found to be proportional to the acid content of standard compounds (Duplissy et al., 2011), it is likely that acid group formation plays an important role in the aging of SOA. Therefore, an OOA aging mechanism that is consistent with measurements (laboratory + field data) is that the ensemble average of the transformation involves both the net addition of COOH and OH functional groups. An alternative explanation for a slope of  $-0.5$  is due to COOH group addition to the site of a C-C bond cleavage. For instance, the replacement of a  $-\text{CH}_2$  group with a  $-\text{COOH}$  group at a C-C bond breakage (without loss of oxygen during the fragmentation process) will result in a slope of  $-0.5$  in the Van Krevelen diagram. Fragmentation is thought to become increasingly important for already oxidized material such as fresh SOA (Kroll et al., 2009, 2011).

## 2.2 Laboratory data

Photooxidation of  $\alpha$ -pinene provides a laboratory case study to illustrate aerosol composition changes in the VK-triangle space for a simpler, globally important, and well-studied SOA system (Fig. 6). The data shown in Fig. 6 includes HR-AMS data from both chamber and flow tube experiments (Chhabra et al., 2010, 2011; Massoli et al., 2010). In the chamber experiments, typical atmospheric OH levels are employed for hours, resulting in moderate oxidation, i.e. O:C  $\sim 0.3$  in the SV-OOA range. OH exposures in the flow tube experiments are much higher and lead to highly oxidized aerosols

7101

(in the LV-OOA range, with an O:C up to  $\sim 1$ ). Taken together, the chamber and flow tube data map out the entire oxidation range of  $\alpha$ -pinene SOA and span the whole range of O:C observed in ambient measurements. The oxidation of  $\alpha$ -pinene also follows a slope of  $\sim -0.5$  in the Van Krevelen diagram, consistent with the observed evolution of SV-OOA to LV-OOA in ambient data. Also shown in Fig. 6 are individual compounds (with known H:C and O:C) that have been identified in  $\alpha$ -pinene SOA (Jaoui and Kamens, 2001; Szmigielski et al., 2007), including both first-generation and higher generation oxidation products. On average, the composition change based on these identified products also follows a slope of  $\sim -0.5$ , consistent with the change in bulk composition measured by the HR-AMS. For example, cis-pinonic acid ( $\text{C}_{10}\text{H}_{16}\text{O}_3$ ) is a typical first-generation product, and its OH oxidation product,  $\alpha,\alpha$ -dimethyltricarballic acid ( $\text{C}_8\text{H}_{12}\text{O}_6$ ), is a tricarboxylic acid formed via fragmentation (Szmigielski et al., 2007). The oxidation of pinonic acid to  $\alpha,\alpha$ -dimethyltricarballic acid also follows a line with a slope of  $\sim -0.5$ . Furthermore, it can be seen from the molecular structures that while the cis-pinonic acid to  $\alpha,\alpha$ -dimethyltricarballic acid transformation involves the loss of 2 carbons, there is a net gain of both OH and COOH functionalities (possibly through the loss of a carbonyl group to the  $\text{C}_2$  fragment followed by the addition of two COOH groups) (Szmigielski et al., 2007), consistent with our hypotheses for the dominant chemical transformations in OOA aging. Further molecular-level studies of SOA aging are needed to elucidate the details within these trends.

## 3 Conclusions

By parameterizing organic aerosol H:C of SOA/OOA in terms of  $f_{43}$ , we are able to transform data in the triangle plot ( $f_{44}$  vs.  $f_{43}$ ) into the Van Krevelen diagram (H:C vs. O:C). Ambient OOA components in the triangle plot map out a triangular space in Van Krevelen diagram, showing a range of H:C at lower oxidation; such variation decreases with increasing oxidation. Taking all the UMR and HR-AMS data together, it is found that on average, the change in the bulk composition of OOA as oxidation

7102

progresses follows a line with a slope  $\sim -0.5$ , which is shallower than the  $-1$  slope proposed by Heald et al. (2010) and indicates that aging of OA is consistent with the addition of both COOH and OH functional groups without fragmentation, and/or the addition of COOH groups with C-C bond cleavage. This simplified view of bulk OOA aging can provide a useful guide for modeling the complex oxidation pathways and changes in OA chemical and physical properties with increased oxidation, and needs to be investigated in detail with molecular-level studies.

**Supplementary material related to this article is available online at:**  
<http://www.atmos-chem-phys-discuss.net/11/7095/2011/acpd-11-7095-2011-supplement.pdf>.

*Acknowledgements.* We thank grants from DOE (BER, ASR program) DEFG0208ER64627, NOAA NA08OAR4310565, and NSF ATM-0919189. We thank Paola Massoli for sharing the Boston College flow tube data and Jesse Kroll for helpful discussions.

## References

- Aiken, A. C., DeCarlo, P. F., and Jimenez, J. L.: Elemental Analysis of Organic Species with Electron Ionization High-Resolution Mass Spectrometry, *Anal. Chem.*, 79, 8350–8358, doi:8310.1021/ac071150w, 2007.
- Aiken, A. C., DeCarlo, P. F., Kroll, J. H., Worsnop, D. R., Huffman, J. A., Docherty, K. S., Ulbrich, I. M., Mohr, C., Kimmel, J. R., Sueper, D., Sun, Y., Zhang, Q., Trimborn, A., Northway, M., Ziemann, P. J., Canagaratna, M. R., Onasch, T. B., Alfarra, M. R., Prevot, A. S. H., Dommen, J., Duplissy, J., Metzger, A., Baltensperger, U., and Jimenez, J. L.: O/C and OM/OC ratios of primary, secondary, and ambient organic aerosols with high-resolution time-of-flight aerosol mass spectrometry, *Environ. Sci. Technol.*, 42, 4478–4485, 2008.
- Aiken, A. C., Salcedo, D., Cubison, M. J., Huffman, J. A., DeCarlo, P. F., Ulbrich, I. M., Docherty, K. S., Sueper, D., Kimmel, J. R., Worsnop, D. R., Trimborn, A., Northway, M., Stone, E. A., Schauer, J. J., Volkamer, R. M., Fortner, E., de Foy, B., Wang, J., Laskin, A., Shutthanandan, V., Zheng, J., Zhang, R., Gaffney, J., Marley, N. A., Paredes-Miranda, G., Arnott, W. P., 7103
- Molina, L. T., Sosa, G., and Jimenez, J. L.: Mexico City aerosol analysis during MILAGRO using high resolution aerosol mass spectrometry at the urban supersite (T0) - Part 1: Fine particle composition and organic source apportionment, *Atmos. Chem. Phys.*, 9, 6633–6653, doi:10.5194/acp-9-6633-2009, 2009.
- Chhabra, P. S., Flagan, R. C., and Seinfeld, J. H.: Elemental analysis of chamber organic aerosol using an aerodyne high-resolution aerosol mass spectrometer, *Atmos. Chem. Phys.*, 10, 4111–4131, doi:10.5194/acp-10-4111-2010, 2010.
- Chhabra, P. S., Ng, N. L., Canagaratna, M. R., Corrigan, A. L., Russell, L. M., Worsnop, D. R., Flagan, R. C., and Seinfeld, J. H.: Elemental Composition and Oxidation of Chamber Organic Aerosol, in preparation, 2011.
- DeCarlo, P. F., Ulbrich, I. M., Crouse, J., de Foy, B., Dunlea, E. J., Aiken, A. C., Knapp, D., Weinheimer, A. J., Campos, T., Wennberg, P. O., and Jimenez, J. L.: Investigation of the sources and processing of organic aerosol over the Central Mexican Plateau from aircraft measurements during MILAGRO, *Atmos. Chem. Phys.*, 10, 5257–5280, doi:10.5194/acp-10-5257-2010, 2010.
- Decesari, S., Mircea, M., Cavalli, F., Fuzzi, S., Moretti, F., Tagliavini, E., and Facchini, M. C.: Source attribution of water-soluble organic aerosol by nuclear magnetic resonance spectroscopy, *Environ. Sci. Technol.*, 41, 2479–2484, 2007.
- Docherty, K. S., Stone, E. A., Ulbrich, I. M., DeCarlo, P. F., Snyder, D. C., Schauer, J. J., Peltier, R. E., Weber, R. J., Murphy, S. M., Seinfeld, J. H., Grover, B. D., Eatough, D. J., and Jimenez, J. L.: Apportionment of Primary and Secondary Organic Aerosols in Southern California during the 2005 Study of Organic Aerosols in Riverside (SOAR-1), *Environ. Sci. Technol.*, 42, 7655–7662, 2008.
- Duplissy, J., DeCarlo, P. F., Dommen, J., Alfarra, M. R., Metzger, A., Barmapadimos, I., Prevot, A. S. H., Weingartner, E., Tritscher, T., Gysel, M., Aiken, A. C., Jimenez, J. L., Canagaratna, M. R., Worsnop, D. R., Collins, D. R., Tomlinson, J., and Baltensperger, U.: Relating hygroscopicity and composition of organic aerosol particulate matter, *Atmos. Chem. Phys.*, 11, 1155–1165, doi:10.5194/acp-11-1155-2011, 2011.
- Heald, C. L., Kroll, J. H., Jimenez, J. L., Docherty, K. S., DeCarlo, P. F., Aiken, A. C., Chen, Q., Martin, S. T., Farmer, D. K., and Artaxo, P.: A simplified description of the evolution of organic aerosol composition in the atmosphere, *Geophys. Res. Lett.*, 37, L08803, doi:10.1029/2010GL042737, 2010.
- Huang, X.-F., He, L.-Y., Hu, M., Canagaratna, M. R., Kroll, J. H., Ng, N. L., Zhang, Y.-H., Lin, Y.,

- Xue, L., Sun, T.-L., Liu, X.-G., Shao, M., Jayne, J. T., and Worsnop, D. R.: Characterization of submicron aerosols at a rural site in Pearl River Delta of China using an Aerodyne High-Resolution Aerosol Mass Spectrometer, *Atmos. Chem. Phys. Discuss.*, 10, 25841–25869, doi:10.5194/acpd-10-25841-2010, 2010a.
- 5 Huang, X.-F., He, L.-Y., Hu, M., Canagaratna, M. R., Sun, Y., Zhang, Q., Zhu, T., Xue, L., Zeng, L.-W., Liu, X.-G., Zhang, Y.-H., Jayne, J. T., Ng, N. L., and Worsnop, D. R.: Highly time-resolved chemical characterization of atmospheric submicron particles during 2008 Beijing Olympic Games using an Aerodyne High-Resolution Aerosol Mass Spectrometer, *Atmos. Chem. Phys.*, 10, 8933–8945, doi:10.5194/acp-10-8933-2010, 2010b.
- 10 Jaoui, M. and Kamens, R. M.: Mass balance of gaseous and particulate products analysis from alpha-pinene/NO<sub>x</sub>/air in the presence of natural sunlight, *J. Geophys. Res.-Atmos.*, 106, 12541–12558, 2001.
- Jimenez, J. L., Canagaratna, M. R., Donahue, N. M., Prevot, A. S. H., Zhang, Q., Kroll, J. H., DeCarlo, P. F., Allan, J. D., Coe, H., Ng, N. L., Aiken, A. C., Docherty, K. S., Ulbrich, I. M., Grieshop, A. P., Robinson, A. L., Duplissy, J., Smith, J. D., Wilson, K. R., Lanz, V. A., Hueglin, C., Sun, Y. L., Tian, J., Laaksonen, A., Raatikainen, T., Rautiainen, J., Vaattovaara, P., Ehn, M., Kulmala, M., Tomlinson, J. M., Collins, D. R., Cubison, M. J., Dunlea, E. J., Huffman, J. A., Onasch, T. B., Alfarra, M. R., Williams, P. I., Bower, K., Kondo, Y., Schneider, J., Drewnick, F., Borrmann, S., Weimer, S., Demerjian, K., Salcedo, D., Cottrell, L., Griffin, R., Takami, A., Miyoshi, T., Hatakeyama, S., Shimono, A., Sun, J. Y., Zhang, Y. M., Dzepina, K., Kimmel, J. R., Sueper, D., Jayne, J. T., Herndon, S. C., Trimborn, A. M., Williams, L. R., Wood, E. C., Middlebrook, A. M., Kolb, C. E., Baltensperger, U., and Worsnop, D. R.: Evolution of Organic Aerosols in the Atmosphere, *Science*, 326, 1525–1529, 2009.
- 20 Kroll, J. H., Smith, J. D., Che, D. L., Kessler, S. H., Worsnop, D. R., and Wilson, K. R.: Measurement of fragmentation and functionalization pathways in the heterogeneous oxidation of oxidized organic aerosol, *Phys. Chem. Chem. Phys.*, 11, 8005–8014, 2009.
- Kroll, J. H., Donahue, N. M., Jimenez, J. L., Kessler, S. H., Canagaratna, M. R., Wilson, K. R., Altieri, K. E., Mazzoleni, L. R., Wozniak, A. S., Bluhm, H., Mysak, E. R., Smith, J. D., Kolb, C. E., and Worsnop, D. R.: Carbon oxidation state as a metric for describing the chemistry of atmospheric organic aerosol, *Nature Chemistry*, 3, 133–139, doi:10.1038/nchem.948, 2011.
- 25 Massoli, P., Lambe, A. T., Ahern, A. T., Williams, L. R., Ehn, M., Mikkila, J., Canagaratna, M. R., Brune, W. H., Onasch, T. B., Jayne, J. T., Petaja, T., Kulmala, M., Laaksonen, A., Kolb, C. E., Davidovits, P., and Worsnop, D. R.: Relationship between aerosol oxidation level and

7105

- hygroscopic properties of laboratory generated secondary organic aerosol (SOA) particles, *Geophys. Res. Lett.*, 37, L24801, doi:10.1029/2010GL045258, 2010.
- Ng, N. L., Canagaratna, M. R., Zhang, Q., Jimenez, J. L., Tian, J., Ulbrich, I. M., Kroll, J. H., Docherty, K. S., Chhabra, P. S., Bahreini, R., Murphy, S. M., Seinfeld, J. H., Hildebrandt, L., Donahue, N. M., DeCarlo, P. F., Lanz, V. A., Prévôt, A. S. H., Dinar, E., Rudich, Y., and Worsnop, D. R.: Organic aerosol components observed in Northern Hemispheric datasets from Aerosol Mass Spectrometry, *Atmos. Chem. Phys.*, 10, 4625–4641, doi:10.5194/acp-10-4625-2010, 2010.
- 5 Ng, N. L., Herndon, S. C., Trimborn, A., Canagaratna, M. R., Croteau, P., Onasch, T. M., Sueper, D., Worsnop, D. R., Zhang, Q., Sun, Y. L., and Jayne, J. T.: An Aerosol Chemical Speciation Monitor (ACSM) for routine monitoring of atmospheric aerosol composition, *Aerosol Sci. Technol.*, in print, 2011.
- Russell, L. M., Bahadur, R., and Ziemann, P. J.: Identifying organic aerosol sources by comparing functional group composition in chamber and atmospheric particles, *Proc. Natl. Acad. Sci. USA*, doi:10.1073/pnas.1006461108, 2011.
- 10 Sun, Y.-L., Zhang, Q., Schwab, J. J., Demerjian, K. L., Chen, W.-N., Bae, M.-S., Hung, H.-M., Hogrefe, O., Frank, B., Rattigan, O. V., and Lin, Y.-C.: Characterization of the sources and processes of organic and inorganic aerosols in New York city with a high-resolution time-of-flight aerosol mass spectrometer, *Atmos. Chem. Phys.*, 11, 1581–1602, doi:10.5194/acp-11-1581-2011, 2011.
- 15 Szmigielski, R., Surratt, J. D., Gomez-Gonzalez, Y., Van der Veken, P., Kourtchev, I., Vermeylen, R., Blockhuys, F., Jaoui, M., Kleindienst, T. E., Lewandowski, M., Offenberg, J. H., Edney, E. O., Seinfeld, J. H., Maenhaut, W., and Claeys, M.: 3-methyl-1,2,3-butanetricarboxylic acid: An atmospheric tracer for terpene secondary organic aerosol, *Geophys. Res. Lett.*, 34, L24811, doi:10.1029/2007GL031338, 2007.
- 20 Van Krevelen, D. W.: Graphical-statistical method for the study of structure and reaction processes of coal, *Fuel*, 24, 269–284, 1950.
- 25 Yu, J. Z., Cocker, D. R., Griffin, R. J., Flagan, R. C., and Seinfeld, J. H.: Gas-phase ozone oxidation of monoterpenes: Gaseous and particulate products, *J. Atmos. Chem.*, 34, 207–258, 1999.
- 30

7106



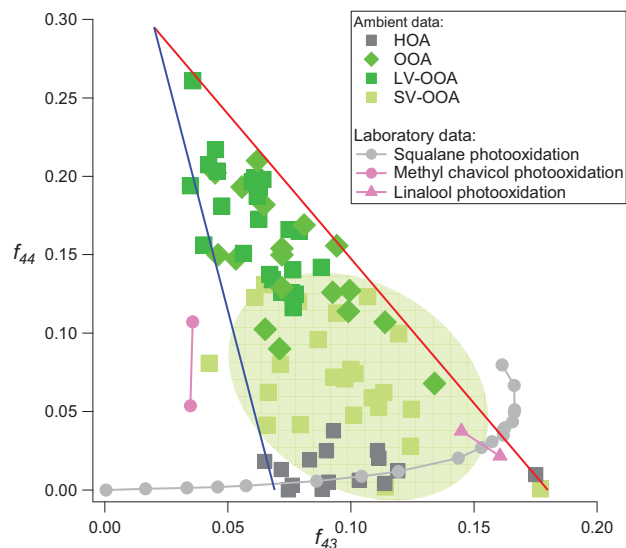


**Fig. 1.** Triangle plot ( $f_{44}$  vs.  $f_{43}$ ) for all the OOA components from 43 ambient AMS datasets as well as selected laboratory data (adapted from Ng et al., 2010). The light green shaded area indicates the region where most of laboratory data fall into.

7107

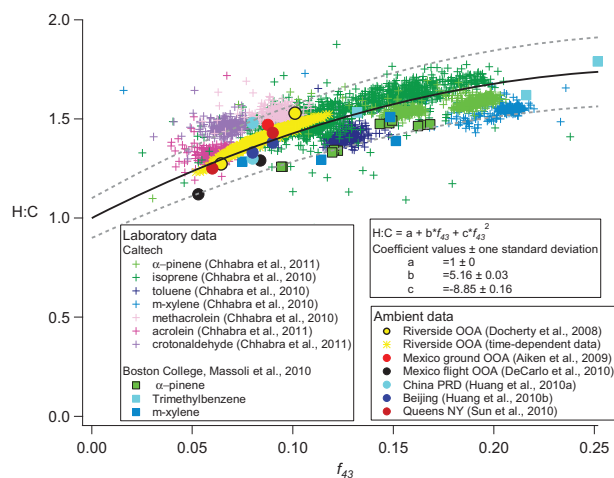


**Fig. 2.** Parameterization of H:C in terms of  $f_{43}$  for SOA/OOA, using OOA components obtained from PMF analysis of HR-AMS ambient datasets and SOA formed in laboratory studies. The dotted gray lines are  $\pm 10\%$  from the fitted line.

7108

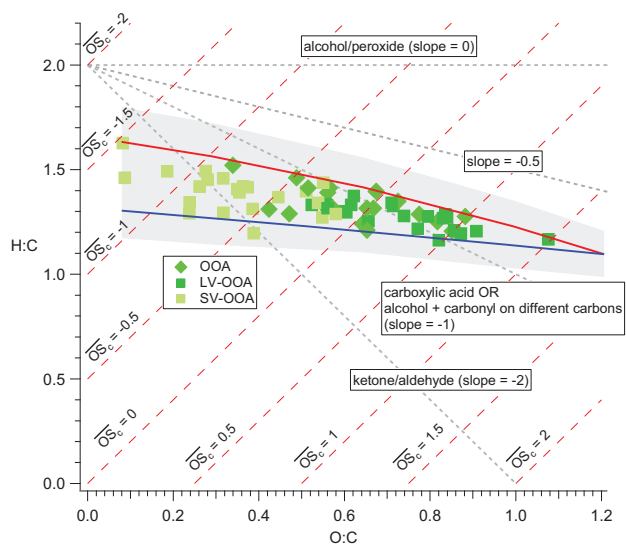


**Fig. 3.** Representation of all the OOA components into the VK-triangle diagram. The left and right sides of the triangle plot become the bottom and top lines in the Van Krevelen diagram, respectively. The light gray shaded region denotes the  $\pm 10\%$  uncertainty in the parameterization. The estimated carbon oxidation states ( $\overline{OS}_C \approx 2 O/C - H/C$ ) are shown with the red dotted lines.

7109

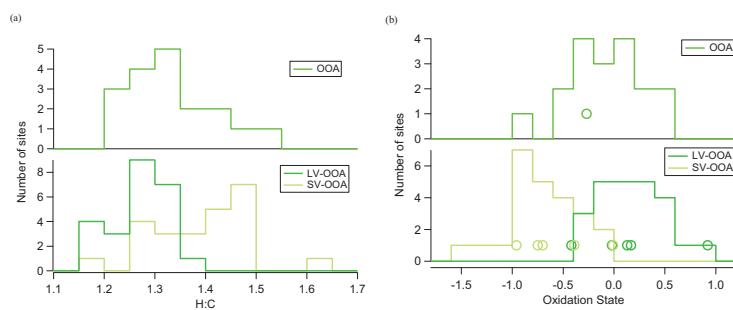


**Fig. 4.** (a) Histogram showing the distribution of the estimated H:C ratios observed across multiple sites. (b) Histogram showing the distribution of the estimated carbon oxidation states ( $\overline{OS}_C \approx 2 O/C - H/C$ ) observed across multiple sites. The open circles are HR-AMS ambient data in which oxidation states are directly calculated from the data.

7110



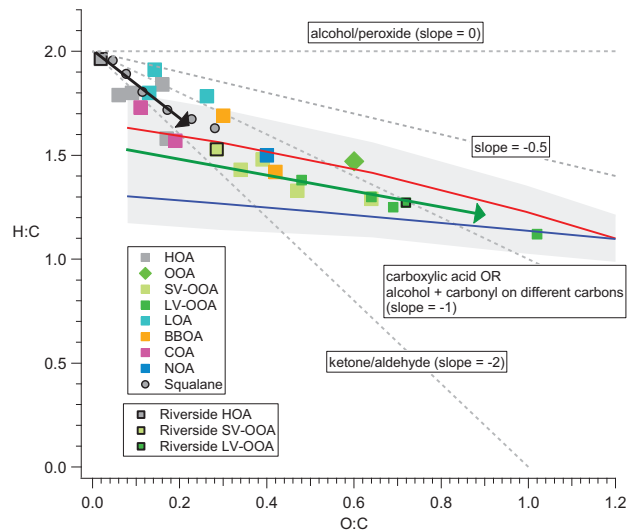


**Fig. 5.** VK-triangle diagram for the OA components from all sites with HR-AMS data and results from the heterogeneous oxidation of squalane. The light gray shaded region denotes the  $\pm 10\%$  uncertainty in the parameterization. (Note: LOA = local OA; BBOA = biomass burning OA; COA = cooking OA; NOA = nitrogen-enriched OA)

7111

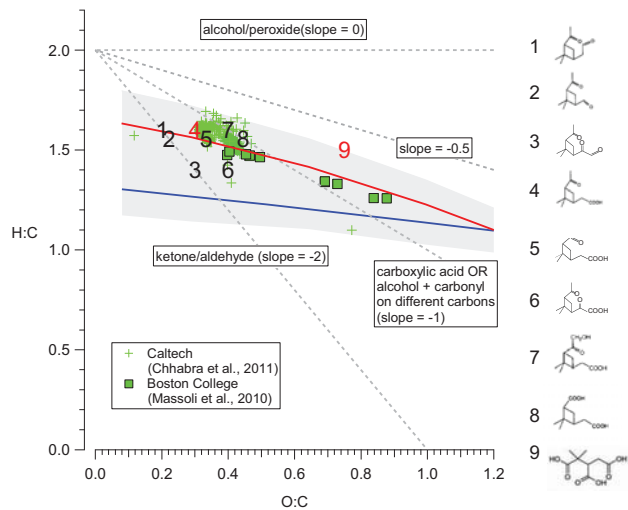


**Fig. 6.** VK-triangle diagram for  $\alpha$ -pinene photooxidation, including HR-AMS data from both chamber and flow tube experiments. The light gray shaded region denotes the  $\pm 10\%$  uncertainty in the parameterization. The numbers correspond to individual molecular products in  $\alpha$ -pinene SOA, with their structures being shown on the right. Product 4 is cis-pinonic acid and product 9 is  $\alpha, \alpha$ -dimethyltricarballic acid.

7112

## Appendix D

# Organic Aerosol Components Observed in Northern Hemispheric Datasets from Aerosol Mass Spectrometry\*

---

\*Reproduced with permission from “Organic aerosol components observed in Northern Hemispheric datasets from aerosol mass spectrometry” by N. L. Ng, M. R. Canagaratna, Q. Zhang, J. L. Jimenez, J. Tian, I. M. Ulbrich, J. H. Kroll, K. S. Docherty, P. S. Chhabra, R. Bahreini, S. M. Murphy, J. H. Seinfeld, L. Hildebrandt, N. M. Donahue, P. F. DeCarlo, V. A. Lanz, A. S. H. Prvt, E. Dinar, Y. Rudich, and D. R. Worsnop *Atmospheric Chemistry and Physics*, 10, 4625–4641, doi:10.5194/acp-10-4625-2010, Copyright 2010 by the Authors. CC Attribution 3.0 License.

## Organic aerosol components observed in Northern Hemispheric datasets from Aerosol Mass Spectrometry

N. L. Ng<sup>1</sup>, M. R. Canagaratna<sup>1</sup>, Q. Zhang<sup>2,\*</sup>, J. L. Jimenez<sup>3,4</sup>, J. Tian<sup>2</sup>, I. M. Ulbrich<sup>3,4</sup>, J. H. Kroll<sup>1,5</sup>, K. S. Docherty<sup>3,4</sup>, P. S. Chhabra<sup>6</sup>, R. Bahreini<sup>3,7</sup>, S. M. Murphy<sup>7</sup>, J. H. Seinfeld<sup>6</sup>, L. Hildebrandt<sup>8</sup>, N. M. Donahue<sup>8</sup>, P. F. DeCarlo<sup>3,9,10</sup>, V. A. Lanz<sup>10</sup>, A. S. H. Prévôt<sup>10</sup>, E. Dinar<sup>11</sup>, Y. Rudich<sup>11</sup>, and D. R. Worsnop<sup>1</sup>

<sup>1</sup>Aerodyne Research, Inc. Billerica, MA, USA

<sup>2</sup>Atmospheric Sciences Research Center, State University of New York, Albany, NY, USA

<sup>3</sup>CIRES, University of Colorado, Boulder, CO, USA

<sup>4</sup>Department of Chemistry and Biochemistry, University of Colorado, Boulder, CO, USA

<sup>5</sup>Department of Civil and Environmental Engineering, Massachusetts Institute of Technology, Cambridge, MA, USA

<sup>6</sup>Department of Chemical Engineering, California Institute of Technology, Pasadena, CA, USA

<sup>7</sup>NOAA, Earth System Research Laboratory, Boulder, CO, USA

<sup>8</sup>Center for Atmospheric Particle Studies, Carnegie Mellon University, Pittsburgh, PA, USA

<sup>9</sup>Department of Atmospheric and Oceanic Science, University of Colorado, Boulder, CO, USA

<sup>10</sup>Laboratory of Atmospheric Chemistry, Paul Scherrer Institut, Villigen, Switzerland

<sup>11</sup>Department of Environmental Sciences, Weizmann Institute of Science, Rehovot 76100, Israel

\*now at: Department of Environmental Toxicology, University of California, Davis, CA, USA

Received: 27 November 2009 – Published in Atmos. Chem. Phys. Discuss.: 23 December 2009

Revised: 14 April 2010 – Accepted: 29 April 2010 – Published: 20 May 2010

**Abstract.** In this study we compile and present results from the factor analysis of 43 Aerosol Mass Spectrometer (AMS) datasets (27 of the datasets are reanalyzed in this work). The components from all sites, when taken together, provide a holistic overview of Northern Hemisphere organic aerosol (OA) and its evolution in the atmosphere. At most sites, the OA can be separated into oxygenated OA (OOA), hydrocarbon-like OA (HOA), and sometimes other components such as biomass burning OA (BBOA). We focus on the OOA components in this work. In many analyses, the OOA can be further deconvolved into low-volatility OOA (LV-OOA) and semi-volatile OOA (SV-OOA). Differences in the mass spectra of these components are characterized in terms of the two main ions  $m/z$  44 ( $\text{CO}_2^+$ ) and  $m/z$  43 (mostly  $\text{C}_2\text{H}_3\text{O}^+$ ), which are used to develop a new mass spectral diagnostic for following the aging of OA components in the atmosphere. The LV-OOA component spectra have higher  $f_{44}$  (ratio of  $m/z$  44 to total signal in the com-

ponent mass spectrum) and lower  $f_{43}$  (ratio of  $m/z$  43 to total signal in the component mass spectrum) than SV-OOA. A wide range of  $f_{44}$  and O:C ratios are observed for both LV-OOA ( $0.17 \pm 0.04$ ,  $0.73 \pm 0.14$ ) and SV-OOA ( $0.07 \pm 0.04$ ,  $0.35 \pm 0.14$ ) components, reflecting the fact that there is a continuum of OOA properties in ambient aerosol. The OOA components (OOA, LV-OOA, and SV-OOA) from all sites cluster within a well-defined triangular region in the  $f_{44}$  vs.  $f_{43}$  space, which can be used as a standardized means for comparing and characterizing any OOA components (laboratory or ambient) observed with the AMS. Examination of the OOA components in this triangular space indicates that OOA component spectra become increasingly similar to each other and to fulvic acid and HULIS sample spectra as  $f_{44}$  (a surrogate for O:C and an indicator of photochemical aging) increases. This indicates that ambient OA converges towards highly aged LV-OOA with atmospheric oxidation. The common features of the transformation between SV-OOA and LV-OOA at multiple sites potentially enable a simplified description of the oxidation of OA in the atmosphere. Comparison of laboratory SOA data with ambient OOA indicates



Correspondence to: M. R. Canagaratna  
 (mrcana@aerodyne.com)

that laboratory SOA are more similar to SV-OOA and rarely become as oxidized as ambient LV-OOA, likely due to the higher loadings employed in the experiments and/or limited oxidant exposure in most chamber experiments.

## 1 Introduction

Organic aerosols (OA) constitute a substantial fraction (20–90%) of submicron aerosols worldwide and a full understanding of their sources, atmospheric processing, and properties is important to assess their impacts on climate, human health, and visibility (Kanakidou et al., 2005; Zhang et al., 2007; Kroll and Seinfeld, 2008; Hallquist et al., 2009). The Aerodyne AMS provides quantitative data on inorganic and organic aerosol species in submicron non-refractory aerosol particles with high-time resolution. In recent years, several techniques have been employed to deconvolve the mass spectra of the organic aerosols acquired with the AMS including custom principal component analysis (CPCA) (Zhang et al., 2005a), multiple component analysis (MCA) (Zhang et al., 2007), hierarchical cluster analysis (Marcolli et al., 2006), positive matrix factorization (PMF) (Paatero and Tapper, 1994; Paatero 1997; Lanz et al., 2007; Nemitz et al., 2008; Aiken et al., 2008; Aiken et al., 2009b; Ulbrich et al., 2009), and the Multilinear Engine (ME-2) (Lanz et al., 2008).

Multivariate analysis by Zhang et al. (2007) showed that OA at multiple sites can be described by two main components: hydrocarbon-like organic aerosol (HOA) and oxygenated organic aerosol (OOA). Biomass burning OA (BBOA) and other local primary sources have also been observed (Jimenez et al., 2009). OOA accounts for a large fraction ( $72\pm 21\%$ ) of the total organic mass at many locations (Zhang et al., 2007; Jimenez et al., 2009). Studies from multiple locations show that the HOA component correlates well with primary tracers such as CO and NO<sub>x</sub> (e.g. Zhang et al., 2005b; Lanz et al., 2007; Aiken et al., 2009b; Ulbrich et al., 2009) and can be considered as a surrogate of combustion primary OA (POA). BBOA correlates with acetonitrile, levoglucosan, and potassium, and can be considered a surrogate of BB POA (Aiken et al., 2009a, b). The OOA component has been shown to be a good surrogate of secondary OA (SOA) in multiple studies, correlating well with secondary species such as O<sub>3</sub> and O<sub>x</sub> (de Gouw et al., 2005; Zhang et al., 2005a, b, 2007; Volkamer et al., 2006; Lanz et al., 2007; Herndon et al., 2008).

In many analyses, two types of OOA have been identified. The two broad subtypes differ in volatility and degree of oxidation (Jimenez et al., 2009), as indicated by the ratio of  $m/z$  44 to total signal in the component mass spectrum ( $f_{44}$ ). The more oxidized component (higher  $f_{44}$ ) has previously been referred to as OOA-1 while the less oxidized component (lower  $f_{44}$ ) has previously been referred to as OOA-2 (Lanz et al., 2007; Aiken et al., 2008, 2009b; Ne-

mitz et al., 2008; Ulbrich et al., 2009). In those studies the OOA-1 represented the more oxidized, aged aerosols and the OOA-2 represented the less oxidized, fresher secondary organic species. Temporal correlations with sulfate and nitrate (Lanz et al., 2007; Ulbrich et al., 2009) as well as direct volatility measurements (Huffman et al., 2009) in those studies further showed that OOA-1 is less volatile than OOA-2. Since the OOA-1 and OOA-2 terminology does not convey the known physicochemical properties of these OOA subcomponents, in the following discussion we will refer to these subcomponents as low-volatility OOA (LV-OOA) and semi-volatile OOA (SV-OOA), respectively. It is important to note that the assignment of LV-OOA and SV-OOA to the components identified at each site is not absolute, meaning that the LV-OOA at one site does not have the same composition as in another site. This is an expected result since factor analysis has been applied separately to each site. Thus here the terminology for the OOA subtypes is relative for each site (i.e., at each site the component with a higher  $f_{44}$  is referred to as LV-OOA and the component with a lower  $f_{44}$  is referred to as SV-OOA regardless of the absolute values of  $f_{44}$ ). An absolute volatility scale for LV-OOA and SV-OOA is being investigated (e.g. Faulhaber et al., 2009; Cappa et al., 2009) but requires a better understanding of the volatility measurements of ambient aerosols (e.g., with thermodenuders).

The goal of this study is to compare and contrast the OOA components identified in multiple field studies in order to better characterize the sources and evolution of OA in the atmosphere. We present results from the factor analysis of 43 AMS datasets. 27 of the datasets, which encompass a majority of the sites in Zhang et al. (2007), are reanalyzed as part of this work. We focus mainly on the OOA component and the reanalysis allows for further deconvolution of the total OOA component reported by Zhang et al. (2007) into LV-OOA and SV-OOA components. The OA components resulting from this work were used by Jimenez et al. (2009) to form the basis of a modeling framework that links oxidation and volatility to capture the evolution of OA in the atmosphere. In this manuscript we combine the factor analysis results from the ambient datasets together to obtain a holistic view of how the AMS ambient component mass spectra change across environments with different sources and aerosol processes. The common features of the component spectra are used to develop a new mass spectral diagnostic for following the atmospheric aging of OA components in the atmosphere. Finally, since the AMS has been employed in many laboratory experiments over the years, a series of chamber data (both published and unpublished) are also integrated and compared to the ambient data. Chamber data provide the basis for simulating SOA formation in the atmosphere. Hence, it is important to evaluate whether the results from chamber experiments are representative of the atmosphere; similarities and differences between ambient OOA and laboratory SOA are examined and discussed.

## 2 Method

The organic aerosol data have been obtained with the Aerodyne quadrupole mass aerosol spectrometer (Q-AMS), the compact time-of-flight mass spectrometer (C-ToF-AMS), or the high-resolution ToF-AMS (HR-ToF-AMS). The instrument design and operation of each version of the AMS has been described in detail by Jayne et al. (2000), Drewnick et al. (2005), and DeCarlo et al. (2006), respectively, and reviewed by Canagaratna et al. (2007). Factor analyses of the data from Riverside, CA, Whistler (Canada), and Mexico City (both ground and aircraft data) are based on high resolution (HR) data from HR-ToF-AMS, while analyses for all other locations are based on unit mass resolution (UMR) data. The details (locations, times, previous publications, etc.) of all datasets included in this study are given in the supplementary material.

In this work we present factor analysis results from 43 AMS datasets. As part of this work, we performed PMF (Paatero and Tapper, 1994; Paatero, 1997) based factor analysis of the organic aerosol mass spectra observed at 27 of the sites. For some of the urban downwind/rural/remote sites, a hybrid of PMF/MCA approach is employed (Cottrell et al., 2008; Nemitz et al., 2008). The factor analyses of the remaining 16 sites were performed previously and the results are discussed in more detail in the corresponding publications: Beijing (Sun et al., 2009), Riverside (Docherty et al., 2008; Huffman et al., 2009), Mexico City (Aiken et al., 2008, 2009a, b; DeCarlo et al., 2009), Pittsburgh (Zhang et al., 2005a, b; Ulbrich et al., 2009), Thompson Farm, NH (Cottrell et al., 2008), Zurich (Lanz et al., 2007), Egbert (Slowik et al., 2010), Crete (Hildebrandt et al., 2010), and the great Alpine region (Lanz et al., 2009). For the sites in Lanz et al. (2009), both PMF and ME-2 are used. In contrast to PMF, ME-2 allows for a priori constraints (partial or total) on the mass spectra and/or time series of the factors (Paatero, 1999; Lanz et al., 2008).

PMF is a multivariate factor analysis technique developed by Paatero and Tapper (1994) and Paatero (1997) to solve the bilinear factor model  $x_{ij} = \sum_p g_{ip} f_{pj} + e_{ij}$  where  $x_{ij}$  are the measured values of  $j$  species in  $i$  samples,  $P$  are factors comprised of constant source profiles ( $f_j$ , mass spectra for AMS data) with varying contributions over the time period of the dataset ( $g_i$ , time series), without any a priori assumptions of either mass spectral or time profile (Lanz et al., 2007; Ulbrich et al., 2009). PMF computes the solution by minimizing the summed least squares errors of the fit weighted with the error estimates of each data point. Solutions are also constrained to have non-negative values. The error weighting and non-negativity constraint result in more physically meaningful solutions that are easier to interpret compared to other receptor models.

The PMF2 executable version 4.2 in the robust mode (Paatero, 1997) is used together with a custom software tool (PMF Evaluation Tool (PET), Ulbrich et al., 2009) in this

analysis. The analysis and input error calculations are performed following the procedures described by Ulbrich et al. (2009). The optimal number of PMF components is determined by carefully examining the scaled residuals, evaluating the component's diurnal cycles and factor correlations with external tracers (including CO, O<sub>3</sub>, NO<sub>x</sub>, NO<sub>y</sub>, SO<sub>2</sub>, NO<sub>3</sub><sup>-</sup>, and SO<sub>4</sub><sup>2-</sup>, when available), and comparing the component spectra with source mass spectra from the AMS mass spectra database (Ulbrich et al., 2009). The PMF2 optimization algorithm starts from random initial conditions, which can be changed by varying the value of the SEED input parameter. Multiple solutions generated with different SEED values are carefully examined to explore the possibility of multiple local minima in the solutions. The uncertainty in component mass spectra and time series due to rotation ambiguity is also examined by performing PMF analysis over a range of FPEAK values. Overall, the effect of positive FPEAK is to create more near-zero values in the mass spectra and decrease the number of near-zero values in the time series; negative FPEAK values have the opposite effect (Ulbrich et al., 2009). For all sites, improved correlations with external tracers or mass spectra are not found for FPEAK values different from 0. Thus the FPEAK=0 solutions, which bound the observed data most closely, are chosen for all the sites analyzed in this study.

Rotational ambiguity can be explored by examining the appearance and disappearance of zero values in the mass spectra and time series of the factors (Paatero, 2008). In typical ambient datasets, a priori information about component time points or fragment ions with true zero values is not known; thus, the appearance of unrealistic zero values in the mass spectra and time series of the solutions can be used to evaluate the most reasonable limits of the FPEAK parameter (Ulbrich et al., 2009). For a few sites where component mass spectra or time series are highly correlated, rotational ambiguity is more significant. The change in mass spectra with FPEAK is more dramatic in components with a smaller mass fraction, as they can change more without causing large changes in the residuals. For instance, in the Pittsburgh dataset (acquired in September 2002) studied by Ulbrich et al. (2009), the variation in  $f_{44}$  and  $f_{43}$  in the SV-OOA component across the range of retained solutions (FPEAK -1.6 to 1.0) was ~30%, for the LV-OOA component ~2%, and for the HOA component ~5% (relative to the solution with FPEAK=0). In general, it is found that the component mass spectra and time series for most sites analyzed in this work do not vary drastically over the reasonable range of FPEAK chosen. For example, the relative uncertainties in OOA component mass spectra for  $f_{44}$  and  $f_{43}$  (these fragments will be discussed in detail in the following sections) are typically <5%. For the Lanz et al. (2009) sites, similar rotational uncertainties are observed except for sites with low  $f_{44}$  in SV-OOA, where an absolute uncertainty of ±5% is estimated.

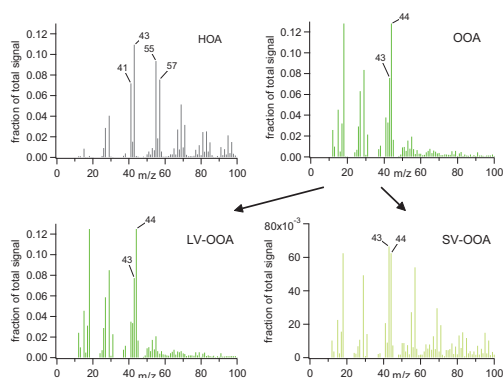


**Fig. 1.** Example mass spectra of the HOA, total OOA, LV-OOA and SV-OOA components identified from the Pittsburgh dataset (Zhang et al., 2007; Ulbrich et al., 2009). Note that the total OOA spectrum is not the average of the LV-OOA and SV-OOA because LV-OOA accounts for a much larger fraction (59%) of OA than SV-OOA (10%) in Pittsburgh.

### 3 Results and discussion

#### 3.1 Overview of organic aerosol components in the Northern Hemisphere

Figure 1 shows example mass spectra of the HOA, total OOA, LV-OOA, and SV-OOA components identified from the Pittsburgh dataset (Zhang et al., 2005b; Ulbrich et al., 2009). The HOA component is distinguished by the clear hydrocarbon signatures in its spectrum, which are dominated by the ion series  $C_nH_{2n+1}^+$  and  $C_nH_{2n-1}^+$  ( $m/z$  27, 29, 41, 43, 55, 57, 69, 71, 83, 85, 97, 99...) that are typical of hydrocarbons. The (total) OOA component is distinguished by the prominent  $m/z$  44 ( $CO_2^+$ ) in its spectrum and the lower relative intensity of higher mass fragments. Figure 2 shows the distribution of  $f_{44}$  for the HOA, total OOA, LV-OOA, and SV-OOA components observed across the multiple sites. The top axis shows O:C ratios estimated using the  $f_{44}$  of the PMF-resolved factor mass spectra and the correlation derived by Aiken et al. (2008). As seen in Fig. 2, both average  $f_{44}$  and O:C for HOA components are generally very low. The OOA components, on the other hand, have higher  $f_{44}$  and O:C values of  $0.14 \pm 0.04$  and  $0.62 \pm 0.15$ . The  $f_{44}$  and O:C ratios for all the LV-OOA and SV-OOA fall into two distinctive groups. The average  $f_{44}$  and O:C ratio for SV-OOA components are  $0.07 \pm 0.04$  and  $0.35 \pm 0.14$ , while those for the LV-OOA components are  $0.17 \pm 0.04$  and  $0.73 \pm 0.14$ . It is important to note that a wide range of  $f_{44}$  and O:C is observed around the average values for both the LV-OOA and SV-OOA components across all sites. This underscores the fact that neither the total OOA nor OOA subtypes are identical across the different sites. Some overlap between the high

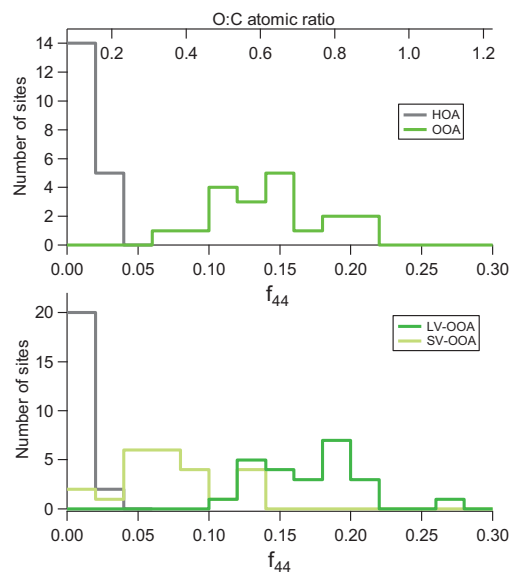


**Fig. 2.** Histograms showing the distribution of  $f_{44}$  and estimated O:C atomic ratios observed across the multiple sites. The top panel corresponds to sites where only one OOA component is obtained. The bottom panel corresponds to sites where both LV-OOA and SV-OOA are resolved.

end of the SV-OOA range and the low end of the LV-OOA range occurs because the names SV-OOA and LV-OOA are relative for each site. Since an absolute scale to define volatility is not available, it is likely that the volatilities of the SV-OOA and LV-OOA components in the overlapping region are not very different from each other.

The different  $f_{44}$  and O:C values observed for the OOA components in Fig. 2 reflect the fact that there is a continuum of OOA properties in ambient aerosol. At each site this continuum is discretized into SV-OOA and LV-OOA components according to the details of the ambient OOA that is observed at that particular site. Figure 3 explicitly shows the O:C atomic ratios and  $f_{44}$  of the OOA, LV-OOA, and SV-OOA components at each site. Similar to Zhang et al. (2007), the sites have been grouped according to their location as either being primarily urban or urban downwind/rural/remote. For some sites only one OOA factor is obtained while for others the range of oxidation is represented by both LV-OOA and SV-OOA components. For sites where both LV-OOA and SV-OOA are resolved, the average OOA O:C observed at any given time point can be reconstructed as a mass-weighted average of the LV-OOA and SV-OOA O:C. In Fig. 3, the mass-weighted average OOA component over the entire campaign is also shown for sites in which LV-OOA and SV-OOA are both resolved. The sites within each location



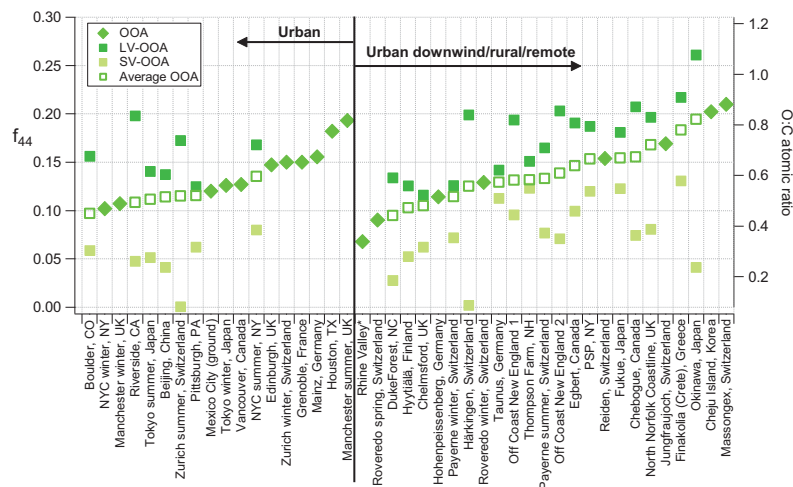


**Fig. 3.**  $f_{44}$  and estimated O:C atomic ratios of the OOA, LV-OOA, and SV-OOA components at each site. The mass-weighted average OOA component over the entire campaign is also shown for sites in which LV-OOA and SV-OOA are both resolved. The sites within each location group are listed in increasing order of the  $f_{44}$  and O:C ratio of the total OOA components and average OOA components. Uncertainties in  $f_{44}$  of these components are discussed in the text. (Note: Rhine Valley\* = Switzerland, Austria, and Liechtenstein.)

group are listed in increasing order of the  $f_{44}$  and O:C ratio of the total OOA component or the average OOA component (for sites with two OOA subtypes). The ability to resolve more than one OOA component depends on the dynamic range of various parameters for a given dataset, such as ambient temperature, the influence of different source regions and ages, and the intensity of the local/regional photochemistry. A single OOA is found for datasets in which the variability in the OOA mass spectrum is small and infrequent, which is typical for sites affected by very aged air masses. On the other hand, two OOA components are resolved for datasets where substantial and repeated changes in the total OOA mass spectrum appear. For instance, Lanz et al. (2009) and Jimenez et al. (2009) showed that the separation of OOA components into SV-OOA and LV-OOA is observed much more frequently in summer datasets than winter datasets, owing to more intense photochemistry, warmer temperatures, and larger temperature changes in summer.

The OOA measured at a given site is highly dependent on the meteorological and transport conditions, SOA precursors, and extent of photochemical aging observed at that site. In the urban Pittsburgh and Zurich datasets, for example, the observed range in OOA O:C is influenced by diurnal temperature fluctuations. These temperature changes separate the aged regional background LV-OOA component from the more local, fresher SV-OOA component (Lanz et al., 2007; Ulbrich et al., 2009). The remote/rural Chebogue Point (Nova Scotia, summer 2004) measurements show a range of O:C that appear to reflect air masses of different

ages and source regions. The more oxidized LV-OOA component at Chebogue correlates well with sulfate and an anthropogenically influenced US outflow factor extracted via principal component analysis of speciated measurements of volatile organic compounds (VOC) by PTR-MS and GC-MS (Millet et al., 2005; Holzinger et al., 2007; Williams et al., 2007). On the other hand, the less oxidized SV-OOA component is observed in the fresher air masses and correlates well with biogenic SOA tracer compounds (e.g., 2,3-pinene diol and pinonaldehyde – oxidation products of terpenes), suggesting that it is associated with SOA formed from biogenic hydrocarbons (Williams et al., 2007).

As discussed by Zhang et al. (2007), de Gouw et al. (2005), and Jimenez et al. (2009), cities act as point sources of HOA, which is quickly diluted in regional air dominated by OOA and overwhelmed by SOA production from the urban emissions. Thus, the relative contribution of OOA (compared to HOA) increases as air is transported from urban to urban downwind/remoted/rural locations. As illustrated in Jimenez et al. (2009), increasing distance from an urban center is often correlated with an increase in photochemical aging and more oxidized OOA. This effect is not obvious in Fig. 3 (i.e., the total OOA and average OOA at urban downwind/rural/remoted sites span a similar range of O:C values as observed in urban sites). This highlights the complexity of the factors that determine the oxidation state of OOA at any given location. In addition to photochemical processing, meteorology and SOA precursors also affect the degree of oxidation of the OOA observed at a given location.

For example, at many of the urban sites considered in this study, there is substantial inflow of regional aged OOA from outside the city because of meteorological conditions, resulting in an overall OA that is almost as oxidized as that found at more remote areas.

### 3.2 Detailed comparison of SV-OOA and LV-OOA components

Figure 1 shows representative mass spectra of LV-OOA and SV-OOA obtained in Pittsburgh, PA (Ulbrich et al., 2009). The different relative intensities of  $m/z$  44 (mostly  $\text{CO}_2^+$ ) in the spectra are used to classify these two subcomponents. Previous studies have shown that  $\text{CO}_2^+$  in AMS spectra can result from thermal decarboxylation of organic acid groups (Alfarra, 2004). Thermal decomposition of acids to yield  $\text{CO}_2$  is well known, and the  $m/z$  44 ( $\text{CO}_2^+$ ) fragment is found to be formed reproducibly by the thermal decarboxylation of oxo-, di- and polycarboxylic acids (Roberts and Caserio, 1964; Alfarra, 2004; Aiken et al., 2007; Takegawa et al., 2007), with dicarboxylic acids such as malic acid and oxalic acid resulting in a much higher  $f_{44}$  than monoacids such as pyruvic acid (Alfarra, 2004). An acyl peroxide standard also gave rise to substantial signal at  $m/z$  44 in the work of Aiken et al. (2007). Currently, there is no laboratory data showing that compounds with multiple functional groups (other than carboxylic acids and acyl peroxides) also give rise to substantial  $f_{44}$  in the AMS. For instance, the mass spectra of methylglyoxal (with two carbonyl groups) and dioctyl sebacate (with two ester groups) have relatively weak signals at  $m/z$  44 (Alfarra, 2004). In addition to  $m/z$  44, the other key mass spectral difference that is typically observed between LV-OOA and SV-OOA components is the relative intensity of  $m/z$  43. Although  $m/z$  43 can, in principle, correspond to  $\text{C}_3\text{H}_7^+$  or  $\text{C}_2\text{H}_3\text{O}^+$ , HR data from Riverside, Mexico City (ground and flight), and Whistler indicate that the oxygenated fragment  $\text{C}_2\text{H}_3\text{O}^+$  contributes a dominant fraction of the  $m/z$  43 fragment ( $\sim 81\text{--}99\%$ ) for ambient OOA, LV-OOA, and SV-OOA components. Since organic acid groups likely decompose to give  $m/z$  44, we hypothesize that the  $\text{C}_2\text{H}_3\text{O}^+$  fragment at  $m/z$  43 is dominated by non-acid oxygenates. According to McLafferty and Turecek (1993), the  $m/z$  43 fragment is a prominent fragment from saturated carbonyl groups, but can also arise from other types of species. High resolution mass spectral studies of laboratory standards are needed to provide further insights.

As  $m/z$  44 and  $m/z$  43 are prominent peaks in the OOA, SV-OOA, and LV-OOA mass spectra and they are representative of different oxygen-containing functional groups, a detailed comparison of these mass fragments from all sites may yield some insights regarding the dynamic evolution of OOA in the atmosphere. Figure 4 shows the  $f_{44}$  vs.  $f_{43}$  for all the OOA components from different locations. Some of the differences in the  $f_{44}$  and  $f_{43}$  values shown in Fig. 4 can possibly arise from instrument-to-instrument variability. In princi-

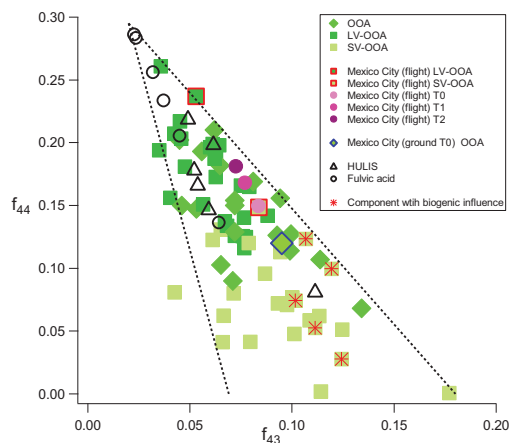


**Fig. 4.**  $f_{44}$  vs.  $f_{43}$  for all the OOA components from different sites, including Mexico city ground and flight data (Aiken et al., 2009b; Jimenez et al., 2009), as well as various HULIS (humic-like substances) and fulvic acid samples. The dotted lines are added to guide the eye and define the triangular space where ambient OOA components fall. The slope and intercept of the line on the left hand side are  $-6.0204$  and  $0.4154$ ; the slope and intercept of the line on the right hand side are  $-1.8438$  and  $0.3319$ , valid for  $0.069 \leq x \leq 0.18$ , and  $y \leq 0.295$ . Uncertainties in  $f_{44}$  and  $f_{43}$  of these components are discussed in the text.

ple, mass spectral data obtained by two different instruments can differ from each other due to differences in hardware and/or the operating conditions of the instrument. All of the UMR data points in Fig. 4 are obtained with Q-AMS instruments. Intercomparisons of UMR Q-AMS laboratory spectra observed by two different groups (Alfarra, 2004; Takegawa et al., 2007) for several diacids (malonic, succinic, glutaric, and adipic acid) show only small differences in  $f_{44}$  and  $f_{43}$  that are on the order of 2% (absolute). Thus, it is unlikely that this variability is enough to affect our interpretation of the general trends observed among the different OOAs.

Since photochemical aging leads to an increase in  $f_{44}$  (Alfarra et al., 2004; de Gouw et al., 2005; Aiken et al., 2008; Kleinman et al., 2008), the  $f_{44}$  axis can be considered as an indicator of atmospheric aging. The Mexico City flight and ground data points in Fig. 4 provide a good example for illustrating the increase in  $f_{44}$  with photochemical aging. Figure 4 shows the Mexico City ground site (T0) and the aircraft data at T0 (above urban area), T1 (30 km downwind,  $\sim 3$  h transport from the urban area), and T2 (60 km downwind,  $\sim 6$  h). The photochemical ages of air masses sampled above these sites increase with distance away from the urban area. The average OOA components for each of these locations clearly indicate the increase in  $f_{44}$  ( $T0_{\text{ground}} < T0_{\text{aircraft}} < T1_{\text{aircraft}} < T2_{\text{aircraft}}$ ) with photochemical age.



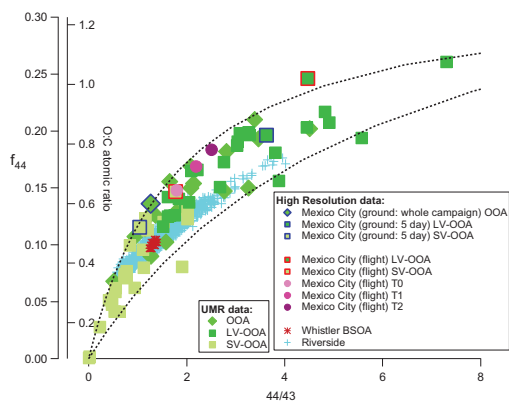


**Fig. 5.**  $f_{44}$  and O:C vs. 44/43 for all the OOA components from different sites, including Mexico city ground (whole campaign and 5 day) (Aiken et al., 2008; Aiken et al., 2009b) and flight data (Jimenez et al., 2009). Also shown are the time-dependent data of the OOA components at Riverside, as well as data obtained during a biogenics SOA event at Whistler. For the UMR data, O:C is estimated using the  $f_{44}$  of the PMF-resolved factor mass spectra and the correlation derived by Aiken et al. (2008); for the HR data the O:C is directly determined by elemental analysis (hence the  $f_{44}$  axis does not apply to the HR data). The two dotted curves represent the mathematical transformation of the two lines in Fig. 4.

Figure 4 also shows  $f_{44}$  and  $f_{43}$  from the AMS mass spectra of various HULIS (humic-like substances) and fulvic acid samples, generated by atomization of the aqueous samples into the AMS. The HULIS samples, composed of high molecular weight polycarboxylic acids, are extracted from various ambient filter samples (Dinar et al., 2006). The fulvic acid samples are from a commercially available standard of humic substance (Suwannee River Fulvic Acid, SRFA), including the bulk sample as well as various size-fractionated samples obtained by microfiltration (Dinar et al., 2006; Graber and Rudich, 2006).

A key feature of Fig. 4 is that the ambient OOA components from all the sites cluster within a well-defined triangular region of the plot. The dotted lines are added to guide the eye and define this space. The SV-OOA and LV-OOA components at multiple sites fall into two distinct regions in this triangle: SV-OOA components are concentrated in the lower half of the triangle, while the LV-OOA components are concentrated in the upper half of the triangle. The total OOA components show an intermediate range of  $f_{44}$ . Results from Morgan et al. (2010) show that data from aircraft measurements in Europe also lie in the region defined by these guide-lines.

The base of the triangular region in Fig. 4 defines the large range in  $f_{43}$  that is observed for the less oxidized SV-OOA components. Since the SV-OOA components represent less oxidized and photochemically younger organics, the variability in  $f_{43}$  for these components likely arises from differences in OOA components arising from different sources and chemical pathways. The following sites likely have strong influence from biogenic SOA sources: Duke Forest, Hyttiälä, Thompson Farm, Chebogue, and Egbert (Allan et al., 2006; Williams et al., 2007; Cottrell et al., 2008; Raatikainen et al., 2010; Slowik et al., 2010). The SV-OOA components from these sites are marked with an asterisk in Fig. 4. They do not appear to cluster at a certain location inside the triangle, indicating that mass spectral characteristics alone are not enough to assign a particular dominant source (e.g., “anthropogenic” vs. “biogenic”) to the OOA components or to different parts of the space in Fig. 4.

In Fig. 4, both the average and range in  $f_{43}$  for OOA components decrease with increasing  $f_{44}$ . This suggests that the OOA components become more chemically similar with increasing O:C and photochemical aging regardless of the original source of the OOA. It is important to note that this ambient trend in OOA composition measured by the AMS is also mirrored in the ambient HULIS sample mass spectra. The HULIS and fulvic acids shown in this study have some of the highest  $f_{44}$  values and fall in the LV-OOA range of the figure. Only one of the HULIS samples falls into the SV-OOA region; this is the OA collected at Kpustza (Hungary) which likely has a large contribution from freshly-formed biogenic SOA, and also has different optical properties than the biomass burning and pollution HULIS which appear in the LV-OOA region (Dinar et al., 2008). Owing to the very limited amount of the extracted and purified material, an acidity measurement of the HULIS samples analyzed in this work was not performed. However, previous  $^1\text{H-NMR}$  studies on HULIS extracted from smoke particles in Brazil showed that their acidic content was as high as 13% (almost 1 carbon out of 7 of the accounted carbons are carboxylic acids) (Tagliavini et al., 2006), comparable to that reported for fulvic acid samples (Ritchie and Perdue, 2003; Dinar et al., 2006). The highly acidic nature of HULIS and fulvic acids is consistent with the large  $f_{44}$  ( $\text{CO}_2^+$ ) fragment in their mass spectra. HULIS is found to constitute a large fraction of water soluble organic compounds in ambient aerosols (e.g. Facchini et al., 2000; Decesari et al., 2001; Fuzzi et al., 2001). The  $f_{44}$  of LV-OOA is very similar to that for HULIS, which is consistent with the convergence of atmospheric OA to the more oxidized LV-OOA (hence higher acidic content) with aging. This continuum of evolution of OA is also observed in the aircraft data discussed in Morgan et al. (2010).

The OOA components shown in Fig. 4 reflect different locations, sources, and degrees of photochemical aging. Each data point in the figure, in effect, represents a different “snapshot” of atmospheric OA as it is formed and aged in the atmosphere. When taken together, all the points provide a

broad view of the process by which ambient OA evolves into LV-OOA. In Fig. 4, this evolution is viewed in terms of changes in  $f_{44}$  and  $f_{43}$ . Fig. 5 shows an alternative view of the same evolution in terms of  $f_{44}$  and O:C vs. 44/43. For the UMR data, O:C is estimated using the method of Aiken et al. (2008); for the HR data the O:C is directly determined by elemental analysis (Aiken et al., 2007, 2008). Mathematically, a line in the  $f_{44}$  vs.  $f_{43}$  plot will transform into a curve in the  $f_{44}$  vs. 44/43 space (derivation shown in Appendix). Hence, the two dotted lines in Fig. 4 become the two dotted curves in Fig. 5. In Fig. 5, the OOA components from all sites (and time-dependent data at Riverside) also map a curve, showing a transition from SV-OOA components at the lower part of curve to LV-OOA components at the top of the curve with increased photochemical aging. It appears the O:C increases sharply at the beginning of oxidation then plateaus around a value of 1.2, suggesting that this may represent a maximum atmospheric oxidation state of the aerosol.

While Fig. 5 is a mathematically equivalent way of viewing the information in Fig. 4, it can potentially provide a more useful way of connecting the AMS observations with other measurements. In particular, measurements of O:C can be obtained with other instruments such as thermal techniques and nanoaerosol mass spectrometry (Pang et al., 2006; Wang et al., 2006). As discussed before,  $m/z$  44 in OOA spectra is thought to be due mostly to acidic groups (-COOH) and the  $m/z$  43 in OOA spectra can potentially be linked to non-acid oxygenates. Thus, the ratio between these two ions may provide a measure of how the chemical functionality of the OOA evolves with oxidation. Recently, a study by Russell et al. (2009) showed that ratios of AMS fragments (rather than the ratio of individual fragments to total OA) showed some correspondence with the relative abundances of various OA functional groups determined with FTIR. For instance, in regions where  $m/z$  44 and  $m/z$  57 are both well above the respective detection limits, it was shown that the 44/57 ratio correlates with the ratio of carboxylic acid to alkane functional groups from FTIR (Russell et al., 2009). Comparisons of the FTIR measurements with 44/43 ratios were not reported by Russell et al. (2009). However, future studies involving simultaneous measurements of laboratory standards, or laboratory SOA (from “simple” systems in which both the gas-phase and product-phase chemistry and products are better characterized) with HR-ToF-AMS and FTIR, NMR, or other techniques may provide more detailed insight into how the 44/43 ratio is related to the chemical functionality of OOA. For instance, a HR-ToF-AMS flow reactor study by Kroll et al. (2009) has suggested that  $C_2H_3O^+$  (nominal mass = 43) and  $CO_2^+$  (nominal mass = 44) may be markers for functionalization reactions and fragmentation reactions, respectively.

### 3.3 Comparison with laboratory data

Over the last two decades, numerous laboratory experiments have been conducted to study the formation of SOA. The results from these experiments form the basis for simulating SOA formation in the atmosphere. In the previous sections, we have provided an overview of the OOA components observed in the ambient atmosphere. In order to allow accurate parameterizations of SOA formation and evolution in the atmosphere, it is desirable that the laboratory conditions be as representative as possible of those in the atmosphere. A careful examination of the similarities and differences between laboratory SOA and ambient OOA provides insights about SOA formation in the atmosphere. A series of laboratory data are compiled from both published and unpublished data (Fig. 6a–c). Figure 6a shows the  $f_{44}$  vs.  $f_{43}$  for SOA formed by the ozonolysis/photooxidation of a suite of biogenic precursors from chamber experiments, including isoprene, monoterpenes ( $\alpha$ -pinene,  $\beta$ -pinene,  $\alpha$ -terpinene, terpinolone, limonene, myrcene), oxygenated terpenes (methyl-chavicol, verbenone, linalool), and sesquiterpenes (longifolene,  $\alpha$ -humulene,  $\beta$ -caryophyllene). Details on SOA formation in these particular experiments have been discussed in other publications (e.g. Gao et al., 2004a, b; Bahreini et al., 2005; Kroll et al., 2006; Lee et al., 2006a, b; Ng et al., 2006, 2007a; Alfara et al., 2006; Zhang et al., 2006; Shilling et al., 2009). Figure 6a also includes flow tube data of the heterogeneous oxidation (by OH radicals) of SOA formed from  $\alpha$ -pinene ozonolysis, denoted by the LBNL data points (Jimenez et al., 2009). Figure 6b shows the chamber data from the photooxidation of a series of aromatic hydrocarbons, including *m*-xylene, toluene, benzene, and 1,3,5-trimethylbenzene (Alfara et al., 2006; Ng et al., 2007b; Hildebrandt et al., 2009). Figure 6c shows the chamber and flow tube data from the photooxidation/heterogeneous oxidation of POA (and also primary vapors in some cases) (George et al., 2007; Sage et al., 2008; Grieshop et al., 2009; Kroll et al., 2009; Presto et al., 2009; Smith et al., 2009). The LBNL squalane data and CMU n-heptadecane data are HR data (the  $m/z$  43 data shown are from the  $C_2H_3O^+$  fragment) and residual analysis has been performed on the UMR diesel and wood smoke data (Sage et al., 2008; Grieshop et al., 2009), allowing for direct comparison of these datasets with ambient OOA components and chamber SOA.

In Fig. 6a, b, and c, the lines connecting the data points indicate the range of  $f_{44}$  and  $f_{43}$  observed in each experiment. As explained in more detail below, the range observed does not necessarily correspond to the beginning and end of the experiments. The two dotted lines in these figures are the same as those in Fig. 4, encompassing the space in which the ambient data fall. It is clear that most laboratory data fall into the same region as the ambient data. There are two exceptions:  $\alpha$ -pinene SOA formed in flow tube experiments (Jimenez et al., 2009), and isoprene SOA formed under low  $NO_x$  ( $H_2O_2$  photolysis) conditions (Kroll et al., 2006). The

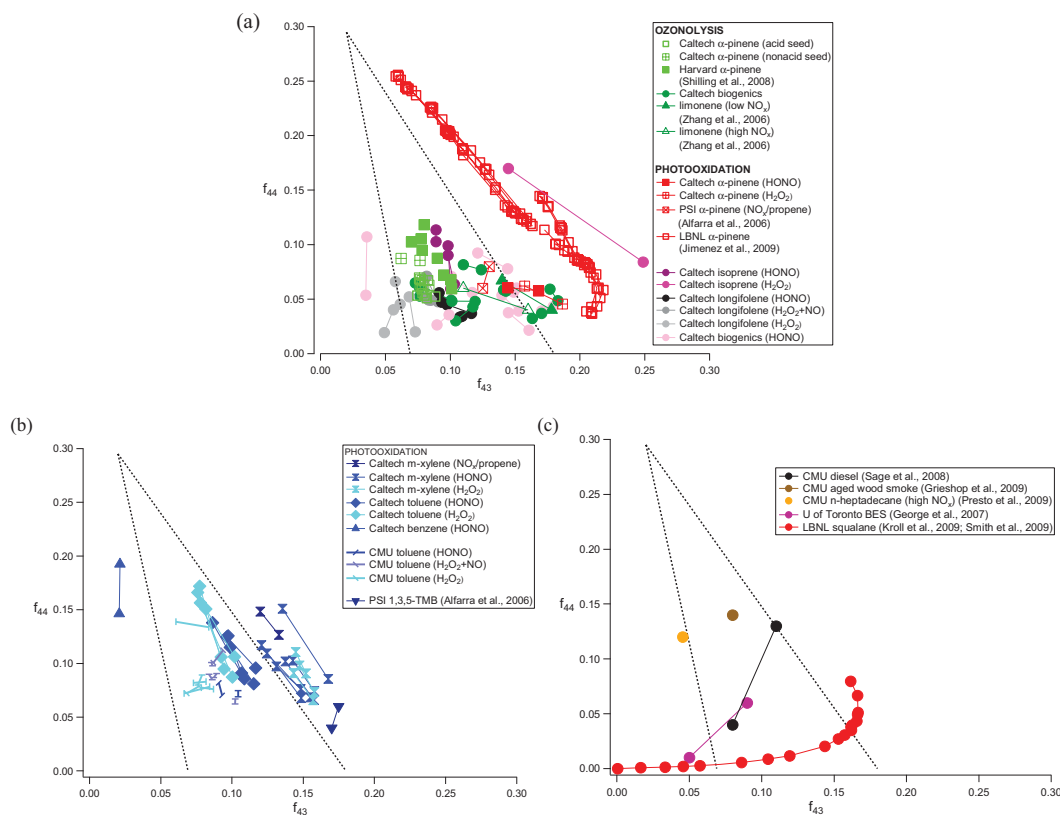


**Fig. 6.** (a)  $f_{44}$  vs.  $f_{43}$  for SOA formed by the ozonolysis/photooxidation of a suite of biogenic precursors from chamber experiments, including isoprene, terpenes, and sesquiterpenes (Gao et al., 2004a, b; Bahreini et al., 2005; Kroll et al., 2006; Lee et al., 2006a, b; Ng et al., 2006; Ng et al., 2007a). Also shown in this figure are flow tube data of the heterogeneous oxidation (by OH radicals) of SOA formed from  $\alpha$ -pinene ozonolysis (LBNL data). The lines connecting the data points indicate the range of  $f_{44}$  and  $f_{43}$  observed in each experiment. For  $\alpha$ -pinene ozonolysis, only the values at the end of the experiment are shown to avoid crowding the plot. The two dotted lines are the same as those in Fig. 4. (b) Chamber data from the photooxidation of a series of aromatic hydrocarbons, including *m*-xylene, toluene, benzene, and 1,3,5-trimethylbenzene (Ng et al., 2007b; Hildebrandt et al., 2009). The lines connecting the data points indicate the range of  $f_{44}$  and  $f_{43}$  observed in each experiment. The two dotted lines are the same as those in Fig. 4. (c) Chamber and flow tube data from the photooxidation/heterogeneous oxidation of POA. The LBNL squalane data and CMU *n*-heptadecane data are HR data (the  $m/z$  43 data shown are from the  $\text{C}_2\text{H}_3\text{O}^+$  fragment). For diesel and wood smoke (Sage et al., 2008; Grieshop et al., 2009), the data shown here are from the residual mass spectra (i.e. spectra in which the POA contribution has been excluded). The LBNL squalane data starts from zero because the experiment starts with HOA. The two dotted lines are the same as those in Fig. 4.

reason for the higher  $f_{43}$  observed in the flow tube experiments is unclear at this point. It is possible that the SOA formed in these experiments experiences a higher degree of heterogeneous oxidation owing to the very high OH levels, which may result in different aerosol compositions compared to the much gentler oxidation in chamber experiments. For the low- $\text{NO}_x$  isoprene SOA, HR data show that other than  $\text{CO}_2^+$ , there is substantial contribution of  $\text{C}_2\text{H}_4\text{O}^+$  at  $m/z$  44 for SOA formed from the photooxidation of erythritol

(Kessler et al., 2010), which is structurally very similar to the tetrols observed in isoprene low- $\text{NO}_x$  SOA (Surratt et al., 2006; Kleindienst et al., 2009). Hence, it is expected that the  $m/z$  44 of the isoprene SOA shown in Fig. 6a will also have substantial contributions from non- $\text{CO}_2^+$  ions, resulting in the relatively higher values compared to other experiments. This issue should be revisited when HR data for most of these reactions become available by plotting  $\text{CO}_2^+/\text{OA}$  instead of  $f_{44}$ .

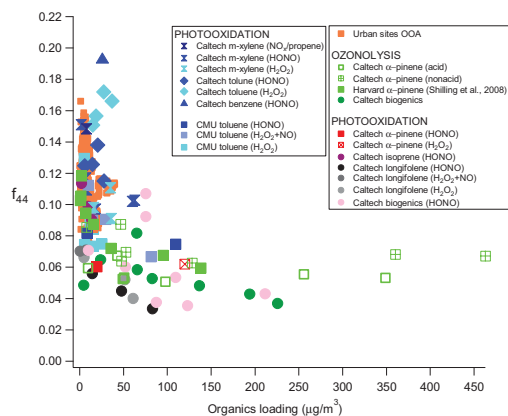


**Fig. 7.**  $f_{44}$  as a function of organics loading (measured with AMS) for the chamber experiments shown in Figs. 6a and b. For each experiment, only the highest  $f_{44}$  value is shown to avoid crowding the plot. The orange points are the OOA data from various urban sites (Beijing, Tokyo summer, NYC summer, Riverside, Pittsburgh).

The majority of the laboratory data (Fig. 6a–c) fall into the triangle region in Fig. 4 as well as the curve envelope in Fig. 5. However, most of the data reside in the lower half of the triangle (and lower half of the curve), indicating that the laboratory SOA is more similar to the less oxidized ambient SV-OOA, and rarely become as oxidized as ambient LV-OOA. Similar to SV-OOA, there is quite a large variability in the  $f_{43}$  in the laboratory data. This is not surprising as the data encompass a wide range of SOA precursors and experimental conditions such as types of oxidants, oxidant concentrations (exposure), initial hydrocarbon concentrations,  $\text{NO}_x$  level, temperature, relative humidity, etc. Possible reasons for laboratory SOA being less oxidized than ambient OOA are: higher loadings employed in many laboratory experiments that favor partitioning of less oxidized species (which would remain in the gas phase under atmospheric conditions) (Duplissy et al., 2008; Shilling et al., 2009) and limited residence time in chambers (which limits the degree of aging accessible in chamber experiments). To explore the first possibility, Fig. 7 shows  $f_{44}$  as a function of OA concentration for all of the chamber experiments in Fig. 6a and b. For each experiment, only the highest  $f_{44}$  value is shown to avoid crowding the plot. Also shown in Fig. 7 are the OOA data from various urban sites (Beijing, Tokyo summer, NYC summer, Riverside, Pittsburgh). These OOA data include only the time periods when variable partitioning of semi-volatiles is expected (i.e. time periods when there is relatively low temperature, and/or changing temperature). The laboratory data with lower loadings overlap the ambient data. When putting all the data together, it is clear that  $f_{44}$  decreases with increasing loading. This is consistent with semivolatile par-

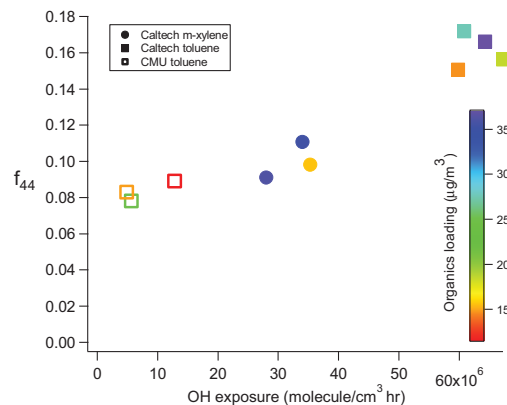


**Fig. 8.**  $f_{44}$  (highest  $f_{44}$  observed in the experiment) vs. the OH exposure for SOA formed from the photooxidation of *m*-xylene and toluene under low- $\text{NO}_x$  ( $\text{H}_2\text{O}_2$ ) conditions (Ng et al., 2007b; Hildebrandt et al., 2009). Each data point is colored according to the loading of that particular experiment.

titition (Odum et al., 1996; Donahue et al., 2006); with increasing OA concentration even the less oxidized and more volatile species will partition into the aerosol phase, resulting in a lower  $f_{44}$ . The change (decreasing  $f_{44}$  with increasing loading) is most dramatic at lower loadings ( $0\text{--}20\ \mu\text{g}/\text{m}^3$ , which are typical in the atmosphere), and it appears to level off for loadings higher than  $\sim 100\ \mu\text{g}/\text{m}^3$ . The effect of loading on composition of SOA formed from a particular system ( $\alpha$ -pinene ozonolysis) has been investigated in a recent study (Shilling et al., 2009) and the results are consistent with this work.

Again, the main reason for the scatter in Fig. 7 likely arises from the wide range of precursors and experimental conditions. However, comparing experiments carried out under similar conditions underscores the importance of oxidation time and oxidant exposure in laboratory experiments. As seen in Fig. 6b, SOA formed from the photooxidation of aromatics in the smaller Carnegie Mellon chamber is substantially less oxidized than in the larger Caltech chamber. Figure 8 shows the  $f_{44}$  (highest  $f_{44}$  observed in the experiment) vs. the OH exposure for low- $\text{NO}_x$  experiments from both datasets; each data point is colored according to the loading of that particular experiment. As seen in Fig. 8, some of the toluene experiments from these two datasets have very similar loadings; however, the  $f_{44}$  observed in the Caltech experiments is substantially higher as a result of the increased OH exposure. The difference in OH exposure arises mainly from the larger oxidation time afforded by the smaller relative wall losses of the larger Caltech chamber, as the OH concentrations employed in both datasets are comparable ( $\sim 1\text{--}3 \times 10^6$  molecules/ $\text{cm}^3$ , estimated from the decay of the hydrocarbon) (Ng et al., 2007b; Hildebrandt et al., 2009). It

is noted that the flow tube  $\alpha$ -pinene data (LBNL data) also have extremely high  $f_{44}$  values, likely a result of the very high OH concentrations (up to  $8 \times 10^{10}$  molecules/cm<sup>3</sup>) used in the flow tube experiments (Jimenez et al., 2009), corresponding to very high levels of atmospheric aging. In summary, both the higher organic mass loadings and the limited aging likely explain why the chamber data do not reach the levels of oxidation observed in the atmosphere.

Several interesting observations can be made when examining the laboratory data in more detail. From Fig. 6a, it appears that the SOA formed from  $\alpha$ -pinene photooxidation has a relatively higher  $f_{43}$  than that formed from  $\alpha$ -pinene ozonolysis. SOA formed from biogenic hydrocarbons spans a similar range in  $f_{44}$  in ozonolysis and photooxidation experiments. However, the evolution of  $m/z$  44 as a function of OA concentration for these two types of experiments is very different, as shown in Fig. 9a ( $\alpha$ -pinene ozonolysis) and Fig. 9b ( $\alpha$ -pinene photooxidation). In both experiments,  $m/z$  44 decreases with increasing OA during the early phase of the experiment. With the very low loading at the initial stage of SOA growth, only the highly oxygenated and least volatile species will partition into the aerosol phase, resulting in a higher  $f_{44}$ . However, these highly oxygenated species are later diluted in the particle phase by the partitioning of less-oxygenated semivolatile species with increased OA concentration. Such behavior has been observed in several previous studies (Bahreini et al., 2005; Baltensperger et al., 2005; Zhang et al., 2006; Duplissy et al., 2008; Shilling et al., 2009). After SOA mass peaks, the loadings decrease owing to wall loss. The  $f_{44}$  in the ozonolysis experiment stays relatively constant during this period. This is not surprising as ozone reacts only with the double bond, and further chemistry ceases after all  $\alpha$ -pinene is consumed. When loadings decrease due to wall loss, one might expect that the semivolatile species would partition back to the gas-phase and result in higher  $f_{44}$  in the SOA. The lack of this observation suggests that the particles lost to the wall still participate in the partitioning, consistent with previous studies (Weitkamp et al., 2007; Hildebrandt et al., 2009). On the other hand, the  $f_{44}$  in the photooxidation experiment continues to increase after peak aerosol growth, indicating further changes in SOA composition with photochemical aging. The increase in  $f_{44}$  with decreased loading (due to wall loss) does not trace the original path as the gas-phase chemistry in the chamber is constantly changing. It is noted that similar behavior is also observed in the ozonolysis and photooxidation of other biogenic hydrocarbons. The evolution of  $f_{44}$  with organic mass loadings is quite different for aromatic hydrocarbons (e.g. *m*-xylene as shown in Fig. 9c). Unlike  $\alpha$ -pinene, the  $f_{44}$  starts increasing from the beginning of the experiment and continues over the course of the experiment. This suggests that the products formed from the photooxidation of *m*-xylene are generally less volatile, consistent with the higher  $f_{44}$  values in aromatic experiments (compared to biogenics experiments). After peak SOA growth, the  $f_{44}$  also

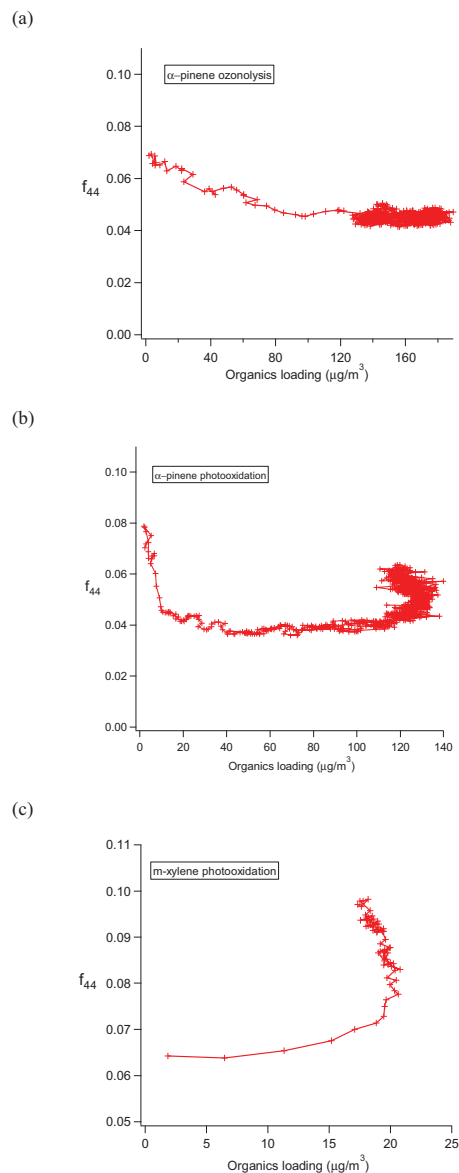


**Fig. 9.** (a): Change in  $f_{44}$  as a function of organics loading over the course of a typical  $\alpha$ -pinene ozonolysis experiment. (b): Change in  $f_{44}$  as a function of organics loading over the course of a typical  $\alpha$ -pinene photooxidation experiment (low- $\text{NO}_x$ ). (c): Change in  $f_{44}$  as a function of organics loading over the course of a typical *m*-xylene photooxidation experiment (low- $\text{NO}_x$ ).



continues to increase as a result of further oxidation. All these observations highlight the dynamics of SOA evolution. While peak aerosol growth is useful for determining SOA yields in chamber experiments, further chemistry can still be ongoing and should not be overlooked.

#### 4 Conclusions

In this study we present results from the factor analysis of 43 AMS datasets (27 of the datasets are reanalyzed in this work) and provide an overview of OOA components in the Northern Hemisphere and their evolution in the atmosphere. At most sites, we are able to resolve the OA into HOA and OOA components. For some sites a BBOA factor is also observed. In many analyses, we can further separate the OOA into LV-OOA and SV-OOA components. A wide range of O:C ratio is observed for both LV-OOA ( $0.73 \pm 0.14$ ) and SV-OOA ( $0.35 \pm 0.14$ ) components, highlighting the range of conditions that give rise to these factors, such as meteorology, SOA precursors, and photochemical aging. The OOA components (OOA, LV-OOA, and SV-OOA) from all sites cluster within a well-defined triangular region in the  $f_{44}$  vs.  $f_{43}$  space. These observations allow for a standardized means of comparing and characterizing any OOA components (laboratory or ambient) observed with the AMS. Viewing laboratory data in this space, for example, allows for a direct connection between laboratory and ambient measurements. A compilation of AMS laboratory SOA data reveals that laboratory SOA falls into the lower half of the triangular region, characteristic of lower O:C ratios and photochemical ages. The laboratory SOA is more similar to SV-OOA components and rarely become as oxidized as LV-OOA components. This likely arises from the higher loadings and limited oxidation time in most laboratory experiments.

While the OOA components observed at the different locations differ according to their respective sources, meteorology, and degrees of photochemical aging, when taken together they provide a generalized view of the photochemical aging process of ambient OA. In particular, the oxidation process results in increasingly similar OOA composition regardless of the original OOA source. Moreover, it appears that the transformation between SV-OOA and LV-OOA at multiple sites shares common features that could potentially enable a simplified description of the atmospheric oxidation of OA. For instance, the transformation shows a clear trend in O:C vs.  $m/z$  44/43 ratios. While the data presented in the O:C vs. 44/43 space (Fig. 5) is mathematically the same as  $f_{44}$  vs.  $f_{43}$  triangular space (Fig. 4), this plot potentially allows one to more readily connect AMS observations with those obtained by other instruments. The ability to make such connections is invaluable because the evolution of OA is a complex and dynamic process and there is no single instrument that can capture all of the important features (Hallquist et al., 2009).

Traditionally, SOA models often employ parameters derived from chamber experiments based on a two product partitioning model (Pankow, 1994; Odum et al., 1996), and more recently, the volatility basis-set approach (Lane et al., 2008; Murphy and Pandis, 2009). While SOA yield parameters derived from chamber experiments have proven to be very useful in providing the basis for SOA simulation in the last ten years or so, a modified representation may be better to capture the dynamic evolution of OA in the atmosphere. The compact view of photochemical SOA oxidation provided by the SV-OOA and LV-OOA components can form the basis of new SOA modeling frameworks. Recently, a two-dimensional volatility basis-set (2D-VBS) modeling framework has been proposed that uses OA volatility and oxidation state (approximated by O:C) as its two basis vectors (Jimenez et al., 2009). The model captures the main features of the evolution of OA in multiple field studies and simulation chambers, showing the transformation from SV-OOA to LV-OOA with increasing photochemical aging in the O:C vs. volatility space. A new framework such as this could form the basis of future modeling approaches, and with additional field measurements, laboratory studies, and inventories one will be able to more accurately predict the formation and evolution of OA in the atmosphere.

#### Appendix A

In Fig. 4, the plot shows  $f_{44}$  vs.  $f_{43}$ . We can re-write  $f_{44}$  as  $44/OA$  and  $f_{43}$  as  $43/OA$ .

Considering a line in this space:

$$\frac{44}{OA} = m \frac{43}{OA} + c \quad (\text{A1})$$

where  $m$  = slope;  $c$  = intercept.

Divide both sides of Eq. (1) by 43:

$$\frac{44}{43 \cdot OA} = \frac{m}{OA} + \frac{c}{43}$$

$$\frac{44}{43} = m + \frac{c \cdot OA}{43}$$

$$\frac{44}{43} - m = \frac{c \cdot OA}{43}$$

$$\frac{1}{\frac{44}{43} - m} = \frac{43}{c \cdot OA}$$

$$\frac{43}{OA} = \frac{c}{\frac{44}{43} - m}$$

Substitute this back to Eq. (1):

$$\frac{44}{OA} = m \frac{c}{\frac{44}{43} - m} + c$$

$$\frac{44}{OA} = \frac{m \cdot c}{\frac{44}{43} - m} + c$$

This is a curve in the 44/OA vs. 44/43 space (Fig. 5).

**Acknowledgements.** Aerodyne Research acknowledges the following funding for various field campaigns: ICARTT (NOAA NA05OAR4310102); NEAQS (NOAA AB133R04SE0480, NOAA RA1330-02-SE-0150); MILARGO (DOE DE-FGOZ-O5ER63982, NSF ATM-0528170). Y. Rudich and J. L. Jimenez acknowledge the financial support of the USA-Israel bi-national science foundation (BSF grant #2008146). I. M. Ulbrich, K. S. Docherty, P. F. DeCarlo, and J. L. Jimenez are grateful for funding from NOAA NA08OAR4310565, NSF ATM-0919189 and DOE DEFG0208ER64627. Q. Zhang acknowledges the support from the Department of Energy's Atmospheric Science Program (Office of Science, BER), Grant no. DEFG02-08ER64627. The authors would like to acknowledge U. Baltensperger, P. J. Ziemann, and L. M. Russell for helpful discussions. We acknowledge the contributions of the following individuals to recently published datasets included in Lanz et al. (2009): Crete (G. J. Engelhart, C. Mohr, and E. Kostenidou); Grenoble (O. Favez, C. George, and B. D'Anna); Rhine Valley (C. Mohr and S. Weimer). We also thank the many other research groups and individuals who contributed datasets included in this work (individual publications are acknowledged in the Tables S1 and S2 in the supplementary material: <http://www.atmos-chem-phys.net/10/4625/2010/acp-10-4625-2010-supplement.pdf>).

Edited by: T. Hoffmann

## References

- Aiken, A. C., DeCarlo, P. F., and Jimenez, J. L.: Elemental Analysis of Organic Species with Electron Ionization High-Resolution Mass Spectrometry, *Anal. Chem.*, **79**, 8350–8358, doi:10.1021/ac071150w, 2007.
- Aiken, A. C., Decarlo, P. F., Kroll, J. H., Worsnop, D. R., Huffman, J. A., Docherty, K. S., Ulbrich, I. M., Mohr, C., Kimmel, J. R., Sueper, D., Sun, Y., Zhang, Q., Trimborn, A., Northway, M., Ziemann, P. J., Canagaratna, M. R., Onasch, T. B., Alfarra, M. R., Prevot, A. S. H., Dommen, J., Duplissy, J., Metzger, A., Baltensperger, U., and Jimenez, J. L.: O/C and OM/OC ratios of primary, secondary, and ambient organic aerosols with high-resolution time-of-flight aerosol mass spectrometry, *Environ. Sci. Technol.*, **42**, 4478–4485, 2008.
- Aiken, A. C., de Foy, B., Wiedinmyer, C., DeCarlo, P. F., Ulbrich, I. M., Wehrli, M. N., Szidat, S., Prevot, A. S. H., Noda, J., Wacker, L., Volkamer, R., Fortner, E., Wang, J., Laskin, A., Shutthanandan, V., Zheng, J., Zhang, R., Paredes-Miranda, G., Arnott, W. P., Molina, L. T., Sosa, G., Querol, X., and Jimenez, J. L.: Mexico City aerosol analysis during MILAGRO using high resolution aerosol mass spectrometry at the urban supersite (T0) – Part 2: Analysis of the biomass burning contribution and the modern carbon fraction, *Atmos. Chem. Phys. Discuss.*, **9**, 25915–25981, doi:10.5194/acpd-9-25915-2009, 2009a.
- Aiken, A. C., Salcedo, D., Cubison, M. J., Huffman, J. A., DeCarlo, P. F., Ulbrich, I. M., Docherty, K. S., Sueper, D., Kimmel, J. R., Worsnop, D. R., Trimborn, A., Northway, M., Stone, E. A., Schauer, J. J., Volkamer, R. M., Fortner, E., de Foy, B., Wang, J., Laskin, A., Shutthanandan, V., Zheng, J., Zhang, R., Gaffney, J., Marley, N. A., Paredes-Miranda, G., Arnott, W. P., Molina, L. T., Sosa, G., and Jimenez, J. L.: Mexico City aerosol analysis during MILAGRO using high resolution aerosol mass spectrometry at the urban supersite (T0) – Part 1: Fine particle composition and organic source apportionment, *Atmos. Chem. Phys.*, **9**, 6633–6653, doi:10.5194/acp-9-6633-2009, 2009b.
- Alfarra, M. R.: Insights into the atmospheric organic aerosols using an aerosol mass spectrometer, Thesis, University of Manchester, UK, 2004.
- Alfarra, M. R., Coe, H., Allan, J. D., Bower, K. N., Boudries, H., Canagaratna, M. R., Jimenez, J. L., Jayne, J. T., Garforth, A. A., Li, S. M., and Worsnop, D. R.: Characterization of urban and rural organic particulate in the lower Fraser valley using two Aerodyne aerosol mass spectrometers, *Atmos. Environ.*, **38**, 5745–5758, 2004.
- Alfarra, M. R., Paulsen, D., Gysel, M., Garforth, A. A., Dommen, J., and Prévôt, A. S. H., Worsnop, D. R., Baltensperger, U., and Coe, H.: A mass spectrometric study of secondary organic aerosols formed from the photooxidation of anthropogenic and biogenic precursors in a reaction chamber, *Atmos. Chem. Phys.*, **6**, 5279–5293, 2006, <http://www.atmos-chem-phys.net/6/5279/2006/>.
- Allan, J. D., Alfarra, M. R., Bower, K. N., Coe, H., Jayne, J. T., Worsnop, D. R., Aalto, P. P., Kulmala, M., Hyotylainen, T., Cavalli, F., and Laaksonen, A.: Size and composition measurements of background aerosol and new particle growth in a Finnish forest during QUEST 2 using an Aerodyne Aerosol Mass Spectrometer, *Atmos. Chem. Phys.*, **6**, 315–327, 2006, <http://www.atmos-chem-phys.net/6/315/2006/>.
- Bahreini, R., Keywood, M. D., Ng, N. L., Varutbangkul, V., Gao, S., Flagan, R. C., Seinfeld, J. H., Worsnop, D. R., and Jimenez, J. L.: Measurements of secondary organic aerosol from oxidation of cycloalkenes, terpenes, and *m*-xylene using an Aerodyne aerosol mass spectrometer, *Environ. Sci. Technol.*, **39**, 5674–5688, 2005.
- Baltensperger, U., Kalberer, M., Dommen, J., Paulsen, D., Alfarra, M. R., Coe, H., Fisseha, R., Gascho, A., Gysel, M., Nyeki, S., Sax, M., Steinbacher, M., Prévôt, A. S. H., Sjogren, S., Weingartner, E., and Zenobi, R.: Secondary organic aerosols from anthropogenic and biogenic precursors, *Faraday Discussions*, **130**, 265–278, 2005.
- Canagaratna, M. R., Jayne, J. T., Jimenez, J. L., Allan, J. D., Alfarra, M. R., Zhang, Q., Onasch, T. B., Drewnick, F., Coe, H., Middlebrook, A., Delia, A., Williams, L. R., Trimborn, A. M., Northway, M. J., DeCarlo, P. F., Kolb, C. E., Davidovits, P., and Worsnop, D. R.: Chemical and microphysical characterization of ambient aerosols with the Aerodyne aerosol mass spectrometer, *Mass Spectrom. Rev.*, **26**, 185–222, 2007.
- Cappa, C. D., Bates, T. S., Quinn, P. K., and Lack, D. A.: Source characterization from ambient measurements of aerosol optical properties, *Geophys. Res. Lett.*, **36**, L14813, doi:10.1029/2009GL038979, 2009.
- Cottrell, L. D., Griffin, R. J., Jimenez, J. L., Zhang, Q., Ulbrich, I., Ziemba, L. D., Beckman, P. J., Sive, B. C., and Talbot, R. W.: Submicron particles at Thompson Farm during ICARTT measured using aerosol mass spectrometry, *J. Geophys. Res.-Atmos.*, **113**, D08212, doi:10.1029/2007JD009192, 2008.
- de Gouw, J. A., Middlebrook, A. M., Warneke, C., Goldan, P. D., Kuster, W. C., Roberts, J. M., Fehsenfeld, F. C., Worsnop, D. R., Canagaratna, M. R., Pszenny, A. A. P., Keene, W. C., Marchewka, M., Bertman, S. B., and Bates, T. S.: Budget of organic carbon in a polluted atmosphere: Results from the New England Air Quality Study in 2002, *J. Geophys. Res.-Atmos.*

- 110, D16305, doi:10.11029/12004JD005623, 2005.
- DeCarlo, P. F., Kimmel, J. R., Trimborn, A., Northway, M. J., Jayne, J. T., Aiken, A. C., Gonin, M., Fuhrer, K., Horvath, T., Docherty, K., Worsnop, D. R., and Jiménez, J. L.: A Field-Deployable High-Resolution Time-of-Flight Aerosol Mass Spectrometer, *Anal. Chem.*, 78, 8281–8289, 2006.
- Decesari, S., Facchini, M. C., Matta, E., Lettini, F., Mircea, M., Fuzzi, S., Tagliavini, E., and Putaud, J. P.: Chemical features and seasonal variation of fine aerosol water-soluble organic compounds in the Po Valley, Italy, *Atmos. Environ.*, 35, 3691–3699, 2001.
- Dinar, E., Taraniuk, I., Graber, E. R., Katsman, S., Moise, T., Anttila, T., Mentel, T. F., and Rudich, Y.: Cloud Condensation Nuclei properties of model and atmospheric HULIS, *Atmos. Chem. Phys.*, 6, 2465–2481, 2006, <http://www.atmos-chem-phys.net/6/2465/2006/>.
- Dinar, E., Abo Riziq, A., Spindler, C., Erlick, C., Kiss, G., and Rudich, Y.: The complex refractive index of atmospheric and model humic-like substances (HULIS) retrieved by a cavity ring down aerosol spectrometer, *Faraday Discussions*, 137, 279–295, 2008.
- Docherty, K. S., Stone, E. A., Ulbrich, I. M., DeCarlo, P. F., Snyder, D. C., Schauer, J. J., Peltier, R. E., Weber, R. J., Murphy, S. M., Seinfeld, J. H., Grover, B. D., Eatough, D. J., and Jimenez, J. L.: Apportionment of Primary and Secondary Organic Aerosols in Southern California during the 2005 Study of Organic Aerosols in Riverside (SOAR-1), *Environ. Sci. Technol.*, 42, 7655–7662, 2008.
- Donahue, N. M., Robinson, A. L., Stanier, C. O., and Pandis, S. N.: Coupled partitioning, dilution, and chemical aging of semivolatile organics, *Environ. Sci. Technol.*, 40, 2635–2643, 2006.
- Drewnick, F., Hings, S. S., DeCarlo, P., Jayne, J. T., Gonin, M., Fuhrer, K., Weimer, S., Jimenez, J. L., Demerjian, K. L., Borrmann, S., and Worsnop, D. R.: A new time-of-flight aerosol mass spectrometer (TOF-AMS) – Instrument description and first field deployment, *Aerosol Sci. Technol.*, 39, 637–658, 2005.
- Duplissy, J., Gysel, M., Alfarra, M. R., Dommen, J., Metzger, A., Prevot, A. S. H., Weingartner, E., Laaksonen, A., Raatikainen, T., Good, N., Turner, S. F., McFiggans, G., and Baltensperger, U.: Cloud forming potential of secondary organic aerosol under near atmospheric conditions, *Geophys. Res. Lett.*, L03818, doi:10.1029/2007GL031075, 2008.
- Facchini, M. C., Decesari, S., Mircea, M., Fuzzi, S., and Loglio, G.: Surface tension of atmospheric wet aerosol and cloud/fog droplets in relation to their organic carbon content and chemical composition, *Atmos. Environ.*, 34, 4853–4857, 2000.
- Faulhaber, A. E., Thomas, B. M., Jiménez, J. L., Jayne, J. T., Worsnop, D. R., and Ziemann, P. J.: Characterization of a thermodesorption particle beam mass spectrometer system for the study of organic aerosol volatility and composition, *Atmos. Meas. Tech.*, 1, 15–31, 2009, <http://www.atmos-meas-tech.net/1/15/2009/>.
- Fuzzi, S., Decesari, S., Facchini, M. C., Matta, E., Mircea, M., and Tagliavini, E.: A simplified model of the water soluble organic component of atmospheric aerosols, *Geophys. Res. Lett.*, 28, 4079–4082, 2001.
- Gao, S., Keywood, M., Ng, N. L., Surratt, J., Varutbangkul, V., Bahreini, R., Flagan, R. C., and Seinfeld, J. H.: Low-molecular-weight and oligomeric components in secondary organic aerosol from the ozonolysis of cycloalkenes and  $\alpha$ -pinene, *J. Phys. Chem. A*, 108, 10147–10164, 2004a.
- Gao, S., Ng, N. L., Keywood, M., Varutbangkul, V., Bahreini, R., Nenes, A., He, J. W., Yoo, K. Y., Beauchamp, J. L., Hodyss, R. P., Flagan, R. C., and Seinfeld, J. H.: Particle phase acidity and oligomer formation in secondary organic aerosol, *Environ. Sci. Technol.*, 38, 6582–6589, 2004b.
- George, I. J., Vlasenko, A., Slowik, J. G., Broekhuizen, K., and Abbatt, J. P. D.: Heterogeneous oxidation of saturated organic aerosols by hydroxyl radicals: uptake kinetics, condensed-phase products, and particle size change, *Atmos. Chem. Phys.*, 7, 4187–4201, 2007, <http://www.atmos-chem-phys.net/7/4187/2007/>.
- Graber, E. R. and Rudich, Y.: Atmospheric HULIS: How humic-like are they? A comprehensive and critical review, *Atmos. Chem. Phys.*, 6, 729–753, 2006, <http://www.atmos-chem-phys.net/6/729/2006/>.
- Grieshop, A. P., Donahue, N. M., and Robinson, A. L.: Laboratory investigations of photochemical oxidation of organic aerosol from wood fires – Part 2: Analysis of aerosol mass spectrometer data, *Atmos. Chem. Phys.*, 9, 2227–2240, 2009, <http://www.atmos-chem-phys.net/9/2227/2009/>.
- Hallquist, M., Wenger, J. C., Baltensperger, U., Rudich, Y., Simpson, D., Claeys, M., Dommen, J., Donahue, N. M., George, C., Goldstein, A. H., Hamilton, J. F., Herrmann, H., Hoffmann, T., Iinuma, Y., Jang, M., Jenkin, M. E., Jimenez, J. L., Kiendler-Scharr, A., Maenhaut, W., McFiggans, G., Mentel, T. F., Monod, A., Prevot, A. S. H., Seinfeld, J. H., Surratt, J. D., Szmigielski, R., and Wildt, J.: The formation, properties and impact of secondary organic aerosol: current and emerging issues, *Atmos. Chem. Phys.*, 9, 5155–5236, 2009, <http://www.atmos-chem-phys.net/9/5155/2009/>.
- Herndon, S. C., Onasch, T. B., Wood, E. C., Kroll, J. H., Canagaratna, M. R., Jayne, J. T., Zavala, M. A., Knighton, W. B., Mazzoleni, C., Dubey, M. K., Ulbrich, I. M., Jimenez, J. L., Seila, R., de Gouw, J. A., de Foy, B., Fast, J., Molina, L. T., Kolb, C. E., and Worsnop, D. R.: Correlation of secondary organic aerosol with odd oxygen in Mexico City, *Geophys. Res. Lett.*, L15804, doi:10.1029/2008GL034058, 2008.
- Hildebrandt, L., Donahue, N. M., and Pandis, S. N.: High formation of secondary organic aerosol from the photooxidation of toluene, *Atmos. Chem. Phys.*, 9, 2973–2986, 2009, <http://www.atmos-chem-phys.net/9/2973/2009/>.
- Hildebrandt, L., Engelhart, G. J., Mohr, C., Kostenidou, E., Lanz, V. A., Bougiatioti, A., DeCarlo, P. F., Prevot, A. S. H., Baltensperger, U., Mihalopoulos, N., Donahue, N. M., and Pandis, S. N.: Aged organic aerosol in the Eastern Mediterranean: the Finokalia Aerosol Measurement Experiment 2008, *Atmos. Chem. Phys.*, 10, 4167–4186, doi:10.5194/acp-10-4167-2010, 2010.
- Holzinger, R., Millet, D. B., Williams, B., Lee, A., Kreisberg, N., Hering, S. V., Jimenez, J., Allan, J. D., Worsnop, D. R., and Goldstein, A. H.: Emission, oxidation, and secondary organic aerosol formation of volatile organic compounds as observed at Chebogue Point, Nova Scotia, *J. Geophys. Res.-Atmos.*, 112, D10S24, doi:10.1029/2006JD007599, 2007.
- Huffman, J. A., Docherty, K. S., Aiken, A. C., Cubison, M. J., Ulbrich, I. M., DeCarlo, P. F., Sueper, D., Jayne, J. T., Worsnop, D. R., Ziemann, P. J., and Jimenez, J. L.: Chemically-resolved



- aerosol volatility measurements from two megacity field studies, *Atmos. Chem. Phys.*, 9, 7161–7182, doi:10.5194/acp-9-7161-2009, 2009.
- Jayne, J. T., Leard, D. C., Zhang, X. F., Davidovits, P., Smith, K. A., Kolb, C. E., and Worsnop, D. R.: Development of an aerosol mass spectrometer for size and composition analysis of submicron particles, *Aerosol Sci. Technol.*, 33, 49–70, 2000.
- Jimenez, J. L., Canagaratna, M. R., and Donahue, N. M., et al.: Evolution of Organic Aerosols in the Atmosphere, *Science*, 326, 1525–1529, doi:10.1126/science.1180353, 2009.
- Kanakidou, M., Seinfeld, J. H., Pandis, S. N., Barnes, I., Dentener, F. J., Facchini, M. C., Van Dingenen, R., Ervens, B., Nenes, A., Nielsen, C. J., Swietlicki, E., Putaud, J. P., Balkanski, Y., Fuzzi, S., Horth, J., Moortgat, G. K., Winterhalter, R., Myhre, C. E. L., Tsigaridis, K., Vignati, E., Stephanou, E. G., and Wilson, J.: Organic aerosol and global climate modelling: a review, *Atmos. Chem. Phys.*, 5, 1053–1123, 2005, <http://www.atmos-chem-phys.net/5/1053/2005/>.
- Kessler, S. H., Smith, J. D., Che, D. L., Wilson, K. R., and Kroll, J. H.: Products of the heterogeneous oxidation of polyhydroxylated organic aerosol species, in preparation, 2010.
- Kleindienst, T. E., Lewandowski, M., Offenber, J. H., Jaoui, M., and Edney, E. O.: The formation of secondary organic aerosol from the isoprene plus OH reaction in the absence of NO<sub>x</sub>, *Atmos. Chem. Phys.*, 9, 6541–6558, 2009, <http://www.atmos-chem-phys.net/9/6541/2009/>.
- Kleinman, L. I., Springston, S. R., Daum, P. H., Lee, Y. N., Nunnemacker, L. J., Senum, G. I., Wang, J., Weinstein-Lloyd, J., Alexander, M. L., Hubbe, J., Ortega, J., Canagaratna, M. R., and Jayne, J.: The time evolution of aerosol composition over the Mexico City plateau, *Atmos. Chem. Phys.*, 8, 1559–1575, 2008, <http://www.atmos-chem-phys.net/8/1559/2008/>.
- Kroll, J. H., Ng, N. L., Murphy, S. M., Flagan, R. C., and Seinfeld, J. H.: Secondary organic aerosol formation from isoprene photooxidation, *Environ. Sci. Technol.*, 40, 1869–1877, 2006.
- Kroll, J. H., and Seinfeld, J. H.: Chemistry of secondary organic aerosol: Formation and evolution of low-volatility organics in the atmosphere, *Atmos. Environ.*, 42, 3593–3624, 2008.
- Kroll, J. H., Smith, J. D., Che, D. L., Kessler, S. H., Worsnop, D. R., and Wilson, K. R.: Measurement of fragmentation and functionalization pathways in the heterogeneous oxidation of oxidized organic aerosol, *Phys. Chem. Chem. Phys.*, 11, 8005–8014, 2009.
- Lane, T. E., Donahue, N. M., and Pandis, S. N.: Simulating secondary organic aerosol formation using the volatility basis-set approach in a chemical transport model, *Atmos. Environ.*, 42, 7439–7451, 2008.
- Lanz, V. A., Alfarra, M. R., Baltensperger, U., Buchmann, B., Hueglin, C., and Prévôt, A. S. H.: Source apportionment of submicron organic aerosols at an urban site by factor analytical modelling of aerosol mass spectra, *Atmos. Chem. Phys.*, 7, 1503–1522, 2007, <http://www.atmos-chem-phys.net/7/1503/2007/>.
- Lanz, V. A., Alfarra, M. R., Baltensperger, U., Buchmann, B., Hueglin, C., Szidat, S., Wehrli, M. N., Wacker, L., Weimer, S., Caseiro, A., Puxbaum, H., and Prévôt, A. S. H.: Source attribution of submicron organic aerosols during wintertime inversions by advanced factor analysis of aerosol mass spectra, *Environ. Sci. Technol.*, 42, 214–220, 2008.
- Lanz, V. A., Prévôt, A. S. H., Alfarra, M. R., Mohr, C., DeCarlo, P. F., Weimer, S., Gianini, M. F. D., Hueglin, C., Schneider, J., Favez, O., D’Anna, B., George, C., and Baltensperger, U.: Characterization of aerosol chemical composition by aerosol mass spectrometry in Central Europe: an overview, *Atmos. Chem. Phys. Discuss.*, 9, 24985–25021, doi:10.5194/acpd-9-24985-2009, 2009.
- Lee, A., Goldstein, A. H., Keywood, M. D., Gao, S., Varutbangkul, V., Bahreini, R., Ng, N. L., Flagan, R. C., and Seinfeld, J. H.: Gas-phase products and secondary aerosol yields from the ozonolysis of ten different terpenes, *J. Geophys. Res.-Atmos.*, 111, D07302, doi:10.1029/2005JD006437, 2006a.
- Lee, A., Goldstein, A. H., Kroll, J. H., Ng, N. L., Varutbangkul, V., Flagan, R. C., and Seinfeld, J. H.: Gas-phase products and secondary aerosol yields from the photooxidation of 16 different terpenes, *J. Geophys. Res.-Atmos.*, 111, D17305, doi:10.1029/2006JD00705, 2006b.
- Marcolli, C., Canagaratna, M. R., Worsnop, D. R., Bahreini, R., de Gouw, J. A., Warneke, C., Goldan, P. D., Kuster, W. C., Williams, E. J., Lerner, B. M., Roberts, J. M., Meagher, J. F., Fehsenfeld, F. C., Marchewka, M., Bertman, S. B., and Middlebrook, A. M.: Cluster analysis of the organic peaks in bulk mass spectra obtained during the 2002 New England air quality study with an Aerodyne aerosol mass spectrometer, *Atmos. Chem. Phys.*, 6, 5649–5666, 2006, <http://www.atmos-chem-phys.net/6/5649/2006/>.
- McLafferty, L. W. and Turecek, F.: Interpretation of Mass Spectra, University Science Books, Sausalito, California, USA, 1993.
- Millet, D. B., Donahue, N. M., Pandis, S. N., Polidori, A., Stanier, C. O., Turpin, B. J., and Goldstein, A. H.: Atmospheric volatile organic compound measurements during the Pittsburgh Air Quality Study: Results, interpretation, and quantification of primary and secondary contributions, *J. Geophys. Res.-Atmos.*, 110, D07S07, doi:10.1029/2004JD004601, 2005.
- Morgan, W. T., Allan, J. D., Bower, K. N., Highwood, E. J., Liu, D., McMeeking, G. R., Northway, M. J., Williams, P. I., Krejci, R., and Coe, H.: Airborne measurements of the spatial distribution of aerosol chemical composition across Europe and evolution of the organic fraction, *Atmos. Chem. Phys.*, 10, 4065–4083, doi:10.5194/acp-10-4065-2010, 2010.
- Murphy, B. N. and Pandis, S. N.: Simulating the Formation of Semivolatile Primary and Secondary Organic Aerosol in a Regional Chemical Transport Model, *Environ. Sci. Technol.*, 43, 4722–4728, 2009.
- Nemitz, E., Jimenez, J. L., Huffman, J. A., Ulbrich, I. M., Canagaratna, M. R., Worsnop, D. R., and Guenther, A. B.: An eddy-covariance system for the measurement of surface/atmosphere exchange fluxes of submicron aerosol chemical species – First application above an urban area, *Aerosol Sci. Technol.*, 42, 636–657, 2008.
- Ng, N. L., Kroll, J. H., Keywood, M. D., Bahreini, R., Varutbangkul, V., Flagan, R. C., Seinfeld, J. H., Lee, A., and Goldstein, A. H.: Contribution of first- versus second-generation products to secondary organic aerosols formed in the oxidation of biogenic hydrocarbons, *Environ. Sci. Technol.*, 40, 2283–2297, 2006.
- Ng, N. L., Chhabra, P. S., Chan, A. W. H., Surratt, J. D., Kroll, J. H., Kwan, A. J., McCabe, D. C., Wennberg, P. O., Sorooshian, A., Murphy, S. M., Dalleska, N. F., Flagan, R. C., and Seinfeld, J. H.: Effect of NO<sub>x</sub> level on secondary organic aerosol (SOA)

- formation from the photooxidation of terpenes, *Atmos. Chem. Phys.*, 7, 5159–5174, 2007a, <http://www.atmos-chem-phys.net/7/5159/2007/>.
- Ng, N. L., Kroll, J. H., Chan, A. W. H., Chhabra, P. S., Flagan, R. C., and Seinfeld, J. H.: Secondary organic aerosol formation from *m*-xylene, toluene, and benzene, *Atmos. Chem. Phys.*, 7, 3909–3922, 2007b, <http://www.atmos-chem-phys.net/7/3909/2007/>.
- Odum, J. R., Hoffmann, T., Bowman, F., Collins, D., Flagan, R. C., and Seinfeld, J. H.: Gas/particle partitioning and secondary organic aerosol yields, *Environ. Sci. Technol.*, 30, 2580–2585, 1996.
- Paatero, P. and Tapper, U.: Positive Matrix Factorization – a Nonnegative Factor Model with Optimal Utilization of Error-Estimates of Data Values, *Environmetrics*, 5, 111–126, 1994.
- Paatero, P.: A weighted non-negative least squares algorithm for three-way ‘PARAFAC’ factor analysis, *Chemometrics Intell. Lab. Syst.*, 38, 223–242, 1997.
- Paatero, P.: The multilinear engine - A table-driven, least squares program for solving multilinear problems, including the *n*-way parallel factor analysis model, *J. Comput. Graph. Stat.*, 8, 854–888, 1999.
- Paatero, P.: Interactive comment on “Interpretation of organic components from positive matrix factorization of aerosol mass spectrometric data” by I. M. Ulbrich et al., *Atmospheric Chemistry and Physics Discussions*, 8, S2059–S2068, 2008.
- Pang, Y., Turpin, B. J., and Gundel, L. A.: On the importance of organic oxygen for understanding organic aerosol particles, *Aerosol Sci. Technol.*, 40, 128–133, 2006.
- Pankow, J. F.: An absorption-model of gas-particle partitioning of organic compounds in the atmosphere, *Atmos. Environ.*, 28, 185–188, 1994.
- Presto, A. A., Miracolo, M. A., Donahue, N. M., Robinson, A. L., Kroll, J. H., and Worsnop, D. R.: Intermediate-Volatility Organic Compounds: A Potential Source of Ambient Oxidized Organic Aerosol, *Environ. Sci. Technol.*, 43, 4744–4749, 2009.
- Raatikainen, T., Vaattovaara, P., Tiitta, P., Miettinen, P., Rautiainen, J., Ehn, M., Kulmala, M., Laaksonen, A., and Worsnop, D. R.: Physicochemical properties and origin of organic groups detected in boreal forest using an aerosol mass spectrometer, *Atmos. Chem. Phys.*, 10, 2063–2077, doi:10.5194/acp-10-2063-2010, 2010.
- Ritchie, J. D. and Perdue, E. M.: Proton-binding study of standard and reference fulvic acids, humic acids, and natural organic matter, *Geochim. Cosmochim. Acta*, 67, 85–96, 2003.
- Roberts, J. D. and Caserio, M. C.: *Basic Principles of Organic Chemistry*, Benjamin, New York, USA, 1964.
- Russell, L. M., Bahadur, R., Hawkins, L. N., Allan, J. D., Baumgardner, D., Quinn, P. K., and Bates, T. S.: Organic aerosol characterization by complementary measurements of chemical bonds and molecular fragments, *Environ.*, 43, 6100–6105, 2009.
- Sage, A. M., Weitkamp, E. A., Robinson, A. L., and Donahue, N. M.: Evolving mass spectra of the oxidized component of organic aerosol: results from aerosol mass spectrometer analyses of aged diesel emissions, *Atmos. Chem. Phys.*, 8, 1139–1152, 2008, <http://www.atmos-chem-phys.net/8/1139/2008/>.
- Shilling, J. E., Chen, Q., King, S. M., Rosenoern, T., Kroll, J. H., Worsnop, D. R., DeCarlo, P. F., Aiken, A. C., Sueper, D., Jimenez, J. L., and Martin, S. T.: Loading-dependent elemental composition of alpha-pinene SOA particles, *Atmos. Chem. Phys.*, 9, 771–782, 2009, <http://www.atmos-chem-phys.net/9/771/2009/>.
- Slowik, J. G., Stroud, C., Bottenheim, J. W., Brickell, P. C., Chang, R. Y.-W., Liggio, J., Makar, P. A., Martin, R. V., Moran, M. D., Shantz, N. C., Sjostedt, S. J., van Donkelaar, A., Vlasenko, A., Wiebe, H. A., Xia, A. G., Zhang, J., Leaitch, W. R., and Abbatt, J. P. D.: Characterization of a large biogenic secondary organic aerosol event from eastern Canadian forests, *Atmos. Chem. Phys.*, 10, 2825–2845, doi:10.5194/acp-10-2825-2010, 2010.
- Smith, J. D., Kroll, J. H., Cappa, C. D., Che, D. L., Liu, C. L., Ahmed, M., Leone, S. R., Worsnop, D. R., and Wilson, K. R.: The heterogeneous reaction of hydroxyl radicals with sub-micron squalane particles: a model system for understanding the oxidative aging of ambient aerosols, *Atmos. Chem. Phys.*, 9, 3209–3222, 2009, <http://www.atmos-chem-phys.net/9/3209/2009/>.
- Sun, J., Zhang, Q., Canagaratna, M. R., Zhang, Y., Ng, N. L., Sun, Y., Jayne, J. T., Zhang, X., Zhang, X., and Worsnop, D. R.: Highly Time- and Size-Resolved Characterization of Submicron Aerosol Particles in Beijing Using an Aerodyne Aerosol Mass Spectrometer, *Atmos. Environ.*, 44, 131–140, 2009.
- Surratt, J. D., Murphy, S. M., Kroll, J. H., Ng, N. L., Hildebrandt, L., Sorooshian, A., Szmigielski, R., Vermeylen, R., Maenhaut, W., Claeys, M., Flagan, R. C., and Seinfeld, J. H.: Chemical composition of secondary organic aerosol formed from the photooxidation of isoprene, *J. Phys. Chem. A*, 110, 9665–9690, 2006.
- Tagliavini, E., Moretti, F., Decesari, S., Facchini, M. C., Fuzzi, S., and Maenhaut, W.: Functional group analysis by HNMR/chemical derivatization for the characterization of organic aerosol from the SMOCC field campaign, *Atmos. Chem. Phys.*, 6, 1003–1019, 2006, <http://www.atmos-chem-phys.net/6/1003/2006/>.
- Takegawa, N., Miyakawa, T., Kawamura, K., and Kondo, Y.: Contribution of selected dicarboxylic and omega-oxocarboxylic acids in ambient aerosol to the *m/z* 44 signal of an Aerodyne aerosol mass spectrometer, *Aerosol Sci. Technol.*, 41, 418–437, 2007.
- Ulbrich, I. M., Canagaratna, M. R., Zhang, Q., Worsnop, D. R., and Jimenez, J. L.: Interpretation of organic components from Positive Matrix Factorization of aerosol mass spectrometric data, *Atmos. Chem. Phys.*, 9, 2891–2918, 2009, <http://www.atmos-chem-phys.net/9/2891/2009/>.
- Volkamer, R., Jimenez, J. L., San Martini, F., Dzepina, K., Zhang, Q., Salcedo, D., Molina, L. T., Worsnop, D. R., and Molina, M. J.: Secondary organic aerosol formation from anthropogenic air pollution: Rapid and higher than expected, *Geophys. Res. Lett.*, 33, L17811, doi:10.1029/2006GL026899, 2006.
- Wang, S. Y., Zordan, C. A., and Johnston, M. V.: Chemical characterization of individual, airborne sub-10-nm particles and molecules, *Anal. Chem.*, 78, 1750–1754, 2006.
- Weitkamp, E. A., Sage, A. M., Pierce, J. R., Donahue, N. M., and Robinson, A. L.: Organic aerosol formation from photochemical oxidation of diesel exhaust in a smog chamber, *Environ. Sci. Technol.*, 41, 6969–6975, 2007.
- Williams, B. J., Goldstein, A. H., Millet, D. B., Holzinger, R., Kreisberg, N. M., Hering, S. V., White, A. B., Worsnop, D. R., Allan, J. D., and Jimenez, J. L.: Chemical speciation of

- organic aerosol during the International Consortium for Atmospheric Research on Transport and Transformation 2004: Results from in situ measurements, *J. Geophys. Res.-Atmos.*, 112, D10S26, doi:10.1029/2006JD007601, 2007.
- Zhang, J., Hartz, K. E. H., Pandis, S. N., and Donahue, N. M.: Secondary organic aerosol formation from limonene ozonolysis: Homogeneous and heterogeneous influences as a function of NO<sub>x</sub>, *J. Phys. Chem. A*, 110, 11053–11063, 2006.
- Zhang, Q., Alfarra, M. R., Worsnop, D. R., Allan, J. D., Coe, H., Canagaratna, M. R., and Jimenez, J. L.: Deconvolution and quantification of hydrocarbon-like and oxygenated organic aerosols based on aerosol mass spectrometry, *Environ. Sci. Technol.*, 39, 4938–4952, 2005a.
- Zhang, Q., Worsnop, D. R., Canagaratna, M. R., and Jimenez, J. L.: Hydrocarbon-like and oxygenated organic aerosols in Pittsburgh: insights into sources and processes of organic aerosols, *Atmos. Chem. Phys.*, 5, 3289–3311, 2005b, <http://www.atmos-chem-phys.net/5/3289/2005/>.
- Zhang, Q., Jimenez, J. L., Canagaratna, M. R., Allan, J. D., Coe, H., Ulbrich, I., Alfarra, M. R., Takami, A., Middlebrook, A. M., Sun, Y. L., Dzepina, K., Dunlea, E., Docherty, K., DeCarlo, P. F., Salcedo, D., Onasch, T., Jayne, J. T., Miyoshi, T., Shimo, A., Hatakeyama, S., Takegawa, N., Kondo, Y., Schneider, J., Drewnick, F., Borrmann, S., Weimer, S., Demerjian, K., Williams, P., Bower, K., Bahreini, R., Cottrell, L., Griffin, R. J., Rautiainen, J., Sun, J. Y., Zhang, Y. M., and Worsnop, D. R.: Ubiquity and dominance of oxygenated species in organic aerosols in anthropogenically-influenced Northern Hemisphere midlatitudes, *Geophys. Res. Lett.*, 34, L13801, doi:10.1029/2007GL029979, 2007.

## Appendix E

# Role of Aldehyde Chemistry and $\text{NO}_x$ Concentrations in Secondary Organic Aerosol Formation\*

---

\*Reproduced with permission from “Role of aldehyde chemistry and  $\text{NO}_x$  concentrations in secondary organic aerosol formation” by A. W. H. Chan, M. N. Chan, J. D. Surratt, P. S. Chhabra, C. L. Loza, J. D. Crouse, L. D. Yee, R. C. Flagan, P. O. Wennberg, and J. H. Seinfeld *Atmospheric Chemistry and Physics*, 10, 7169–7188, doi:10.5194/acp-10-7169-2010, Copyright 2010 by the Authors. CC Attribution 3.0 License.

## Role of aldehyde chemistry and NO<sub>x</sub> concentrations in secondary organic aerosol formation

A. W. H. Chan<sup>1</sup>, M. N. Chan<sup>2</sup>, J. D. Surratt<sup>1,\*</sup>, P. S. Chhabra<sup>1</sup>, C. L. Loza<sup>1</sup>, J. D. Crounse<sup>1</sup>, L. D. Yee<sup>2</sup>, R. C. Flagan<sup>1,2</sup>, P. O. Wennberg<sup>2,3</sup>, and J. H. Seinfeld<sup>1,2</sup>

<sup>1</sup>Division of Chemistry and Chemical Engineering, California Institute of Technology, Pasadena, CA, USA

<sup>2</sup>Division of Engineering and Applied Science, California Institute of Technology, Pasadena, CA, USA

<sup>3</sup>Division of Geological and Planetary Sciences, California Institute of Technology, Pasadena, CA, USA

\*now at: Department of Environmental Sciences and Engineering, The University of North Carolina at Chapel Hill, Chapel Hill, NC, USA

Received: 7 April 2010 – Published in Atmos. Chem. Phys. Discuss.: 19 April 2010

Revised: 13 July 2010 – Accepted: 16 July 2010 – Published: 4 August 2010

**Abstract.** Aldehydes are an important class of products from atmospheric oxidation of hydrocarbons. Isoprene (2-methyl-1,3-butadiene), the most abundantly emitted atmospheric non-methane hydrocarbon, produces a significant amount of secondary organic aerosol (SOA) via methacrolein (a C<sub>4</sub>-unsaturated aldehyde) under urban high-NO<sub>x</sub> conditions. Previously, we have identified peroxy methacryloyl nitrate (MPAN) as the important intermediate to isoprene and methacrolein SOA in this NO<sub>x</sub> regime. Here we show that as a result of this chemistry, NO<sub>2</sub> enhances SOA formation from methacrolein and two other  $\alpha,\beta$ -unsaturated aldehydes, specifically acrolein and crotonaldehyde, a NO<sub>x</sub> effect on SOA formation previously unrecognized. Oligoesters of dihydroxycarboxylic acids and hydroxynitrooxycarboxylic acids are observed to increase with increasing NO<sub>2</sub>/NO ratio, and previous characterizations are confirmed by both online and offline high-resolution mass spectrometry techniques. Molecular structure also determines the amount of SOA formation, as the SOA mass yields are the highest for aldehydes that are  $\alpha,\beta$ -unsaturated and contain an additional methyl group on the  $\alpha$ -carbon. Aerosol formation from 2-methyl-3-buten-2-ol (MBO232) is insignificant, even under high-NO<sub>2</sub> conditions, as PAN (peroxy acyl nitrate, RC(O)OONO<sub>2</sub>) formation is structurally unfavorable. At atmospherically relevant NO<sub>2</sub>/NO ratios (3–8), the SOA yields from isoprene high-NO<sub>x</sub> photooxidation are 3 times greater than previously measured at lower NO<sub>2</sub>/NO ratios. At sufficiently high NO<sub>2</sub> concentrations, in systems of  $\alpha,\beta$ -

unsaturated aldehydes, SOA formation from subsequent oxidation of products from acyl peroxy radicals+NO<sub>2</sub> can exceed that from RO<sub>2</sub>+HO<sub>2</sub> reactions under the same inorganic seed conditions, making RO<sub>2</sub>+NO<sub>2</sub> an important channel for SOA formation.

### 1 Introduction

Organic matter is ubiquitous in atmospheric aerosols and accounts for a major fraction of particulate matter mass (Zhang et al., 2007a). Most particulate organic matter (POM) is secondary in origin, comprising condensable oxidation products of gas-phase volatile organic compounds (VOCs) (Hallquist et al., 2009). Despite the importance of secondary organic aerosol (SOA), its sources and formation processes are not fully understood. Global modeling studies predict that oxidation of biogenic hydrocarbons dominates the global SOA burden owing to high emissions and efficient SOA production (Chung and Seinfeld, 2002; Kanakidou et al., 2005; Henze and Seinfeld, 2006). This is supported by observations of high levels of modern (hence biogenic) carbon in ambient particulate organic matter, even in urban centers such as Nashville, TN, Tampa, FL and Atlanta, GA (Lewis et al., 2004; Lewis and Stiles, 2006; Weber et al., 2007). However, field observations have repeatedly shown that SOA formation is highly correlated with anthropogenic tracers, such as CO and acetylene (de Gouw et al., 2005, 2008).

A considerable body of laboratory chamber studies have investigated the dependence of SOA yields (mass of SOA formed per mass of hydrocarbon reacted) on NO<sub>x</sub> level, which can vary greatly between urban and remote

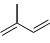
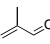
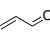
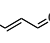
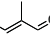
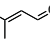
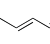
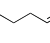
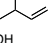
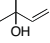


Correspondence to: J. H. Seinfeld  
(seinfeld@caltech.edu)

areas. For photooxidation and ozonolysis of monoterpenes (Hatakeyama et al., 1991; Ng et al., 2007a; Zhang et al., 2007b; Presto et al., 2005), monocyclic (Song et al., 2005; Hurley et al., 2001; Ng et al., 2007b) and polycyclic aromatic compounds (Chan et al., 2009b), SOA yields are larger under low-NO<sub>x</sub> conditions; for sesquiterpenes, the reverse is true (Ng et al., 2007a). SOA formation from photooxidation of isoprene exhibits especially complex behavior depending on the NO<sub>x</sub> level (Kroll et al., 2006). The effect of NO<sub>x</sub> level on SOA formation has generally been attributed to the relative reaction rates of peroxy radicals (RO<sub>2</sub>) with NO and HO<sub>2</sub> and the difference in volatilities of the products from the respective pathways (Kroll and Seinfeld, 2008). Under high-NO<sub>x</sub> conditions, RO<sub>2</sub>+NO dominates and leads to formation of fragmentation products or organic nitrates, which are generally volatile (Presto et al., 2005). On the contrary, the RO<sub>2</sub>+HO<sub>2</sub> pathway, which is competitive only when [NO] ≪ 1 ppb, produces less volatile hydroxyhydroperoxides and peroxy acids, leading to higher SOA yields (Johnson et al., 2005). RO<sub>2</sub>+NO<sub>2</sub> reactions have not been considered as important for SOA formation due to the short lifetime of peroxy nitrates (< 1 s); the notable exceptions are acyl peroxy nitrates (PANs) and pernitric acid (PNA). As a result, the so-called “high-NO<sub>x</sub>” yields (corresponding to urban NO<sub>x</sub> levels) have typically been measured under high-NO conditions. For example, the overall SOA mass yield for isoprene photooxidation ranges from 0.01–0.05 under low-NO<sub>x</sub> conditions (Kroll et al., 2006) to 0.002–0.03 under high-NO<sub>x</sub> (high-NO) conditions (Kroll et al., 2005a; Dommen et al., 2006). Owing to the large emissions of isoprene (Guenther et al., 2006), isoprene has been estimated to be the single largest source of SOA globally (Henze and Seinfeld, 2006; Carlton et al., 2009).

In a recent study of the mechanism of SOA formation from isoprene, it was shown that aerosol-phase 2-methylglyceric acid (2-MG) and its oligoesters are produced from methacrolein oxidation through the peroxy methacryloyl nitrate (MPAN) channel, as the SOA from MPAN oxidation is similar in composition to that from high-NO<sub>x</sub> oxidation of isoprene and methacrolein (Surratt et al., 2010). Since MPAN is formed from the reversible reaction of methacryloyl peroxy radicals with NO<sub>2</sub>, SOA formation can be highly sensitive to the NO<sub>2</sub> concentration, an effect of gas-phase aldehyde chemistry that had previously not been recognized. Given the large emissions and the substantial fraction of isoprene reacting under high-NO<sub>x</sub> conditions (a recent modeling study predicts that globally up to two-thirds of isoprene reacts under high-NO<sub>x</sub> conditions (Paulot et al., 2009)), it is essential to understand more generally how gas-phase aldehyde chemistry and both NO and NO<sub>2</sub> affect SOA yield and composition. Here we present the results of a systematic study of the effect of NO<sub>2</sub>/NO ratio on SOA formation from methacrolein and two other α, β-unsaturated aldehydes, acrolein and crotonaldehyde. In addition, other structurally similar aldehydes and alcohols are studied to provide insight

**Table 1.** Hydrocarbons studied.

Name	Structure	OH rate constant, cm <sup>3</sup> molec <sup>-1</sup> s <sup>-1</sup>
isoprene		1 × 10 <sup>-10</sup> <sup>a</sup>
methacrolein		2.9 × 10 <sup>-11</sup> <sup>a</sup>
acrolein		2.0 × 10 <sup>-11</sup> <sup>a</sup>
crotonaldehyde ( <i>cis</i> and <i>trans</i> )		3.5 × 10 <sup>-11</sup> <sup>a</sup>
2-methyl-2-butenal (2M2B)		unknown
3-methyl-2-butenal (3M2B)		6.2 × 10 <sup>-11</sup> <sup>c</sup>
2-pentenal		unknown
4-pentenal		unknown
2-methyl-3-buten-1-ol (MBO231)		unknown
2-methyl-3-buten-2-ol (MBO232)		3.9 × 10 <sup>-11</sup> <sup>d</sup>

<sup>a</sup> Atkinson and Arey (2003); <sup>b</sup> Magneron et al. (2002); <sup>c</sup> Tuazon et al. (2005); <sup>d</sup> Fantechi et al. (1998).

into the reaction mechanism and to establish the role of PAN-type compounds as important SOA intermediates.

## 2 Experimental section

### 2.1 Experimental protocols

Experiments were carried out in the Caltech dual 28-m<sup>3</sup> Teflon chambers. Details of the facilities have been described previously (Cocker et al., 2001; Keywood et al., 2004). Before each experiment, the chambers were flushed with dried purified air for >24 h (~4–6 air changes), until the particle number concentration < 100 cm<sup>-3</sup> and the volume concentration < 0.1 μm<sup>3</sup> cm<sup>-3</sup>. In all experiments, inorganic seed particles were injected by atomization of a 0.015 M aqueous ammonium sulfate solution. The parent hydrocarbon was then introduced into the chamber by injecting a known volume of the liquid hydrocarbon into a glass bulb, and the vapor was carried into the chamber with 5 L min<sup>-1</sup> of purified air.

**Table 2.** Experimental conditions and results.

Date <sup>a</sup> (DD/MM/YY)	Compound	[HC] <sub>0</sub> , ppb	OH precursor	NO <sub>x</sub> addition	[NO] <sub>0</sub> <sup>b</sup> , ppb	[NO <sub>2</sub> ] <sub>0</sub> <sup>b</sup> , ppb	NO <sub>2</sub> /NO <sup>c</sup>	V <sub>0</sub> <sup>d</sup> , μm <sup>3</sup> cm <sup>-3</sup>	ΔM <sub>0</sub> <sup>e</sup> , μg m <sup>-3</sup>	SOA Yield
14/07/09	methacrolein	277	HONO	+NO	725	365	0.5	11.4	10.1	0.019
16/07/09	methacrolein	285	HONO	+NO <sub>2</sub>	296	692	1.7	12.3	24.5	0.052
19/07/09	methacrolein	257	HONO	–	527	407	0.7	12.1	14.4	0.030
31/07/09 <sup>f</sup>	methacrolein	232	HONO	+NO	653	394	0.5	11.7	13.3	0.030
12/09/09	methacrolein	255	CH <sub>3</sub> ONO	+NO+NO <sub>2</sub>	222	799	10.0	13.9	276.3	0.392
15/09/09	methacrolein	67	CH <sub>3</sub> ONO	+NO+NO <sub>2</sub>	164	549	5.8	14.8	39.9	0.211
17/09/09	methacrolein	20	CH <sub>3</sub> ONO	+NO+NO <sub>2</sub>	170	602	3.6	16.0	10.8	0.194
19/09/09	methacrolein	48	CH <sub>3</sub> ONO	+NO+NO <sub>2</sub>	167	582	4.7	13.2	28.8	0.213
21/09/09	methacrolein	32	CH <sub>3</sub> ONO	+NO+NO <sub>2</sub>	176	657	4.2	14.4	22.4	0.242
16/12/09	methacrolein	32	CH <sub>3</sub> ONO	+NO+NO <sub>2</sub>	243	444	2.7	13.9	6.8	0.079
17/12/09 <sup>g</sup>	methacrolein	32	CH <sub>3</sub> ONO	+NO+NO <sub>2</sub>	233	518	2.7	16.2	6.7	0.075
08/08/09	isoprene	523	HONO	–	312	510	7.7	10.8	65.2	0.044
23/09/09	isoprene	228	CH <sub>3</sub> ONO	+NO+NO <sub>2</sub>	293	825	8.4	16.0	47.4	0.074
24/09/09	isoprene	94	CH <sub>3</sub> ONO	+NO+NO <sub>2</sub>	271	735	5.0	14.8	16.0	0.061
25/09/09	isoprene	153	CH <sub>3</sub> ONO	+NO+NO <sub>2</sub>	316	859	6.1	18.7	27.2	0.064
27/09/09	isoprene	44	CH <sub>3</sub> ONO	+NO+NO <sub>2</sub>	259	715	4.0	15.8	5.2	0.042
30/09/09	isoprene	33	CH <sub>3</sub> ONO	+NO+NO <sub>2</sub>	289	768	3.4	18.4	2.9	0.031
15/08/09	acrolein	676	HONO	–	214	389	2.5	13.2	21.3	0.022
16/08/09	acrolein	540	HONO	+NO	550	359	0.8	11.2	4.4	0.006
17/08/09	acrolein	611	HONO	+NO <sub>2</sub>	233	630	2.0	13.2	9.9	0.015
28/09/09	acrolein	220	CH <sub>3</sub> ONO	+NO+NO <sub>2</sub>	313	830	5.5	19.2	16.6	0.035
18/08/09	crotonaldehyde	293	HONO	–	214	371	2.3	12.1	14.0	0.019
19/08/09	crotonaldehyde	297	HONO	+NO	600	416	1.1	12.3	9.0	0.013
20/08/09	crotonaldehyde	361	HONO	+NO <sub>2</sub>	245	625	2.6	12.2	12.9	0.017
29/09/09	crotonaldehyde	74	CH <sub>3</sub> ONO	+NO+NO <sub>2</sub>	248	664	3.8	16.4	9.2	0.044
26/12/09	2-pentenal	174	CH <sub>3</sub> ONO	+NO+NO <sub>2</sub>	230	548	6.7	13.9	18.1	0.03
27/12/09	4-pentenal	191	CH <sub>3</sub> ONO	+NO+NO <sub>2</sub>	243	488	6.5	15.8	8.2	0.012
28/12/09	2M2B	277	CH <sub>3</sub> ONO	+NO+NO <sub>2</sub>	240	706	9.3	13.8	376.7	0.391
29/12/09	3M2B	207	CH <sub>3</sub> ONO	+NO+NO <sub>2</sub>	268	747	8.7	16.1	5.6	0.008
31/12/09	MBO231	589	CH <sub>3</sub> ONO	+NO+NO <sub>2</sub>	308	493	13.2	16.8	87.6	0.042
22/02/10	MBO231	329	CH <sub>3</sub> ONO	+NO+NO <sub>2</sub>	351	768	7.8	14.5	21.9	0.019
24/02/10	MBO231	300	HONO	+NO	642	514	1.8	14.2	<2	<0.002
25/02/10	MBO231	378	CH <sub>3</sub> ONO	+NO+NO <sub>2</sub>	346	793	5.5	17.5	10.7	0.008
01/01/10	MBO232	492	CH <sub>3</sub> ONO	+NO+NO <sub>2</sub>	251	442	11.4	14.8	<2	<0.002
23/02/10	MBO232	388	CH <sub>3</sub> ONO	+NO+NO <sub>2</sub>	345	809	8.4	17.1	<2	<0.002

<sup>a</sup> All experiments carried out at temperatures of 293–295 K and RH of 9–11%. <sup>b</sup> As measured by chemiluminescence NO<sub>x</sub> monitor. Note interference on NO<sub>2</sub> signal from HONO and CH<sub>3</sub>ONO. <sup>c</sup> Estimated by photochemical modeling (see Appendix). <sup>d</sup> V<sub>0</sub>: volume concentration of ammonium sulfate seed. <sup>e</sup> ΔM<sub>0</sub>: mass concentration of SOA. <sup>f</sup> Gas-phase nitric acid added during experiment. <sup>g</sup> Low O<sub>2</sub> experiment.

To study the sensitivity of aerosol yields and composition to relative concentrations of NO and NO<sub>2</sub>, different OH precursors were used. Use of nitrous acid (HONO) and methyl nitrite (CH<sub>3</sub>ONO) as OH precursors allows for SOA yield measurements over a wide range of NO<sub>2</sub>/NO ratios. For “high NO” experiments, OH radicals were generated from photolysis of HONO. We refer to these experiments as “high NO” experiments because NO concentrations are sufficiently high that RO<sub>2</sub>+NO ≫ RO<sub>2</sub>+NO<sub>2</sub>, most notably for acyl peroxy radicals, even though NO<sub>2</sub> concentrations are high (>100 ppb). HONO was prepared by adding 15 mL of 1 wt% aqueous NaNO<sub>2</sub> dropwise into 30 mL of 10 wt% sulfuric acid in a glass bulb. A stream of dry air was then passed through the bulb, sending HONO into the chamber. During this process, NO and NO<sub>2</sub> formed as side products and were also introduced into the chamber. To achieve high NO<sub>2</sub>

concentrations, CH<sub>3</sub>ONO was employed as the OH precursor. These experiments are referred to as “high NO<sub>2</sub>” experiments, as NO<sub>2</sub> concentrations are sufficiently higher than NO concentrations such that PAN formation is favored over reaction of acyl peroxy radicals with NO. CH<sub>3</sub>ONO was vaporized into an evacuated 500 mL glass bulb and introduced into the chamber with an air stream of 5 L min<sup>-1</sup>. The mixing ratio of CH<sub>3</sub>ONO injected was estimated to be 200–400 ppb, based on the vapor pressure in the glass bulb measured using a capacitance manometer (MKS). In all experiments, varying amounts of NO and NO<sub>2</sub> were also added from gas cylinders (Scott Marrin) both to ensure high-NO<sub>x</sub> conditions and to vary the NO<sub>2</sub>/NO ratio. For the C<sub>5</sub> unsaturated aldehydes and 2-methyl-3-buten-2-ol (MBO232), only high NO<sub>2</sub> experiments were conducted. Abbreviations, structures, and OH rate constants (Atkinson and Arey, 2003; Magneron et al.,



2002; Tuazon et al., 2005; Fantechi et al., 1998) of the compounds studied are listed in Table 1, and initial conditions of the experiments are summarized in Table 2.

## 2.2 Materials

The parent hydrocarbons studied and their stated purities are as follows: isoprene (Aldrich, 99%), methacrolein (Aldrich, 95%), acrolein (Fluka,  $\geq 99\%$ ), crotonaldehyde (Aldrich, 98%, predominantly *trans*), trans-2-pentenal (Alfa Aesar, 96%), 4-pentenal (Alfa Aesar, 97%), trans-2-methyl-2-butenal (Aldrich, 96+%), 3-methyl-2-butenal (Sigma-Aldrich, 97%), 2-methyl-3-buten-1-ol (Aldrich, 98%), and 2-methyl-3-buten-2-ol (Aldrich, 98%). CH<sub>3</sub>ONO was synthesized following the method described by Taylor et al. (1980). 9 g of NaNO<sub>2</sub> was added to a mixture of 50 mL of methanol and 25 mL of water. 25 mL of 50 wt% sulfuric acid solution was added dropwise into the solution. The CH<sub>3</sub>ONO vapor was carried in a small stream of ultra high purity N<sub>2</sub> through a concentrated NaOH solution and an anhydrous CaSO<sub>4</sub> trap to remove any sulfuric acid and water, respectively. The CH<sub>3</sub>ONO was then collected in a cold trap immersed in a dry ice/acetone bath (−80 °C) and stored under liquid N<sub>2</sub> temperature.

## 2.3 Measurements

Aerosol size distribution, number and volume concentrations were measured with a differential mobility analyzer (DMA, TSI, 3081) coupled with a condensation nuclei counter (TSI, CNC-3760). The volume concentration was corrected for particle wall loss by applying size-dependent first-order loss coefficients, obtained in a separate seed-only experiment, using methods described in Keywood et al. (2004). Aerosol volume concentrations are converted to mass concentrations assuming a density of 1.4 g cm<sup>−3</sup> (Kroll et al., 2005a). Concentrations of isoprene, methacrolein, methyl vinyl ketone (MVK), acrolein, and crotonaldehyde were monitored using a gas chromatograph with flame ionization detector (GC/FID, Agilent 6890N), equipped with an HP-PLOT Q column (15 m × 0.53 mm ID × 30 μm thickness, J&W Scientific). For 2M2B, 3M2B, 2-pentenal, 4-pentenal, MBO231 and MBO232 experiments, the GC/FID was equipped with an HP-5 column (15 m × 0.53 mm ID × 1.5 μm thickness, Hewlett Packard). A commercial chemiluminescence NO/NO<sub>x</sub> analyzer (Horiba, APNA 360) was used to monitor NO and NO<sub>x</sub>. Both HONO and CH<sub>3</sub>ONO produce interference on the NO<sub>2</sub> signal from the NO<sub>x</sub> monitor. Concentrations of NO and NO<sub>2</sub> are estimated by photochemical modeling (see Appendix). Temperature, RH, and ozone (O<sub>3</sub>) were continuously monitored.

A custom-modified Varian 1200 triple-quadrupole chemical ionization mass spectrometer (CIMS) was used to continuously monitor gas-phase species over each experiment. Details of the operation of the CIMS can be found in a num-

ber of previous reports (Crouse et al., 2006; Paulot et al., 2009). The CIMS was operated in negative ion mode, in which CF<sub>3</sub>O<sup>−</sup> is used as the reagent ion, and in positive ion mode of proton transfer mass spectrometry (PTR-MS). In the negative mode, the reagent ion CF<sub>3</sub>O<sup>−</sup> clusters with the analyte, R, forming ions at mass-to-charge ratios ( $m/z$ ) MW+85 (R·CF<sub>3</sub>O<sup>−</sup>), or, with more acidic species, at  $m/z$  MW+19 (HF·R<sub>H</sub><sup>−</sup>). In the positive mode, positively charged water clusters,  $n(\text{H}_2\text{O})\text{H}^+$ , react via proton transfer with the analyte, R, to form the positively charged ion, R· $n(\text{H}_2\text{O})\cdot\text{H}^+$ . In some cases, tandem mass spectrometry (MS/MS) was used to separate isobaric compounds. In brief, the parent ions selected in the first quadrupole undergo collision-induced dissociation (CID) in the second quadrupole. The parent ions of isobaric compounds can exhibit different CID patterns and yield different daughter ions. Hence, with the third quadrupole acting as a second mass filter for the daughter ions, this allows for separate measurement of these isobaric compounds (see Supplementary Material). The significance of this separation will be discussed in a later section.

Real-time particle mass spectra were collected continuously by an Aerodyne High Resolution Time-of-Flight Aerosol Mass Spectrometer (DeCarlo et al., 2006; Canagaratna et al., 2007), hereby referred to as the AMS. The AMS switched once every minute between the high resolution “W-mode” and the lower resolution, higher sensitivity “V-mode”. The “V-mode” data were analyzed using a fragmentation table to separate sulfate, ammonium, and organic spectra and to time-trace specific mass-to-charge ratios. “W-mode” data were analyzed using a separate high-resolution spectra toolbox known as PIKA to determine the chemical formulas contributing to distinct  $m/z$  ratios (DeCarlo et al., 2006).

Aerosol samples were also collected on Teflon filters and analyzed by offline mass spectrometry. Detailed sample collection and extraction protocol are described in Surratt et al. (2008). Filter extraction using 5 mL of high-purity methanol (i.e., LC-MS Chromasolv Grade) was performed by 45 min of sonication. The filter extracts were then analyzed by a Waters ACQUITY ultra performance liquid chromatography (UPLC) system, coupled with a Waters LCT Premier TOF mass spectrometer equipped with an ESI source operated in the negative (−) mode, allowing for accurate mass measurements (i.e., determination of molecular formulas) to be obtained for each observed ion. Operation conditions and parameters for the UPLC/(−)ESI-TOFMS measurement have been described by Surratt et al. (2008).

## 3 SOA formation

The importance of isoprene as an SOA source was suggested by identification of 2-methyltetrols and 2-methylglyceric acid (2-MG) in both ambient POM (Claeys et al., 2004; Edney et al., 2005; Ion et al., 2005; Kourtchev et al., 2005)



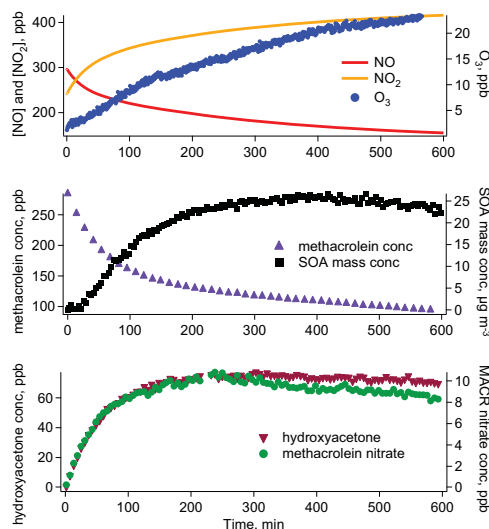


**Fig. 1.** Concentration profiles of gas-phase species during a typical methacrolein/high-NO<sub>2</sub> experiment (15/09/09). In this experiment, additional methacrolein/high-NO experiment (16/07/09). Concentrations of NO and NO<sub>2</sub> shown here are calculated from a photochemical model (see Appendix).

and laboratory aerosol generated from isoprene photooxidation (Edney et al., 2005; Surratt et al., 2006; Szmigielski et al., 2007; Kleindienst et al., 2009). Methacrolein, a first-generation oxidation product of isoprene, has been shown to produce SOA upon further oxidation (Kroll et al., 2006; Surratt et al., 2006) and has been identified as the precursor to aerosol-phase 2-MG and its corresponding oligoester products (Surratt et al., 2006; Szmigielski et al., 2007). A recent study shows aerosol formation from methacrolein oxidation proceeds via subsequent oxidation of MPAN (Surratt et al., 2010). Here we focus our attention on photooxidation of methacrolein under high-NO<sub>x</sub> conditions to establish the effect of relative NO and NO<sub>2</sub> concentrations on SOA yields and composition. Acrolein, crotonaldehyde, 2-methyl-2-butenal (2M2B), 3-methyl-2-butenal (3M2B), 2-pentenal, and 4-pentenal differ from methacrolein by one or two methyl groups, and studying their SOA formation provides insight into the mechanism of formation of low-volatility products. Furthermore, aerosol formation from photooxidation of 2-methyl-3-buten-2-ol (MBO232), an atmospherically important unsaturated alcohol (Harley et al., 1998), and structurally similar 2-methyl-3-buten-1-ol (MBO231) is studied to investigate the role of PAN-like compounds in SOA formation.

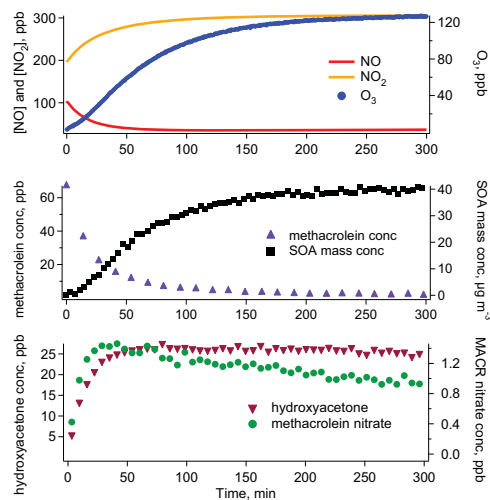


**Fig. 2.** Concentration profiles of gas-phase species during a typical methacrolein/high-NO<sub>2</sub> experiment (15/09/09). Additional NO (100 ppb) and NO<sub>2</sub> (200 ppb) were injected prior to irradiation. Concentrations of NO and NO<sub>2</sub> shown here are calculated from a photochemical model (see Appendix). As a result of the higher OH concentrations from CH<sub>3</sub>ONO than from HONO, more methacrolein was reacted and the concentrations of methacrolein nitrate relative to those of hydroxyacetone were lower than those in high-NO experiments, owing to a more rapid consumption by OH.

### 3.1 Methacrolein

Figures 1 and 2 show typical concentration profiles of various gas-phase species in methacrolein/HONO (high NO) and methacrolein/CH<sub>3</sub>ONO (high NO<sub>2</sub>) photooxidation experiments, respectively. In all experiments, NO concentrations remain above 50 ppb during SOA growth, at which conditions RO<sub>2</sub>+HO<sub>2</sub> or RO<sub>2</sub>+RO<sub>2</sub> reactions are not competitive with those of RO<sub>2</sub> with NO and NO<sub>2</sub>. Products of these reactions, such as methacrylic acid and methacrylic peracid, are not observed by CIMS. Instead, hydroxyacetone and methacrolein nitrate, products from RO<sub>2</sub>+NO reactions, are observed. During these experiments, RO<sub>2</sub> and HO<sub>2</sub> produced from methacrolein oxidation react with NO to produce NO<sub>2</sub>, which photolyzes to form ozone. As a result, ozone concentrations reach a maximum of up to 126 ppb. Despite relatively high levels of ozone, reaction rates of methacrolein and peroxy methacryloyl nitrate (MPAN) with ozone are still slow compared to those with OH, as efficient photolysis of HONO or CH<sub>3</sub>ONO leads to OH concentrations > 3 × 10<sup>6</sup> molec cm<sup>-3</sup>, estimated from the methacrolein decay. For high-NO experiments, the initial decay of methacrolein slows down after 5 h, consistent with the HONO signal (CIMS (-) *m/z* 66) approaching zero. In

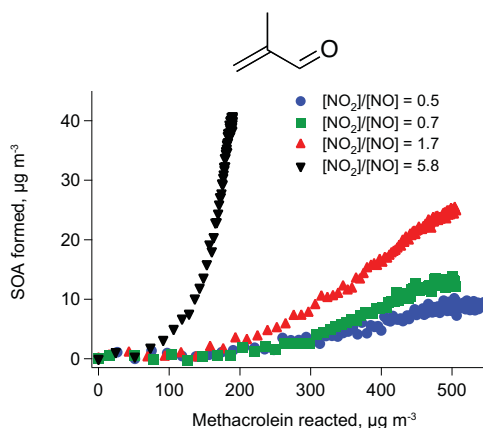


**Fig. 3.** Time-dependent SOA growth curves for methacrolein photooxidation.  $\text{NO}_2/\text{NO}$  ratios are computed from photochemical modeling (see Appendix). In the high-NO experiments ( $\text{NO}_2/\text{NO} < 2$ ) HONO was used as the OH precursor, and the  $\text{NO}_2/\text{NO}$  ratio was varied by adding different amounts of NO or  $\text{NO}_2$ . In the high- $\text{NO}_2$  experiment (black triangles),  $\text{CH}_3\text{ONO}$  was used as the OH precursor.

these experiments, more than 70% of the initial methacrolein is consumed before SOA growth ceases. In the high- $\text{NO}_2$  experiments, more than 90% of the initial methacrolein is consumed before SOA growth ceases.

Mass concentrations of SOA versus the concentration of methacrolein reacted, so-called “time-dependent growth curves”, are shown in Fig. 3. As reported previously, under high-NO conditions (with HONO as the OH precursor), when additional NO is added before irradiation, aerosol formation (mass yield of 0.019) from photooxidation of 277 ppb of methacrolein is suppressed (Surratt et al., 2010). In contrast, SOA yields are higher when no additional NO is added (0.030 from 257 ppb methacrolein), and the highest when 350 ppb of additional  $\text{NO}_2$  (instead of NO) is injected (0.052 from 285 ppb methacrolein) (Surratt et al., 2010). In all high-NO experiments, the  $\text{NO}_2/\text{NO}$  ratio remains low ( $< 2$ ), owing to presence of NO impurity in HONO synthesis and production of NO during HONO photolysis. The observed dependence of SOA yields on  $\text{NO}_2/\text{NO}$  ratio is not a result of condensation of nitric acid from  $\text{OH} + \text{NO}_2$ , as the experiments were conducted under dry ( $< 10\%$  RH) conditions. In confirmation of this conclusion, addition of gas-phase nitric acid in one experiment (31/07/09) did not lead to additional aerosol growth.

In the high- $\text{NO}_2$  experiments,  $\text{CH}_3\text{ONO}$  was used as the OH precursor and lower NO concentrations are expected, owing to relatively pure  $\text{CH}_3\text{ONO}$  synthesis and no net production of NO from  $\text{CH}_3\text{ONO}$  photolysis (see Appendix). Higher SOA yields are observed at higher  $\text{NO}_2/\text{NO}$  ratios;

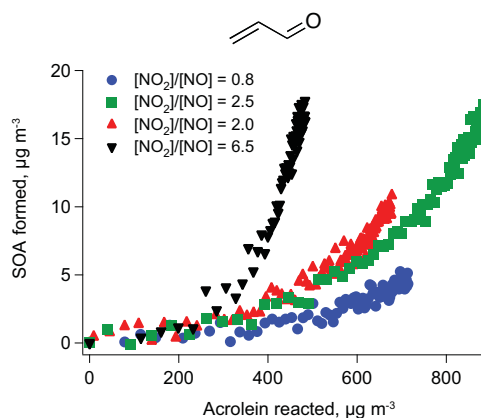


**Fig. 4.** Time-dependent SOA growth curves for acrolein photooxidation. Similar to methacrolein photooxidation,  $\text{NO}_2/\text{NO}$  ratios are computed from photochemical modeling (see Appendix). In the high-NO experiments ( $\text{NO}_2/\text{NO} < 3$ ), HONO was used as the OH precursor, and the  $\text{NO}_2/\text{NO}$  ratio was varied by adding different amounts of NO or  $\text{NO}_2$ . In the experiment in which  $\text{NO}_2$  was added (red triangles), high levels of  $\text{NO}_2$  depress OH concentrations, resulting in less acrolein reacted. Concentrations of NO did not drop as rapidly as in other high-NO experiments, leading to a lower  $\text{NO}_2/\text{NO}$  ratio. In the high- $\text{NO}_2$  experiment (black triangles),  $\text{CH}_3\text{ONO}$  was used as the OH precursor.

correspondingly, much lower concentrations of methacrolein are required to produce the same amount of SOA (see Fig. 3). Also, owing to the high concentrations of  $\text{CH}_3\text{ONO}$  injected, more than 90% of the initial methacrolein is consumed before  $\text{CH}_3\text{ONO}$  is depleted. For example, when 255 ppb of initial methacrolein is oxidized using  $\text{CH}_3\text{ONO}$  as OH precursor (12/09/09), the SOA yields are more than 5 times larger than when a similar amount of methacrolein is reacted using HONO as OH precursor. This rules out a larger extent of reaction as the cause of the high observed SOA yields.  $\text{HO}_2$  concentrations, quantified from the pernitric acid signal on the CIMS ( $(-)\ m/z\ 98$ ) and modelled  $\text{NO}_2$  concentrations, do not exceed 60 ppt in all experiments. At organic loadings of  $10\text{--}20\ \mu\text{g m}^{-3}$ , SOA mass yields of methacrolein/high- $\text{NO}_2$  and methacrolein/high-NO photooxidation are roughly 0.19 and 0.03, respectively.

### 3.2 Acrolein and crotonaldehyde

Figures 4 and 5 show SOA growth curves for acrolein and crotonaldehyde photooxidation, respectively. The SOA yields of these compounds are lower than those of methacrolein, with maximum yields of roughly 0.08 at the highest loadings ( $> 100\ \mu\text{g m}^{-3}$ ). These compounds exhibit a similar dependence of SOA growth on  $\text{NO}_2/\text{NO}$  ratio to that of methacrolein: SOA formation is suppressed with addition

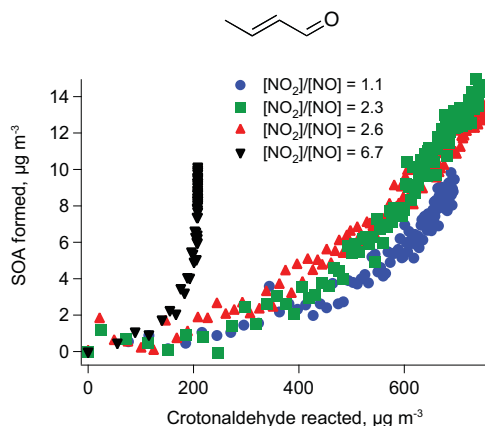


**Fig. 5.** Time-dependent SOA growth curves for crotonaldehyde photooxidation. Similar to methacrolein photooxidation, NO<sub>2</sub>/NO ratios are computed from photochemical modeling (see Appendix). In the high-NO experiments (NO<sub>2</sub>/NO < 3), HONO was used as the OH precursor, and the NO<sub>2</sub>/NO ratio was varied by adding different amounts of NO or NO<sub>2</sub>. In the high-NO<sub>2</sub> experiment (black triangles), CH<sub>3</sub>ONO was used as the OH precursor.

of NO, and enhanced with addition of NO<sub>2</sub>. SOA yields are highest in the high-NO<sub>2</sub> experiments. Oxidation products analogous to those found in the methacrolein system, such as glycolaldehyde and hydroxynitrates, are observed in the gas phase at similar yields.

### 3.3 Other aldehydes and methylbutenols (MBO)

The growth curves for 2M2B and 3M2B photooxidation are shown in Fig. 6. Significant SOA growth is observed for 2M2B (277 ppb) photooxidation under high-NO<sub>2</sub> conditions, with mass yields exceeding 0.35. Similar to methacrolein, 2M2B contains a methyl group in the  $\alpha$ -position. Interestingly, photooxidation of 3M2B under similar NO<sub>x</sub> conditions and hydrocarbon loadings (207 ppb), produces less SOA (mass yield < 0.01). 3M2B is a structural isomer of 2M2B with the methyl group in the  $\beta$ -position. The trend in SOA yields between 2M2B and 3M2B is consistent with that observed for methacrolein and crotonaldehyde, their C<sub>4</sub> analogs. The SOA yields from 2-pentenal, a straight-chain  $\alpha,\beta$ -unsaturated aldehyde, are higher than those from 4-pentenal, in which the olefinic bond is not adjacent to the aldehyde group (see Fig. 6).

We also carried out MBO232 and MBO231 photooxidation under high-NO<sub>2</sub> conditions. Both MBO's are structurally similar to isoprene and, upon high-NO<sub>x</sub> photooxidation, produce an aldehyde (i.e., hydroxy-methylpropanal, HMPR) analogous to methacrolein. Previous results have shown that aerosol formation from MBO232 photooxidation

under high-NO conditions is negligible, with mass yields of < 0.001 (Carrasco et al., 2007; Chan et al., 2009a). Here we do not observe SOA growth even at high NO<sub>2</sub>/NO ratios. Gas-phase compounds such as glycolaldehyde and HMPR are observed at molar yields of 0.6 and 0.3, respectively, consistent with those published in previous product studies (Carrasco et al., 2007; Chan et al., 2009a). On the other hand, MBO231, a structural isomer with the hydroxyl group in the 1-position, produces a significant amount of SOA (mass yields of 0.008–0.042) upon oxidation under high-NO<sub>2</sub> conditions, comparable to that of isoprene under similar conditions (see Fig. 6). Under high-NO conditions, no SOA is formed. The dependence of SOA yields from MBO231 on NO<sub>2</sub>/NO ratio is therefore consistent with that observed in unsaturated aldehydes.

## 4 Chemical composition of SOA

### 4.1 Offline chemical analysis

In previous work, offline chemical analysis of SOA from photooxidation of isoprene, methacrolein, and MPAN by UPLC/(–)ESI-TOFMS has been presented (Surratt et al., 2010). The same compounds are detected in the methacrolein experiments in this work under both high-NO and high-NO<sub>2</sub> conditions, and are summarized in Table 3. Four series of oligoester products from 2-methylglyceric acid (2-MG) and C<sub>4</sub>-hydroxynitrooxycarboxylic acid are identified in the SOA. The compounds in the 2-MG oligoester series differ by 102 Da, corresponding to esterification of a 2-MG monomer unit (Surratt et al., 2006). The accurate masses of the identified ions confirm their elemental compositions, and their structures are proposed based on detailed characterization by tandem MS and GC/MS analyses with prior trimethylsilylation (Szmigielski et al., 2007).

All ions detected by UPLC/(–)ESI-TOFMS in acrolein and crotonaldehyde SOA are listed in the Supplementary Material. It is noteworthy that the identities of detected aerosol-phase products are the same regardless of the OH precursor used. The ions detected in acrolein SOA differ from those found in methacrolein SOA by one methyl group for every monomer unit, and those detected in crotonaldehyde SOA have the same exact mass and elemental composition as those in methacrolein SOA. Detected [M-H]<sup>–</sup> ions in SOA from 2M2B and 2-pentenal can also be found in the Supplementary Material. No filter sample was collected for 3M2B owing to low aerosol loading. Aerosol-phase products of methacrolein, acrolein, crotonaldehyde, 2M2B and 2-pentenal are structural analogs of each other, and the structures for the deprotonated ions are proposed based on those characterized previously in isoprene and methacrolein SOA (Surratt et al., 2006; Szmigielski et al., 2007). Interestingly, SOA produced from 4-pentenal is composed of entirely different products, and hence no structures are proposed at this

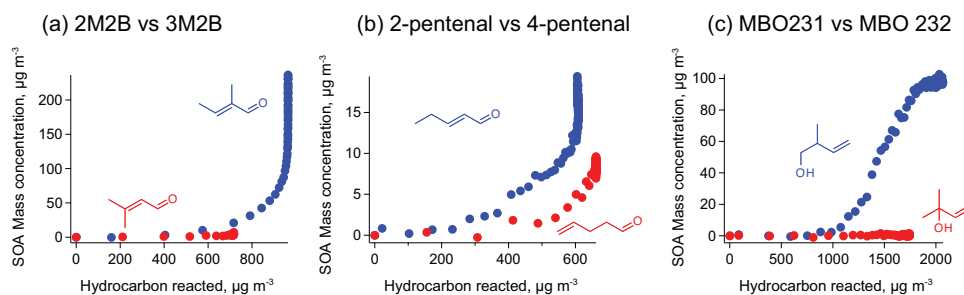


**Fig. 6.** Comparisons of time-dependent SOA growth from photooxidation of (a) 2M2B and 3M2B, (b) 2-pentenal and 4-pentenal, and (c) MBO231 and MBO 231 under high-NO<sub>2</sub> conditions. Within each plot, initial concentrations of parent hydrocarbons are comparable (see Table 2).

**Table 3.** SOA constituents detected by UPLC/(–)ESI-TOFMS and AMS in methacrolein experiments. All ions were detected in both high-NO and high-NO<sub>2</sub> experiments, unless otherwise noted.

		UPLC/ESI-TOFMS Measured Mass	TOFMS Suggested Ion Formula	Error (mDa)	i-Fit	# of 2-MG Monomer Units ( <i>n</i> )	Structure	AMS Suggested Ion Formula <sup>c</sup>
	[M – H] <sup>–a</sup>							[M – OH] <sup>+b</sup>
		not detected				1		103
Oligoester Series 1	221	221.0661	C <sub>8</sub> H <sub>13</sub> O <sub>7</sub> <sup>–</sup>	1.6	0.3	2		205
	323	323.0979	C <sub>12</sub> H <sub>19</sub> O <sub>10</sub> <sup>–</sup>	0.1	22.6	3		<sup>d</sup>
	425	425.1290	C <sub>16</sub> H <sub>25</sub> O <sub>13</sub> <sup>–</sup>	–0.5	48.0	4		<sup>d</sup>
	527 <sup>e</sup>	527.1609	C <sub>20</sub> H <sub>31</sub> O <sub>16</sub> <sup>–</sup>	–0.3	3.7	5		<sup>d</sup>
Oligoester Series 2	266	266.0507	C <sub>8</sub> H <sub>12</sub> NO <sub>6</sub> <sup>–</sup>	–0.5	32.8	1		<sup>d</sup>
	368	368.0831	C <sub>12</sub> H <sub>18</sub> NO <sub>12</sub> <sup>–</sup>	0.2	11.4	2		<sup>d</sup>
	470	470.1149	C <sub>16</sub> H <sub>24</sub> NO <sub>15</sub> <sup>–</sup>	0.3	56.3	3		<sup>d</sup>
	572	572.1510	C <sub>20</sub> H <sub>30</sub> NO <sub>18</sub> <sup>–</sup>	4.7	1.0	4		<sup>d</sup>
Oligoester Series 3 <sup>f</sup>		not detected				1		131
	249	249.0616	C <sub>9</sub> H <sub>13</sub> O <sub>8</sub> <sup>–</sup>	0.6	2.7	2		233
	351	351.0912	C <sub>13</sub> H <sub>19</sub> O <sub>11</sub> <sup>–</sup>	–1.5	46.9	3		<sup>d</sup>
	453	453.1248	C <sub>17</sub> H <sub>25</sub> O <sub>14</sub> <sup>–</sup>	0.4	63.7	4		<sup>d</sup>
	555 <sup>e</sup>	555.1610	C <sub>21</sub> H <sub>31</sub> O <sub>17</sub> <sup>–</sup>	4.9	3.0	5		<sup>d</sup>
Oligoester Series 4 <sup>g</sup>		not detected				1		145
	263	263.0740	C <sub>10</sub> H <sub>15</sub> O <sub>8</sub> <sup>–</sup>	–2.7	4.7	2		247
	365	365.1061	C <sub>14</sub> H <sub>21</sub> O <sub>11</sub> <sup>–</sup>	–2.3	54.9	3		<sup>d</sup>
	467	467.1434	C <sub>18</sub> H <sub>27</sub> O <sub>14</sub> <sup>–</sup>	3.3	23.7	4		<sup>d</sup>
	569	569.1711	C <sub>18</sub> H <sub>27</sub> O <sub>14</sub> <sup>–</sup>	–0.7	20.0	5		<sup>d</sup>
Oligoester Series 5	311	311.0333	C <sub>8</sub> H <sub>11</sub> N <sub>2</sub> O <sub>11</sub> <sup>–</sup>	–3.0	58.9	0		<sup>d</sup>
	413	413.0664	C <sub>12</sub> H <sub>17</sub> N <sub>2</sub> O <sub>14</sub> <sup>–</sup>	–1.6	71.9	1		<sup>d</sup>
	515 <sup>e</sup>	515.1039	C <sub>16</sub> H <sub>23</sub> N <sub>2</sub> O <sub>17</sub> <sup>–</sup>	4.2	3.6	2		<sup>d</sup>
Other Oligoesters	458 <sup>e</sup>	458.0558	C <sub>12</sub> H <sub>16</sub> N <sub>3</sub> O <sub>16</sub> <sup>–</sup>	2.7	3.3	n/a		<sup>d</sup>

<sup>a</sup> Observed by UPLC/(–)ESI-TOFMS. <sup>b</sup> Observed by AMS V mode. <sup>c</sup> Suggested by AMS high-resolution W mode.

<sup>d</sup> Not observed by AMS, most likely due to fragmentation of nitrate group, or below detection limit. <sup>e</sup> Detected in high-NO<sub>2</sub> experiments only. <sup>f</sup> This oligoester series involves the esterification with formic acid. <sup>g</sup> C<sub>6</sub>H<sub>11</sub>O<sub>3</sub><sup>+</sup> also detected. <sup>h</sup> This oligoester series involves the esterification with acetic acid.

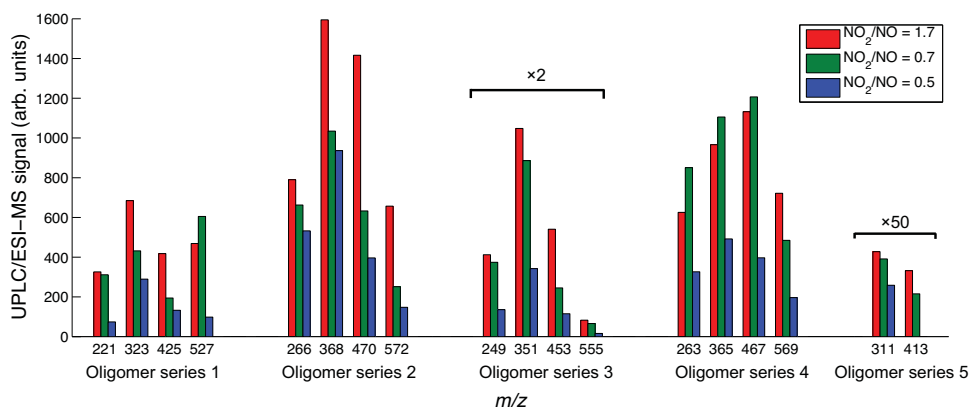


**Fig. 7.** Absolute peak areas (normalized by sampling volume) of all deprotonated ions detected by UPLC/(-)ESI-TOFMS in methacrolein/high-NO experiments, listed in Table 3. The positive dependence of oligoester abundance on NO<sub>2</sub>/NO ratios is consistent with the observed trend in overall SOA growth.

time. The significance of this result will be discussed in a later section.

While the identities of the detected aerosol-phase compounds are independent of the OH precursor, the relative amounts vary greatly and exhibit a strong correlation with NO<sub>2</sub>/NO ratio. Figure 7 shows the extracted ion signals for the oligoester products detected by UPLC/(-)ESI-TOFMS in the methacrolein high-NO experiments. The amount of identified aerosol-phase components shows the same dependence on NO<sub>2</sub>/NO ratio as the total amount of SOA growth. In general, the abundance of each compound decreases when NO is added and increases when NO<sub>2</sub> is added.

#### 4.2 Online AMS measurements

AMS V-mode organic spectra of SOA from high-NO<sub>2</sub> photooxidation of isoprene and methacrolein are shown in Fig. 8. The mass fragments above  $m/z$  200 likely contain more than 5 carbon atoms, and display a repetitive pattern, indicative of oligomer formation. In addition, 102 Da differences between major peaks were also observed, consistent with previous AMS and LC/MS results (Surratt et al., 2006). Elemental formulas based on accurate mass measurements are determined from high-resolution W-mode data for a number of the major ion peaks observed, as shown in Fig. 9. The ions suggested by these elemental formulas differ from many of the ions detected by UPLC/(-)ESI-TOFMS by an O<sup>2-</sup> group. The observed AMS ions are consistent with loss of a hydroxyl group from the molecular ion (i.e.  $\alpha$ -cleavage of a hydroxyl group under electron impact ionization). In UPLC/(-)ESI-TOFMS, these compounds are detected in their deprotonated form (loss of H<sup>+</sup>). As shown in Table 3, the oligoesters are detected by both online and offline high-resolution mass

spectrometry, and the agreement between the two techniques confirms that the oligoesters identified are indeed present in the SOA, and that the observations by offline aerosol analysis are not the result of filter sampling artifacts. AMS organic spectra of SOA from oxidation of acrolein and crotonaldehyde show similar features, and accurate mass measurements of a number of the major peaks correspond to the products analogous to those found in the methacrolein system (see Supplementary Material).

#### 5 Effect of NO<sub>2</sub>/NO ratios on SOA yield and composition

As mentioned in the Introduction, studies on the effect of NO<sub>x</sub> concentrations on SOA formation has shown that for most systems, SOA yields are inversely correlated with NO<sub>x</sub> concentrations (Hatakeyama et al., 1991; Hurley et al., 2001; Presto et al., 2005; Song et al., 2005; Zhang et al., 2007b; Ng et al., 2007a,b; Chan et al., 2009b). The “NO<sub>x</sub> effect” on SOA formation has been described as a competition of the chemistries for RO<sub>2</sub> between HO<sub>2</sub> (the high-yield pathway) and NO (the low-yield pathway), such that the ratio of HO<sub>2</sub> to NO is critical in determining the branching ratio between these two pathways (Kroll and Seinfeld, 2008; Henze et al., 2008). Aerosol yields from isoprene photooxidation are also sensitive to HO<sub>2</sub>/NO ratios, with higher yields measured under HO<sub>2</sub>-dominated conditions (using H<sub>2</sub>O<sub>2</sub> as OH source) (Kroll et al., 2006) than under NO-dominated conditions (using HONO or NO<sub>x</sub> cycling as OH source) (Kroll et al., 2005b; Pandis et al., 1991; Dommen et al., 2006). Addition of NO also suppresses SOA growth in low-NO<sub>x</sub> experiments, indicating that the RO<sub>2</sub>+NO pathway yields

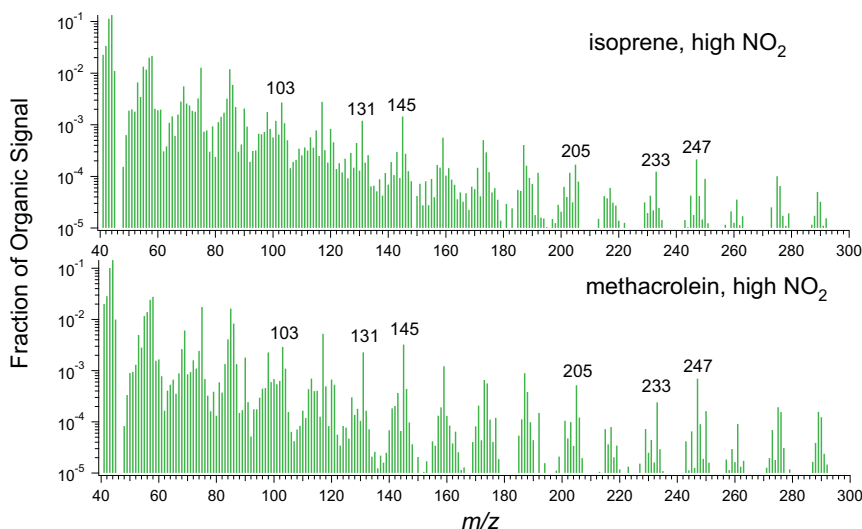


**Fig. 8.** AMS V-mode organic spectra of SOA from high-NO<sub>2</sub> photooxidation of isoprene and methacrolein. The labelled ion peaks differ from compounds listed in Table 3 by an O<sup>2-</sup> group. The accurate masses are confirmed by W-mode high-resolution analysis, as shown in Fig. 9. Separation of 102 Da between major peaks is consistent with esterification with a 2-MG monomer.

more volatile products, and hence less SOA (Kroll et al., 2006). However, under the experimental conditions in the present study, RO<sub>2</sub>+HO<sub>2</sub> reactions are not expected to be significant. Rather, the dependence of SOA yield on the NO<sub>2</sub>/NO ratio is consistent with analysis of SOA composition, which is consistent with MPAN, a product of the acyl peroxy radical+NO<sub>2</sub> reaction, being the intermediate in SOA formation. Although the absolute concentrations of NO<sub>2</sub> in these experiments are a factor of 10 higher than ambient levels, we expect the OH-adduct of alkenes and aldehydes studied here to react predominantly with O<sub>2</sub> to form alkyl peroxy or acyl peroxy radicals. Compounds with nitro functional groups (R-NO<sub>2</sub>), such as those found in the aromatic systems (Calvert et al., 2002), were not detected in these experiments.

Based on the proposed mechanism shown in Fig. 10, the acyl peroxy radical formed from abstraction of the aldehydic hydrogen atom of an unsaturated aldehyde react with either NO or NO<sub>2</sub>. The reversible reaction of RO<sub>2</sub> with NO<sub>2</sub> forms a PAN-type compound (MPAN for methacrolein), which, in the absence of competing reactions, reaches thermal equilibrium. The irreversible reaction of RO<sub>2</sub> with NO leads to fragmentation into CO<sub>2</sub> and a vinyl radical, which subsequently forms volatile gas-phase products, such as formaldehyde and CO (Orlando et al., 1999). At [OH]=2×10<sup>6</sup> molec cm<sup>-3</sup>, the reaction of MPAN with OH has a rate comparable to that of thermal decomposition (Orlando et al., 2002), and leads to formation of aerosol products. Hence, the SOA formation potential for this system depends critically on the NO<sub>2</sub>/NO

ratio. High NO<sub>2</sub>/NO ratios shift the thermal equilibrium towards the unsaturated PAN, and SOA formation increases as the fraction of PAN reacting with OH radicals increases. At low NO<sub>2</sub>/NO ratios, acyl peroxy radicals react predominantly with NO, leading to relatively volatile products.

Previous measurements of isoprene SOA yields under high-NO<sub>x</sub> conditions have been carried out using photolysis of HONO (Kroll et al., 2005a) or the recycling of HO<sub>x</sub> and NO<sub>x</sub> to generate OH (so-called classical photooxidation) (Pandis et al., 1991; Dommen et al., 2006). Low SOA yields were observed as NO concentrations remained high during the experiments. In fact, SOA growth occurred only after NO concentrations decreased to less than 10 ppb (Kroll et al., 2005a; Dommen et al., 2006). It was proposed that after NO has been consumed, aerosol formation commences as the RO<sub>2</sub>+HO<sub>2</sub> pathway becomes competitive. However, such a mechanism is inconsistent with the major differences in composition observed between high- and low-NO<sub>x</sub> SOA products. High-NO<sub>x</sub> SOA from isoprene photooxidation is dominated by esterification products of C<sub>4</sub>-carboxylic acids, whereas under low-NO<sub>x</sub> conditions, SOA is dominated by peroxides and C<sub>5</sub>-tetrols (Surratt et al., 2006). It is more likely that the decrease in NO concentration (and increase in NO<sub>2</sub> concentration) leads to a transition from an RO<sub>2</sub>+NO dominated regime to an RO<sub>2</sub>+NO<sub>2</sub> dominated regime, resulting in significant SOA formation via the MPAN route.



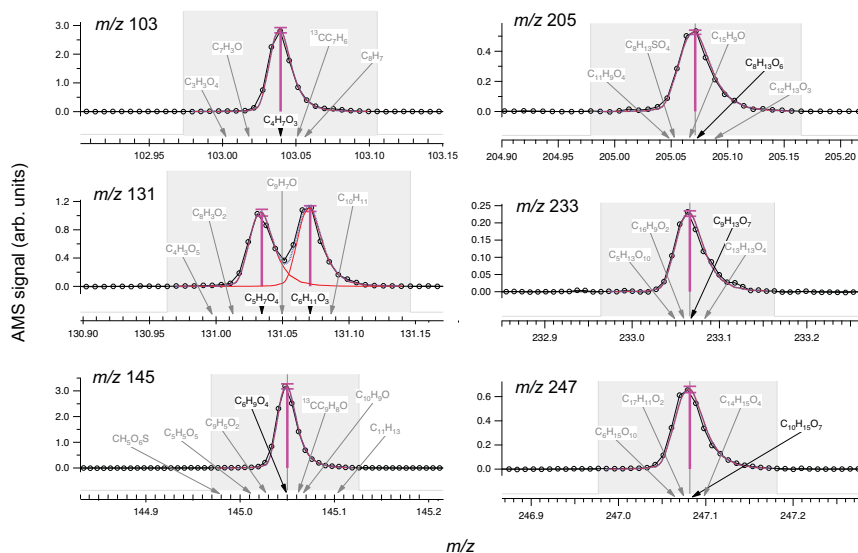


**Fig. 9.** High-resolution W-mode AMS peaks of a number of the major fragment ions observed in methacrolein/high-NO<sub>2</sub> experiments. Knowledge of the accurate masses allow assignments of molecular formulas, corresponding to loss of hydroxyl groups from compounds detected by offline analysis, suggesting that detection of compounds listed in Table 3 is not a result of sampling artifacts. *m/z* 131 contains two different ions, only one of which is consistent with compounds detected by offline UPLC/(–)ESI-TOFMS analysis.

At NO<sub>2</sub>/NO ratios (between 3 and 8) higher than in previous studies (and more relevant to urban conditions), SOA yields from isoprene are approximately 3 times larger than previously measured. The yields even exceed those under low-NO<sub>x</sub> conditions at the same organic aerosol loadings, as shown in Fig. 11. This is, in fact, consistent with observations from Kroll et al. (2006) that at very low NO<sub>x</sub> concentrations, addition of NO actually increases SOA yield. It is likely that under very low NO concentrations, the NO<sub>2</sub>/NO ratio increases rapidly, as NO is quickly converted to NO<sub>2</sub>. SOA yields are therefore higher than those in the absence of NO, as RO<sub>2</sub> (from methacrolein)+NO<sub>2</sub> forms SOA more efficiently than RO<sub>2</sub> (from isoprene)+HO<sub>2</sub>. However, further increasing NO decreases the NO<sub>2</sub>/NO ratio. RO<sub>2</sub> (from methacrolein)+NO becomes more dominant, forms volatile products and leads to a decrease in SOA yield. It must be noted that the effect of RO<sub>2</sub> radical chemistry on SOA formation is complex and can be unique to different systems (Kroll and Seinfeld, 2008). Also, the acidity of the inorganic seed can increase SOA yields significantly: Surratt et al. (2010) shows that SOA yields from isoprene low-NO<sub>x</sub> photooxidation can be as high as 0.29. Detailed knowledge of the chemical mechanism is required to predict the effect of NO<sub>x</sub> conditions on SOA production.

## 6 Role of PAN in SOA formation

### 6.1 Unsaturated aldehydes

One can infer from the shapes of the growth curves the relative timescales of the reaction steps of SOA formation. In all high-NO<sub>2</sub> experiments, a greater extent of reaction is achieved than in high-NO experiments, and SOA formation continues after the parent hydrocarbon is completely consumed; this behavior is characterized by a vertical portion (“hook”) at the end of the SOA growth curve. The presence of this vertical portion indicates that SOA formation results from further reaction of first-generation products, which is the rate-limiting step in the mechanism (see Figs. 3–5). This observation is consistent with our previous results showing that first-generation products of methacrolein, such as hydroxyacetone and MPAN, are themselves still volatile (Surratt et al., 2010). SOA is instead formed from the further OH reaction of MPAN, which has a comparable rate coefficient to that of methacrolein (Orlando et al., 2002).

Formation of dihydroxycarboxylic acids (e.g. 2-MG), hydroxynitrooxycarboxylic acids, and corresponding oligoesters appears to be important SOA formation pathways for the five  $\alpha,\beta$ -unsaturated aldehydes studied here (methacrolein, acrolein, crotonaldehyde, 2M2B, 2-pentenal). All of the SOA constituents detected by offline UPLC/(–)ESI-TOFMS in these systems are structural

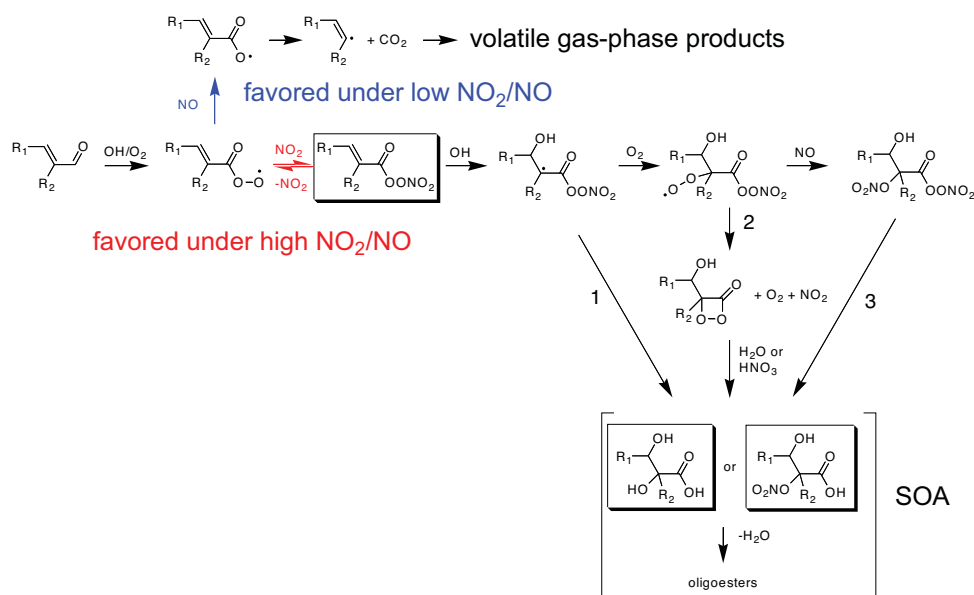


**Fig. 10.** Proposed mechanism to form aerosol-phase products from  $\alpha,\beta$ -unsaturated aldehydes. The pathways highlighted in red are favored under high  $\text{NO}_2/\text{NO}$  ratios and lead to aerosol formation. The pathways highlighted in blue are favored under low  $\text{NO}_2/\text{NO}$  ratios and lead to fragmentation into volatile products. Aerosol formation from OH-reaction of unsaturated PANs can proceed via 3 possible routes (routes 1–3), and detailed investigation of each route is discussed in the main text.

analogs of each other, as confirmed by the online AMS operated in the high-resolution W-mode. Based on similarities in SOA growth trends and composition, we expect that the formation of SOA products proceeds via pathways similar to those elucidated in Surratt et al. (2010) (see Fig. 10). Although oxidation of these aldehydes can lead to  $\alpha$ -dicarbonyls, such as glyoxal and methylglyoxal, which can undergo reactive uptake under humid conditions (Liggio et al., 2005; Kroll et al., 2005b; Volkamer et al., 2009), these compounds are not expected to contribute significantly to SOA formation under dry conditions. In addition, the AMS spectra for acrolein and crotonaldehyde SOA do not show peaks that are characteristic of glyoxal and its oligomers, as described in Liggio et al. (2005) and Galloway et al. (2009).

While MPAN is clearly the intermediate in SOA formation from methacrolein, the exact mechanism by which MPAN leads to such aerosol-phase products as 2-MG and hydroxynitrooxycarboxylic acids has not been established. From the oligoesters observed in the aerosol phase, it appears that the  $\text{C}_4$  backbone of MPAN remains intact. Following OH addition to the double bond, the only known gas-phase pathway that would preserve the carbon backbone is formation of hydroxynitrates. (Fragmentation of the MPAN-alkoxy radical would break up the  $\text{C}_4$  backbone and yield smaller products.) The nitrooxy functional groups could then be hydrolyzed to

hydroxyl groups (Sato, 2008) to form 2-MG and high-MW oligoesters (Route 3 in Fig. 10). However, gas-phase abundances of  $\text{C}_4$ - (for methacrolein and crotonaldehyde) or  $\text{C}_5$ - (for 2M2B, 3M2B and 2-pentenal) hydroxynitrate-PAN, the supposed SOA intermediate in all these systems, do not correlate with the amount of aerosol formed. Substitution of the  $\alpha$ -carbon atom by methyl groups (from crotonaldehyde to methacrolein, or from 3M2B to 2M2B) leads to an increase in the amount of SOA formed by more than a factor of 4, but no increase in gas-phase signal of the hydroxynitrate-PAN is observed (see Fig. 12), implying that it is unlikely the SOA-forming channel.

Another possible mechanism is that in which after OH addition to the double bond in MPAN the OH-adduct undergoes intramolecular rearrangement before addition of  $\text{O}_2$ , leading to formation of 2-MG and oligoesters (Route 1 in Fig. 10). Such isomerization can be competitive with  $\text{O}_2$  addition, as the O-O bond in the peroxy nitrate moiety is weak. In one experiment (17/12/09), the chambers were flushed with nitrogen to lower the oxygen content to 2%, thereby slowing down addition of  $\text{O}_2$  by a factor of 10. Compared to another experiment with 21%  $\text{O}_2$  (16/12/09), no increase in aerosol formation is observed, suggesting that SOA formation likely involves  $\text{O}_2$  addition to the MPAN-OH adduct, though it is also possible that the intramolecular rearrangement reaction



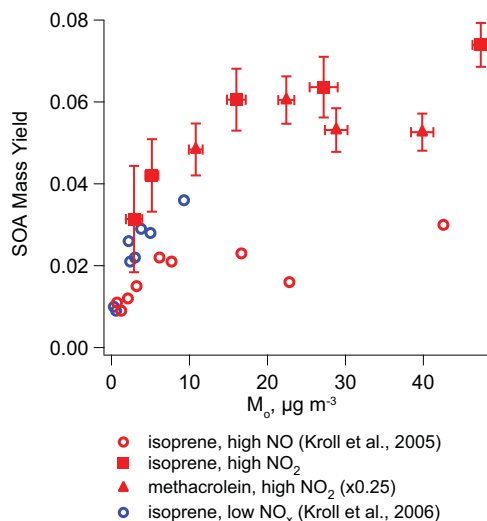


**Fig. 11.** SOA mass yields from isoprene photooxidation under neutral seed conditions as a function of organic loading. The solid markers indicate SOA yields measured in this study, using CH<sub>3</sub>ONO as the OH precursor under high NO<sub>2</sub>/NO ratios (between 3 and 8). The SOA yields for methacrolein (solid red triangles) have been multiplied by 0.25 to account for the gas-phase product yield of methacrolein from isoprene high-NO<sub>x</sub> oxidation. The SOA yields measured under high-NO<sub>2</sub>/NO conditions are higher than both high-NO (open red circles) and low-NO<sub>x</sub> conditions (open blue circles) under neutral seed conditions. With an acidified seed, SOA yields can be as high as 0.29 (Surratt et al., 2010).

is sufficiently fast that O<sub>2</sub> addition is not competitive at these O<sub>2</sub> levels.

From the trends of SOA formation observed in the unsaturated aldehyde systems, it appears that the chemical environment of the carbon atom adjacent to the aldehyde group plays an important role in determining the extent of SOA formation. Low-volatility oligoesters are formed only when the  $\alpha$ - and  $\beta$ -carbon atoms are unsaturated; SOA yields of 4-pentenal, for which the olefinic bond is in the 4-position, are lower than those of 2-pentenal, and the SOA products are not analogous to those found in SOA from  $\alpha$ ,  $\beta$ -unsaturated aldehydes (see Fig. 13). SOA formation is correlated with fraction of OH addition to the  $\beta$ -carbon atom, which forms a radical at the  $\alpha$  site: SOA yields of crotonaldehyde and 2-pentenal (in which OH addition to the  $\beta$ -carbon is favored) exceed those of 3M2B (in which OH addition to the  $\alpha$ -carbon is favored), even though 3M2B has an equal or higher molecular weight. This suggests that an interaction responsible for producing low-volatility species occurs between the peroxy nitrate functional group and the  $\alpha$ -carbon (likely a radical species) that our experiments are not able to precisely re-

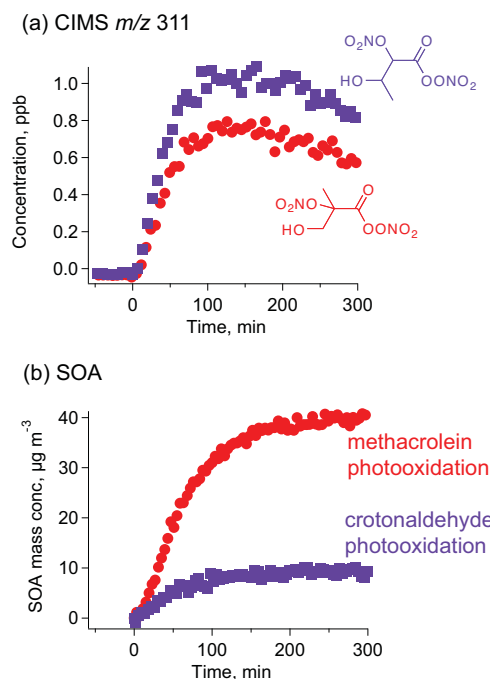


**Fig. 12.** Time trends of (a) gas-phase CIMS  $m/z$  311 and (b) SOA growth during high-NO<sub>2</sub> photooxidation of methacrolein (red) and crotonaldehyde (purple).  $m/z$  311 corresponds to the unit mass of CF<sub>3</sub>O<sup>-</sup> adduct of C<sub>4</sub>-hydroxynitrate-PAN. The observed gas-phase signals of C<sub>4</sub>-hydroxynitrate-PAN in both experiments are within 20% of each other, but the amount of SOA formed from methacrolein photooxidation is about a factor of 4 higher. A similar difference was observed between 2M2B and 3M2B photooxidation. This suggests that C<sub>4</sub>- and C<sub>5</sub>-hydroxynitrate-PANs are not precursors to low-volatility aerosol-phase products.

veal. We hypothesize that the peroxy radical undergoes self cyclization to form a highly reactive dioxoketone intermediate, which subsequently reacts with H<sub>2</sub>O or HNO<sub>3</sub> heterogeneously to form the low-volatility products observed in the SOA (see Fig. 10). This intermediate is likely short-lived, and further work is required to identify this species and its role in SOA formation.

One possible explanation for the higher SOA yields observed from methacrolein and 2M2B is that for these compounds SOA formation is favored by steric hindrance. With an additional methyl group on the  $\alpha$  carbon, steric repulsion causes the methyl group to move away from the neighbouring peroxy nitrate functional group by rotation of the C-C bond. As a result, the intramolecular reaction leading to SOA formation can be enhanced, consistent with the relatively higher SOA yields. For the other  $\alpha$ ,  $\beta$ -unsaturated

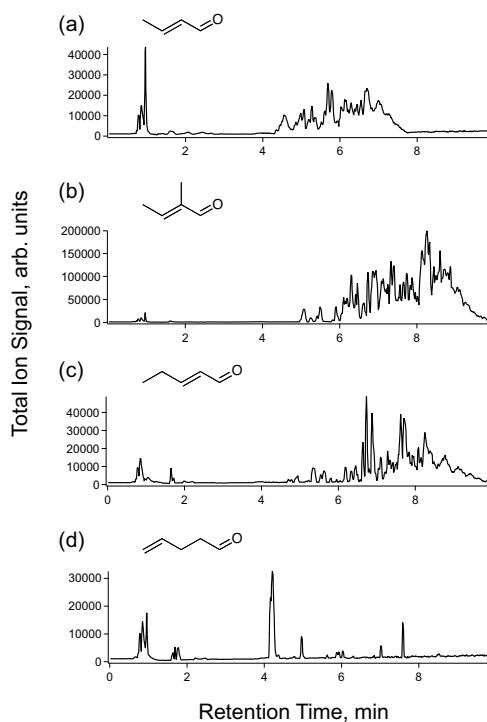
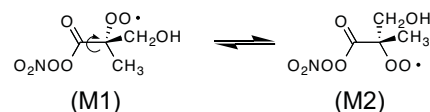


**Fig. 13.** UPLC/(-)ESI-TOFMS base peak ion chromatograms (BPCs) for high- $\text{NO}_2$  photooxidation of (a) crotonaldehyde (b) 2M2B (c) 2-pentenal and (d) 4-pentenal. The exact masses and elemental composition of detected  $[\text{M}-\text{H}]^-$  ions are listed in the Supplementary Material. Compounds detected in crotonaldehyde, 2M2B and 2-pentenal SOA are likely similar. (SOA products from  $\text{C}_5$  2M2B and 2-pentenal are less polar than those from crotonaldehyde, a  $\text{C}_4$  compound, and therefore have longer retention times in reverse-phase chromatography.) The chemical composition of 4-pentenal SOA is significantly different from those all 3 other aldehydes, and no oligoester products are detected, suggesting a different SOA formation mechanism.

aldehydes, this interaction is likely not favored, as the hydrogen atom on the  $\alpha$  carbon is in plane with the peroxy nitrate group in the most stable rotational conformer (see Fig. 14). The interaction between the peroxy nitrate group and the added functional group is reduced, corresponding to lower SOA formation. Thermodynamic calculations of the relative stabilities of the conformers are required to confirm this hypothesis.

#### Methacrolein:



#### Crotonaldehyde:

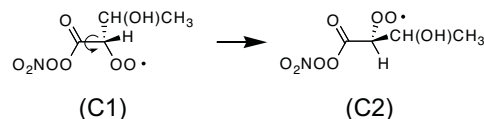


**Fig. 14.** Rotational conformers of hypothesized SOA intermediate in methacrolein and crotonaldehyde mechanism. For methacrolein, the methyl group on the  $\alpha$ -carbon presents significant steric hindrance, which favors the conformer M2. This increases the interaction between the peroxy radical and the peroxy nitrate group, leading to significant SOA formation. For crotonaldehyde, the hydrogen atom presents much smaller steric hindrance, favoring the conformer C2. As a result, the peroxy radical is out of plane with the PAN group, and the reaction to form SOA can be less favorable.

## 6.2 Methylbutenols (MBO)

MBO232 is a biogenic hydrocarbon potentially important in forest photochemistry (Harley et al., 1998). The SOA yields of MBO232 photooxidation have been shown to be negligible, under both high- and low- $\text{NO}_x$  conditions (Carrasco et al., 2007; Chan et al., 2009a). In this study, SOA formation from MBO232 photooxidation is below detection limit, even at high  $\text{NO}_2/\text{NO}$  ratios (which would favor any PAN formation). This is likely linked to the lack of PAN products from MBO232 oxidation. The fate of the alkoxy radical formed from OH-initiated oxidation of MBO232 is shown in Fig. 15. Scission of the C-C bond adjacent to the tertiary carbon is favored, leading to high yields of glycolaldehyde ( $>0.6$ ). Formation of 2-hydroxymethylpropanal (2-HMPR) following scission of the C-C bond adjacent to the primary carbon is not the favored route, and hence the yields of 2-HMPR are relatively low ( $<0.4$ ). Furthermore, OH oxidation of 2-HMPR proceeds by OH abstraction of the aldehydic hydrogen, but owing to the neighbouring hydroxyl group, decomposition to acetone and CO is favored over addition of  $\text{O}_2$  to form an acyl peroxy radical. Carrasco et al. (2006) found no PAN formation from photooxidation of 2-HMPR, despite high  $\text{NO}_2/\text{NO}$  ratios.

MBO231 photooxidation produces, in contrast, substantial amounts of SOA, at mass yields of 0.008 – 0.042. In MBO231, the hydroxyl group is in the 1-position and is not adjacent to the double bond. Decomposition of the analogous alkoxy radical therefore proceeds by scission of the C-C

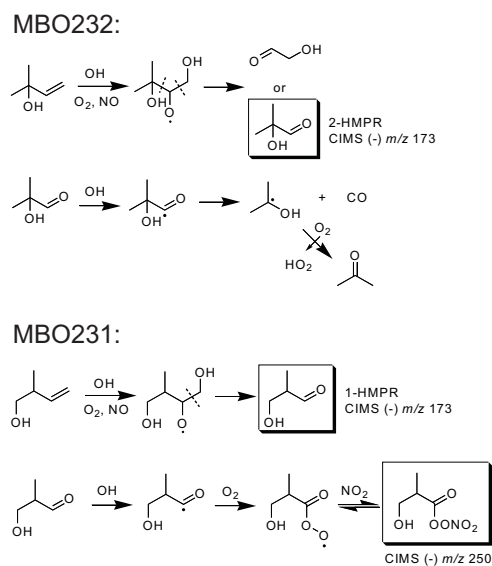


**Fig. 15.** Mechanism of MBO231 and MBO232 photooxidation under high-NO<sub>x</sub> conditions. The dashed lines indicate possible locations of C-C bond scission under decomposition of alkoxy radicals. For MBO232, 2-HMPR formation is relatively small, as scission of the C-C bond with the 4-carbon is not favored. In addition, the acyl radical from H-abstraction of 2-HMPR rapidly decomposes to CO and acetone. As a result, PAN formation is unlikely. For MBO231, 1-HMPR formation is favored from the decomposition of the alkoxy radical. Furthermore, OH reaction of 1-HMPR leads to an acyl peroxy radical, which reacts with NO<sub>2</sub> to form a C<sub>4</sub>-hydroxy-PAN.

bond adjacent to the primary carbon, favoring the formation of 1-HMPR; observed HMPR (CIMS (-)*m/z* 173) concentrations in MBO231 photooxidation were twice as high as those in MBO232 photooxidation. Also, following abstraction of the aldehydic hydrogen from 1-HMPR, addition of O<sub>2</sub> to form an acyl peroxy radical is favored over decomposition to CO. Under high-NO<sub>2</sub> conditions, the acyl peroxy radical can react with NO<sub>2</sub> to form a C<sub>4</sub>-hydroxy-PAN (see Fig. 15). Tandem mass spectrometry was used to distinguish gas-phase C<sub>4</sub>-hydroxy-PAN from the isobaric C<sub>5</sub> dihydroxynitrate, both observed at (-)*m/z* 250 (see Supplementary Material for details). The C<sub>5</sub> dihydroxynitrate is a first generation oxidation product of both MBO231 and MBO232 formed from RO<sub>2</sub>+NO at molar yields of 0.10–0.15 (Chan et al., 2009a). In high-NO photooxidation of MBO231 and high-NO<sub>2</sub> photooxidation of MBO232, no C<sub>4</sub>-hydroxy-PAN was observed in the gas phase, corresponding to negligible aerosol formation. In high-NO<sub>2</sub> photooxidation of MBO231, C<sub>4</sub>-hydroxy-PAN is a major gas-phase product, and SOA formation is significant. The identification of C<sub>4</sub>-hydroxy-PAN

is further supported by the ratios of ion signals of *m/z* 250 to *m/z* 251, its <sup>13</sup>C isotopologue, which indicate that the signal at *m/z* 250 was dominated by a C<sub>4</sub> compound during MBO231 high-NO<sub>2</sub> photooxidation, and by a C<sub>5</sub> compound during MBO232 photooxidation. Hence, the low SOA yields from MBO232 are due to the lack of PAN formation, illustrating the potentially important role of PAN compounds as SOA intermediates.

## 7 Conclusions

In this work, we systematically investigate the effect of relative NO and NO<sub>2</sub> concentrations on SOA formation from aldehyde photooxidation under high-NO<sub>x</sub> conditions. A strong positive correlation of SOA yields with NO<sub>2</sub>/NO ratio is observed for methacrolein (a major oxidation product of isoprene responsible for SOA formation) and two related α,β-unsaturated aldehydes, acrolein and crotonaldehyde. Oligoester products from dihydroxycarboxylic acids and hydroxynitrooxycarboxylic acids are also observed to depend on NO<sub>2</sub>/NO ratio, confirming that PAN chemistry plays an important role in formation of these low-volatility products. Offline high-resolution aerosol mass spectrometry reveals that analogous oligoester products are major constituents in SOA formed from all α,β-unsaturated aldehydes studied here. By comparing SOA formation from structurally similar aldehydes, we establish that SOA formation is favored when the α-carbon is substituted by a methyl group and the olefinic bond is in the 2-position, such as in methacrolein and 2M2B. The experimental data suggest that SOA formation proceeds via an intramolecular reaction involving the peroxy nitrate functional group, following the addition of O<sub>2</sub> to the MPAN+OH adduct. No aerosol formation is observed from MBO232, an atmospherically important unsaturated alcohol, even at high NO<sub>2</sub>/NO ratios, as PAN formation is structurally unfavorable.

Understanding the overall effect of NO<sub>x</sub> on SOA yields is important, as SOA yields can vary greatly depending on NO<sub>x</sub> conditions. In most photooxidation systems, addition of OH, followed by O<sub>2</sub>, to an olefinic bond results in formation of a hydroxyperoxy radical. The competition between the RO<sub>2</sub>+HO<sub>2</sub> pathway (which forms low-volatility hydroperoxides) and the RO<sub>2</sub>+NO pathway (which forms volatile organic nitrates and fragmentation products) determines the SOA yields. In the isoprene-high-NO<sub>x</sub> system, owing to the MPAN chemistry, aerosol formation proceeds via OH abstraction of the aldehydic hydrogen from methacrolein. As a result, a competition exists between reaction of the acyl peroxy radical with NO<sub>2</sub>, leading to formation of MPAN and SOA, and with NO to form volatile fragmentation products. The present work shows the importance of the RO<sub>2</sub>+NO<sub>2</sub> pathway of unsaturated aldehyde photooxidation as a route leading to SOA formation. This could have important implications on SOA formation from

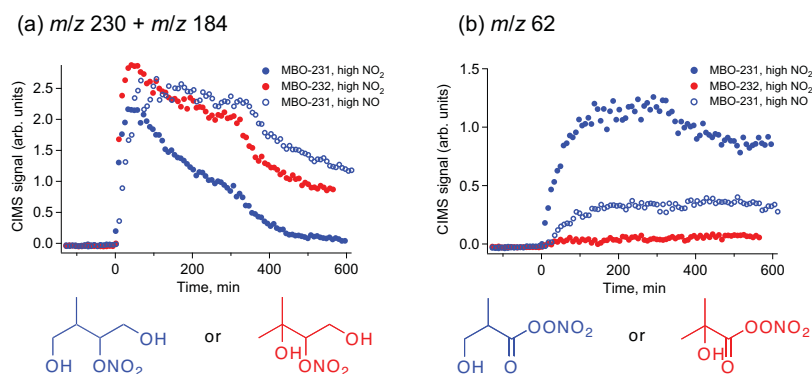


**Fig. 16.** Gas-phase ion signals of C<sub>4</sub>-hydroxy-PAN and C<sub>5</sub>-dihydroxynitrate from photooxidation of MBO231 and MBO232, as observed by negative chemical ionization-tandem mass spectrometry of  $m/z$  250. Neutral losses of HF or CF<sub>2</sub>O are associated with the C<sub>5</sub>-dihydroxynitrate under CID of the parent ion  $m/z$  250, leading to daughter ions of 230 and 184, respectively. The daughter ion  $m/z$  62, most likely NO<sub>3</sub><sup>-</sup>, is associated with the C<sub>4</sub>-hydroxy-PAN. (See Supplementary Material for more details.) After 300 minutes of irradiation, more OH precursor was added to further react oxidation products. PAN formation was observed only from MBO231 oxidation and is positively correlated with NO<sub>2</sub>/NO, similar to unsaturated aldehydes.

other atmospheric compounds, especially those with conjugated double bonds. For example, photooxidation of aromatic compounds (Calvert et al., 2002) can lead to  $\alpha$ ,  $\beta$ -unsaturated aldehydes, which can form significant amounts of low-volatility products via a PAN intermediate. At atmospherically relevant NO<sub>2</sub>/NO ratios, SOA yields from isoprene are 0.031–0.074 at organic aerosol loadings of 3–47  $\mu\text{g m}^{-3}$ ; these values are 3 times higher than those previously measured under high-NO conditions. The yields exceed even those measured under low-NO<sub>x</sub> conditions. An implication of these results is that atmospheric SOA formation from aldehydes may be significantly underestimated in current models, since an appreciable fraction of SOA is generated in areas where NO<sub>2</sub>/NO ratios are high.

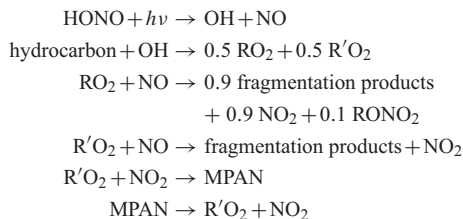
Radiocarbon (<sup>14</sup>C) studies have repeatedly shown that ambient organic aerosol is dominated by biogenic carbon, suggesting that biogenic hydrocarbons are an important source of SOA. However, field measurements have shown that organic aerosol levels tend to be correlated with anthropogenic tracers such as CO and acetylene. From satellite observations one can infer that while the source of carbon in many regions is most likely biogenic, the aerosol formation from biogenic hydrocarbons is significantly enhanced by anthropogenic activities (i.e. NO<sub>x</sub> and SO<sub>x</sub> emissions (Goldstein et al., 2009; Carlton et al., 2010)). The present work moves in the direction of reconciling these two seemingly contradictory observations of biogenic carbon versus anthropogenic enhancement. Here we show that the SOA yields from photooxidation of isoprene under atmospherically relevant NO<sub>2</sub>/NO ratios are significantly larger than those previously measured under lower NO<sub>2</sub>/NO ratios. Moreover, the SOA yields un-

der these conditions are larger than those under low-NO<sub>x</sub> conditions, suggesting that SOA formation from isoprene, the most abundantly emitted non-methane biogenic hydrocarbon, can be more efficient in urban high-NO<sub>x</sub> plumes than in remote regions.

## Appendix A

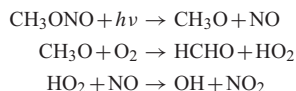
### Photochemical modeling to estimate NO and NO<sub>2</sub> concentrations

Owing to interference with the NO<sub>2</sub> signal by HONO and CH<sub>3</sub>ONO in the chemiluminescence NO<sub>x</sub> monitor, we estimate NO and NO<sub>2</sub> concentrations during chamber experiments by photochemical modeling. In experiments in which HONO is the source of OH, the photolysis rate of HONO is estimated from the first-order decay of the  $m/z$  66 signal on the CIMS, which correspond to the HF·ONO<sup>-</sup> ion. The initial mixing ratio of HONO was estimated based on the decay of parent hydrocarbon and known rate constants (Atkinson and Arey, 2003; Magneron et al., 2002). Previous comparison to a GC/NO<sub>2</sub> analyzer allows us to determine the HONO interference on the NO<sub>2</sub> signal, and hence the amount of NO and NO<sub>2</sub> produced during HONO synthesis (Chan et al., 2009b). The initial mixing ratio of NO<sub>2</sub> is therefore the sum of the concentrations of NO<sub>2</sub> impurity from HONO synthesis (calculated by multiplying the NO<sub>2</sub> signal after HONO injection by a known factor) and additional NO<sub>2</sub> injected (the increase in NO<sub>2</sub> signal from direct injection). For unsaturated aldehydes, the photochemical model includes the following reactions:



RO<sub>2</sub> denotes the peroxy radical produced by OH addition to the C=C double bond, followed by O<sub>2</sub>. R'O<sub>2</sub> denotes the acyl peroxy radical produced by OH abstraction of the aldehydic hydrogen, followed by O<sub>2</sub> addition. These two channels (OH addition and abstraction) have a branching ratio of 1:1 for methacrolein (Tuazon and Atkinson, 1990). Other reactions involving O<sub>3</sub>, HO<sub>x</sub>, NO<sub>x</sub> are also included in the mechanism. For MBO231 and MBO232, the reactions described in Chan et al. (2009a) are used. The calculated NO<sub>2</sub>/NO ratios averaged over the first 200 min of irradiation (the period during which SOA formation occurred, see Fig. 1) are listed in Table 2.

For the high-NO<sub>2</sub> experiments, CH<sub>3</sub>ONO was used as the OH precursor:



The photolysis rate of CH<sub>3</sub>ONO was estimated by the first-order decay of the CH<sub>3</sub>ONO signal on GC/FID. The initial mixing ratio of CH<sub>3</sub>ONO was determined from the measured vapor pressure of CH<sub>3</sub>ONO in the injection bulb. The modeled decay of the hydrocarbon is consistent with that observed by GC/FID. FTIR analysis shows no NO or NO<sub>2</sub> impurities are produced during CH<sub>3</sub>ONO synthesis ([NO<sub>2</sub>] was less than 0.6% of [CH<sub>3</sub>ONO]). In the photochemical calculations, the initial NO and NO<sub>2</sub> concentrations are determined from the increase in NO and NO<sub>2</sub> signals from direct injection. The calculated NO<sub>2</sub>/NO ratios averaged over the first 100 min of irradiation are listed in Table 2 (see Fig. 2).

**Supplementary material related to this article is available online at:**  
<http://www.atmos-chem-phys.net/10/7169/2010/acp-10-7169-2010-supplement.pdf>.

*Acknowledgements.* This research was funded by US Department of Energy Biological and Environmental Research Program DE-FG02-05ER63983, US Environmental Protection Agency STAR grant RD-83374901, US National Science Foundation grant ATM-0432377, and the Electric Power Research Institute. This publication has not been formally reviewed by the EPA. The views

expressed in this document are solely those of the authors and EPA does not endorse any products mentioned in this publication. The authors would like to thank K. E. Kautzman and A. J. Kwan for experimental assistance, and F. Paulot for helpful discussion.

Edited by: M. Gysel

## References

- Atkinson, R. and Arey, J.: Atmospheric degradation of volatile organic compounds, *Chem. Rev.*, 103, 4605–4638, 2003.
- Calvert, J. G., Atkinson, R., Becker, K. H., Kamens, R. M., Seinfeld, J. H., Wallington, T. J., and Yarwood, G.: The mechanisms of atmospheric oxidation of aromatic hydrocarbons, Oxford University Press, 2002.
- Canagaratna, M. R., Jayne, J. T., Jimenez, J. L., Allan, J. D., Alfarra, M. R., Zhang, Q., Onasch, T. B., Drewnick, F., Coe, H., Middlebrook, A., Delia, A., Williams, L. R., Trimborn, A. M., Northway, M. J., DeCarlo, P. F., Kolb, C. E., Davidovits, P., and Worsnop, D. R.: Chemical and microphysical characterization of ambient aerosols with the Aerodyne aerosol mass spectrometer, *Mass. Spec. Rev.*, 26, 185–222, 2007.
- Carlton, A. G., Wiedinmyer, C., and Kroll, J. H.: A review of Secondary Organic Aerosol (SOA) formation from isoprene, *Atmos. Chem. Phys.*, 9, 4987–5005, doi:10.5194/acp-9-4987-2009, 2009.
- Carlton, A. G., Pinder, R. W., Bhavsar, P. V. and Pouliot, G. A.: To what extent can biogenic SOA be controlled? *Environ. Sci. Technol.*, 44, 3376–3380, 2010.
- Carrasco, N., Doussin, J. F., Picquet-Varrault, B., and Carlier, P.: Tropospheric degradation of 2-hydroxy-2-methylpropanal, a photo-oxidation product of 2-methyl-3-buten-2-ol: Kinetic and mechanistic study of its photolysis and its reaction with OH radicals, *Atmos. Environ.*, 40, 2011–2019, 2006.
- Carrasco, N., Doussin, J. F., O'Connor, M., Wenger, J. C., Picquet-Varrault, B., Durand-Jolibois, R., and Carlier, P.: Simulation chamber studies of the atmospheric oxidation of 2-methyl-3-buten-2-ol: Reaction with hydroxyl radicals and ozone under a variety of conditions, *J. Atmos. Chem.*, 56, 33–55, 2007.
- Chan, A. W. H., Galloway, M. M., Kwan, A. J., Chhabra, P. S., Keutsch, F. N., Wennberg, P. O., Flagan, R. C., and Seinfeld, J. H.: Photooxidation of 2-methyl-3-buten-2-ol (MBO) as a potential source of secondary organic aerosol, *Environ. Sci. Technol.*, 43, 4647–4652, 2009a.
- Chan, A. W. H., Kautzman, K. E., Chhabra, P. S., Surratt, J. D., Crouse, J. D., Kürten, A., Wennberg, P. O., Flagan, R. C., Seinfeld, J. H.: Secondary organic aerosol formation from photooxidation of naphthalene and alkylnaphthalenes: implications for oxidation of intermediate volatility organic compounds (IVOCs), *Atmos. Chem. Phys.*, 9, 3049–3060, doi:10.5194/acp-9-3049-2009, 2009.
- Chung, S. H. and Seinfeld, J. H.: Global distribution and climate forcing of carbonaceous aerosols, *J. Geophys. Res.-Atmos.*, 107, doi:10.1029/2001JD001397, 2002.
- Claeys, M., Graham, B., Vas, G., Wang, W., Vermeylen, R., Pashynska, V., Cafmeyer, J., Guyon, P., Andreae, M. O., Artaxo, P., and Maenhaut, W.: Formation of secondary organic aerosols through photooxidation of isoprene, *Science*, 303, 1173–1176, 2004.



- Cocker, D. R., Flagan, R. C., and Seinfeld, J. H.: State-of-the-art chamber facility for studying atmospheric aerosol chemistry, *Environ. Sci. Technol.*, 35, 2594–2601, 2001.
- Crouse, J. D., McKinney, K. A., Kwan, A. J., and Wennberg, P. O.: Measurement of gas-phase hydroperoxides by chemical ionization mass spectrometry, *Anal. Chem.*, 78, 6726–6732, 2006.
- de Gouw, J. A., Middlebrook, A. M., Warneke, C., Goldan, P. D., Kuster, W. C., Roberts, J. M., Fehsenfeld, F. C., Worsnop, D. R., Canagaratna, M. R., Pszenny, A. A. P., Keene, W. C., Marchewka, M., Bertman, S. B., and Bates, T. S.: Budget of organic carbon in a polluted atmosphere: Results from the New England Air Quality Study in 2002, *J. Geophys. Res.-Atmos.*, 110, D16305, doi:10.1029/2004JD005623, 2005.
- de Gouw, J. A., Brock, C. A., Atlas, E. L., Bates, T. S., Fehsenfeld, F. C., Goldan, P. D., Holloway, J. S., Kuster, W. C., Lerner, B. M., Mathew, B. M., Middlebrook, A. M., Onasch, T. B., Peltier, R. E., Quinn, P. K., Senff, C. J., Stohl, A., Sullivan, A. P., Trainer, M., Warneke, C., Weber, R. J., and Williams, E. J.: Sources of particulate matter in the northeastern United States in summer: 1. Direct emissions and secondary formation of organic matter in urban plumes, *J. Geophys. Res.-Atmos.*, 113, D08301, doi:10.1029/2007JD009243, 2008.
- DeCarlo, P. F., Kimmel, J. R., Trimborn, A., Northway, M. J., Jayne, J. T., Aiken, A. C., Gonin, M., Fuhrer, K., Horvath, T., Docherty, K. S., Worsnop, D. R., and Jimenez, J. L.: Field-deployable, high-resolution, time-of-flight aerosol mass spectrometer, *Anal. Chem.*, 78, 8281–8289, 2006.
- Dommen, J., Metzger, A., Duplissy, J., Kalberer, M., Alfarra, M. R., Gascho, A., Weingartner, E., Prevot, A. S. H., Verheggen, B., and Baltensperger, U.: Laboratory observation of oligomers in the aerosol from isoprene/NO<sub>x</sub> photooxidation, *Geophys. Res. Lett.*, 33, L13805, doi:10.1029/2006GL026523, 2006.
- Edney, E. O., Kleindienst, T. E., Jaoui, M., Lewandowski, M., Offenberger, J. H., Wang, W., and Claeys, M.: Formation of 2-methyl tetrols and 2-methylglyceric acid in secondary organic aerosol from laboratory irradiated isoprene/NO<sub>x</sub>/SO<sub>2</sub>/air mixtures and their detection in ambient PM<sub>2.5</sub> samples collected in the eastern United States, *Atmos. Environ.*, 39, 5281–5289, 2005.
- Fantechi, G., Jensen, N. R., Hjorth, J., and Peeters, J.: Determination of the rate constants for the gas-phase reactions of methyl butenol with OH radicals, ozone, NO<sub>3</sub> radicals, and Cl atoms, *Int. J. Chem. Kinet.*, 30, 589–594, 1998.
- Galloway, M. M., Chhabra, P. S., Chan, A. W. H., Surratt, J. D., Flagan, R. C., Seinfeld, J. H., and Keutsch, F. N.: Glyoxal uptake on ammonium sulphate seed aerosol: reaction products and reversibility of uptake under dark and irradiated conditions, *Atmos. Chem. Phys.*, 9, 3331–3345, doi:10.5194/acp-9-3331-2009, 2009.
- Goldstein, A. H., Koven, C. D., Heald, C. L., and Fung, I. Y.: Biogenic carbon and anthropogenic pollutants combine to form a cooling haze over the southeastern United States, *Proc. Natl. Acad. Sci. USA*, 106, 8835–8840, 2009.
- Guenther, A., Karl, T., Harley, P., Wiedinmyer, C., Palmer, P. I., and Geron, C.: Estimates of global terrestrial isoprene emissions using MEGAN (Model of Emissions of Gases and Aerosols from Nature), *Atmos. Chem. Phys.*, 6, 3181–3210, doi:10.5194/acp-6-3181-2006, 2006.
- Hallquist, M., Wenger, J. C., Baltensperger, U., Rudich, Y., Simpson, D., Claeys, M., Dommen, J., Donahue, N. M., George, C., Goldstein, A. H., Hamilton, J. F., Herrmann, H., Hoffmann, T., Iinuma, Y., Jang, M., Jenkin, M. E., Jimenez, J. L., Kiendler-Scharr, A., Maenhaut, W., McFiggans, G., Mentel, Th. F., Monod, A., Prvt, A. S. H., Seinfeld, J. H., Surratt, J. D., Szmigielski, R., and Wildt, J.: The formation, properties and impact of secondary organic aerosol: current and emerging issues, *Atmos. Chem. Phys.*, 9, 5155–5236, doi:10.5194/acp-9-5155-2009, 2009.
- Harley, P., Fridd-Stroud, V., Greenberg, J., Guenther, A., and Vasconcellos, P.: Emission of 2-methyl-3-buten-2-ol by pines: A potentially large natural source of reactive carbon to the atmosphere, *J. Geophys. Res.-Atmos.*, 103, 25479–25486, 1998.
- Hatakeyama, S., Izumi, K., Fukuyama, T., Akimoto, H., and Washida, N.: Reactions of OH with alpha-pinene and beta-pinene in air – Estimate of global CO production from the atmospheric oxidation of terpenes, *J. Geophys. Res.-Atmos.*, 96, 947–958, 1991.
- Henze, D. K. and Seinfeld, J. H.: Global secondary organic aerosol from isoprene oxidation, *Geophys. Res. Lett.*, 33, L09812, doi:10.1029/2006GL025976, 2006.
- Henze, D. K., Seinfeld, J. H., Ng, N. L., Kroll, J. H., Fu, T.-M., Jacob, D. J., and Heald, C. L.: Global modeling of secondary organic aerosol formation from aromatic hydrocarbons: high- vs. low-yield pathways, *Atmos. Chem. Phys.*, 8, 2405–2420, doi:10.5194/acp-8-2405-2008, 2008.
- Hurley, M. D., Sokolov, O., Wallington, T. J., Takekawa, H., Karasawa, M., Klotz, B., Barnes, I., and Becker, K. H.: Organic aerosol formation during the atmospheric degradation of toluene, *Environ. Sci. Technol.*, 35, 1358–1366, 2001.
- Ion, A. C., Vermeylen, R., Kourtchev, I., Cafmeyer, J., Chi, X., Gelencsár, A., Maenhaut, W., and Claeys, M.: Polar organic compounds in rural PM<sub>2.5</sub> aerosols from K-puszta, Hungary, during a 2003 summer field campaign: Sources and diel variations, *Atmos. Chem. Phys.*, 5, 1805–1814, doi:10.5194/acp-5-1805-2005, 2005.
- Johnson, D., Jenkin, M. E., Wirtz, K., and Martin-Reviejo, M.: Simulating the formation of secondary organic aerosol from the photooxidation of aromatic hydrocarbons, *Environ. Chem.*, 2, 35–48, 2005.
- Kanakidou, M., Seinfeld, J. H., Pandis, S. N., Barnes, I., Dentener, F. J., Facchini, M. C., Van Dingenen, R., Ervens, B., Nenes, A., Nielsen, C. J., Swietlicki, E., Putaud, J. P., Balkanski, Y., Fuzzi, S., Horth, J., Moortgat, G. K., Winterhalter, R., Myhre, C. E. L., Tsigaridis, K., Vignati, E., Stephanou, E. G., and Wilson, J.: Organic aerosol and global climate modelling: a review, *Atmos. Chem. Phys.*, 5, 1053–1123, doi:10.5194/acp-5-1053-2005, 2005.
- Keywood, M. D., Varutbangkul, V., Bahreini, R., Flagan, R. C., and Seinfeld, J. H.: Secondary organic aerosol formation from the ozonolysis of cycloalkenes and related compounds, *Environ. Sci. Technol.*, 38, 4157–4164, 2004.
- Kleindienst, T. E., Lewandowski, M., Offenberger, J. H., Jaoui, M., and Edney, E. O.: The formation of secondary organic aerosol from the isoprene + OH reaction in the absence of NO<sub>x</sub>, *Atmos. Chem. Phys.*, 9, 6541–6558, doi:10.5194/acp-9-6541-2009, 2009.
- Kourtchev, I., Ruuskanen, T., Maenhaut, W., Kulmala, M., and Claeys, M.: Observation of 2-methyltetrols and related photooxidation products of isoprene in boreal forest aerosols from

- Hyytiälä, Finland, *Atmos. Chem. Phys.*, 5, 2761–2770, doi: 10.5194/acp-5-2761-2005, 2005.
- Kroll, J. H. and Seinfeld, J. H.: Chemistry of secondary organic aerosol: Formation and evolution of low-volatility organics in the atmosphere, *Atmos. Environ.*, 42, 3593–3624, 2008.
- Kroll, J. H., Ng, N. L., Murphy, S. M., Flagan, R. C., and Seinfeld, J. H.: Secondary organic aerosol formation from isoprene photooxidation under high-NO<sub>x</sub> conditions, *Geophys. Res. Lett.*, 32, L18808, doi:10.1029/2005GL023637, 2005a.
- Kroll, J. H., Ng, N. L., Murphy, S. M., Varutbangkul, V., Flagan, R. C., and Seinfeld, J. H.: Chamber studies of secondary organic aerosol growth by reactive uptake of simple carbonyl compounds, *J. Geophys. Res.-Atmos.*, 110, D23207, doi:10.1029/2005JD006004, 2005b.
- Kroll, J. H., Ng, N. L., Murphy, S. M., Flagan, R. C., and Seinfeld, J. H.: Secondary organic aerosol formation from isoprene photooxidation, *Environ. Sci. Technol.*, 40, 1869–1877, 2006.
- Lewis, C. W. and Stiles, D. C.: Radiocarbon content of PM<sub>2.5</sub> ambient aerosol in Tampa, FL, *Aerosol. Sci. Tech.*, 40, 189–196, 2006.
- Lewis, C. W., Klouda, G. A., and Ellenson, W. D.: Radiocarbon measurement of the biogenic contribution to summertime PM-2.5 ambient aerosol in Nashville, TN, *Atmos. Environ.*, 38, 6053–6061, 2004.
- Liggio, J., Li, S. M., and McLaren, R.: Heterogeneous reactions of glyoxal on particulate matter: Identification of acetals and sulfate esters, *Environ. Sci. Technol.*, 39, 1532–1541, 2005.
- Magneron, I., Thevenet, R., Mellouki, A., Le Bras, G., Moortgat, G. K., and Wirtz, K.: A study of the photolysis and OH-initiated oxidation of acrolein and trans-crotonaldehyde, *J. Phys. Chem. A*, 106, 2526–2537, 2002.
- Ng, N. L., Chhabra, P. S., Chan, A. W. H., Surratt, J. D., Kroll, J. H., Kwan, A. J., McCabe, D. C., Wennberg, P. O., Sorooshian, A., Murphy, S. M., Dalleska, N. F., Flagan, R. C., and Seinfeld, J. H.: Effect of NO<sub>x</sub> level on secondary organic aerosol (SOA) formation from the photooxidation of terpenes, *Atmos. Chem. Phys.*, 7, 5159–5174, doi:10.5194/acp-7-5159-2007, 2007a.
- Ng, N. L., Kroll, J. H., Chan, A. W. H., Chhabra, P. S., Flagan, R. C., and Seinfeld, J. H.: Secondary organic aerosol formation from m-xylene, toluene, and benzene, *Atmos. Chem. Phys.*, 7, 3909–3922, doi:10.5194/acp-7-3909-2007, 2007b.
- Orlando, J. J., Tyndall, G. S., and Paulson, S. E.: Mechanism of the OH-initiated oxidation of methacrolein, *Geophys. Res. Lett.*, 26, 2191–2194, 1999.
- Orlando, J. J., Tyndall, G. S., Bertman, S. B., Chen, W. C., and Burkholder, J. B.: Rate coefficient for the reaction of OH with CH<sub>2</sub>=C(CH<sub>3</sub>)C(O)OONO<sub>2</sub> (MPAN), *Atmos. Environ.*, 36, 1895–1900, 2002.
- Pandis, S. N., Paulson, S. E., Seinfeld, J. H., and Flagan, R. C.: Aerosol formation in the photooxidation of isoprene and beta-pinene, *Atmos. Environ.*, 25, 997–1008, 1991.
- Paulot, F., Crounse, J. D., Kjaergaard, H. G., Kurten, A., St Clair, J. M., Seinfeld, J. H., and Wennberg, P. O.: Unexpected epoxide formation in the gas-phase photooxidation of isoprene, *Science*, 325, 730–733, 2009.
- Presto, A. A., Hartz, K. E. H., and Donahue, N. M.: Secondary organic aerosol production from terpene ozonolysis. 2. Effect of NO<sub>x</sub> concentration, *Environ. Sci. Technol.*, 39, 7046–7054, 2005.
- Sato, K.: Detection of nitrooxypolyols in secondary organic aerosol formed from the photooxidation of conjugated dienes under high-NO<sub>x</sub> conditions, *Atmos. Environ.*, 42, 6851–6861, 2008.
- Song, C., Na, K. S., and Cocker, D. R.: Impact of the hydrocarbon to NO<sub>x</sub> ratio on secondary organic aerosol formation, *Environ. Sci. Technol.*, 39, 3143–3149, 2005.
- Surratt, J. D., Murphy, S. M., Kroll, J. H., Ng, N. L., Hildebrandt, L., Sorooshian, A., Szmigielski, R., Vermeylen, R., Maenhaut, W., Claeys, M., Flagan, R. C., and Seinfeld, J. H.: Chemical composition of secondary organic aerosol formed from the photooxidation of isoprene, *J. Phys. Chem. A*, 110, 9665–9690, 2006.
- Surratt, J. D., Gomez-Gonzalez, Y., Chan, A. W. H., Vermeylen, R., Shahgholi, M., Kleindienst, T. E., Edney, E. O., Offenberg, J. H., Lewandowski, M., Jaoui, M., Maenhaut, W., Claeys, M., Flagan, R. C., and Seinfeld, J. H.: Organosulfate formation in biogenic secondary organic aerosol, *J. Phys. Chem. A*, 112, 8345–8378, 2008.
- Surratt, J. D., Chan, A. W. H., Eddingsaas, N. C., Chan, M. N., Loza, C. L., Kwan, A. J., Hersey, S. P., Flagan, R. C., Wennberg, P. O., and Seinfeld, J. H.: Reactive intermediates revealed in secondary organic aerosol formation from isoprene, *Proc. Natl. Acad. Sci. USA*, 107, 6640–6645, 2010.
- Szmigielski, R., Surratt, J. D., Vermeylen, R., Szmigielska, K., Kroll, J. H., Ng, N. L., Murphy, S. M., Sorooshian, A., Seinfeld, J. H., and Claeys, M.: Characterization of 2-methylglyceric acid oligomers in secondary organic aerosol formed from the photooxidation of isoprene using trimethylsilylation and gas chromatography/ion trap mass spectrometry, *J. Mass. Spectrom.*, 42, 101–116, 2007.
- Taylor, W. D., Allston, T. D., Moscato, M. J., Fazekas, G. B., Kozlowski, R., and Takacs, G. A.: Atmospheric photo-dissociation lifetimes for nitromethane, methyl nitrite, and methyl nitrate, *Int. J. Chem. Kinet.*, 12, 231–240, 1980.
- Tuazon, E. C. and Atkinson, R.: A product study of the gas-phase reaction of methacrolein with the OH radical in the presence of NO<sub>x</sub>, *Int. J. Chem. Kinet.*, 22, 591–602, 1990.
- Tuazon, E. C., Aschmann, S. M., Nishino, N., Arey, J., and Atkinson, R.: Kinetics and products of the OH radical-initiated reaction of 3-methyl-2-butenal, *Phys. Chem. Chem. Phys.*, 7, 2298–2304, 2005.
- Volkamer, R., Ziemann, P. J., and Molina, M. J.: Secondary Organic Aerosol Formation from Acetylene (C<sub>2</sub>H<sub>2</sub>): seed effect on SOA yields due to organic photochemistry in the aerosol aqueous phase, *Atmos. Chem. Phys.*, 9, 1907–1928, doi:10.5194/acp-9-1907-2009, 2009.
- Weber, R. J., Sullivan, A. P., Peltier, R. E., Russell, A., Yan, B., Zheng, M., de Gouw, J., Warneke, C., Brock, C., Holloway, J. S., Atlas, E. L., and Edgerton, E.: A study of secondary organic aerosol formation in the anthropogenic-influenced southeastern United States, *J. Geophys. Res.-Atmos.*, 112, D13302, doi:10.1029/2007JD008408, 2007.
- Zhang, Q., Jimenez, J. L., Canagaratna, M. R., Allan, J. D., Coe, H., Ulbrich, I., Alfarra, M. R., Takami, A., Middlebrook, A. M., Sun, Y. L., Dzepina, K., Dunlea, E., Docherty, K., DeCarlo, P. F., Salcedo, D., Onasch, T., Jayne, J. T., Miyoshi, T., Shimo, A., Hatakeyama, S., Takegawa, N., Kondo, Y., Schneider, J., Drewnick, F., Borrmann, S., Weimer, S., Demerjian, K., Williams, P., Bower, K., Bahreini, R., Cottrell, L., Griffin,

7188

A. W. H. Chan et al.: High-NO<sub>x</sub> SOA formation from aldehydes

R. J., Rautiainen, J., Sun, J. Y., Zhang, Y. M., and Worsnop, D. R.: Ubiquity and dominance of oxygenated species in organic aerosols in anthropogenically-influenced Northern Hemisphere midlatitudes, *Geophys. Res. Lett.*, 34, L13801, doi:10.1029/2007GL029979, 2007a.

Zhang, Y., Huang, J. P., Henze, D. K., and Seinfeld, J. H.: Role of isoprene in secondary organic aerosol formation on a regional scale, *J. Geophys. Res.-Atmos.*, 112, D20207, doi:10.1029/2007JD008675, 2007b.



## Appendix F

# Modeling of Secondary Organic Aerosol Yields from Laboratory Chamber Data\*

---

\*Reproduced with permission from “Modeling of secondary organic aerosol yields from laboratory chamber data” by M. N. Chan, A. W. H. Chan, P. S. Chhabra, J. D. Surratt, and J. H. Seinfeld *Atmospheric Chemistry and Physics*, 9, 5669–5680, doi:10.5194/acp-9-5669-2009, Copyright 2010 by the Authors. CC Attribution 3.0 License.

## Modeling of secondary organic aerosol yields from laboratory chamber data

M. N. Chan<sup>1</sup>, A. W. H. Chan<sup>2</sup>, P. S. Chhabra<sup>2</sup>, J. D. Surratt<sup>2</sup>, and J. H. Seinfeld<sup>1,2</sup>

<sup>1</sup>Division of Engineering and Applied Science, California Institute of Technology, Pasadena, CA, USA

<sup>2</sup>Division of Chemistry and Chemical Engineering, California Institute of Technology, Pasadena, CA, USA

**Abstract.** Laboratory chamber data serve as the basis for constraining models of secondary organic aerosol (SOA) formation. Current models fall into three categories: empirical two-product (Odum), product-specific, and volatility basis set. The product-specific and volatility basis set models are applied here to represent laboratory data on the ozonolysis of  $\alpha$ -pinene under dry, dark, and low-NO<sub>x</sub> conditions in the presence of ammonium sulfate seed aerosol. Using five major identified products, the model is fit to the chamber data. From the optimal fitting, SOA oxygen-to-carbon (O/C) and hydrogen-to-carbon (H/C) ratios are modeled. The discrepancy between measured H/C ratios and those based on the oxidation products used in the model fitting suggests the potential importance of particle-phase reactions. Data fitting is also carried out using the volatility basis set, wherein oxidation products are parsed into volatility bins. The product-specific model is most likely hindered by lack of explicit inclusion of particle-phase accretion compounds. While prospects for identification of the majority of SOA products for major volatile organic compounds (VOCs) classes remain promising, for the near future empirical product or volatility basis set models remain the approaches of choice.

tween the gas and particle phases (Pankow, 1994a,b; Odum et al., 1996; Hallquist et al., 2009). Gas-particle partitioning of each compound is described by an equilibrium partitioning coefficient,  $K_p$ ,

$$K_p = \frac{P}{GM} \sim \frac{1}{c^*} \quad (1)$$

where  $G$  is the mass concentration per unit volume of air ( $\mu\text{g m}^{-3}$ ) of the semivolatile species in the gas phase,  $P$  is the mass concentration per unit volume of air ( $\mu\text{g m}^{-3}$ ) of the semivolatile species in the particle phase, and  $M$  is the mass concentration per unit volume of air ( $\mu\text{g m}^{-3}$ ) of the total absorbing particle phase. The equilibrium partitioning coefficient,  $K_p$  ( $\text{m}^3 \mu\text{g}^{-1}$ ), is inversely proportional to the saturation vapor concentration,  $c^*$  ( $\mu\text{g m}^{-3}$ ), of the pure semivolatile compound (see Appendix A).  $M$  refers only to the portion of the particulate matter participating in absorptive partitioning (organic aerosol into which semivolatile organics can partition and the aqueous portion of the particles in the case of water-soluble organics). Note that as long as some absorbing mass is present, some fraction of a given semivolatile compound partitions into the particle phase, even if its gas-phase concentration is below its saturation vapor concentration,  $c^*$ .

Oxidation of a parent VOC leads to a variety of semivolatile products, each with its own saturation vapor concentration. Moreover, the semivolatile oxidation products may be formed from first- or higher generation gas-phase reactions, and the products themselves may react further in the gas phase to yield compounds of either lower (in the case of addition of more functional groups) or greater (in the case in which the carbon backbone of the molecule is cleaved) volatility.

### 1 Introduction

Laboratory chamber data are needed to determine secondary organic aerosol (SOA) yields from volatile organic compounds (VOCs). The fundamental concept on which all descriptions of SOA formation lies is that SOA comprises a mixture of semivolatile organic compounds that partition be-



Correspondence to: J. H. Seinfeld  
(seinfeld@caltech.edu)

The fraction  $F$  of a semivolatile compound in the particle phase can be expressed in terms of  $K_p$  or  $c^*$  as

$$F = \frac{P}{G + P} = \frac{MK_p}{1 + MK_p} = \frac{1}{1 + c^*/M} \quad (2)$$

As the amount of absorbing material ( $M$ ) increases, compounds of greater volatility (larger  $c^*$ , smaller  $K_p$ ) will partition increasingly into the particle phase. When  $c^*=M$ , half of the semivolatile mass resides in the particle phase. If  $M \gg c^*$ , essentially all of the semivolatile species is in the particle phase.

In the first basic model of SOA formation, Odum et al. (1996) represented the process of SOA formation by  $n$  semivolatile products and showed that the SOA yield  $Y$ , defined as the mass of aerosol formed per mass of hydrocarbon reacted, can be expressed as

$$Y = M \sum_i \frac{\alpha_i K_{p,i}}{1 + MK_{p,i}} \quad (3)$$

where  $\alpha_i$  is the mass-based stoichiometric coefficient for product  $i$  (mass of  $i$  produced per mass of parent VOC reacted). Note that  $Y$  can exceed 1.0 as a result of the increase of molecular mass of oxidation products (the designation "aerosol mass fraction" is also used for  $Y$ ). Equation (3) is an equilibrium model in that it relates the amount of each product formed to the amount of VOC reacted regardless of number of chemical steps involved. While, in principle,  $n$  can be as large as desired, in the application of the Odum model usually  $n=2$ . The two products are not necessarily associated with actual compounds, and the 4 parameters,  $\alpha_1$ ,  $\alpha_2$ ,  $K_{p,1}$ , and  $K_{p,2}$ , are estimated by optimal fitting of Eq. (3) to the data.

SOA forms when gas-phase oxidation products of a hydrocarbon precursor partition between the gas and particle phases. Products with lower vapor pressures partition preferentially to the particle phase; compounds that are more highly functionalized tend to have lower vapor pressures. The degree of partitioning to the particle phase depends also on the quantity of absorbing organic material in that phase into which the compounds can condense; as the mass of absorbing material increases, compounds of higher vapor pressure that tend not to partition to the particle phase under low mass loadings do so at the higher mass loadings. The result is that SOA at low mass loading tends to be enriched in the least volatile (and most oxygenated) products (Bahreini et al., 2005; Shilling et al., 2008). In typical chamber experiments, a range of initial hydrocarbon precursor concentrations is employed in order to determine SOA yields as a function of the mass concentration of organic particles generated. When chamber experiments are conducted over a range of initial VOC concentrations, such experiments afford a view of the full spectrum of oxidation products, thereby facilitating the formulation of chemical mechanisms.

Laboratory chamber studies are limited in duration to about 12 h or so, as constrained by particle deposition on the

chamber walls, whereas the typical atmospheric lifetime of a particle is considerably longer. Chamber studies capture the initial multi-hour VOC oxidation but not that which takes place on a multi-day time scale. The sequence of reactions and associated SOA formation that occur over the duration of a chamber experiment can be termed as the *chamber phase*. (Stanier et al. (2008) have referred to this as the "prompt" phase.) The chamber or prompt phase chemistry begins with oxidant (OH, O<sub>3</sub>, NO<sub>3</sub>) attack on the VOC, initiating a series of reactions, which can depend critically on NO<sub>x</sub> level, leading to semivolatile products. Experimentally-derived SOA yields reflect the extent of SOA formation over the chamber phase. Reactions that occur on a time scale longer than a chamber experiment can be termed the *aging phase*, during which the following processes may occur: (1) particle-phase accretion reactions that convert semivolatile condensed products to essentially non-volatile compounds; (2) gas-phase oxidation reactions of chamber phase semivolatile products that are too slow to be important during the chamber phase but are capable of producing compounds of even lower volatility over the aging phase; and (3) gas-particle reactions that convert some particulate material to volatile products. Over the typical time scale and spatial grid scale of atmospheric models, SOA formation occurring on the chamber phase time scale can be considered as taking place essentially instantaneously, suggesting that an equilibrium partitioning model for this phase is appropriate. Over the longer aging time scale, the equilibrium partitioning can be considered to be slowly perturbed as chemical aging takes place.

## 2 Form of SOA model

If a number of products accounting for a significant fraction of the total mass of SOA have been identified, these major products can serve as SOA surrogates in a product-specific model (Pankow et al., 2001; Seinfeld et al., 2001). Upon estimating the vapor pressures, the values of  $K_p$  of the major products can be determined. For the product-specific model, major identified particle-phase products are chosen as SOA surrogates to represent other chemically similar compounds, and to give a reasonable approximation of gas/particle partitioning of all other products (Pankow et al., 2001). The simulated SOA composition may allow a first approximation of the properties of SOA (e.g., water uptake and cloud condensation nuclei activity). The SOA composition changes with organic mass loading, and the amount of hydrocarbon precursors reacted can be tracked. Using the simulated SOA composition, one can also calculate the aerosol oxygen-to-carbon (O/C) and hydrogen-to-carbon (H/C) ratios at different loadings. Simulated ratios for O/C and H/C can be compared with those measured.

An alternative approach is the *volatility basis set*, in which the range of products is specified in terms of volatility bins (Donahue et al., 2006; Stanier et al., 2008). The product

volatilities can be segmented into order-of-magnitude volatility bins (expressed as values of  $c^*$ ). Since SOA products are grouped into volatility bins, specific information about the chemical composition of SOA is not required. For the volatility basis set, Stanier et al. (2008) present a methodology for selecting the maximum and minimum values of  $c^*$ , and logarithmic spacing between  $c^*$  values then determines the number of volatility bins.

Either treatment has the potential to reproduce the measured concentrations of major reaction products (both gas-phase and particle-phase), even in the absence of details of major particle-phase reactions. On the other hand, if an equilibrium state is not attained during the chamber phase, the kinetics of gas-phase and particle-phase reactions determine the SOA composition. In such cases, development of kinetic models in which reaction products undergo reactions in both gas-phase and particle-phase is needed to describe the SOA formation (Chan et al., 2007).

The goal of this work is to evaluate the product-specific approach to SOA modeling, using a system that has been relatively well characterized in the laboratory: ozonolysis of  $\alpha$ -pinene. Because of a general lack of complete product identification for any SOA system, as well as uncertainty about the properties of the products, in practical terms, parameters in the model need to be determined by optimal fitting of the model to chamber data.

### 3 Ozonolysis of $\alpha$ -pinene

#### 3.1 Product-specific model

Ozonolysis of  $\alpha$ -pinene is, in many respects, an excellent test case for an SOA model. A number of experimental studies exist in the literature, and relatively complete product identification has been carried out. Oxocarboxylic acids, hydroxy oxocarboxylic acids, dicarboxylic acids, oxoaldehydes, and organic peroxides are the major classes of SOA products identified (Yu et al., 1999; Docherty et al., 2005). For the purposes of evaluating the product-specific model it is assumed that there are five major products: pinonic acid, pinic acid, pinonaldehyde, a hydroperoxide, and terpenylic acid (Table 1). These compounds are chosen to reflect the current understanding of the gas-phase products formed in the ozonolysis of  $\alpha$ -pinene.

The vapor pressure of a product  $i$  is estimated by using a group contribution method developed by Pankow and Asher (2008). At a given temperature, the  $K_{p,i}$  of the product  $i$  is determined by assuming that its activity coefficient,  $\zeta_i$ , is unity, and the molecular weight of product  $i$  is taken as the mean molecular weight of the surrogate mixture,  $\overline{MW}$ , as a first approximation. These assumptions may be reasonable as the range of molecular weights of products is small (168–200 g mol<sup>-1</sup>, see Table 1) and the amount of water present in the particle phase is not significant under dry conditions

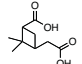
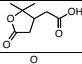
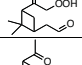
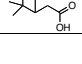
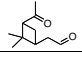
(<5%–40% RH). Bilde and Pandis (2001) measured the vapor pressure of semivolatile products formed from oxidation of biogenic monoterpenes using a laminar flow reactor with uncertainty of  $\pm 50\%$ . They reported a vapor pressure of  $1.989 \times 10^{-10}$  atm for pinic acid at 293 K, which is comparable to the estimated value ( $4.605 \times 10^{-10}$  atm) using the Pankow and Asher (2008) model. At a given temperature, the estimated vapor pressures of the major products using the Pankow and Asher (2008) model are lower than that estimated by Jenkin (2004). Hence, the present estimated  $K_p$  values of major products are larger than those reported by Jenkin (2004). For example, Jenkin (2004) estimated a higher vapor pressure of pinic acid of  $4.7 \times 10^{-4}$  torr (or  $6.18 \times 10^{-7}$  atm) at 298 K compared to that reported by Bilde and Pandis (2001) ( $4.213 \times 10^{-10}$  atm).

When the vapor pressure estimation is carried out for the  $\alpha$ -pinene/ozone system, two sets of two products each are estimated to have very similar  $K_p$  values. For example, at 293 K, the estimated value of  $K_p$  of hydroxy pinonic acid ( $K_p=0.2802$ ) is very close to that of pinic acid ( $K_p=0.2822$ ), and the estimated  $K_p$  of pinonic acid ( $K_p=0.0018$ ) is close to that of hydroxy pinonaldehyde ( $K_p=0.0017$ ). In such a case, two products of essentially identical vapor pressures cannot be distinguished, and a single product is chosen to represent the two products. Pinonic acid is chosen to represent the pinonic acid, norpinonic acid, hydroxy pinonaldehyde, and isomers. Pinic acid is chosen to represent pinic acid, norpinic acid, hydroxy pinonic acid, and isomers.

The basic chamber data are considered to be in the form of particle mass concentration as a function of VOC reacted. The actual chamber data are in the form of aerosol volume concentration. Aerosol density needed to convert volume to mass concentration is estimated by comparing the aerosol number distribution measured by a differential mobility analyzer with that obtained from the Aerodyne Aerosol Mass Spectrometer (AMS), through the theoretical relationship between mobility diameter and vacuum aerodynamic diameter. Ng et al. (2006) have shown that for the oxidation of a number of hydrocarbons with a single double bond, the growth curve for one experiment over the course of the experiment (“time-dependent growth curve”) follows that of final SOA growth over different experiments. This suggests that in this case the time-dependent SOA growth data can also be used for model data fitting.

Data from ozonolysis of  $\alpha$ -pinene are obtained from experiments conducted under dry, dark, and low-NO<sub>x</sub> conditions in the presence of dry (NH<sub>4</sub>)<sub>2</sub>SO<sub>4</sub> particles (Ng et al., 2006; Pathak et al., 2007; Shilling et al., 2008). The SOA yield data cover a range of organic mass loading (0.5–411  $\mu\text{g m}^{-3}$ ) and are used for the parameterization to model the SOA yield relevant to atmospheric conditions (Presto and Donahue, 2006). An effective SOA density of 1.25 g cm<sup>-3</sup> is applied for conversion of volume to mass concentration in determination of SOA yield. It is noted that Shilling

**Table 1.** Major products chosen to represent the ozonolysis of  $\alpha$ -pinene under dry, dark, and low-NO<sub>x</sub> conditions in the presence of dry ammonium sulfate particles. <sup>a</sup> Vapor pressure is determined at 293 K using a model developed by Pankow and Asher (2008).  $K_p$  is determined at 293 K with the assumption of activity coefficient of the products equal to one and the molecular weight of product  $i$  is used as mean molecular weight in organic absorbing phase, as a first approximation. <sup>b</sup> (Claeys et al., 2009) <sup>c</sup> The enthalpy of vaporization,  $\Delta H_v$  (kJ mol<sup>-1</sup>) of the product is estimated by plotting the estimated vapor pressure of the product against temperature. The  $\Delta H_v$  of the product can be estimated from the slope of the line following the Clausius-Clapeyron equation.

Product	Chemical structure	O/C	H/C	$\Delta H_v^c$	Product-Specific Model				Volatility Basis Set		
					$(K_p \times 1 \text{ case})$		$(K_p \times 100 \text{ case})$		$K_p$ (e <sup>a</sup> )	$\alpha$	$\alpha$ from Product-Specific Model ( $K_p \times 100 \text{ case}$ )
Pinic acid C <sub>10</sub> H <sub>16</sub> O <sub>4</sub> (MW: 186)		0.444	1.556	99.89	0.2822 (3.544)	0.2308	28.22 (0.0354)	0.0563	100 (0.01)	0.0707	0.0563 (Pinic acid: e <sup>a</sup> = 0.0354)
Terpenylic acid <sup>b</sup> C <sub>8</sub> H <sub>12</sub> O <sub>4</sub> (MW: 172)		0.5	1.5	76.73	0.0332 (30.12)	0.0172	3.32 (0.3012)	0.0132	10 (0.1)	0.0110	0.0131 (Terpenylic acid: e <sup>a</sup> = 0.3012)
Hydroperoxide C <sub>10</sub> H <sub>16</sub> O <sub>3</sub> (MW: 200)		0.4	1.6	83.99	0.0029 (344.8)	0.0181	0.29 (3.448)	0.0173	1 (1)	0.0120	0.0172 (Hydroperoxide: e <sup>a</sup> = 3.448)
Pinonic acid C <sub>10</sub> H <sub>16</sub> O <sub>3</sub> (MW: 184)		0.3	1.6	81.72	0.0018 (555.6)	0.6883	0.18 (5.556)	0.1573	0.1 (10)	0.1603	0.1573 (Pinonic acid: e <sup>a</sup> = 5.556)
									0.01 (100)	0.0210	-
Pinonaldehyde C <sub>10</sub> H <sub>16</sub> O <sub>2</sub> (MW: 168)		0.2	1.6	69.53	1.145 × 10 <sup>-5</sup> (87334)	1	1.145 × 10 <sup>-3</sup> (873.34)	0.9380	0.001 (1000)	0.9554	0.9380 (Pinonaldehyde: e <sup>a</sup> = 873.34)

et al. (2009) reported a higher effective SOA density (1.73–1.4 g cm<sup>-3</sup>) at low organic mass loading (0.5–7 μg m<sup>-3</sup>). The SOA yield data from Shilling et al. (2008) are adjusted to 293 K, using a temperature correction factor suggested by Pathak et al. (2007). Generally, the time-dependent SOA yield data reported by Ng et al. (2006) are in good agreement with the final SOA yield data reported by Pathak et al. (2007) and Shilling et al. (2008) but are lower than those reported by Shilling et al. (2008) for organic mass loadings less than 2 μg m<sup>-3</sup>. Measurement uncertainties may explain part of the variability in SOA yield data reported by Ng et al. (2006) at low organic mass loading.

Data, plotted as SOA yield,  $Y$ , versus organic mass loading,  $M$ , are shown in Fig. 1. The SOA yield increases rapidly at low organic mass loading and more slowly at high organic mass loading. Shown in Fig. 1 are the optimal fits to the product-specific and volatility basis set models. In order to evaluate the effect of uncertainty in  $K_p$  values, results are shown for the estimated values of  $K_p$  (termed  $K_p \times 1$  case) and the estimated values of  $K_p$  increased by a factor of 100 (termed  $K_p \times 100$  case). Previous modeling studies on this system have also shown that an overall increase of  $K_p$  of all products of a factor on the order of 10<sup>2</sup> is needed to explain the partitioning (Jenkin, 2004; Chen and Griffin, 2005). In each case, the  $\alpha_i$  values are determined by optimal fitting to the data. Different sets of  $\alpha_i$  values produce essentially the same goodness of fit to the overall mass yield. The sets can be discriminated according to how well they fit the SOA composition as compared to that measured. The  $\alpha_i$  values are chosen to give the best fit to experimental SOA yields

and SOA composition. As shown in Fig. 1, the predicted SOA yields agree well with the experimental SOA yield data in both  $K_p \times 1$  and  $K_p \times 100$  cases. The  $K_p \times 100$  case gives a better estimation of SOA yields at low organic mass loading than the  $K_p \times 1$  case. However, the optimized curves underpredict the SOA yield data reported by Shilling et al. (2008) when the organic mass loading is less than  $\sim 2 \mu\text{g m}^{-3}$ .

For the  $K_p \times 1$  case, the predicted SOA yields are lower than the measured ones at low organic mass loading. The data fitting produces the unrealistic result that the mass yield of the pinonaldehyde is unity. The sum of fitted molar yields exceeds 1. One likely explanation is the uncertainty in the estimation of the  $K_p$  of major products (vapor pressure and activity coefficient). The estimated vapor pressure of the products using the group contribution method is too high, and the products are estimated to be too volatile. In order to match experimental SOA yields, large mass yields of the products are predicted so that a significant amount of the products is partitioned into the particle phase. This results in unrealistically high mass yields of the products. Another likely explanation is that other products (gas-phase and/or particle-phase) of higher  $K_p$  (and lower volatilities) are present. Particle-phase reaction products (e.g., oligomers and esters), which are likely present, tend to have higher molecular weights and lower volatilities (Gao et al., 2004; Inuma et al., 2004; Müller et al., 2008), effectively enhancing the  $K_p$  values (Kroll and Seinfeld, 2005). For example, an ester, which is formed between pinic acid and hydroxy pinonic acid, has been detected (Müller et al., 2008). At 293 K, the estimated  $K_p$  of the ester is  $4.96 \times 10^5$ , which is

much larger than that of hydroxy pinonic acid ( $K_p=0.2802$ ) and of pinic acid ( $K_p=0.2822$ ).

### 3.2 Volatility basis set model

The volatility basis set model is also applied to fit the experimental SOA yields. The estimated volatility (or  $c^*$ ) of products spans from 0.035 to  $873 \mu\text{g m}^{-3}$ . A volatility basis set of six volatility bins is chosen and the volatility bins are separated by an order-of-magnitude ( $c^*$ : 0.01, 0.1, 1, 10, 100, and  $1000 \mu\text{g m}^{-3}$ ). The mass of aerosol in bin  $i$  is obtained by optimal fitting to the experimental SOA yield data. Figure 1 shows that for the volatility basis set, the predicted SOA yields agree well with the experimental SOA yield data, even at low organic mass loading ( $<0.5 \mu\text{g m}^{-3}$ ). This suggests that products with volatility as low as  $c^*=0.01 \mu\text{g m}^{-3}$  (or  $K_p=100 \mu\text{g}^{-1} \text{m}^3$ ) are present. The quantity of aerosol in the volatility bin  $i$  is in good agreement with that of the product  $i$  with similar  $K_p$  or  $c^*$  (Table 1) in the  $K_p \times 100$  case. Overall, the volatility basis set produces the smallest fitting error of SOA yield prediction over the whole range of organic mass loading (mean absolute fractional error,  $\text{err}=0.1572$ ) compared to the  $K_p \times 1$  case ( $\text{err}=0.1688$ ) and the  $K_p \times 100$  case ( $\text{err}=0.1598$ ).

### 3.3 Temperature dependence of SOA yield

We also investigate temperature dependence of SOA yield using the product-specific model (only the  $K_p \times 100$  case which gives a better description of SOA yields is shown). The temperature-dependent vapor pressure of the products can be estimated using the group contribution method developed by Pankow and Asher (2008). The temperature dependence of the structural groups ( $b(T)$ ) are assumed to follow  $b(T)=B_1/T+B_2+B_3T+B_4 \ln T$ . The  $B$  coefficients are obtained by optimal fitting to a number of compounds. In the calculation of the  $K_p$ , it is assumed that the activity coefficient is unity and the molecular weight of the product is taken as the mean molecular weight of the surrogate mixture. The  $\alpha$  values determined at 293 K are assumed to be constant over the temperature range studied (273–313 K). The enthalpy of vaporization,  $\Delta H_v$  of the products can also be estimated by the group contribution method. By plotting the estimated vapor pressure of the product against the temperature, the  $\Delta H_v$  of the product can be estimated from the slope of the line following the Clausius-Clapeyron equation (see Appendix A). Estimated values of  $\Delta H_v$  of major products are listed in Table 1.

As shown in Fig. 2, the predicted SOA yield increases as the temperature decreases, as lower temperature favors the partitioning of gas-phase reaction products into the particle phase. The model predicts a stronger temperature dependence of SOA yield than that observed by Pathak et al. (2007). The predicted SOA yields agree well with those measured at 293 and 303 K. The mean absolute fractional

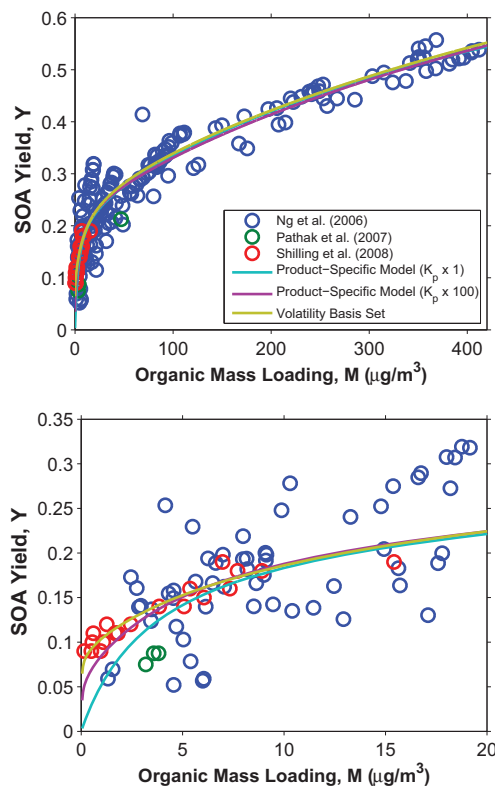


**Fig. 1.** SOA yield from ozonolysis of  $\alpha$ -pinene at different organic mass loading,  $M$ . Data represent experiments conducted under dry, dark, and low- $\text{NO}_x$  conditions in the presence of dry ammonium sulfate particles (Ng et al., 2006; Pathak et al., 2007; Shilling et al., 2008). Top panel: organic mass loading: 0–411  $\mu\text{g m}^{-3}$ ; bottom panel: organic mass loading: 0–20  $\mu\text{g m}^{-3}$ . SOA yield data are adjusted to 293 K, using a temperature correction factor. Lines show the model fit with the parameters given in Table 1.

error between the measured and predicted SOA yields,  $\text{err}$ , is 0.1666 and 0.0895 at 293 and 303 K, respectively. On the other hand, the predicted SOA yields are higher than those measured at 288 K ( $\text{err}=0.6728$ ) and 273 K ( $\text{err}=0.6266$ ) but slightly lower than those measured at 313 K ( $\text{err}=0.1968$ ).

In the product-specific model, the temperature dependence of the vapor pressure of major products is estimated directly using the group contribution method (Pankow and Asher, 2008). In this approach, uncertainties in the vapor pressure estimation method will lead to uncertainties in data fitting. Uncertainty in the vapor pressure estimation using the group contribution method is likely one factor contributing to a relatively large deviation between measured and predicted values at lower temperatures in the present study.



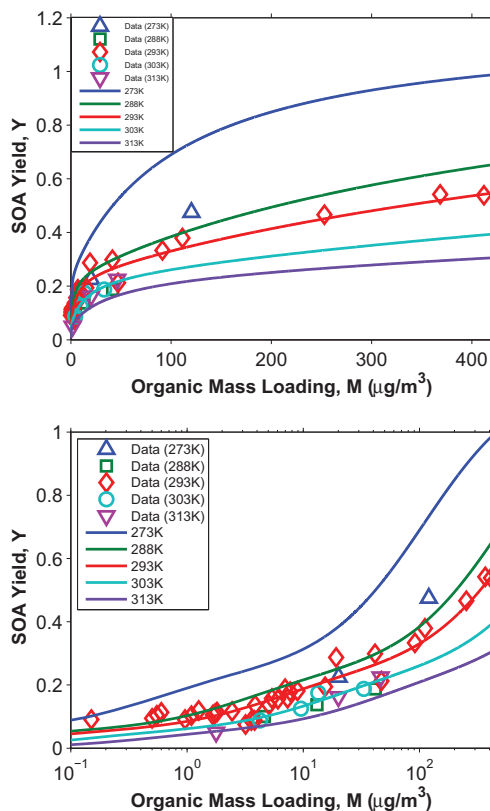


**Fig. 2.** Temperature dependence of SOA yield of ozonolysis of  $\alpha$ -pinene obtained from experiments conducted under dry, dark, and low- $\text{NO}_x$  conditions in the presence of dry ammonium sulfate particles. Data (293 K) are the final SOA yields from Ng et al. (2006), Pathak et al. (2007) and Shilling et al. (2008). Data from Shilling et al. (2008) have been adjusted to 293 K. Data at other temperatures are obtained from Pathak et al. (2007). The lines show the model fit at different temperatures for the  $K_p \times 100$  case.

#### 4 SOA composition

At a given temperature and organic mass loading,  $M$ , the mass yield of the product  $i$ ,  $Y_i$  can be determined as:

$$Y_i = \frac{M_i}{\Delta HC} = \frac{MK_{p,i}}{1 + MK_{p,i}} \alpha_i \quad (4)$$

where the mass-based stoichiometric coefficient of the product  $i$ ,  $\alpha_i$ , is obtained from the parameterization of SOA yield data using the product-specific model (Table 1).  $M_i$  is the concentration of product  $i$  in the particle phase ( $\mu\text{g m}^{-3}$ ). The SOA yield,  $Y$ , is the sum of the mass yields of all prod-

ucts (SOA yield,  $Y = \sum_i Y_i$ , at a given organic mass loading. The ratio of mass yield of product  $i$  to total yield ( $Y_i/Y$ ) is the relative contribution of the product  $i$  to the total SOA yield (or total SOA mass).

Figure 3 shows the predicted relative contributions of the products to the SOA yield at different organic mass loading for the  $K_p \times 100$  case. The predicted SOA composition is compared to the measured concentration of the corresponding classes of compounds in chamber experiments. Yu et al. (1999) reported the product distribution of ozonolysis of  $\alpha$ -pinene at 306 K and organic mass loading of  $38.8 \mu\text{g m}^{-3}$ : hydroxy pinonic acid (17.7%), pinic acid and norpinic acid (22.5%), pinonic acid and norpinonic acid, and isomers (36.5%), hydroxy pinonaldehyde (15.9%), and pinonaldehyde and norpinonaldehyde (7.4%). It is noted that organic peroxides, particle-phase reaction products (e.g., oligomers and esters), and terpenylic acid were not reported in Yu et al. (1999). Docherty et al. (2005) estimated that organic peroxides contribute  $\sim 47\%$  of the SOA mass at high organic mass loading. The concentration of terpenylic acid in chamber SOA has not been reported previously (Claeys et al., 2009). A smaller effective density of  $1 \text{ g cm}^{-3}$  was used to calculate the SOA mass in Yu et al. (1999). This change in density will increase the reported percentage of products. In addition, the relative abundance of products reported by Yu et al. (1999) may be overestimated if the organic peroxides, terpenylic acid, or other unidentified products contribute significantly to the SOA mass at the given organic mass loading.

As shown in the bottom panel of Fig. 3, for the  $K_p \times 100$  case, the predicted percentage of pinonic acid is about 51%, which is close to the sum of the percentages of pinonic acid and norpinonic acid and isomers and hydroxy pinonaldehyde (52.4%). The predicted percentage of pinonaldehyde is also close to that of pinonaldehyde and norpinonaldehyde (7.4%). On the other hand, the predicted percentage of pinic acid is about 28%, which is smaller than the sum of the percentages of pinic acid and norpinic acid and hydroxy pinonic acid (40.2%). For organic peroxides, using a hydroperoxide as surrogate gives  $\sim 7\%$  of SOA yield, which is lower than that reported by Docherty et al. (2005) at high organic mass loading. The percentage of terpenylic acid contributes about 5% of the SOA yield. Overall, the  $K_p \times 100$  case may give a good first estimation of the gas/particle partitioning and composition of the SOA products at the given organic mass loading and temperature.

#### 5 O/C and H/C ratios

The chemical composition of SOA formed from ozonolysis of  $\alpha$ -pinene has been recently characterized by an Aerodyne high-resolution time-of-flight aerosol mass spectrometer (HR-ToF-AMS) at 298 K (Shilling et al., 2009). This characterization provides measurement of the O/C and H/C ratios at different organic mass loadings; these data provide

additional information about the SOA composition and impose important constraints on the SOA parameterization. As shown in Figs. 4 and 5, the data show that the O/C ratio decreases as the organic mass loading increases, while the H/C ratio increases (Shilling et al., 2009). This observation indicates, as expected, that the SOA is more oxygenated at low organic mass loading than at high organic mass loading.

O/C and H/C ratios of the SOA can also be determined from the predicted SOA composition. At a given organic mass loading, the number of moles of product  $i$ ,  $m_i$  can be calculated from its particle-phase mass concentration and molecular weight. The number of carbon atoms,  $n_{C,i}$ , (O/C) $_i$  and (H/C) $_i$  ratios of the product  $i$  are known (Table 1). The O/C and H/C ratios of the SOA can be determined as follows:

$$O/C = \frac{\sum_i m_i \cdot n_{C,i} \cdot (O/C)_i}{\sum_i m_i \cdot n_{C,i}} \quad (5)$$

$$H/C = \frac{\sum_i m_i \cdot n_{C,i} \cdot (H/C)_i}{\sum_i m_i \cdot n_{C,i}} \quad (6)$$

At 298 K, for the  $K_p \times 1$  case (Fig. 4, upper panel), the modeled O/C ratios decrease from  $\sim 0.44$  to  $\sim 0.36$  as the organic mass loading increases from  $0.5 \mu\text{g m}^{-3}$  to  $150 \mu\text{g m}^{-3}$ . The predicted O/C ratios are higher than those in Shilling et al. (2009), except at low organic mass loading ( $< 1 \mu\text{g m}^{-3}$ ). The predicted ratios decrease less rapidly as the organic mass loading increases. For the  $K_p \times 100$  case (Fig. 4, lower panel), the predicted O/C ratios agree quite well with those measured; predicted O/C ratios decrease from 0.43 to 0.30 as the organic mass loading increases. On the other hand, in both  $K_p \times 1$  and  $K_p \times 100$  cases, the predicted H/C ratios exceed those measured at these loadings (Fig. 5).

The O/C ratios of selected major products range from 0.2 to 0.5, which cover the range of the experimental O/C ratios. On the other hand, the H/C ratios of the selected major products range from 1.5 to 1.6, which exceed the reported H/C ratios (1.38–1.51). Using the experimentally identified gas-phase reaction products, the predicted H/C ratios do not match those reported at low organic mass loading. Notably, the H/C ratios of the major SOA products identified in the literature range from 1.5 to 1.6. In addition to uncertainties in determination of the O/C and H/C ratios, the formation of oligomers or organic peroxides will shift the H/C ratio without greatly affecting the O/C ratio (Shilling et al., 2009). Formation of esters can alter the H/C and O/C ratios (Müller et al., 2008). The discrepancy in the H/C ratios based on known gas-phase products and those measured stresses the potential importance of particle-phase reactions on the determination of SOA yield and composition in the ozonolysis of  $\alpha$ -pinene under dry, dark, and low- $\text{NO}_x$  conditions.

Figures 4 and 5 also show the temperature dependence of the O/C and H/C ratios in the temperature range (273–313 K). For the both  $K_p \times 1$  and  $K_p \times 100$  cases (Fig. 4,

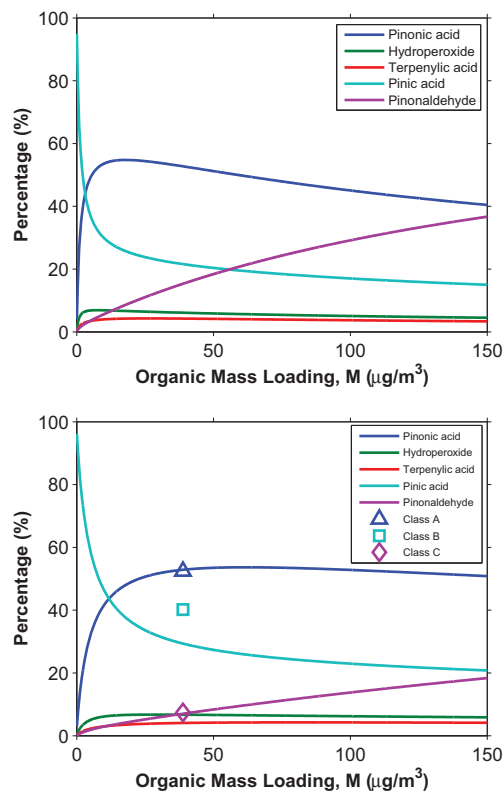


**Fig. 3.** Relative contributions of the modeled products to the SOA yield at different organic mass loadings for  $K_p \times 100$  case at different temperatures (solid lines). Top panel: 293 K; bottom panel: 306 K; Class A data point refers to the sum of the percentages of pinonic acid, norpinonic acid and isomers, and hydroxy pinonaldehyde (Yu et al., 1999); Class B data point refers to the sum of the percentages of pinic acid, norpinic acid, and hydroxy pinonic acid (Yu et al., 1999); Class C data point refers to the sum of the percentages of pinonaldehyde and norpinonaldehyde (Yu et al., 1999).

the modeled O/C ratio increases when the temperature increases. On the other hand, the modeled H/C ratio decreases when the temperature increases (Fig. 5). At a higher temperature, the less volatile gas-phase products which are usually more oxygenated (i.e., usually a higher O/C ratio and a lower H/C ratio) partition preferentially into the particle phase. As shown in Fig. 3 ( $K_p \times 100$  case), the contribution of pinic acid, which is the least volatile product and is more oxygenated, increases when the temperature increases from 293 to 306 K. On the other hand, the relative abundance of pinonaldehyde, which is the most volatile product and is the least oxygenated, decreases with increasing temperature.



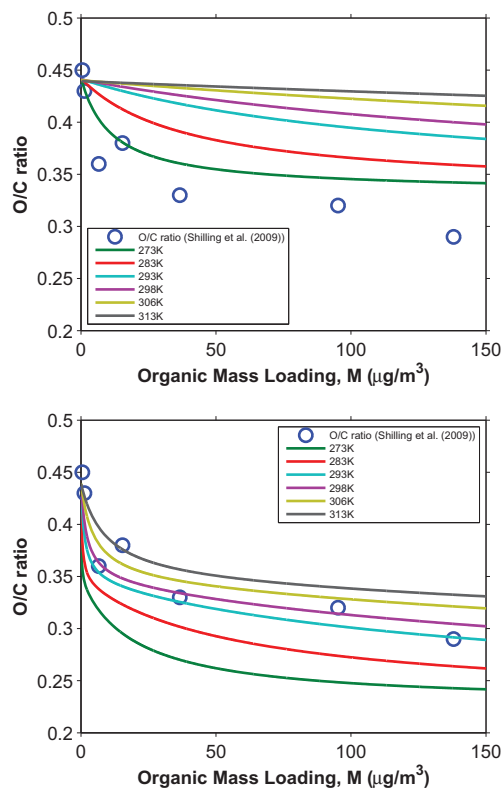


**Fig. 4.** O/C ratio of SOA formed from the ozonolysis of  $\alpha$ -pinene under dry, dark, and low-NO<sub>x</sub> conditions in the presence of dry ammonium sulfate particles as a function of organic mass loading,  $M$ , at different temperatures. Top panel:  $K_p \times 1$  case; bottom panel:  $K_p \times 100$  case; Blue open circles represent measured O/C ratios reported by Shilling et al. (2009) at 298 K.

The effect of particle-phase reactions on O/C and H/C ratios at different temperatures is not considered.

We also report here on an  $\alpha$ -pinene ozonolysis experiment conducted in the Caltech laboratory chamber under dry, dark, and low-NO<sub>x</sub> conditions in the presence of dry (NH<sub>4</sub>)<sub>2</sub>SO<sub>4</sub> particles to generate a data set comparable to that of Shilling et al. (2008, 2009). The chemical composition of the SOA was continuously monitored using an Aerodyne HR-ToF-AMS. Details of the experiment are given in Appendix B. Figure 6 shows the time evolution of  $\alpha$ -pinene concentration, organic mass loading, and aerosol O/C and H/C ratios. Once the ozone is injected,  $\alpha$ -pinene oxidation commences, and the organic mass loading increases almost immediately. When  $\alpha$ -pinene is completely reacted, organic aerosol mass loading remains unchanged. These observations are consistent with those reported by Ng et al. (2006).

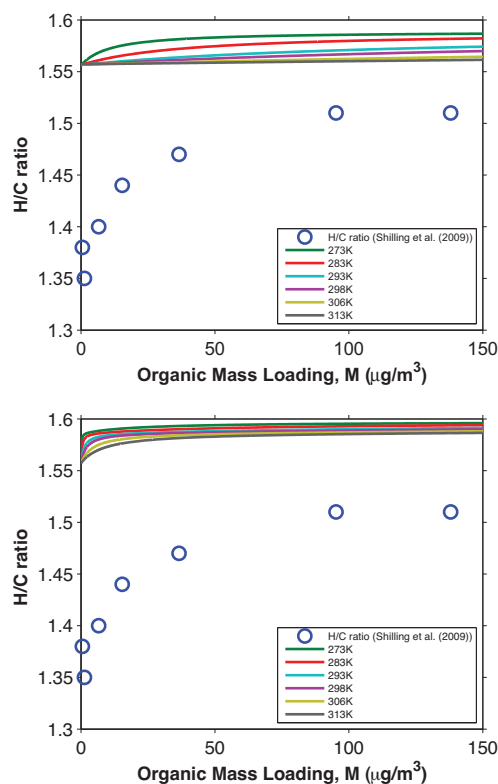


**Fig. 5.** H/C ratio of SOA formed from the ozonolysis of  $\alpha$ -pinene under dry, dark, and low-NO<sub>x</sub> conditions in the presence of dry ammonium sulfate particles as a function of organic mass loading,  $M$ , at different temperatures. Top panel:  $K_p \times 1$  case; bottom panel:  $K_p \times 100$  case; Blue open circles represent measured H/C ratios reported by Shilling et al. (2009) at 298 K.

Measured O/C and H/C ratios as a function of organic mass loading are shown in Fig. 7. The data scatter reflects the inherent uncertainty in measurement of O/C and H/C ratios at low organic mass loading. Generally, the H/C ratio increases as time increases, while the O/C ratio decreases. The trends in O/C and H/C ratios are in good agreement with those reported by Shilling et al. (2009). The absolute values of the O/C ratios are slightly lower than those reported by Shilling et al. (2009), but well within the experimental uncertainty. When all  $\alpha$ -pinene is consumed and the SOA growth has leveled out ( $\sim 58 \mu\text{g m}^{-3}$ ), O/C and H/C ratios and fragment mass spectrum (not shown here) remain unchanged. As discussed by Ng et al. (2006), the first oxidation step in the ozonolysis of  $\alpha$ -pinene (a hydrocarbon with a single double bond) is most likely the rate-determining step in SOA formation. Either the condensable products are the initial reaction

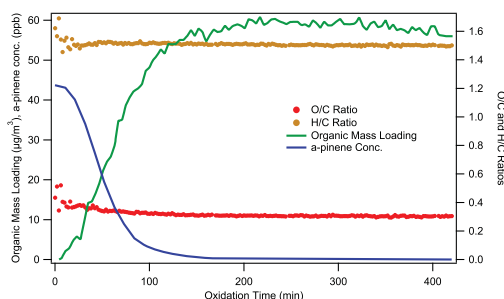


**Fig. 6.** Time evolution of  $\alpha$ -pinene concentration, organic mass loading, and O/C and H/C ratios during ozonolysis of  $\alpha$ -pinene under dry, dark, and low- $\text{NO}_x$  conditions in the presence of dry ammonium sulfate particles. Experiment conducted in the Caltech laboratory chamber. Conditions given in Appendix B.

products of the parent hydrocarbon oxidation (first- or higher generation products), or subsequent reactions (in either the gas or particle phase) proceed at relatively fast rates. Thus, the instantaneous product spectrum can be considered as that at equilibrium during the chamber phase.

To determine the extent to which an equilibrium state is achieved, the chemical composition of SOA can be measured by the Aerodyne HR-ToF-AMS over the course of the chamber experiments. The change in element-to-carbon ratios (e.g., O/C, H/C ratios) can provide insight about the change in SOA composition. If the ratios or the mass spectra do not vary with time, this may suggest that an equilibrium state is achieved within the timescale of the chamber experiment. In that case, major experimentally identified products (both particle-phase and gas-phase reaction products) can be chosen as SOA surrogates in the product-specific model. In addition, the O/C, H/C, N/C, or S/C ratios can be calculated from the detailed gas-chemistry model coupled with gas/particle partitioning theory.

Recently, Dzepina et al. (2009) suggest that the O/C ratio and volatility can be used to compare modeled and measured SOA. The authors calculate O/C ratios using various models and compare these to the measured O/C ratios of ambient Mexico City aerosol. They find that O/C ratios predicted by different models do not agree and are generally lower than the measured ratios.

In the present study, we show that although good agreement in O/C ratio between observations and predictions can exist, a discrepancy in H/C ratio is not removed by data fitting. Hence, in addition to the O/C ratio, other element-to-carbon ratios such as H/C are important for modeling fitting and comparison. S/C and N/C ratios could be used once accurate determinations can be made using the AMS. These element-to-carbon ratios can also be calculated using detailed gas-chemistry models coupled with gas/particle par-

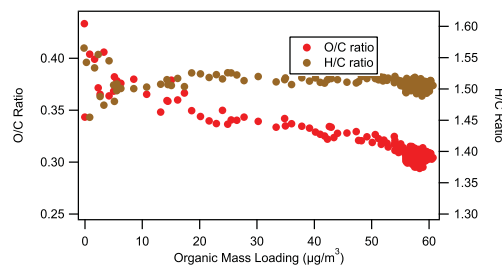


**Fig. 7.** O/C and H/C ratios of SOA formed from the ozonolysis of  $\alpha$ -pinene under dry, dark, and low- $\text{NO}_x$  conditions in the presence of dry ammonium sulfate particles as function of organic mass loading,  $M$ . Experiment conducted in the Caltech laboratory chamber. Conditions given in Appendix B.

tioning theory and can be used as additional constraints on the SOA parameterization in chamber experiments and modeling studies.

## 6 Discussion

SOA yields from volatile organic compounds are determined from laboratory chamber data. Gas-particle partitioning of semivolatile oxidation products forms the basis of all current models of SOA formation. As identification of aerosol-phase products has become feasible using advanced mass spectrometric techniques, we investigate the extent to which a product-specific model, certain parameters of which are determined from chamber data, can be used to represent SOA formation. In the present work we address this question using data on SOA formation in the  $\alpha$ -pinene/ozone system. While the product specific model can be fitted to available chamber data, fitting of the product-specific model required increasing estimated equilibrium partitioning coefficients by two orders of magnitude, and the predicted fractional contributions of the selected products to SOA are unreasonable in several respects and no better than a fitting of the data to a volatility basis set representation.

The performance of the product-specific model is most likely hindered by lack of explicit inclusion of particle-phase accretion compounds that are almost certainly present but have yet to be identified in this system. Prospects for identification of the majority of SOA products for major VOC classes remain promising. However, for the near future, empirical product Odum-type or volatility basis set models remain the approaches of choice.

## Appendix A

### The gas-particle partitioning coefficient

The gas-particle partitioning coefficient for compound  $i$  to a condensed phase of  $i$  only is given by (Pankow, 1994a,b)

$$K_{p,i} = \frac{RT}{10^6 MW_i p_{L,i}^o} \quad (\text{A1})$$

where  $R=8.2 \times 10^{-5} \text{ m}^3 \text{ atm mol}^{-1} \text{ K}^{-1}$ ,  $MW_i$ =molecular weight of  $i$  ( $\text{g mol}^{-1}$ ) and  $p_{L,i}^o$  is the vapor pressure of pure  $i$  as a liquid (atm). When multiple condensed-phase compounds exist

$$K_{p,i} = \frac{RTf}{10^6 \overline{MW} \zeta_i p_{L,i}^o} \quad (\text{A2})$$

where  $f$ =weight fraction of the total particulate matter that is the absorbing phase,  $\overline{MW}$  is the mean molecular weight of the absorbing organic phase ( $\text{g mol}^{-1}$ ), and  $\zeta_i$ =mole-fraction based activity coefficient.  $K_{p,i}$  varies as a function of  $T$ , through both its explicit dependence on  $T$  as well as the strong dependence of  $p_{L,i}^o$  on  $T$ . The value of  $K_{p,i}$  is also influenced by  $\zeta_i$  and  $\overline{MW}$  owing to the types and amounts of condensed-phase compounds.

The vapor pressure of each component obeys the Clausius-Clapeyron equation,

$$p_{L,i}^o(T) = p_{L,i}^o(T_o) \exp \left[ -\frac{\Delta H_{v,i}}{R} \left( \frac{1}{T} - \frac{1}{T_o} \right) \right] \quad (\text{A3})$$

For a set of compounds at a given  $T$ ,  $p_{L,i}^o$  tends to decrease with increasing  $\Delta H_{v,i}$ .

The variation of gas-partitioning coefficient with temperature results from variation of  $p_{L,i}^o$  as well as the explicit dependence on  $T$ ,

$$\begin{aligned} \frac{K_{p,i}(T)}{K_{p,i}(T_o)} &= \left( \frac{T}{T_o} \right) \frac{p_{L,i}^o(T_o)}{p_{L,i}^o(T)} \\ &= \left( \frac{T}{T_o} \right) \exp \left[ -\frac{\Delta H_{v,i}}{R} \left( \frac{1}{T} - \frac{1}{T_o} \right) \right] \end{aligned} \quad (\text{A4})$$

Following Pankow and Chang (2008), one may choose  $\Delta H_v=100 \text{ kJ mol}^{-1}$  as a “reference”  $\Delta H_{v,i}$  value, so that any  $\Delta H_{v,i}$  can be written as a multiple of the reference value,  $\Delta H_{v,i}=a_i \times 100 \text{ kJ mol}^{-1}$ . For  $T_o=293 \text{ K}$ , for  $a=1$ , a 10 K decrease in  $T$  leads to

$$\begin{aligned} \frac{K_{p,i}(283)}{K_{p,i}(293)} &= \left( \frac{283}{293} \right) \exp \left[ -\frac{100}{R} \left( \frac{1}{283} - \frac{1}{293} \right) \right] \\ &= 4.1 \end{aligned} \quad (\text{A5})$$

Thus, for a compound with  $\Delta H_v=100 \text{ kJ mol}^{-1}$ , a 10 K decrease in temperature leads to a factor of 4 increase in  $K_{p,i}$ . For a compound with  $a_i=0.5$ , the increase of  $K_{p,i}$  for a 10 K decrease in  $T$  is  $\sim$  a factor of 2. Note that the factor  $(T/T_o)$  exerts only a minor effect compared to that from the temperature dependence of  $p_{L,i}^o$ .

## Appendix B

### Measurement of O/C and H/C ratios of SOA from $\alpha$ -pinene ozonolysis

To provide an additional set of data on the O/C ratio of SOA generated from  $\alpha$ -pinene ozonolysis, an experiment was performed in one of the dual Caltech 28-m<sup>3</sup> Teflon chambers. Details of the facility have been described elsewhere (Cocker et al., 2001; Keywood et al., 2004). Before the experiment, the chamber was flushed continuously with dry, purified air for at least 24 h. Aerosol number concentration, size distribution, and volume concentrations were measured by a differential mobility analyzer (DMA, TSI model 3081) coupled with a condensation nucleus counter (TSI model 3760). Ammonium sulfate seed particles were generated by atomizing an aqueous solution of 0.015 M  $(\text{NH}_4)_2\text{SO}_4$  with a constant-rate atomizer. The volume concentration of the seed particles was  $12 \mu\text{m}^3 \text{ cm}^{-3}$ .

The parent hydrocarbon,  $\alpha$ -pinene, and an OH scavenger, cyclohexane, were then introduced separately by injecting known volumes of the liquid hydrocarbon into a glass bulb, subsequently carried into the chamber by an air stream at  $5 \text{ L min}^{-1}$ . The mixing ratio of  $\alpha$ -pinene was monitored with a gas chromatograph coupled with a flame ionization detector (GC-FID, Agilent model 6890N). The initial mixing ratio of  $\alpha$ -pinene was 44 ppb. The estimated mixing ratio of cyclohexane was 37 ppm, which corresponds to a rate of cyclohexane + OH 100 times faster than that of  $\alpha$ -pinene + OH.

Ozone was generated with a UV lamp ozone generator (EnMet Corporation, MI), and monitored with a commercial ozone analyzer (Horiba Instruments, CA). Ozone injection was stopped after the ozone concentration reached 180 ppb. The aerosol growth data were corrected for wall deposition of particles. First-order size dependent wall loss coefficients were determined from a separate seed-only experiment. The final SOA volume was  $46 \mu\text{m}^3 \text{ cm}^{-3}$ , as measured by the DMA.

Real-time particle mass spectra were collected continuously by an Aerodyne High Resolution Time-of-Flight Aerosol Mass Spectrometer (HR-ToF-AMS). The HR-ToF-AMS is described in detail elsewhere (Canagaratna et al. (2007) and references therein). The HR-ToF-AMS switched once every minute between the high resolution “W-mode” and the lower resolution, higher sensitivity “V-mode”. The “V-mode” data were analyzed using a fragmentation table to separate sulfate, ammonium, and organic spectra and to time-trace specific mass-to-charge ratios. “W-mode” data were analyzed using a separate high-resolution spectra toolbox known as PIKA to determine the chemical formulas contributing to distinct mass-to-charge ratios (DeCarlo et al., 2006).

To determine elemental ratios, the computational toolbox Analytical Procedure for Elemental Separation (APES) was used. This toolbox applies the analysis procedure described

in Aiken et al. (2007) to the high-resolution “W-mode” data. The particle-phase signal of  $\text{CO}^+$  and the organic contribution to  $\text{H}_x\text{O}^+$  ions were estimated as described in Aiken et al. (2008). It is noted that chamber air is cleaned through a series of chemical denuders and filters. Fourier transform infrared spectroscopy measurements show that the concentrations of  $\text{CO}_2$  in the chamber air is nominally the same as that in the atmosphere. Due to the relatively large SOA loadings generated in this study, the sensitivity of the O/C calculation to the  $\text{CO}_2$  concentration input is relatively small.

**Acknowledgements.** This work was supported by the Office of Science (BER), U.S. Department of Energy, Grant No. DE-FG02-05ER63983 and the U.S. Environmental Protection Agency under STAR Agreement RD-833749. It has not been formally reviewed by the EPA. The views expressed in this document are solely those of the authors and the EPA does not endorse any products or commercial services mentioned in this publication.

Edited by: A. Nenes

## References

- Aiken, A. C., DeCarlo, P. F., and Jimenez, J. L.: Elemental analysis of organic species with electron ionization high-resolution mass spectrometry, *Anal. Chem.*, 79, 8350–8358, 2007.
- Aiken, A. C., Decarlo, P. F., Kroll, J. H., Worsnop, D. R., Huffman, J. A., Docherty, K. S., Ulbrich, I. M., Mohr, C., Kimmel, J. R., Sueper, D., Sun, Y., Zhang, Q., Trimborn, A., Northway, M., Ziemann, P. J., Canagaratna, M. R., Onasch, T. B., Alfarra, M. R., Prevot, A. S. H., Dommen, J., Duplissy, J., Metzger, A., Baltensperger, U., and Jimenez, J. L.: O/C and OM/OC ratios of primary, secondary, and ambient organic aerosols with high-resolution time-of-flight aerosol mass spectrometry, *Environ. Sci. Technol.*, 42, 4478–4485, 2008.
- Bahreini, R., Keywood, M. D., Ng, N. L., Varutbangkul, V., Gao, S., Flagan, R. C., Seinfeld, J. H., Worsnop, D. R., and Jimenez, J. L.: Measurements of secondary organic aerosol from oxidation of cycloalkenes, terpenes, and m-xylene using an Aerodyne aerosol mass spectrometer, *Environ. Sci. Technol.*, 39, 5674–5688, 2005.
- Bilde, M. and Pandis, S. N.: Evaporation rates and vapor pressures of individual aerosol species formed in the atmospheric oxidation of alpha- and beta-pinene, *Environ. Sci. Technol.*, 35, 3344–3349, 2001.
- Canagaratna, M. R., Jayne, J. T., Jimenez, J. L., Allan, J. D., Alfarra, M. R., Zhang, Q., Onasch, T. B., Drewnick, F., Coe, H., Middlebrook, A., Delia, A., Williams, L. R., Trimborn, A. M., Northway, M. J., DeCarlo, P. F., Kolb, C. E., Davidovits, P., and Worsnop, D. R.: Chemical and microphysical characterization of ambient aerosols with the aerodyne aerosol mass spectrometer, *Mass. Spectrom. Rev.*, 26, 185–222, 2007.
- Chan, A. W. H., Kroll, J. H., Ng, N. L., and Seinfeld, J. H.: Kinetic modeling of secondary organic aerosol formation: effects of particle- and gas-phase reactions of semivolatile products, *Atmos. Chem. Phys.*, 7, 4135–4147, 2007, <http://www.atmos-chem-phys.net/7/4135/2007/>.
- Chen, J. J. and Griffin, R. J.: Modeling secondary organic aerosol formation from oxidation of alpha-pinene, beta-pinene, and d-limonene, *Atmos. Environ.*, 39, 7731–7744, 2005.
- Claeys, M., Iinuma, Y., Szmigielski, R., Surratt, J. D., Blockhuys, F., Van Alsenoy, C., Böge, O., Sierau, B., Gómez-González, Y., Vermeylen, R., Van der Veken, P., Shahgholi, M., Chan, A. W. H., Herrmann, H., Seinfeld, J. H., and Maenhaut, W.: Terpenylic acid and related compounds from the oxidation of  $\alpha$ -pinene: Implications for new particle formation and growth above forests, *Environ. Sci. Technol.*, in press, 2009.
- Cocker, D. R., Flagan, R. C., and Seinfeld, J. H.: State-of-the-art chamber facility for studying atmospheric aerosol chemistry, *Environ. Sci. Technol.*, 35, 2594–2601, 2001.
- DeCarlo, P. F., Kimmel, J. R., Trimborn, A., Northway, M. J., Jayne, J. T., Aiken, A. C., Gonin, M., Fuhrer, K., Horvath, T., Docherty, K. S., Worsnop, D. R., and Jimenez, J. L.: Field-deployable, high-resolution, time-of-flight aerosol mass spectrometer, *Anal. Chem.*, 78, 8281–8289, 2006.
- Docherty, K. S., Wu, W., Lim, Y. B., and Ziemann, P. J.: Contributions of organic peroxides to secondary aerosol formed from reactions of monoterpenes with O<sub>3</sub>, *Environ. Sci. Technol.*, 39, 4049–4059, 2005.
- Donahue, N. M., Robinson, A. L., Stanier, C. O., and Pandis, S. N.: Coupled partitioning, dilution, and chemical aging of semivolatile organics, *Environ. Sci. Technol.*, 40, 2635–2643, 2006.
- Dzepina, K., Volkamer, R. M., Madronich, S., Tulet, P., Ulbrich, I. M., Zhang, Q., Cappa, C. D., Ziemann, P. J., and Jimenez, J. L.: Evaluation of new secondary organic aerosol models for a case study in Mexico City, *Atmos. Chem. Phys. Discuss.*, 9, 4417–4488, 2009, <http://www.atmos-chem-phys-discuss.net/9/4417/2009/>.
- Gao, S., Keywood, M., Ng, N. L., Surratt, J., Varutbangkul, V., Bahreini, R., Flagan, R. C., and Seinfeld, J. H.: Low-molecular-weight and oligomeric components in secondary organic aerosol from the ozonolysis of cycloalkenes and alpha-pinene, *J. Phys. Chem. A*, 108, 10147–10164, 2004.
- Hallquist, M., Wenger, J. C., Baltensperger, U., Rudich, Y., Simpson, D., Claeys, M., Dommen, J., Donahue, N. M., George, C., Goldstein, A. H., Hamilton, J. F., Herrmann, H., Hoffmann, T., Iinuma, Y., Jang, M., Jenkin, M. E., Jimenez, J. L., Kiendler-Scharr, A., Maenhaut, W., McFiggans, G., Mentel, Th. F., Monod, A., Prévôt, A. S. H., Seinfeld, J. H., Surratt, J. D., Szmigielski, R., and Wildt, J.: The formation, properties and impact of secondary organic aerosol: current and emerging issues, *Atmos. Chem. Phys.*, 9, 5155–5235, 2009, <http://www.atmos-chem-phys.net/9/5155/2009/>.
- Iinuma, Y., Boge, O., Gnauk, T., and Herrmann, H.: Aerosol-chamber study of the alpha-pinene/O<sub>3</sub> reaction: influence of particle acidity on aerosol yields and products, *Atmos. Environ.*, 38, 761–773, 2004.
- Jenkin, M. E.: Modelling the formation and composition of secondary organic aerosol from  $\alpha$ - and  $\beta$ -pinene ozonolysis using MCM v3, *Atmos. Chem. Phys.*, 4, 1741–1757, 2004, <http://www.atmos-chem-phys.net/4/1741/2004/>.
- Keywood, M. D., Varutbangkul, V., Bahreini, R., Flagan, R. C., and Seinfeld, J. H.: Secondary organic aerosol formation from the ozonolysis of cycloalkenes and related compounds, *Environ. Sci. Technol.*, 38, 4157–4164, 2004.

- Kroll, J. H. and Seinfeld, J. H.: Representation of secondary organic aerosol laboratory chamber data for the interpretation of mechanisms of particle growth, *Environ. Sci. Technol.*, 39, 4159–4165, 2005.
- Müller, L., Reinnig, M.-C., Warnke, J., and Hoffmann, Th.: Unambiguous identification of esters as oligomers in secondary organic aerosol formed from cyclohexene and cyclohexene/alpha-pinene ozonolysis, *Atmos. Chem. Phys.*, 8, 1423–1433, 2008, <http://www.atmos-chem-phys.net/8/1423/2008/>.
- Ng, N. L., Kroll, J. H., Keywood, M. D., Bahreini, R., Varutbangkul, V., Flagan, R. C., Seinfeld, J. H., Lee, A., and Goldstein, A. H.: Contribution of first- versus second-generation products to secondary organic aerosols formed in the oxidation of biogenic hydrocarbons, *Environ. Sci. Technol.*, 40, 2283–2297, 2006.
- Odum, J. R., Hoffmann, T., Bowman, F., Collins, D., Flagan, R. C., and Seinfeld, J. H.: Gas/particle partitioning and secondary organic aerosol yields, *Environ. Sci. Technol.*, 30, 2580–2585, 1996.
- Pankow, J. F.: An absorption-model of gas-particle partitioning of organic-compounds in the atmosphere, *Atmos. Environ.*, 28, 185–188, 1994a.
- Pankow, J. F.: An absorption-model of the gas aerosol partitioning involved in the formation of secondary organic aerosol, *Atmos. Environ.*, 28, 189–193, 1994b.
- Pankow, J. F. and Asher, W. E.: SIMPOL.1: a simple group contribution method for predicting vapor pressures and enthalpies of vaporization of multifunctional organic compounds, *Atmos. Chem. Phys.*, 8, 2773–2796, 2008, <http://www.atmos-chem-phys.net/8/2773/2008/>.
- Pankow, J. F. and Chang, E. I.: Variation in the sensitivity of predicted levels of atmospheric organic particulate matter (OPM), *Environ. Sci. Technol.*, 42, 7321–7329, 2008.
- Pankow, J. F., Seinfeld, J. H., Asher, W. E., and Erdakos, G. B.: Modeling the formation of secondary organic aerosol. 1. Application of theoretical principles to measurements obtained in the alpha-pinene/, beta-pinene/, sabinene/, Delta(3)-carene/, and cyclohexene/ozone systems, *Environ. Sci. Technol.*, 35, 1164–1172, 2001.
- Pathak, R. K., Stanier, C. O., Donahue, N. M., and Pandis, S. N.: Ozonolysis of alpha-pinene at atmospherically relevant concentrations: Temperature dependence of aerosol mass fractions (yields), *J. Geophys. Res.-Atmos.*, 112, D03201, doi:10.1029/2006JD007436, 2007.
- Presto, A. A. and Donahue, N. M.: Investigation of alpha-pinene plus ozone secondary organic aerosol formation at low total aerosol mass, *Environ. Sci. Technol.*, 40, 3536–3543, 2006.
- Seinfeld, J. H., Erdakos, G. B., Asher, W. E., and Pankow, J. F.: Modeling the formation of secondary organic aerosol (SOA). 2. The predicted effects of relative humidity on aerosol formation in the alpha-pinene-, beta-pinene-, sabinene-, Delta(3)-Carene-, and cyclohexene-ozone systems, *Environ. Sci. Technol.*, 35, 1806–1817, 2001.
- Shilling, J. E., Chen, Q., King, S. M., Rosenoern, T., Kroll, J. H., Worsnop, D. R., McKinney, K. A., and Martin, S. T.: Particle mass yield in secondary organic aerosol formed by the dark ozonolysis of alpha-pinene, *Atmos. Chem. Phys.*, 8, 2073–2088, 2008, <http://www.atmos-chem-phys.net/8/2073/2008/>.
- Shilling, J. E., Chen, Q., King, S. M., Rosenoern, T., Kroll, J. H., Worsnop, D. R., DeCarlo, P. F., Aiken, A. C., Sueper, D., Jimenez, J. L., and Martin, S. T.: Loading-dependent elemental composition of alpha-pinene SOA particles, *Atmos. Chem. Phys.*, 9, 771–782, 2009, <http://www.atmos-chem-phys.net/9/771/2009/>.
- Stanier, C. O., Donahue, N., and Pandis, S. N.: Parameterization of secondary organic aerosol mass fractions from smog chamber data, *Atmos. Environ.*, 42, 2276–2299, 2008.
- Yu, J. Z., Cocker, D. R., Griffin, R. J., Flagan, R. C., and Seinfeld, J. H.: Gas-phase ozone oxidation of monoterpenes: Gaseous and particulate products, *J. Atmos. Chem.*, 34, 207–258, 1999.